

**FACULTY
OF MATHEMATICS
AND PHYSICS**
Charles University



**UNIVERSITY
OF TRIESTE**

DOCTORAL THESIS

Jan Matoušek

**Nucleon spin structure studies in
Drell–Yan process at COMPASS**

Department of Low Temperature Physics, Faculty of Mathematics and Physics,
Charles University
and
Department of Physics, University of Trieste

Supervisors of the thesis: prof. Miroslav Finger
prof. Anna Martin

Study programme: Physics

Study branch: Subnuclear Physics at Charles University
Nuclear, Subnuclear and Medical Physics,
XXIX cycle at University of Trieste

Prague 2018

I declare that I carried out this doctoral thesis independently, and only with the cited sources, literature and other professional sources.

I understand that my work relates to the rights and obligations under the Act No. 121/2000 Sb., the Copyright Act, as amended, in particular the fact that the Charles University has the right to conclude a license agreement on the use of this work as a school work pursuant to Section 60 subsection 1 of the Copyright Act.

In date

signature of the author

Jointly-supervised doctoral thesis

Title: Nucleon spin structure studies in Drell–Yan process at COMPASS

Author: Jan Matoušek

Department I: Department of Low Temperature Physics, Faculty of Mathematics and Physics, Charles University

Department II: Department of Physics, University of Trieste

Supervisor I: prof. Miroslav Finger (Department I)

Supervisor II: prof. Anna Martin (Department II)

Abstract:

The nucleon structure is presently described by Transverse Momentum Dependent (TMD) Parton Distribution Functions (PDFs), which generalise the collinear PDFs, adding partonic spin and transverse momentum degrees of freedom. The recent HERMES and COMPASS data on hadron production in deep inelastic scattering (SIDIS) of leptons off transversely polarised nucleons have provided a decisive validation of this framework. Nevertheless, the TMD PDFs should be studied in complementary reactions, like pp hard scattering and Drell–Yan processes.

In particular the Sivers TMD PDF, which encodes the correlation between the nucleon transverse spin and quark transverse momentum and appears in the Sivers Transverse Spin Asymmetry (TSA), is expected to have opposite sign in Drell–Yan and SIDIS. In 2015 COMPASS measured for the first time the Drell–Yan process on a transversely polarised target $\pi^- p^\uparrow \rightarrow \mu^- \mu^+ X$ to test this prediction and the results have been recently published. The main topic of my thesis is the first measurement of the TSAs weighted with the dimuon transverse momentum in this data. These asymmetries complement the conventional TSAs and their advantage is that they do not contain convolutions over intrinsic transverse momenta. My analysis work is described in detail and the results are compared with calculations based on the extraction of the Sivers function from the recently measured weighted Sivers asymmetry in SIDIS.

The thesis also contains a theoretical introduction and the description of the apparatus focused on the polarised target and its monitoring system to which I contributed. Finally, a chapter dedicated to the first original analysis in my PhD, the measurement of a Sivers-like asymmetry in the J/ψ production in SIDIS, which is related to the gluon Sivers function, is included as well.

Keywords:

nucleon structure, parton distributions, Drell–Yan, J/ψ , SIDIS, COMPASS

Doktorská práce pod dvojím vedením

Název: Studium spinové struktury nukleonu s pomocí procesu Drell–Yan v experimentu COMPASS

Autor: Jan Matoušek

Abstrakt:

Struktura nukleonů je v současné době popisována pomocí partonových distribučních funkcí závislých na příčné hybnosti (TMD PDF), které zobecňují kolineární PDF a zohledňují spin a příčnou hybnost partonů. Nedávná měření produkce hadronů v hluboce nepružném rozptylu (SIDIS) leptonů na příčně polarizovaných protonech, provedená na experimentech HERMES a COMPASS, přinesla důkazy platnosti tohoto modelu. Nicméně, je důležité studovat také další reakce, jako jsou tvrdé srážky protonů a proces Drell–Yan.

Například, Siversova TMD PDF, která popisuje korelaci spinu nukleonu a příčné hybnosti kvarku a projevuje se jako Siversova asymetrie, by měla mít opačné znaménko v procesech Drell–Yan a SIDIS. V roce 2015 COMPASS naměřil Drell–Yan proces s příčně polarizovaným terčem $\pi^- p^\uparrow \rightarrow \mu^- \mu^+ X$, aby tuto předpověď jako první ověřil. Výsledky byly nedávno publikovány. Hlavním tématem mojí práce je první měření spinových asymetrií vážených příčnou hybností mionového páru ze stejných dat. Vážené asymetrie doplňují ty klasické, jejich výhoda spočívá v absenci konvoluce přes vnitřní příčné hybnosti kvarku a antikvarku. Toto měření je detailně popsáno a výsledky jsou porovnány s výpočtem, založeným na extrakci Siversovy funkce z nedávno publikovaného měření vážené Siversovy asymetrie v SIDIS.

Kromě toho práce obsahuje teoretický úvod a popis experimentu, s důrazem na polarizovaný terč a jeho monitorovací systém, na kterém jsem se podílel. Konečně je v práci zahrnuta i kapitola popisující první analýzu dat provedenou v rámci mého doktorského studia, měření Siversovy asymetrie v produkci J/ψ v SIDIS, která souvisí se Siversovou funkcí gluonů.

Klíčová slova:

struktura nukleonu, partonové distribuce, Drell–Yan, J/ψ , SIDIS, COMPASS

Tesi di dottorato in cotutela

Titolo: Studio della struttura di spin del nucleone nel processo Drell–Yan a COMPASS

Autore: Jan Matoušek

Sommario:

La struttura partonica del nucleone è attualmente descritta dalle funzioni di distribuzione partoniche dipendenti dal momento trasverso (TMD PDF), che estendono le PDF collineari includendo lo spin e il momento trasverso dei partoni. Questi nuovi sviluppi teorici sono fortemente supportati dai recenti risultati di COMPASS e HERMES sulla produzione di adroni nella diffusione fortemente inelastica (SIDIS) di leptoni su nucleoni polarizzati trasversalmente. Naturalmente è necessario studiare le TMD PDF in processi complementari, come il Drell–Yan e la diffusione pp ad alta energia.

In particolare è previsto che la TMD PDF di Sivers, che descrive la correlazione tra lo spin trasverso del nucleone e interviene nell'asimmetria di spin trasverso (TSA) di Sivers, abbia segno opposto in SIDIS a Drell–Yan. Per verificare questa predizione fondamentale, nel 2015 COMPASS ha misurato per la prima volta in processo Drell–Yan $\pi^- p^\uparrow \rightarrow \mu^- \mu^+ X$ e i risultati sono stati pubblicati recentemente. Lo scopo principale della mia tesi è stato la misura, dagli stessi dati, delle TSA pesate con il momento trasverso. Il vantaggio di queste asimmetrie rispetto a quelle standard è che non contengono convoluzioni sui momenti trasversi dei partoni. Il mio lavoro di analisi è descritto in dettaglio nella tesi. I risultati sono confrontati con valori calcolati ottenuti estraendo la funzione di Sivers dalle corrispondenti asimmetrie misurate in SIDIS, altra parte originale del mio lavoro.

La tesi include anche un'introduzione teorica e la descrizione dell'apparato sperimentale, e in particolare del bersaglio polarizzato e del suo sistema di monitor al quale ho contribuito. Infine, un capitolo è dedicato alla prima analisi originale del mio lavoro di dottorato: la misura dell'asimmetria di Sivers per J/ψ prodotte in SIDIS, interessante perché legata alla funzione di Sivers dei gluoni.

Parole chiave:

struttura del nucleone, distribuzioni partoniche, Drell–Yan, J/ψ , SIDIS, COMPASS

I would like to express my gratitude to my supervisors and to the COMPASS Collaboration and the COMPASS Trieste group in particular. In addition, the work would have not been possible without the support of my wife and family.

Contents

| | |
|--|-----------|
| Introduction | 3 |
| 1 Theoretical introduction | 5 |
| 1.1 The structure of the nucleon | 5 |
| 1.1.1 Deep inelastic scattering | 5 |
| 1.1.2 DIS in parton model | 6 |
| 1.1.3 Parton distribution functions | 9 |
| 1.1.4 Transverse momentum dependent parton distributions | 11 |
| 1.1.5 The parton distributions in QCD | 15 |
| 1.1.6 Gluon distributions | 17 |
| 1.2 Semi-inclusive deep inelastic scattering | 17 |
| 1.2.1 Structure functions in the TMD factorisation | 18 |
| 1.2.2 Sivers asymmetry | 22 |
| 1.2.3 Access to gluon TMDs in SIDIS | 22 |
| 1.2.4 Semi-inclusive J/ψ leptonproduction | 23 |
| 1.3 Drell–Yan process | 25 |
| 1.3.1 Structure functions in the TMD approach | 28 |
| 1.3.2 Standard azimuthal asymmetries | 30 |
| 1.4 Present knowledge of the PDFs | 31 |
| 1.4.1 Collinear PDFs | 31 |
| 1.4.2 Transverse momentum dependent PDFs | 35 |
| 1.5 Disentangling the convolution by transverse momentum weighting | 38 |
| 1.5.1 Weighted Sivers asymmetry in SIDISs | 38 |
| 1.5.2 Weighting with q_T in Drell-Yan | 39 |
| 2 The COMPASS experiment | 44 |
| 2.1 Beamline and target area | 44 |
| 2.2 The polarised target | 46 |
| 2.2.1 The superconducting magnet | 47 |
| 2.2.2 The dilution cryostat | 48 |
| 2.2.3 Monitoring of the dilution cryostat | 50 |
| 2.2.4 Nuclear polarisation | 51 |
| 2.2.5 Polarisation measurement and target operation | 53 |
| 2.3 Spectrometer | 54 |
| 2.3.1 Tracking | 55 |
| 2.3.2 Particle identification and calorimetry | 56 |
| 2.3.3 Trigger | 57 |
| 2.4 Data acquisition and detector control | 58 |
| 3 Measurement of the transverse spin asymmetries | 60 |
| 3.1 Event reconstruction | 60 |
| 3.2 Data selection | 61 |
| 3.3 Extraction of transverse spin asymmetries | 61 |
| 3.3.1 Conventional TSAs | 62 |
| 3.3.2 Weighted TSA | 64 |

| | | |
|----------|--|------------|
| 3.4 | Polarisation dilution effects | 66 |
| 4 | Sivers-like asymmetry in the J/ψ leptonproduction | 68 |
| 4.1 | Event selection | 68 |
| 4.2 | Kinematic distributions | 70 |
| 4.3 | The asymmetry calculation | 71 |
| 4.4 | Background-corrected asymmetries | 74 |
| 4.5 | Results and discussion | 75 |
| 5 | Drell–Yan data analysis | 77 |
| 5.1 | Measurement of the standard TSAs | 77 |
| 5.2 | Measurement of the weighted TSAs | 80 |
| 5.2.1 | Event selection for the weighted TSAs | 80 |
| 5.2.2 | Measurement of the asymmetries | 85 |
| 5.2.3 | Systematic uncertainty | 88 |
| 6 | Results and interpretation of the weighted asymmetries | 102 |
| 6.1 | Weighted TSAs in Drell–Yan | 102 |
| 6.2 | Sivers function from SIDIS data | 105 |
| 6.3 | Projection for the weighted Sivers TSA in Drell–Yan | 113 |
| | Conclusion | 119 |
| | Bibliography | 122 |
| | List of Abbreviations | 136 |

Introduction

Since the pioneering deep inelastic scattering (DIS) experiments at SLAC in the late sixties, which discovered the constituents of hadrons — the partons, the high-energy particle collisions with large momentum transfers have continued to deliver new information about the hadron structure. The reactions can be factorised into a hard part, which can be calculated in perturbative QCD, and soft parts, which depend on hadron structure or on parton fragmentation into final state and need to be determined experimentally. In the collinear picture, with the parton transverse momentum component \mathbf{k}_T integrated over, the nucleon structure is described at leading order by three parton distribution functions (PDFs): the number density, the helicity and the transversity, which depend on the fraction x of the nucleon momentum carried by the parton and on the squared momentum transfer Q^2 . Beyond this collinear approximation the description has been generalised to include \mathbf{k}_T and all possible correlations among parton spin, \mathbf{k}_T , and parent nucleon spin. At leading twist the correlations are encoded in eight transverse momentum dependent (TMD) PDFs, which depend on x , Q^2 , and \mathbf{k}_T^2 . The recent HERMES and COMPASS data on semi-inclusive deep inelastic scattering (SIDIS) of leptons off transversely polarised nucleons $\ell N^\uparrow \rightarrow \ell' h X$ provide important experimental evidence to validate this theoretical framework. In other words, the observed Transverse Spin azimuthal Asymmetries (TSA) can be attributed to correlations between the parent nucleon spin and quark transverse polarisation (transversity PDF) or quark \mathbf{k}_T (Sivers TMD PDF).

This thesis focuses on the Sivers function, which can be related to orbital angular momentum of partons. In SIDIS, the Sivers function of quarks gives rise to a left–right asymmetry (with respect to the plane defined by the exchanged virtual photon and the nucleon spin direction) in the production of the final-state hadrons. It has recently been measured to be positive for positive hadrons produced on protons by HERMES and COMPASS. On the contrary, little is known experimentally about the gluon Sivers function. One of the possible ways of accessing it is a measurement of a Sivers-like asymmetry of hadrons, produced in lepton scattering off transversely polarised nucleons via the photon–gluon fusion (PGF) process $\gamma^* g \rightarrow q\bar{q}$. This can be done utilising the fact that the leading process $\gamma^* q \rightarrow q$ is suppressed in production of hadrons characterised by a large transverse momentum. Results obtained using this approach were recently published by COMPASS. An alternative option to single out the PGF process is to look for heavy-flavoured quark pairs in the production of the open-charm, or charmonium. The latter approach inspired the first measurement of a Sivers-like asymmetry in J/ψ production using COMPASS data collected in 2010. It is the first original analysis described in this thesis, namely in Chapter 4.

Most of the thesis is, however, dedicated to the quark Sivers function and to its measurement in Drell–Yan lepton pair production in hadron collisions. In spite of the achievements of the TMD framework in the description of SIDIS, it is crucial to investigate complementary reactions, like pp hard scattering and Drell–Yan processes. These measurements allow for an important test of the validity of the TMD PDF framework, which predicts that the two T-odd TMD PDFs — the Sivers and Boer–Mulders distributions — bear opposite signs when they are

measured in SIDIS and Drell–Yan reactions or in W^\pm and Z-boson production in pp collisions. Results of the W^\pm and Z production have been recently published by the STAR experiment at RHIC. The test of the fundamental QCD prediction of the change of sign of the Sivers function has been the main motivation of the COMPASS Drell–Yan programme. In 2015 COMPASS has done the first-ever polarised Drell–Yan experiment measuring the reaction $\pi^- p^\uparrow \rightarrow \mu^+ \mu^- X$ with a 190 GeV/c pion beam and a transversely polarised proton target. The SIDIS and Drell–Yan measurements at COMPASS have thus been done in almost the same kinematic domain. The results, consistent with the change of sign prediction, have been published very recently.

In the extraction of the TMD PDFs from the measured asymmetries one faces the problem of the convolutions over transverse momenta. In SIDIS, the outgoing hadron transverse momentum originates in the struck quark intrinsic \mathbf{k}_T and in the fragmentation process and in the asymmetries the TMD PDFs are convoluted with TMD fragmentation functions. Similarly, the transverse momentum of the Drell–Yan dilepton is a sum of the transverse momenta of quark and antiquark from the two colliding hadrons and in the asymmetries the convolutions of the corresponding PDFs appear. The usual solution to the problem is to assume a certain functional form (often Gaussian) of the PDF dependence on \mathbf{k}_T^2 . A different approach proposed in the late nineties consists in weighting of the spin-dependent part of the cross-sections with appropriate powers of the outgoing hadron transverse momentum P_{hT} in SIDIS or dilepton transverse momentum q_T in Drell–Yan, that is to measure so-called weighted TSAs. The P_{hT} -weighted TSAs in SIDIS were first extracted in 2005 by HERMES using only part of the final statistics. Recently, COMPASS has measured the P_{hT}/z -weighted Sivers asymmetry using the 2010 SIDIS data and the results are expected to be published soon. In this thesis, the weighted TSAs in the Drell–Yan process are measured for the first time using the COMPASS data from 2015. Thanks to the weighting, the interpretation of the asymmetries is quite direct. The weighted Sivers asymmetry is compared with the estimate obtained using the Sivers function extracted from the weighted TSA measured in SIDIS. The result, which provides useful hints for the future work, is described in Chapter 6.

The thesis is organised as follows: in Chapter 1 the theoretical framework and the present experimental knowledge on TMD PDFs are summarised. The apparatus for the Drell–Yan measurement is described in Chapter 2. A particular attention is paid to the polarised target and its monitoring system, which has been upgraded with my contribution as the technical part of the PhD. Chapter 3 is dedicated to the data analysis in general and in particular to the methods used for the extraction of both the standard and weighted TSAs. In Chapter 4 the measurement of the Sivers-like asymmetry in the J/ψ lepton production is discussed. The analysis of the Drell–Yan data and the extraction of the weighted asymmetries is described in Chapter 5. This has been the central part of the PhD work. The results are discussed in Chapter 6 focusing on the Sivers asymmetry. In addition, this Chapter describes the first extraction of the Sivers function from the SIDIS weighted TSA, which is utilised to provide an estimate for the corresponding asymmetry in Drell–Yan process.

1. Theoretical introduction

1.1 The structure of the nucleon

1.1.1 Deep inelastic scattering

Before we introduce the parton distribution functions, which describe the nucleon structure, it is useful to discuss the process that lead to their formulation — the deep inelastic scattering (DIS) of leptons off nucleons

$$\ell(l) + N(P) \rightarrow \ell(l') + X. \quad (1.1)$$

We denote by P the momentum of the target nucleon and by l and l' the momenta of the incident and scattered lepton. The lowest-order diagram of the process is shown in Fig. 1.1(a). In the following, we neglect the lepton mass, unless stated otherwise.

The initial state of the reaction is characterised by the centre-of-mass energy squared $s = (l + P)^2$, or the lepton beam energy E . The final state is commonly described by relativistic invariants

$$Q^2 = -q^2 = -(l - l')^2 = 2EE'(1 - \cos \theta), \quad x = \frac{Q^2}{2P \cdot q}, \quad (1.2)$$

$$y = \frac{P \cdot q}{P \cdot l} = \frac{E_{\text{lab}} - E'_{\text{lab}}}{E_{\text{lab}}}, \quad W^2 = (P + q)^2. \quad (1.3)$$

The variable Q^2 is usually preferred over the squared mass of the exchanged space-like photon q^2 , which is negative. θ is the scattering angle. Both the Bjorken x and the inelasticity y take on values between 0 and 1. W has an interpretation as the invariant mass of the hadronic system X . Only two of the four variables are independent. Usually (x, Q^2) or (x, y) are used to describe the final state of the DIS reaction. In the case of an elastic scattering, only one variable is independent (it is easy to find that $x = 1$ and $W = M$, the mass of the nucleon). The scattering is called deep inelastic, if $Q^2 \gg M^2$ and $E' - E \gg M$.

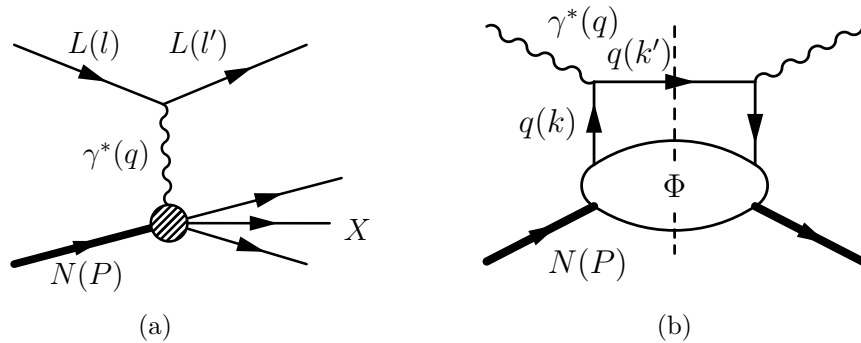


Figure 1.1: The DIS process at leading order (a) and the hadronic tensor in parton model, represented by the so-called handbag diagram (b). The ovals denote non-perturbative contributions.

The DIS cross-section is [1]

$$d\sigma = \frac{1}{4P \cdot l} \frac{e^4}{Q^4} L_{\mu\nu} W^{\mu\nu} 2\pi \frac{d^3\mathbf{l}'}{(2\pi)^3 2E'}. \quad (1.4)$$

The leptonic tensor $L_{\mu\nu}$ is defined as (lepton mass m is retained here, and we sum over final state lepton spin $s_{\ell'}$)

$$\begin{aligned} L_{\mu\nu} &= \sum_{s_{\ell'}} [\bar{u}(l', s_{\ell'}) \gamma_{\mu} u(l, s_{\ell})]^* [\bar{u}(l', s_{\ell'}) \gamma_{\nu} u(l, s_{\ell})] \\ &= \text{Tr} \left[(l + m) \frac{1 + \gamma_5 \not{s}_{\ell}}{2} \gamma_{\mu} (l' + m) \gamma_{\nu} \right] \\ &= 2 \left(l_{\mu} l'_{\nu} + l_{\nu} l'_{\mu} - g_{\mu\nu} l \cdot l' \right) + 2m \varepsilon_{\mu\nu\rho\sigma} s_{\ell}^{\rho} q^{\sigma}, \end{aligned} \quad (1.5)$$

where $u(l)$ is the usual Dirac bi-spinor, satisfying the free-particle Dirac equation $(\not{p} - m)u(p) = 0$. The tensor can be decomposed into a symmetric and an anti-symmetric part under $\mu \leftrightarrow \nu$ interchange. Only the latter depends on the lepton polarisation. When the lepton is polarised longitudinally, its spin vector is $s_{\ell}^{\mu} = (\lambda_{\ell}/m)l^{\mu} = \mathcal{O}(E/m)$, where $\lambda_{\ell} = \pm 1$. When it is polarised transversely, the spin vector is $\mathcal{O}(1)$, so the antisymmetric part is suppressed by a factor m/E . Therefore, we discuss only the cases of unpolarised or longitudinally polarised leptons.

The hadronic tensor $W^{\mu\nu}$ is a non-perturbative quantity. Phenomenologically, it can be written as a general Lorentz tensor, which can be constructed from P , q , the nucleon polarisation S , and basic tensors of rank two. Parity conservation and gauge invariance restrict the number of independent components, so the tensor can be written in terms of four real, dimension-less structure functions¹ F_1 , F_2 , g_1 , and g_2 . The functions depend on two variables, usually x and Q^2 are used. The first two parametrise the symmetric part of $W^{\mu\nu}$, the latter two the anti-symmetric one.

Averaging over the lepton beam and target nucleon spins, the cross-section is given by the symmetric parts of the two tensors and reads [2]

$$\frac{d\sigma}{dx dQ^2} = \frac{4\pi\alpha^2}{Q^4} \left[y^2 F_1(x, Q^2) + \left(1 - y - \frac{xyM^2}{s} \right) \frac{F_2(x, Q^2)}{x} \right]. \quad (1.6)$$

The mild dependence of F_1 and F_2 on Q^2 , discovered at SLAC [3, 4] and usually referred to as Bjorken scaling, together with the rapid decrease of the elastic eN scattering cross-section with Q^2 , lead to the formulation of the parton model [5].

Differences of cross-sections with opposite nucleon polarisation probe the anti-symmetric parts of the leptonic and hadronic tensors. When the spin \mathbf{S} is parallel to the virtual photon momentum \mathbf{q} , the difference depends only on g_1 . When it is perpendicular, it probes the sum $g_1 + g_2$. Note that in both cases, the lepton needs to be longitudinally polarised. [1]

1.1.2 DIS in parton model

In the parton model the DIS off nucleons is pictured as a scattering off quasi-free point-like nucleon constituents — partons. The cross-section is written as

¹In most of the thesis, the symbol g_1 is reserved for parton helicity distribution following the Amsterdam notation. When speaking of the structure function, it is always explicitly stated.

an incoherent sum of cross-sections from scattering on the partons, which are treated as free, and any interaction between the struck parton and the nucleon remnants is ignored. At leading order (LO) only charged partons, which can be identified with quarks and antiquarks, contribute. The hadronic tensor $W^{\mu\nu}$ is then represented by the handbag diagram shown in Fig. 1.1(b). The contribution from quarks reads [1] (the one from antiquarks being analogous)

$$W^{\mu\nu} = \frac{1}{2\pi} \sum_q e_q^2 \sum_X \int \frac{d^3 \mathbf{P}_X}{(2\pi)^3 2E_X} \int d^4 k \int d^4 k' \delta(k'^2) \delta^{(4)}(P - k - P_X) \times \delta^{(4)}(k + q - k') [\bar{u}(k') \gamma^\mu \phi(k; P, S)]^* [\bar{u}(k') \gamma^\nu \phi(k; P, S)], \quad (1.7)$$

where e_q is the charge of a quark of flavour² q in units of positron charge, \bar{u} is the free field quark bi-spinor, and ϕ is a Dirac vector of matrix elements of the quark field $\psi(\xi) = e^{-ik \cdot \xi} u(k)$ between the nucleon and its remnant

$$\phi_i(k; P, S) = \langle X | \psi_i(0) | PS \rangle. \quad (1.8)$$

Note, that we omit the flavour index q in the case of ϕ , ψ , and Φ .

We define the quark–quark correlation matrix as

$$\Phi_{ij} = \sum_X \int \frac{d^3 \mathbf{P}_X}{(2\pi)^3 2E_X} (2\pi)^4 \delta^{(4)}(P - k - P_X) \langle PS | \psi_j(0) | X \rangle \langle X | \psi_i(0) | PS \rangle, \quad (1.9)$$

which can be substituted to the definition of the hadronic tensor, obtaining [1]

$$W^{\mu\nu} = \sum_q e_q^2 \int \frac{d^4 k}{(2\pi)^4} \delta[(k + q)^2] \text{Tr}[\Phi \gamma^\mu (\not{k} + \not{q}) \gamma^\nu]. \quad (1.10)$$

We work in a frame, where the virtual photon and nucleon are collinear and nucleon momentum is large (so-called infinite momentum frame). It is convenient to use the Sudakov decomposition of vectors. An arbitrary vector v^μ is parametrised as

$$v^\mu = (v \cdot p) p^\mu + (v \cdot n) n^\mu + v_{\text{T}}^\mu, \quad v_{\text{T}}^\mu = (0, \mathbf{v}_{\text{T}}, 0), \quad (1.11)$$

where p^μ and n^μ are light-like vectors (Λ is an arbitrary constant)

$$p^\mu = \frac{1}{\sqrt{2}}(\Lambda, 0, 0, \Lambda), \quad n^\mu = \frac{1}{\sqrt{2}}(\Lambda^{-1}, 0, 0, -\Lambda^{-1}). \quad (1.12)$$

The vectors have the properties $p \cdot n = 1$ and $p^- = 0 = n^+$, where $v^\pm = 1/\sqrt{2}(v^0 \pm v^3)$ denote the components of a vector v^μ in the light-cone coordinates. The modulus squared of an arbitrary vector can be written as $v^2 = 2(v \cdot p)(v \cdot n) - \mathbf{v}_{\text{T}}^2$.

In this decomposition, we can parametrise the nucleon and virtual photon momenta as

$$P^\mu = p^\mu + \frac{M^2}{2} n^\mu \approx p^\mu, \quad q^\mu \approx (P \cdot q) n^\mu - x p^\mu, \quad (1.13)$$

where we have utilised $P^+ \gg M$ and the DIS condition $Q^2 \gg M^2$. The quark momentum is decomposed as

$$k^\mu = \alpha P^\mu + \frac{k^2 + \mathbf{k}_{\text{T}}^2}{2\alpha} + k_{\text{T}}^\mu \approx \alpha P^\mu + k_{\text{T}}^\mu. \quad (1.14)$$

²The letter q denotes both quark flavour and virtual photon momentum.

The approximate equality is a property of the parton model, where the handbag-diagram contribution to the hadronic tensor is assumed to be dominated by small values of k^2 and \mathbf{k}_T^2 . It corresponds to the fact that the partons are almost free inside of the nucleon and their Fermi motion is slow as compared to the nucleon velocity in the chosen frame. The on-shell condition of the outgoing quark implies

$$\delta[(k+q)^2] \approx \delta[-Q^2 + 2\alpha P \cdot q] = \frac{1}{2P \cdot q} \delta(\alpha - x) = \frac{1}{2P \cdot q} \delta\left(\frac{k^+}{P^+} - x\right), \quad (1.15)$$

that is, the Bjorken variable x is the fraction of the nucleon momentum, carried by the struck parton, $k^\mu \approx xP^\mu + k_T^\mu$. In addition, the transverse component is effectively integrated over in the inclusive DIS and may be omitted as well.

The hadronic tensor in Eq. (1.10) can be split into the symmetric and anti-symmetric parts, which play role in the unpolarised and polarised DIS, respectively. The symmetric part can be written, using $k^\mu + q^\mu \approx (P \cdot q)n^\mu$, as [1]

$$W_{\mu\nu}^{(S)} = \frac{1}{2} \sum_q e_q^2 \int \frac{d^4k}{(2\pi)^4} \delta\left(x - \frac{k^+}{P^+}\right) [n_\mu \text{Tr}(\Phi\gamma_\nu) + n_\nu \text{Tr}(\Phi\gamma_\mu) + g_{\mu\nu} n^\rho \text{Tr}(\Phi\gamma_\rho)]. \quad (1.16)$$

At leading twist (that is twist-two, considering only contributions $\mathcal{O}(P^+)$ in the infinite momentum frame) there is only one vector available: $p^\mu \approx P^\mu$ (as $n^\mu = \mathcal{O}(1/P^+)$ and $k \approx xp^\mu$). Therefore we parametrise the vector quantity [1]

$$\frac{1}{2} \int \frac{d^4k}{(2\pi)^4} \delta\left(x - \frac{k^+}{P^+}\right) \text{Tr}(\gamma^\mu \Phi) = f_1(x) P^\mu, \quad (1.17)$$

where $f_1(x)$ is the quark number density, also known as the unpolarised quark parton distribution function (PDF). Finally, we obtain for the hadronic tensor

$$W_{\mu\nu}^{(S)} = \sum_q e_q^2 (n_\mu P_\nu + n_\nu P_\mu - g_{\mu\nu}) f_1^q(x). \quad (1.18)$$

The structure functions can be written in terms of f_1^q [1]

$$F_2(x) = 2xF_1(x) = \sum_q e_q^2 x [f_1^q(x) + f_1^{\bar{q}}(x)], \quad (1.19)$$

where we have added the antiquark distributions $f_1^{\bar{q}}$ for completeness, which are analogous to the quark ones. The proportionality of F_1 and F_2 is called Callan–Gross relation.

The parton model expression for the anti-symmetric part of the hadronic tensor is (using again $k^\mu + q^\mu \approx (P \cdot q)n^\mu$) [1]

$$W_{\mu\nu}^{(A)} = \frac{1}{2} \sum_q e_q^2 \int \frac{d^4k}{(2\pi)^4} \delta\left(x - \frac{k^+}{P^+}\right) \varepsilon_{\mu\nu\rho\sigma} n^\rho \text{Tr}(\gamma^\sigma \gamma_5 \Phi). \quad (1.20)$$

This time we are dealing with a pseudo-vector quantity. At leading twist, the only one available is the longitudinal part (with respect to the photon momentum) of the nucleon spin $S_L^\mu = (\lambda_N/M)P^\mu = \mathcal{O}(P^+)$ (its transverse part S_T is $\mathcal{O}(1)$). The anti-symmetric part of the hadronic tensor is therefore parametrised as [1]

$$W_{\mu\nu}^{(A)} = \lambda_N \varepsilon_{\mu\nu\rho\sigma} n^\rho p^\sigma \sum_q e_q^2 \Delta f^q(x), \quad (1.21)$$

where $\Delta f^q(x)$ is the longitudinal polarisation (helicity) distribution of quarks. We can see that at leading twist only longitudinal polarisation contributes to DIS. The transverse nucleon polarisation manifests itself only at twist three level [1].

In the following, we observe the Amsterdam (or Jaffe–Ji–Mulders) classification of the parton distribution functions, where the parton helicity distribution is denoted g_1^q . Only in this Section, to prevent confusion with the structure function g_1 , we use the alternative notation Δf^q . The structure function g_1 , including the contribution of anti-quarks, in the parton model reads [1]

$$g_1(x) = \frac{1}{2} \sum_q e_q^2 [\Delta f^q(x) + \Delta f^{\bar{q}}(x)]. \quad (1.22)$$

1.1.3 Parton distribution functions

In the previous Section, two leading twist parton distribution functions (PDFs) — the quark number density and helicity — have been introduced to understand the deep-inelastic scattering of leptons off nucleons. In other processes, different distribution functions that can be derived from the quark–quark correlation matrix Φ may play a role. The matrix Φ has been defined in Eq. (1.9) and in Fig. 1.1(b). It can be written in a more compact form as [1]

$$\Phi_{ij}(k, P, S) = \int d^4\xi e^{ik \cdot \xi} \langle PS | \bar{\psi}_j(0) \psi_i(\xi) | PS \rangle, \quad (1.23)$$

where the indices i, j label Dirac components of the quark fields, summation over colour is implicit, and flavour label is omitted. The matrix can be constructed, in general, from the combinations of the basic tensors of rank two, the vectors k^μ , P^μ , and the pseudo-vector S^μ . Requiring hermiticity and parity invariance the number of free parameters reduces to twelve.

At leading twist in the infinite momentum frame $k^\mu \approx xP^\mu + k_T^\mu$ and $S^\mu \approx (\lambda_N/M)P^\mu + S_T^\mu$. Ignoring the quark transverse momentum for now (integrated over in DIS), the most general form of the matrix is characterised by only three free real parameters $A_n(k^2, k \cdot P)$, [1]

$$\Phi(k, P, S) = \frac{1}{2} [A_1 \not{P} + A_2 \lambda_N \gamma_5 \not{P} + A_3 \not{P} \gamma_5 \not{S}_T]. \quad (1.24)$$

After integration over k with the constraint $x = k^+/P^+$, the functions A_n yield the quark number density $f_1(x)$, helicity $g_1(x)$ (or $\Delta f(x)$), which we know from the DIS, and a new distribution $h_1(x)$, called transversity. Using the definition of the quark–quark correlation matrix and fixing $\lambda_N = 1$ and $\mathbf{S}_T = (1, 0, 0)$, they can be written as [1]

$$f_1(x) = \frac{1}{2} \int \frac{d^4k}{(2\pi)^4} \text{Tr}(\gamma^+ \Phi) \delta(k^+ - xP^+) \quad (1.25)$$

$$g_1(x) = \frac{1}{2} \int \frac{d^4k}{(2\pi)^4} \text{Tr}(\gamma^+ \gamma_5 \Phi) \delta(k^+ - xP^+) \quad (1.26)$$

$$h_1(x) = \frac{1}{2} \int \frac{d^4k}{(2\pi)^4} \text{Tr}(\gamma^+ \gamma^1 \gamma_5 \Phi) \delta(k^+ - xP^+) \quad (1.27)$$

It can be shown, that the leading twist distribution functions have probabilistic interpretations: $f_1^q(x)$ is the probability of finding inside a nucleon with

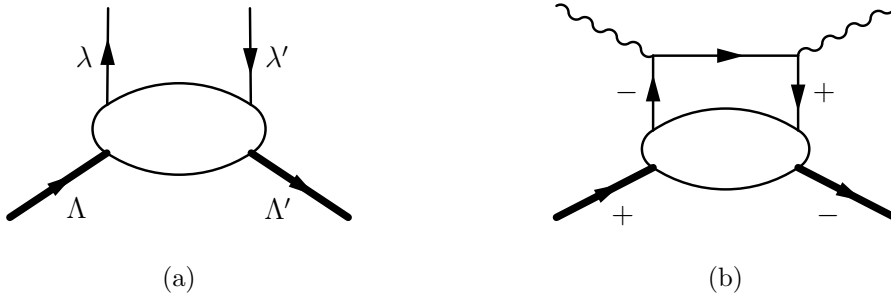


Figure 1.2: (a) The quark–nucleon forward amplitude $\mathcal{A}_{\Lambda\lambda,\Lambda'\lambda'}$ in the helicity basis. (b) The helicity amplitude forbidden by chirality conservation. The labels on the figures denote helicities.

momentum P^μ a quark with flavour a and longitudinal momentum xP^μ . The helicity $g_1^q(x)$ gives the difference of probabilities of finding a quark with helicity $+$ and $-$ assuming the nucleon has helicity $+$. Similarly, the transversity $h_1^q(x)$ is the number density of quarks with transverse polarisation \uparrow minus the number density of quarks polarised \downarrow , assuming the parent nucleon polarisation \uparrow . An important notice is that the helicity allows for the probabilistic interpretation only in the longitudinal polarisation basis, while the transversity has the probabilistic meaning only in the transverse polarisation basis. In the case of antiquarks, the correlation matrix is $\bar{\Phi}$, with the roles of ψ and $\bar{\psi}$ interchanged. The probabilistic interpretation remains the same [1].

When the correlation matrix $\Phi(k, P, S)$ is integrated over k , we obtain

$$\Phi = \int d^4k \Phi(k, P, S) = \frac{1}{2} \left[g_V \not{P} + g_A \lambda_N \gamma_5 \not{P} + g_T \not{P} \gamma_5 \not{S}_T \right], \quad (1.28)$$

where the three constants g_V , g_A , and g_T are called vector, axial, and tensor charge. The vector charge is actually the valence number. They can be calculated from the quark and antiquark distribution functions as [1]

$$g_V^q = \int_0^1 dx \left[f_1^q(x) - f_1^{\bar{q}}(x) \right], \quad (1.29)$$

$$g_A^q = \int_0^1 dx \left[g_1^q(x) + g_1^{\bar{q}}(x) \right], \quad (1.30)$$

$$g_T^q = \int_0^1 dx \left[h_1^q(x) - h_1^{\bar{q}}(x) \right]. \quad (1.31)$$

The DIS hadronic tensor is related to the imaginary part of the forward virtual Compton scattering amplitude via the optical theorem. Therefore, the leading twist quark distribution functions can be written in terms of quark–nucleon forward amplitudes in the helicity basis $\mathcal{A}_{\Lambda\lambda,\Lambda'\lambda'}$, where the subscripts denote nucleon and quark helicities. The amplitude is illustrated in Fig. 1.2(a). Helicity conservation $\lambda + \Lambda = \lambda' + \Lambda'$ and parity invariance lead to only three independent amplitudes: $\mathcal{A}_{++,++}$, $\mathcal{A}_{+,-,+}$, and $\mathcal{A}_{+,-,-}$. In the case of the first two the quark helicity is preserved ($\lambda = \lambda'$, while the last one flips the quark helicity. The

relations to the quark distribution functions read

$$f_1(x) \propto \mathfrak{S}(\mathcal{A}_{++,+} + \mathcal{A}_{+-,+}), \quad (1.32)$$

$$g_1(x) \propto \mathfrak{S}(\mathcal{A}_{++,+} - \mathcal{A}_{+-,+}), \quad (1.33)$$

$$h_1(x) \propto \mathfrak{S}(\mathcal{A}_{+,-,-}). \quad (1.34)$$

Now it is easy to understand, why the transversity distribution is absent in the inclusive DIS. It would be linked to the Compton process shown in Fig. 1.2(b), which is forbidden by the mass-less quark helicity (i.e. chirality) conservation in the QED vertices. To access h_1 , one needs to study other processes. The role of transversity was first realised in the case of a double transversely polarised Drell–Yan process [6], but this channel has not been studied so far. Later, its presence in semi-inclusive DIS was suggested [7].

In addition, Eq. (1.34) tells us that there is no leading twist transversity distribution of gluons in nucleons, as the helicity conservation condition implies $\Lambda - \Lambda' = \lambda' - \lambda$, which can not be met for the spin-half nucleon and spin-one gluon if the helicity of the gluon is flipped.

From the probabilistic meaning of the leading twist distribution functions it is clear that $f_1(x) > 0$, $|g_1(x)| \leq f_1(x)$ and $|h_1(x)| \leq f_1(x)$. Another restriction can be derived from their relations (1.32–1.34) to the quark–nucleon forward amplitudes, the Soffer inequality [8]

$$f_1(x) + g_1(x) \geq 2|h_1(x)|. \quad (1.35)$$

1.1.4 Transverse momentum dependent parton distributions

Both in semi-inclusive deep inelastic scattering (SIDIS) and Drell–Yan processes the transverse motion of quarks in nucleons can not be neglected, as in these cases we measure the transverse momentum of a particle that inherits part of the quark intrinsic transverse momentum. The quark momentum is now given by

$$k^\mu \approx xP^\mu + k_{\text{T}}^\mu, \quad (1.36)$$

where $k_{\text{T}}^\mu = \mathcal{O}(1)$, i.e. suppressed by one power of P^+ with respect to the longitudinal component. With this additional vector at hand, the number of free parameters needed to describe the quark–quark correlation matrix (1.23) at leading twist increases, [1]

$$\begin{aligned} \Phi(k, P, S) = \frac{1}{2} & \left[\not{P} A_1 + \varepsilon_{\mu\nu\rho\sigma} \gamma^\mu \frac{P^\nu k_{\text{T}}^\rho S_{\text{T}}^\sigma}{M} \tilde{A}_1 \right. \\ & + \lambda_N \gamma_5 \not{P} A_2 + \frac{\mathbf{k}_{\text{T}} \cdot \mathbf{S}_{\text{T}}}{M} \gamma_5 \not{P} \tilde{A}_2 \\ & + \not{P} \gamma_5 \not{S}_{\text{T}} A_3 + \frac{\mathbf{k}_{\text{T}} \cdot \mathbf{S}_{\text{T}}}{M^2} \not{P} \gamma_5 \not{k}_{\text{T}} \tilde{A}_3 + \frac{\lambda_N}{M} \not{P} \gamma_5 \not{k}_{\text{T}} \tilde{A}_4 \\ & \left. + \varepsilon_{\mu\nu\rho\sigma} \gamma^\mu \gamma^\nu \gamma_5 \frac{P^\rho k_{\text{T}}^\sigma}{M} \tilde{A}_5 \right]. \end{aligned} \quad (1.37)$$

We have introduced new real functions $\tilde{A}_n(k^2, k \cdot P)$. In total, the matrix is now described by 8 functions. Powers of the nucleon mass M are present to keep

the functions dimension-less. We can project the vector, axial vector, and tensor components

$$\frac{1}{2P^+} \text{Tr}(\gamma^+ \Phi) = A_1 - \frac{\varepsilon_{ij} k_T^i S_T^j}{M} \tilde{A}_1, \quad (1.38)$$

$$\frac{1}{2P^+} \text{Tr}(\gamma^+ \gamma_5 \Phi) = \lambda_N A_2 + \frac{\mathbf{k}_T \cdot \mathbf{S}_T}{M} \tilde{A}_2, \quad (1.39)$$

$$\frac{1}{2P^+} \text{Tr}(i\sigma^{i+} \gamma_5 \Phi) = S_T^i A_3 + \frac{\mathbf{k}_T \cdot \mathbf{S}_T}{M^2} k_T^i \tilde{A}_3 + \frac{\lambda_N}{M} k_T^i \tilde{A}_4 - \frac{\varepsilon^{ij} k_{Tj}}{M} \tilde{A}_5, \quad (1.40)$$

where indices i and j label transverse coordinates and $\sigma^{\mu\nu} = \frac{i}{2}(\gamma^\mu \gamma^\nu - \gamma^\nu \gamma^\mu)$. Integration of the vector and axial vector components over \mathbf{k}_T is survived only by the A_1 and $\lambda_N A_2$ terms, respectively. Further integration over k^+ and k^- with the constraint $k^+ = xP^+$ yields the familiar number density and helicity distributions. However, in the case of the tensor component there is a \mathbf{k}_T -even part in one of the new terms, as

$$\int d^2 \mathbf{k}_T (\mathbf{k}_T \cdot \mathbf{S}_T) k_T^i = \int d^2 \mathbf{k}_T k_{Tj} S_T^j k_T^i = \frac{\mathbf{k}_T^2}{2} S_T^i. \quad (1.41)$$

The \mathbf{k}_T -even part needs to be included in the definition of the \mathbf{k}_T -integrated transversity distribution (see Eq. (1.27))

$$\begin{aligned} h_1(x) &= \frac{1}{2} \int \frac{d^4 k}{(2\pi)^4} \text{Tr}(\gamma^+ \gamma^i \gamma_5 \Phi) \delta(k^+ - xP^+) \\ &= \int \frac{d^4 k}{(2\pi)^4} \left(A_3 + \frac{\mathbf{k}_T^2}{2M^2} \tilde{A}_3 \right) \delta(k^+ - xP^+). \end{aligned} \quad (1.42)$$

Therefore, the right-hand-side of Eq. (1.40) is rearranged according to

$$(\mathbf{k}_T \cdot \mathbf{S}_T) k_T^i = -k_T^i k_T^j S_{Tj} = \frac{\mathbf{k}_T^2}{2} S_T^i - \left(k_T^i k_T^j + \frac{\mathbf{k}_T^2}{2} g^{ij} \right) S_{Tj}. \quad (1.43)$$

If we integrate only over the longitudinal components k^+ , k^- and not over the transverse ones, we obtain the eight transverse momentum dependent (TMD) PDFs. Three of them are just generalisations of the collinear PDFs, the others are new. First we adopt the standard notation [1]

$$\begin{aligned} \Phi^{[\Gamma]} &= \frac{1}{2} \int \frac{dk^+ dk^-}{(2\pi)^4} \text{Tr}(\Gamma \Phi) \delta(k^+ - xP^+) \\ &= \int \frac{d\xi^- d^2 \boldsymbol{\xi}_T}{2(2\pi)^3} e^{i(xP^+ \xi^- - \mathbf{k}_T \cdot \boldsymbol{\xi}_T)} \langle PS | \bar{\psi}(0) \Gamma \psi(0, \xi^-, \boldsymbol{\xi}_T) | PS \rangle. \end{aligned} \quad (1.44)$$

Now we can write for the vector component

$$\Phi^{[\gamma^+]} = \mathcal{P}_{q/N}(x, \mathbf{k}_T) = f_1(x, \mathbf{k}_T^2) - \frac{\varepsilon_{ij} k_T^i S_T^j}{M} f_{1T}^\perp(x, \mathbf{k}_T^2), \quad (1.45)$$

where $\mathcal{P}_{q/N}$ is the probability of finding a quark with longitudinal momentum fraction x and transverse momentum \mathbf{k}_T in the nucleon, and $f_{1T}^\perp(x, \mathbf{k}_T^2)$ is a new TMD PDF, called Sivers function. It describes the correlation between the quark

transverse momentum and nucleon transverse spin. If the Sivers function was positive and we looked from the infinite momentum frame towards the quark, more quarks would appear to be moving to the left than to the right. Defining azimuthal angles of the nucleon transverse polarisation and quark transverse momentum as³

$$\mathbf{S}_T = (|\mathbf{S}_T| \cos \phi_S, -|\mathbf{S}_T| \sin \phi_S), \quad \mathbf{k}_T = (|\mathbf{k}_T| \cos \phi_k, -|\mathbf{k}_T| \sin \phi_k), \quad (1.46)$$

we obtain for the probability

$$\mathcal{P}_{q/N\uparrow}(x, \mathbf{k}_T) - \mathcal{P}_{q/N\downarrow}(x, \mathbf{k}_T) = 2|\mathbf{S}_T| \frac{|\mathbf{k}_T|}{M} \sin(\phi_S - \phi_k) f_{1T}^\perp(x, \mathbf{k}_T^2). \quad (1.47)$$

The history of the Sivers function is rather interesting. It was proposed a long time ago [9] to explain azimuthal asymmetries observed in hadron production in single transversely polarised hard scatterings. Soon after it was argued to be zero, as $\varepsilon_{ij} k_T^i S_T^j = (\mathbf{k}_T \times \mathbf{S}_T) \cdot \mathbf{P}/|\mathbf{P}|$ is time-reversal odd. Such a time reversal is sometimes referred to as naive, as only the directions of momenta are reversed, but the initial and final states are not interchanged [10]. However, later it has been shown that in the QCD-improved parton model (Sec. 1.1.5) it does not have to vanish, but that it is process-dependent [11]. Another interesting point is that it may be linked to an axial asymmetry of an impact-parameter-dependent parton distribution, i.e. distribution of quarks in transverse position space, which in turn would be induced by orbital angular momentum of quarks [12].

The axial component integrated over k^+ and k^- reads

$$\Phi^{[\gamma^+\gamma_5]} = \mathcal{P}_{q/N}(x, \mathbf{k}_T) \lambda(x, \mathbf{k}_T) = \lambda_N g_1(x, \mathbf{k}_T^2) + \frac{\mathbf{k}_T \cdot \mathbf{S}_T}{M} g_{1T}(x, \mathbf{k}_T^2), \quad (1.48)$$

where $\lambda(x, \mathbf{k}_T)$ is the quark helicity density and $g_{1T}(x, \mathbf{k}_T^2)$ is a new TMD PDF, which describes longitudinal polarisation of quarks in a transversely polarised nucleon. The two contributions to the longitudinal polarisation of quarks can be written in terms of probabilities as

$$\mathcal{P}_{q+/N+}(x, \mathbf{k}_T) - \mathcal{P}_{q-/N+}(x, \mathbf{k}_T) = \lambda_N g_1(x, \mathbf{k}_T^2), \quad (1.49)$$

$$\mathcal{P}_{q+/N\uparrow}(x, \mathbf{k}_T) - \mathcal{P}_{q-/N\uparrow}(x, \mathbf{k}_T) = |\mathbf{S}_T| \frac{|\mathbf{k}_T|}{M} \cos(\phi_S - \phi_k) g_{1T}(x, \mathbf{k}_T^2). \quad (1.50)$$

Finally, let us have a look on quark transverse polarisation, which is described by the vector

$$\mathbf{s}_T = (|\mathbf{s}_T| \cos \phi_s, -|\mathbf{s}_T| \sin \phi_s), \quad (1.51)$$

where $|\mathbf{s}_T| = 1$ in the case of full quark transverse polarisation. The tensor component has the richest structure,

$$\begin{aligned} \Phi^{[i\sigma^{i+}\gamma_5]} &= \mathcal{P}_{q/N}(x, \mathbf{k}_T) s_T^i(x, \mathbf{k}_T) \\ &= S_T^i h_1(x, \mathbf{k}_T^2) - S_{Tj} \frac{2k_T^i k_T^j + \mathbf{k}_T^2 g^{ij}}{2M^2} h_{1T}^\perp(x, \mathbf{k}_T^2) \\ &\quad + \lambda_N \frac{k_T^i}{M} h_{1L}^\perp(x, \mathbf{k}_T^2) - \frac{\varepsilon^{ij} k_{Tj}}{M} h_1^\perp(x, \mathbf{k}_T^2). \end{aligned} \quad (1.52)$$

³The minus ensures the polarity of ϕ_S is the same as usually used in SIDIS.

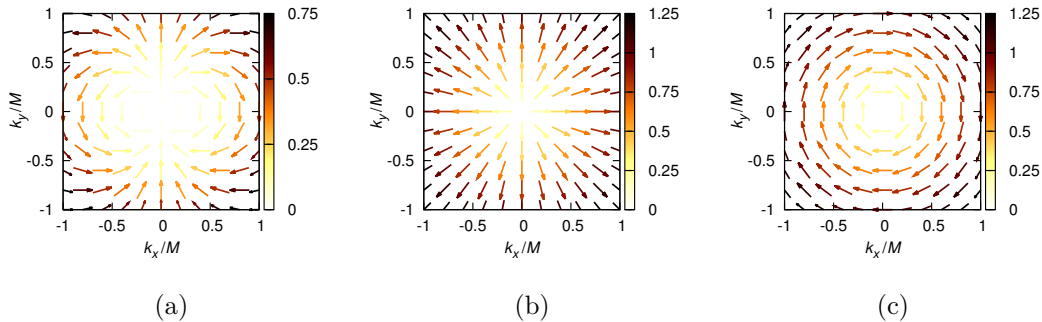


Figure 1.3: The kinematic factors accompanying h_{1T}^\perp (a), h_{1L}^\perp (b), and h_1^\perp (c) for $\mathbf{S}_T = (0, 1, 0)$. Position of the centre of each arrow corresponds to the quark transverse momentum, its direction denotes the preferred quark polarisation, and the colour shows the modulus of the factor.

There are three new TMD PDFs (or just TMDs, for short). The so-called pretzelosity $h_{1T}^\perp(x, \mathbf{k}_T^2)$, together with transversity, determines the transverse polarisation distribution of quarks in a transversely polarised nucleon

$$\begin{aligned} \mathcal{P}_{q\uparrow/N\uparrow}(x, \mathbf{k}_T) - \mathcal{P}_{q\downarrow/N\uparrow}(x, \mathbf{k}_T) &= \cos(\phi_S - \phi_s) h_1(x, \mathbf{k}_T^2) \\ &+ \frac{\mathbf{k}_T^2}{2M^2} \cos(2\phi_k - \phi_S - \phi_s) h_{1T}^\perp(x, \mathbf{k}_T^2). \end{aligned} \quad (1.53)$$

Unlike in the case of transversity, the correlation between quark transverse momentum and spin plays a role. As can be seen in Fig. 1.3(a), if it is nonzero, quarks in a nucleon polarised along the y -axis may be polarised in all transverse directions, depending on their momentum. Note, that only the magnitude of the kinematic factors is shown on the plot. The TMDs are expected to behave roughly as $e^{-\mathbf{k}_T^2/C}$.

The $h_{1L}^\perp(x, \mathbf{k}_T^2)$ describes transverse polarisation of quarks in a longitudinally polarised nucleon. The polarisation asymmetry in this case is

$$\mathcal{P}_{q\uparrow/N+}(x, \mathbf{k}_T) - \mathcal{P}_{q\downarrow/N+}(x, \mathbf{k}_T) = \frac{|\mathbf{k}_T|}{M} \cos(\phi_k - \phi_s) h_{1L}^\perp(x, \mathbf{k}_T^2). \quad (1.54)$$

Therefore, if both the nucleon helicity and h_{1L}^\perp are positive, the quarks are polarised along the direction of their transverse motion. It is illustrated in Fig. 1.3(b). The functions h_{1L}^\perp and g_{1T} are sometimes referred to as worm-gear TMDs.

Finally, the correlation between quark transverse polarisation and momentum may exist in an unpolarised nucleon (or even in a spin-less hadron) as well. This effect is described by the Boer–Mulders function $h_1^\perp(x, \mathbf{k}_T^2)$. The quark transverse polarisation then reads

$$\mathcal{P}_{q\uparrow/N}(x, \mathbf{k}_T) - \mathcal{P}_{q\downarrow/N}(x, \mathbf{k}_T) = \frac{|\mathbf{k}_T|}{M} \sin(\phi_s - \phi_k) h_1^\perp(x, \mathbf{k}_T^2). \quad (1.55)$$

From the expression, or from Fig. 1.3(c), we can see that the quark polarisation in this case would be perpendicular to its transverse momentum. As well as the Sivers function, it was believed to be zero due to time-reversal invariance arguments, but later it has been proven allowed and process-dependent.

| | | Parent hadron polarisation | | |
|------------------------|---|-------------------------------|-------------------------------|---|
| | | Unpolarised | Longitudinal | Transverse |
| Parton polarisation | U | f_1 (number density) | | f_{1T}^\perp (Sivers) |
| | L | | g_1 (helicity) | g_{1T} (worm-gear) |
| | T | h_1^\perp (Boer–Mulders) | h_{1L}^\perp (worm-gear) | h_1 (transversity) h_{1T}^\perp (pretzelosity) |

Table 1.1: Overview of the leading-twist TMD PDFs.

All eight leading-twist TMD PDFs are summarised in Tab.1.1. A remark on the notation is in place. We utilise the so-called Amsterdam (or Jaffe–Ji–Mulders) notation of the quark distribution functions, where the letters f , g , and h denote unpolarised, longitudinally polarised, and transversely polarised quark distributions, respectively. The subscript 1 labels leading-twist quantities. The subscripts L or T indicate longitudinal or transverse polarisation of the parent nucleon. Finally, the superscript \perp denotes the presence of transverse momenta with uncontracted Lorentz indices.

The eight listed TMDs cover all correlations allowed at leading twist between the nucleon (or hadron, in general) spin, parton spin, and parton transverse momentum. Whether the correlations actually exist in nature has to be determined by experiments. An important point is that the TMDs are considered to be intrinsic properties of hadrons, they are believed to be universal. Various processes can be factorised in a hard part, calculable by the perturbative QCD, and a non-perturbative part containing the same TMDs.

Beyond the leading twist, i.e. considering $\mathcal{O}(1/P^+)$ or stronger suppressed quantities, more parton distributions appear. Their origin is both kinematic (e.g. the quark mass can no longer be neglected) and dynamic (quark-quark-gluon correlations). They allow no probabilistic interpretation. [1]

1.1.5 The parton distributions in QCD

The QCD induces a weak (logarithmic) dependence of the PDFs on the energy scale, at which the distributions are defined. In the DIS, the role of the energy scale is played by Q^2 . The dependence, sometimes referred to as scaling violation, can be understood to arise from the finer resolution of the probe (the virtual photon in DIS) at a harder scale, which allows it to resolve more virtual partons that dress each quark. Unlike the x -dependence, which is given by the low-energy, non-perturbative QCD, the Q^2 -dependence is calculable. It is prescribed by the DGLAP equations [13–15], which allow to evolve a PDF known at a certain Q^2 to a different Q^2 . As the evolution arises from gluon emissions by the quarks and gluon splittings into $q\bar{q}$, the DGLAP equations couple the distributions of quarks and gluons. The evolution needs to be taken into account when data from experiments with different mean Q^2 are compared or combined in the so-called

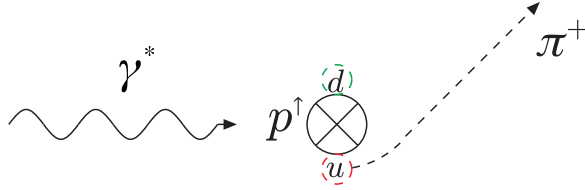


Figure 1.4: Sivers asymmetry in SIDIS induced by the chromodynamic lensing. The proton polarisation points into the plane. The figure was adapted from [10].

global fits.

The emissions of soft gluons by the quark before it encounters the hard probe should alter not only the longitudinal component of the quark momentum, but its transverse momentum as well. Therefore, the \mathbf{k}_T^2 -dependence of the TMD PDFs should be also subject to evolution. While the collinear DGLAP evolution of the \mathbf{k}_T -integrated PDFs has been known for long time, the so-called TMD evolution, being considerably more complex, has been worked out only recently [16].

Another consequence of QCD is the presence of a path-dependent Wilson link operator between the quark fields in the definition of the quark–quark correlation matrix Φ , which is needed to make it gauge-invariant [1]. Its presence has an important consequence that the naively time-reversal odd terms of the matrix are no longer forbidden, a fact that has been uncovered relatively recently [11, 17].

The Wilson link can be associated to initial or final state interactions — exchange of soft gluons — between the struck quark and the spectator quarks. This has led to an adjustment in our understanding of the parton distributions and their universality. The x variable represents the longitudinal momentum of the quark before it interacts with the hard probe, as it is determined only from the kinematic properties of the target nucleon and the scattered lepton. However, the \mathbf{k}_T^2 can be accessed only via measurement of a particle descending from the quark, e.g. a hadron produced by quark fragmentation in the Semi-Inclusive DIS (SIDIS). The \mathbf{k}_T^2 of the TMD PDFs measured in SIDIS represents the asymptotic transverse momentum of the active quark after it has absorbed the virtual photon and left the target nucleon (but before it fragments into hadrons) Thus the TMDs include the final-state interaction between the struck quark and the target remnant. [10].

In the Drell–Yan reaction the role is played by the initial-state interaction instead. It has been shown that, for this reason, the time reversal odd TMDs (Sivers and Boer–Mulders functions) accessed in SIDIS and Drell–Yan bear opposite signs [11]

$$f_{1T}^\perp|_{\text{SIDIS}} = -f_{1T}^\perp|_{\text{DY}}, \quad h_1^\perp|_{\text{SIDIS}} = -h_1^\perp|_{\text{DY}}. \quad (1.56)$$

In hadron production in hadronic collisions, where both initial and final state interactions contribute, the measured TMDs may differ from the ones we know from SIDIS not only by sign, but by non-trivial factors.

The origin of the time-reversal odd TMDs as well as the change of sign phenomenon may be qualitatively understood as a consequence of the so-called chromodynamic lensing by the initial or final state interactions [10, 12]. It is illustrated in Fig. 1.4. The proton is transversely polarised, allowing for an asymmetry in

the orbital angular momentum of quarks. Thanks to the steep decrease of quark density with x , the asymmetry translates into a left–right flavour asymmetry in the impact parameter space, as is indicated on the figure. The attractive final state interactions bend the trajectory of the struck quark, producing a left–right asymmetry in the resulting hadron transverse momenta.

1.1.6 Gluon distributions

Already in the early SLAC DIS experiments it became apparent, that, apart from the quarks, there must be other, electrically neutral, partons in the nucleons. The integral of the structure function F_2 on an isoscalar target was measured,

$$\frac{1}{2} \int_0^1 dx [F_2^p(x) + F_2^n(x)] \approx \frac{5}{18} \sum_q \int_0^1 dx x f_1^q(x), \quad (1.57)$$

where the integrals on the right-hand-side represent the total fraction of the nucleon momentum carried by the quarks of flavour q . The result implicated that only roughly a half of the proton momentum is carried by all the quarks [2]. Of course, in QCD the rest originates from the gluons, which bind the quarks together and dress them. The mentioned experiment tells us, that already at Q^2 typical for fixed-target experiments the gluons are abundant in the nucleons. This is, in fact, in line with the small masses of the current quarks.

As the gluon and quark distributions mix in the Q^2 evolution, it is possible to determine the gluon PDFs from the scaling violations in the DIS structure functions. Direct measurements are possible as well, but the final states originating predominantly from gluons have to be chosen carefully. One of the theoretically cleanest is the prompt photon production $H_a H_b \rightarrow \gamma X$, which proceeds via the hard subprocess $qg \rightarrow q\gamma$. However, background photons (e.g. from incompletely reconstructed π^0 decays) make the measurement of this channel very challenging. In hadronic collisions, subprocesses with π^0 or jets in the final state are also sensitive to gluons, but always suffer from admixture of quark distributions. Another subprocess sensitive to gluons exists in leptonproduction — the so-called photon–gluon fusion (PGF) $\gamma^* g \rightarrow q\bar{q}$ [10, 18], which we discuss in Sec. 1.2.3.

While the gluon number density PDF is rather well known, its helicity has large uncertainties and there is very little experimental evidence on the other TMDs. The gluon Sivers function [19, 20] attracts a particular interest, as it may be linked to gluon orbital angular momentum via the above-mentioned chromodynamic lensing picture. The process-dependence of the gluon Sivers function is more involved, as there are two gauge-links. Therefore, two independent universal functions are needed to obtain gluon Sivers function in any process [21].

1.2 Semi-inclusive deep inelastic scattering

In semi-inclusive deep inelastic scattering (SIDIS), a lepton scatters off a nucleon and the scattered lepton and at least one of the hadrons produced in the collision are detected,

$$\ell(l, \lambda) + N(P, S) \rightarrow \ell(l') + h(P_h) + X, \quad (1.58)$$

where the momenta of the particles, as well as the lepton helicity λ and nucleon spin four-vector S , are given in parenthesis. As in the case of the fully inclusive

DIS, we consider the one-photon exchange approximation, indicated in Fig. 1.5 and 1.6(a). In addition to the DIS variables, defined in Eq. (1.2, 1.3), the relative energy of the final state hadron

$$z = \frac{P \cdot P_h}{P \cdot q}, \quad (1.59)$$

and its transverse momentum \mathbf{P}_{hT} with respect to the exchanged virtual photon direction are usually introduced [22]. The process is described in the γ -nucleon reference frame, which is a target rest frame with the z -axis defined by the virtual photon momentum and the xz -plane being the lepton scattering plane. The planes and the relevant azimuthal angles are shown in Fig. 1.5. We restrict ourselves to the case of a transversely polarised nucleon, so

$$S^\mu = (0, \mathbf{S}_T, 0), \quad \mathbf{S}_T = (|\mathbf{S}_T| \cos \phi_S, |\mathbf{S}_T| \sin \phi_S). \quad (1.60)$$

Assuming single photon exchange, and that the final-state hadron h has spin zero, the SIDIS cross-section can be written in a model-independent way as [22]

$$\begin{aligned} \frac{d\sigma_{\text{SIDIS}}}{dx dy dz d\phi_S d\phi_h dP_{hT}^2} &= \frac{\alpha^2}{xyQ^2} \left(1 + \frac{\gamma^2}{2x} \right) \\ &\times \left\{ \frac{2 - 2y + y^2}{2} F_{\text{UU},T} + (1 - y) F_{\text{UU},L} + (2 - y) \sqrt{1 - y} \cos \phi_h F_{\text{UU}}^{\cos \phi_h} \right. \\ &\quad + (1 - y) \cos(2\phi_h) F_{\text{UU}}^{\cos 2\phi_h} + \lambda y \sqrt{1 - y} \sin \phi_h F_{\text{LU}}^{\sin \phi_h} \\ &\quad + |\mathbf{S}_T| \left[\sin(\phi_h - \phi_S) \left(\frac{2 - 2y + y^2}{2} F_{\text{UT},T}^{\sin(\phi_h - \phi_S)} + (1 - y) F_{\text{UT},L}^{\sin(\phi_h - \phi_S)} \right) \right. \\ &\quad \left. + (1 - y) \left(\sin(\phi_h + \phi_S) F_{\text{UT}}^{\sin(\phi_h + \phi_S)} + \sin(3\phi_h - \phi_S) F_{\text{UT}}^{\sin(3\phi_h - \phi_S)} \right) \right] \\ &\quad + \lambda |\mathbf{S}_T| \left[\frac{2y - y^2}{2} \cos(\phi_h - \phi_S) F_{\text{LT}}^{\cos(\phi_h - \phi_S)} + y \sqrt{1 - y} \cos \phi_S F_{\text{LT}}^{\cos \phi_S} \right. \\ &\quad \left. + y \sqrt{1 - y} \cos(2\phi_h - \phi_S) F_{\text{LT}}^{\cos(2\phi_h - \phi_S)} \right] \left. \right\}, \quad (1.61) \end{aligned}$$

where α is the fine structure constant and the structure functions F_X^Y depend on x , Q^2 , z and P_{hT}^2 . The first two subscripts denote polarisation of the beam and target, the third one (if present) specifies the polarisation of the virtual photon. In writing down the cross-section, we have applied the approximation $Q^2 \gg 2Mx$ to the so-called depolarisation factors, which are the functions of x/Q^2 and y and stand in front of the structure functions [22].

The cross-section is model-independent, as it has been obtained in the same way as the inclusive DIS cross-section in Eq. (1.6) has been, i.e. by contraction of the leptonic tensor with a general Lorentz tensor built up from the available four-vectors and restricted only by basic requirements on invariance.

1.2.1 Structure functions in the TMD factorisation

In the parton model the virtual photon strikes a quark (or antiquark), which later ‘fragments’ into a hadron h . Here we assume independent hadronisation of

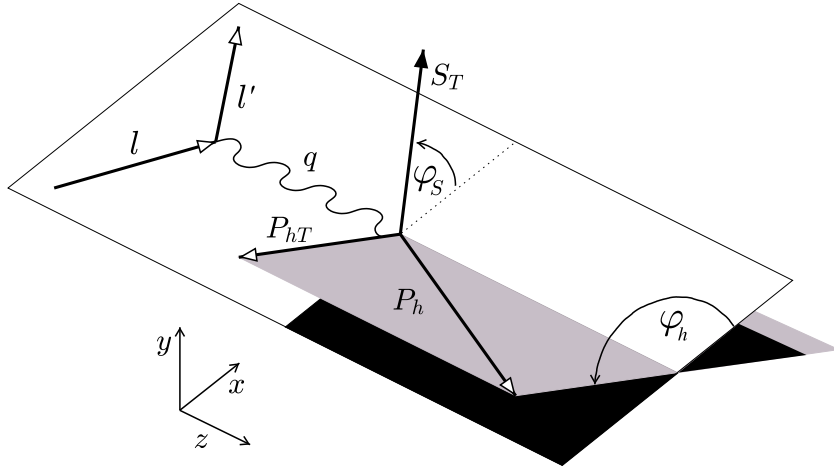


Figure 1.5: The $\gamma^* N$ frame in SIDIS (figure adapted from [10]).

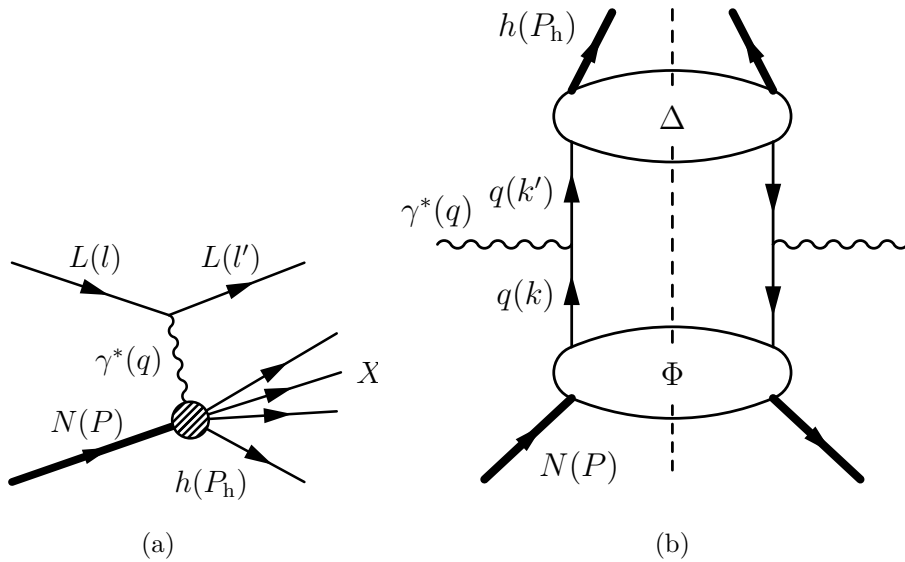


Figure 1.6: The Feynman diagram of the semi-inclusive DIS at leading order (a) and the representation of the lower vertex in the parton model (b).

the struck quark and of the spectator quarks. Of course, the final state hadrons are in fact formed in a mutual interaction between the quarks. However, the approach works thanks to the integration over the unobserved hadronic states X . The relevant handbag diagram is shown in Fig. 1.6(b). The hadronic tensor in the parton model reads [1]

$$W^{\mu\nu} = \sum_q e_q^2 \int \frac{d^4k}{(2\pi)^4} \int \frac{d^4k'}{(2\pi)^4} \delta^{(4)}(k+q-k') \text{Tr}[\Phi\gamma^\mu\Delta\gamma^\nu], \quad (1.62)$$

where k'^μ is the momentum of the fragmenting (scattered) quark, Φ is the quark–quark correlation matrix known from the fully inclusive DIS, and Δ is the so-called decay matrix — a new quark–quark correlation matrix describing the fragmentation of the quark into the measured hadron h ,

$$\begin{aligned} \Delta_{ij}(k'; P_h, S_h) &= \sum_X \int \frac{d^3\mathbf{P}_X}{(2\pi)^3 2E_X} (2\pi)^4 \delta^{(4)}(P_h + P_X - k') \\ &\quad \times \langle 0|\psi_i(0)|P_h S_h, X\rangle \langle P_h S_h, X|\bar{\psi}_j(0)|0\rangle. \end{aligned} \quad (1.63)$$

As in the case of the matrix Φ , a general parametrisation can be build up from the basic tensors and the three available four-vectors: the fragmenting quark momentum k'^μ , the outgoing hadron momentum P_h^μ , and its spin S_h^μ . It is convenient to work in the hN frame, where $\hat{z} \parallel \mathbf{P} \parallel \mathbf{P}_h$, $P^\mu = P^-$ and $P_h^\mu = P_h^+$. We denote the transverse components of vectors in such frame with the subscript \perp , as opposed to the γ^*N frame, where we use T . In particular, the transverse component of the fragmenting quark momentum is \mathbf{k}'_\perp . It can be shown (e.g. [1]), that the invariant z is the fraction of the fragmenting quark momentum transferred to the hadron h , so we can write

$$P_h^\mu = z k'^\mu + p_\perp^\mu, \quad p_\perp^\mu = -z k'_\perp{}^\mu. \quad (1.64)$$

The difference between the transverse components in γ^*N and hN is given by order of $1/Q$ corrections [1]. In the former frame \mathbf{P}_h has a transverse component \mathbf{P}_{hT} , while in the latter \mathbf{q}_T has a transverse component \mathbf{q}_\perp . The two are related, $\mathbf{P}_{hT} \approx -z\mathbf{q}_\perp$. Finally, the four-dimensional delta function from Eq. (1.62) can be, neglecting the order of $1/Q$ corrections, decomposed as

$$\delta^{(4)}(k+q-k') \approx \delta(k^+ - xP^+) \delta\left(k'^- - \frac{1}{z}P_h^-\right) \delta^{(2)}\left(\mathbf{k}_T - \frac{1}{z}\mathbf{P}_{hT} + \frac{1}{z}\mathbf{p}_\perp\right). \quad (1.65)$$

The matrix Δ has the same structure as the matrix Φ , the vectors k'^μ , P_h^μ and S_h^μ correspond to k^μ , P^μ and S^μ respectively. After integration of Δ over k' with the constraint $z = P_h^-/k'^-$ it can be described by only three free parameters $D_1(z)$, $G_1(z)$ and $H_1(z)$. They are called fragmentation functions (FFs). Similarly to the f_1 PDF, the function $D_1(z)$ describes the probability of finding a hadron with longitudinal fraction z inside the fragmenting quark. The probabilistic interpretation of G_1 and H_1 is analogous to g_1 and h_1 PDFs respectively.

If we integrate only over the longitudinal components of k' (with the same constraint), we obtain the transverse momentum dependent (TMD) FFs, which depend apart from z also on the transverse momentum that the hadron obtains in the fragmentation. Some authors use \mathbf{p}_\perp^2 as the second argument of the TMD

FFs, while the others prefer $\mathbf{k}_\perp'^2$. We utilise the former option. As in the case of PDFs, there are eight \mathbf{p}_\perp -dependent FFs. Three of them are generalisations of D_1 , G_1 , and H_1 . The naming convention for the FFs is similar to that of the PDFs: The letters D, G, H refer to the polarisation of the fragmenting quark, the subscripts T and L denote the polarisation of the produced hadron, and the superscript \perp signals the presence of the transverse momentum. An interesting example is the naive-time-reversal odd Collins function $H_1^\perp(z, \mathbf{p}_\perp^2)$, which describes the correlation of the produced hadron transverse momentum and fragmenting quark spin. Therefore, it can act as a ‘quark polarimeter’ and reveal the transverse polarisation of quarks inside nucleons via the azimuthal distribution of the final state hadrons.

Many of the FFs refer to the polarisation of the hadron h , so they are absent in the most common experiment — the SIDIS production of unidentified charged hadrons, which is dominated by production of spin-less π and K. We restrict ourselves to this case. The measurement of the polarising FFs is possible in the production of hadrons with a self-analysing decay, such as Λ .

Using the outlined parametrisation of the two correlators Φ and Δ in terms of TMD PDFs and FFs one can calculate the SIDIS cross-section and find the expressions for the structure functions appearing in Eq. (1.61). First, we introduce the notation for the convolution [22]

$$\begin{aligned} \mathcal{C}[w(\mathbf{k}_T, \mathbf{p}_\perp) f D] &= x \sum_q e_q^2 \int d^2 \mathbf{k}_T d^2 \mathbf{p}_\perp \delta^{(2)}(\mathbf{p}_\perp + z \mathbf{k}_T - \mathbf{P}_{hT}) \\ &\times w(\mathbf{k}_T, \mathbf{p}_\perp) f^q(x, \mathbf{k}_T^2) D^q(z, \mathbf{p}_\perp^2), \end{aligned} \quad (1.66)$$

where $w(\mathbf{k}_T, \mathbf{p}_\perp)$ is an arbitrary function and the summation runs over quarks and antiquarks. The expressions for the structure functions appearing in Eq. (1.61) are available up to the twist three [22]), here we show only the ones relevant for the Sivers effect, i.e. the amplitudes of the constant and of the $\sin(\phi_h - \phi_S)$ azimuthal modulations,

$$F_{UU,T} = \mathcal{C}[f_1 D_1], \quad (1.67)$$

$$F_{UU,L} = 0, \quad (1.68)$$

$$F_{UT,T}^{\sin(\phi_h - \phi_S)} = \mathcal{C}\left[\frac{\mathbf{P}_{hT} \cdot \mathbf{p}_\perp}{M_N} f_{1T}^\perp D_1\right], \quad (1.69)$$

$$F_{UT,L}^{\sin(\phi_h - \phi_S)} = 0. \quad (1.70)$$

A note on convention for the Sivers function sign is in place. In SIDIS, we use the following: looking along the virtual photon direction towards the nucleon with its spin pointing up, the quarks tend to move to the right if their Sivers function is positive. The choice is the same as in Ref. [23, 24] and opposite to Ref. [22, 25]. It seems to be at variance with the Trento convention [26] for SIDIS. However, due to the discussed sign change, the quarks appear to be moving preferably to the left in Drell–Yan, so we are actually in line with the convention for that process.

1.2.2 Siverson asymmetry

Being interested only in the Siverson effect, we substitute the azimuthal angle $\phi_S = \Phi_{\text{Siv}} - \phi_h$ and integrate Eq. (1.61) over ϕ_h yielding

$$\begin{aligned} \frac{d\sigma_{\text{SIDIS}}}{dx dy dz d\Phi_{\text{Siv}} d\mathbf{P}_{hT}^2} &= C(x, y) \left[F_{\text{UU},T}(x, y, z, \mathbf{P}_{hT}^2) \right. \\ &\quad \left. + |\mathbf{S}_T| \sin(\Phi_{\text{Siv}}) F_{\text{UT},T}^{\sin(\phi_h - \phi_S)}(x, y, z, \mathbf{P}_{hT}^2) \right] \\ &= \sigma_0(x, y, z, \mathbf{P}_{hT}^2) + |\mathbf{S}_T| \sin \Phi_{\text{Siv}} \sigma_{\text{Siv}}(x, y, z, \mathbf{P}_{hT}^2). \end{aligned} \quad (1.71)$$

We note that the dependence of the structure functions on y is induced only by the scale dependence of the TMDs.

The Siverson asymmetry is defined as the relative magnitude of the $\sin \Phi_{\text{Siv}}$ modulation amplitude

$$A_{\text{UT},T}^{\sin(\phi_h - \phi_S)}(x, y, z, P_{hT}^2) = \frac{\sigma_{\text{Siv}}(x, y, z, P_{hT}^2)}{\sigma_0(x, y, z, P_{hT}^2)} = \frac{F_{\text{UT},T}^{\sin(\phi_h - \phi_S)}(x, y, z, P_{hT}^2)}{F_{\text{UU},T}(x, y, z, P_{hT}^2)}. \quad (1.72)$$

The advantage of such transverse spin asymmetries (TSAs) is that many experimental uncertainties cancel in the ratios. One has to bear in mind that if one integrates over some of the variables, it is the cross-section and not the asymmetry, which needs to be integrated over these variables. The consequence is that the expression for the Siverson asymmetry differential only in x is simple:

$$A_{\text{UT},T}^{\sin(\phi_h - \phi_S)}(x) = \frac{\int dy dz d\mathbf{P}_{hT}^2 \sigma_{\text{Siv}}}{\int dy dz d\mathbf{P}_{hT}^2 \sigma_0} = \frac{F_{\text{UT},T}^{\sin(\phi_h - \phi_S)}(x)}{F_{\text{UU},T}(x)}, \quad (1.73)$$

while in the case of other variables things are more complex, as the function C from Eq. (1.71) depends on x and y . E.g. for the asymmetry depending on z we obtain

$$A_{\text{UT},T}^{\sin(\phi_h - \phi_S)}(z) = \frac{\int dy dx d\mathbf{P}_{hT}^2 \sigma_{\text{Siv}}}{\int dy dx d\mathbf{P}_{hT}^2 \sigma_0} = \frac{\int dx C(x) F_{\text{UT},T}^{\sin(\phi_h - \phi_S)}(x, z)}{\int dx C(x) F_{\text{UU},T}(x, z)}. \quad (1.74)$$

The integrals in the last two equations run over the experimentally accessible phase space and are implicitly weighted with acceptance.

1.2.3 Access to gluon TMDs in SIDIS

There is a subprocess sensitive to gluon distributions in lepton production — the so-called photon–gluon fusion (PGF) $\gamma^* q \rightarrow q\bar{q}$ [10, 18]. The background in this case comes from the virtual photo-absorption $\gamma^* q \rightarrow q$, which is the leading subprocess, and from the QCD Compton scattering $\gamma^* q \rightarrow gq$. Diagrams of all the three processes are shown in Fig. 1.7. The leading subprocess produces one jet of hadrons, while the other two produce two jets. At fixed-target energies individual hadrons are observed and the best representation of a jet is its leading hadron. Thus one may look for hadrons with large transverse momentum. This approach has been proposed for the measurement of the gluon helicity. If a cut is applied on the transverse momentum difference or on the transverse momenta

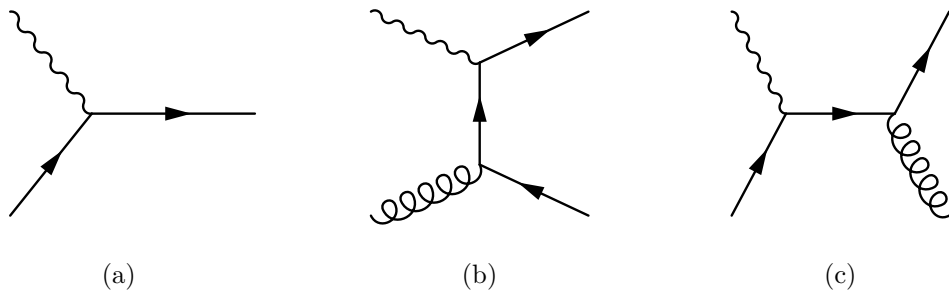


Figure 1.7: The Feynman diagrams of hard subprocesses in lepton–nucleon scattering: the leading virtual photo-absorption process (a), photon–gluon fusion (b), and QCD Compton scattering (c).

of the hadrons themselves, the leading subprocess is suppressed. However, a mixture of the three remains and their fractions have to be determined by a Monte Carlo (MC) simulation. A multi-dimensional cut to enhance the PGF fraction can be provided by a neural network algorithm trained on a MC event sample as done by the SMC experiment [27]. Alternatively, the neural network can be utilised not to reject events, but to assign probabilities to each event of being induced by the three subprocesses. The asymmetries for the three subprocesses can then be extracted simultaneously from a set of equations. This approach was used by COMPASS to measure the gluon helicity [28, 29] and, recently, a Sivers-like asymmetry for gluons [30, 31].

A different approach to single out the PGF in the DIS is to utilise the fact that the presence of heavy flavoured quarks (charm and bottom) in the nucleon is negligible, so the production of hadrons containing the heavy quarks proceeds predominantly via the PGF. One may utilise hadrons that carry the heavy flavour openly [32, 33]. For example, COMPASS has studied the production of D^0 and \bar{D}^0 in SIDIS [34]. Another option is to focus on charmonia (bottomonia) production, as is discussed in the next section for the case of J/ψ .

1.2.4 Semi-inclusive J/ψ leptonproduction

In the PGF process, a $c\bar{c}$ pair can be produced. As the photon is colour-less, the pair inherits the colour octet state of the gluon. In order to transform into the colour singlet charmonium, the colour needs to be carried away. The original colour singlet model assumed that this happens already in the hard scattering via radiation of a hard gluon, as is indicated in Fig. 1.8(a). However, this model has been found to disagree with Tevatron data [35].

The newer charmonium production models are based on the non-relativistic QCD (NRQCD) factorisation, where one assumes that it is a two step process. First, the $c\bar{c}$ pair is produced in the hard scattering either in the colour singlet or in the octet state, the latter option is shown in Fig. 1.8(b). Second, the formation of the asymptotic states happens later and non-perturbatively. In the colour evaporation model (CEM) [36] the colour state of the initial pair plays no role, as it is smeared away in non-perturbative long-range fluctuations of quarks and

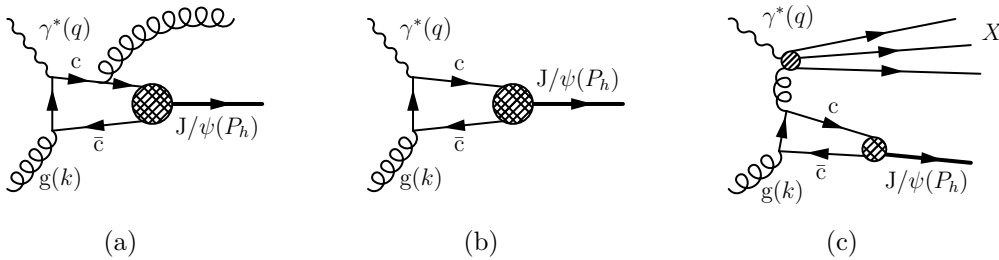


Figure 1.8: In the colour singlet model only the process (a) contributes to the charmonium production. In the CEM or COM models the colour octet quark pair can transform into the colour singlet charmonium (b). One of the possible backgrounds is the resolved photon process (c).

gluons, which are considered complex enough for the asymptotic probabilities of all possible colour configurations to obey statistical counting. The cross-section for charmonium production in CEM is proportional to the $c\bar{c}$ pair cross-section integrated from the two charm quark threshold to the two D meson threshold [37]

$$\sigma_{\gamma g \rightarrow CX} = \frac{1}{9} \int_{2m_c}^{2m_D} dM_{c\bar{c}} \frac{d\sigma_{\gamma g \rightarrow c\bar{c}X}}{dM_{c\bar{c}}}, \quad (1.75)$$

where $M_{c\bar{c}}$ is the invariant mass of the diquark. The only free parameter of the model is the ratio of a particular charmonium state production rate over all charmonia, e.g. $\sigma_{\gamma g \rightarrow J/\psi X} = \rho_{J/\psi} \sigma_{\gamma g \rightarrow CX}$.

The colour octet model (COM) [38] describes the evolution of the $c\bar{c}$, which can be created in the hard process in various colour, spin and angular momentum states, into a physical quarkonium by NRQCD matrix elements. In photoproduction, the cross-section reads [39]

$$\sigma_{\gamma g \rightarrow J/\psi X} = \sum_n \sigma_{\gamma g \rightarrow [c\bar{c}]_n X} \langle 0 | \mathcal{O}_n^{J/\psi} | 0 \rangle, \quad (1.76)$$

where $\sigma_{\gamma g \rightarrow [c\bar{c}]_n X}$ denotes the short-distance cross-section for producing an on-shell $c\bar{c}$ pair in a state labelled by n . The NRQCD matrix elements $\langle 0 | \mathcal{O}_n^{J/\psi} | 0 \rangle$ give the probability for this pair to form the J/ψ particle. The matrix elements are organised in an expansion in powers of v^2 , the average velocity of the charm quark in the J/ψ rest frame squared. The colour singlet states are LO in v^2 , but they are suppressed in the hard scattering. The colour octet states are LO in the hard scattering and suppressed by a factor of v^4 in the NRQCD matrix elements [39].

A Sivers-like asymmetry in the leptonproduction of J/ψ ,

$$\ell + N^\dagger \rightarrow \ell' + J/\psi + X, \quad (1.77)$$

induced by the gluon Sivers function has been discussed in the literature. In [37, 40] the asymmetry has been studied using low-virtuality leptonproduction (photoproduction) approximation and the CEM model. The lepton–nucleon (ℓN) collinear frame has been used. In this case the Sivers TMD couples to the Weizsacker–Williams distribution of photons in a lepton, generalised to provide photon transverse momentum dependence. Sizeable estimates of a $\sin(\phi_h - \phi_S)$ modulation

amplitude in the ℓN frame are obtained, although they need to be treated with care, the Siverson function of gluons being basically unknown.

Recently, the same asymmetry has been addressed in the TMD framework [21], using the $\gamma^* N$ frame and the COM model of the charmonium creation. The formalism is similar to the one outlined in Sec. 1.2.1. The difference with respect to the lepton production of charged hadrons, where just one out of many hadrons created in the fragmentation of the struck quark is observed, is that here the $c\bar{c}$ pair forms exclusively the J/ψ , so $z = 1$. The transverse momentum of the gluon directly translates to the transverse momentum of the J/ψ in this approach. Amplitudes of the $\sin(\phi_h - \phi_S)$ modulation of the cross-section up to 20% are predicted, depending on the assumptions for the unknown gluon Siverson function. The measurement of this asymmetry at COMPASS is described in Chap. 4.

In fact, the reaction $\ell N^\dagger \rightarrow \ell' J/\psi X$ offers a rich azimuthal structure. The measurement of the $\cos 2\phi_h$ asymmetry has been proposed [21]. On top of that, the self-analysing nature of the decay of the J/ψ into muons gives the possibility to study the correlation between the polarisation of the J/ψ and the orientation of the lepton scattering plane, production plane, or the polarisation of the target.

The PGF is not the only process leading to the charmonium production. Background could get contributions from the diffractive production and from the so-called resolved photon process, where the photon couples like a hadron through its partonic structure (Fig. 1.8(c)). While the former is important at $z = 1$, the latter is expected to contribute at small z .

1.3 Drell–Yan process

In this section we describe the Drell–Yan reaction, i.e., the production of a lepton pair with large invariant mass in a hadronic collision [41], for the case of a spinless hadron H_a and a transversely polarised hadron H_b :

$$H_a(P_a) + H_b(P_b, S) \rightarrow \ell^-(l^-) + \ell^+(l^+) + X. \quad (1.78)$$

Here $P_{a,b}$ are the momenta of the beam and of the target hadron, S is the spin four-vector of the target hadron, and l^- and l^+ are the momenta of the final state lepton pair. It is convenient to define $q = l^- + l^+$. In Fig. 1.9(a), the reaction (1.78) is shown at leading order, where it proceeds via annihilation of a quark–antiquark pair into a virtual photon with momentum q , which finally decays into the dilepton.

We mostly follow the notations of Ref. [25]. In particular, the same reference frames, depicted in Fig. 1.10, are used. The target frame is a rest frame of the target particle, with \hat{z}_{TF} axis parallel to the beam momentum and \hat{x}_{TF} axis defined by \mathbf{q}_{T} , the transverse component of \mathbf{q} with respect to \hat{z} . The Collins–Soper frame is obtained from the target frame by two subsequent Lorentz boosts: first along \hat{z}_{TF} so that the longitudinal component of \mathbf{q} vanishes, second along \hat{x}_{TF} making the transverse component zero as well. For further convenience, we define in addition the target spin frame as the rest frame of the target hadron with $\hat{z}_{\text{TSF}} = \hat{z}_{\text{TF}}$ and $\hat{y}_{\text{TSF}} = \mathbf{S}_{\text{T}}/S_{\text{T}}$. In this frame the azimuthal angle of \mathbf{q}_{T} is $\pi/2 - \phi_S$, so $\mathbf{q}_{\text{T}} = (q_{\text{T}} \sin \phi_S, q_{\text{T}} \cos \phi_S)$.

The model-independent cross-section of the process is in the general case given by [25]:

$$\begin{aligned}
\frac{d\sigma_{\text{DY}}}{d^4q d\Omega} = & \frac{\alpha^2}{CQ^2} \left\{ (1 + \cos^2 \theta) F_{\text{U}}^1 + (1 - \cos^2 \theta) F_{\text{U}}^2 \right. \\
& + \sin 2\theta \cos \phi F_{\text{U}}^{\cos \phi} + \sin^2 \theta \cos 2\phi F_{\text{U}}^{\cos 2\phi} \\
& + |S_{\text{T}}| \left[\sin \phi_{\text{S}} \left((1 + \cos^2 \theta) F_{\text{T}}^1 + (1 - \cos^2 \theta) F_{\text{T}}^2 \right) \right. \\
& + \sin 2\theta \left(\sin(\phi + \phi_{\text{S}}) F_{\text{T}}^{\sin(\phi + \phi_{\text{S}})} + \sin(\phi - \phi_{\text{S}}) F_{\text{T}}^{\sin(\phi - \phi_{\text{S}})} \right) \\
& \left. \left. + \sin^2 \theta \left(\sin(2\phi + \phi_{\text{S}}) F_{\text{T}}^{\sin(2\phi + \phi_{\text{S}})} + \sin(2\phi - \phi_{\text{S}}) F_{\text{T}}^{\sin(2\phi - \phi_{\text{S}})} \right) \right] \right\}, \tag{1.79}
\end{aligned}$$

where θ and ϕ are the polar and azimuthal angle of the momentum \mathbf{l}^- of the lepton in the Collins–Soper frame; ϕ_{S} is the angle between \mathbf{q}_{T} and the transverse component of the target spin vector \mathbf{S}_{T} in any target rest frame where $\hat{\mathbf{z}} = \mathbf{P}_a/|\mathbf{P}_a|$. Note that such a class of frames includes both the target frame and target spin frame. Finally, C is a kinematic factor given by $C = 4\sqrt{(P_a \cdot P_b)^2 - M_a^2 M_b^2}$. The structure functions F_X^Y depend on three independent variables. They can be for example $Q^2 = q^2$ and the Bjorken variables

$$x_a = q^2/(2P_a \cdot q), \quad x_b = q^2/(2P_b \cdot q). \tag{1.80}$$

Equivalently we can use the transverse part of q in the target frame q_{T} instead of Q^2 . A summary of the notation is given in Tab. 1.2.

On the left-hand side we can see that the cross-section is differential in six variables — four components of q and the solid angle Ω . The solid angle stands for the direction of the momentum of the lepton, so we can write $d\Omega = d\cos\theta d\phi$. The virtual photon momentum q can be easily decomposed in the target spin frame, where $q = (q_0, q_{\text{T}} \sin \phi_{\text{S}}, q_{\text{T}} \cos \phi_{\text{S}}, q_{\text{L}})$, yielding $d^4q = \frac{1}{2} dq_0 dq_{\text{L}} dq_{\text{T}}^2 d\phi_{\text{S}}$. Finally, the components q_0 and q_{L} can be substituted by x_a and x_b yielding an equation with the same variables explicitly written on both sides,

$$\begin{aligned}
\frac{d\sigma_{\text{DY}}}{dx_a dx_b dq_{\text{T}}^2 d\phi_{\text{S}} d\cos\theta d\phi} = & \frac{J(x_{a,b}, P_{a,b})}{2} \frac{d\sigma_{\text{DY}}}{d^4q d\Omega} \\
= & C_0(x_{a,b}, P_{a,b}) \left\{ (1 + \cos^2 \theta) F_{\text{U}}^1(x_a, x_b, q_{\text{T}}) + \dots \right\}. \tag{1.81}
\end{aligned}$$

For massless hadrons the Jacobian $J = s/2$ [25], In the general case the expression is lengthy. We use the shorthand notation $\alpha^2 J/(2CQ^2) = C_0$.

When the cross-section is integrated over the angle ϕ_{S} , we obtain the angular distribution of the unpolarised Drell–Yan reaction. Traditionally, it is written as [25]

$$\begin{aligned}
\frac{dN}{d\Omega} = & \frac{d\sigma_{\text{DY}}}{d^4q d\Omega} \left(\frac{d\sigma_{\text{DY}}}{d^4q} \right)^{-1} \\
= & \frac{3}{4\pi} \frac{1}{\lambda + 3} \left(1 + \lambda \cos^2 \theta + \mu \sin 2\theta \cos \phi + \frac{\nu}{2} \sin^2 \theta \cos 2\phi \right), \tag{1.82}
\end{aligned}$$

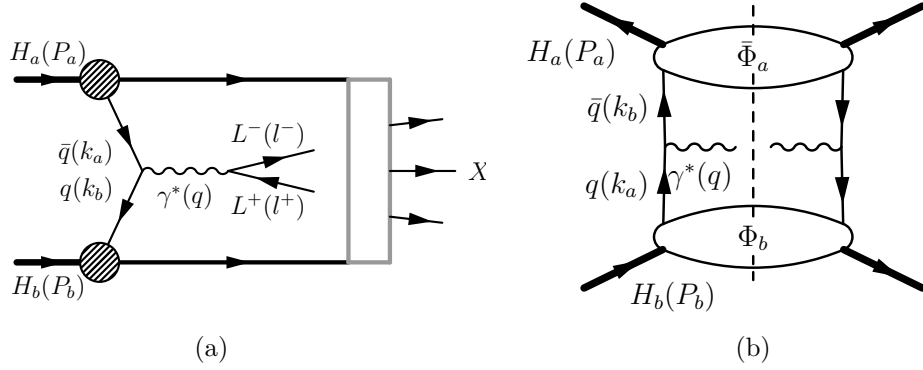


Figure 1.9: Drell–Yan process at leading order (a) and its handbag diagram (b).

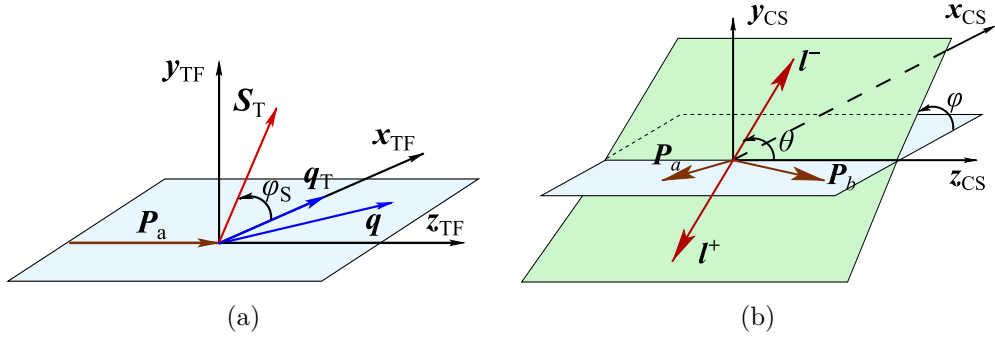


Figure 1.10: The reference frames used: (a) the target frame, (b) the Collins–Soper frame, and the definition of the angles θ , ϕ , and ϕ_S .

| | |
|--------------------------------------|---|
| P_a, P_b | beam and target hadron momenta |
| $\mathbf{S}_T, S_T = \mathbf{S}_T $ | transverse (w.r.t. \hat{z}_{TF}) part of the target polarisation |
| l^-, l^+ | lepton and antilepton momenta |
| $q = l^- + l^+$ | virtual photon momentum |
| $Q^2 = q^2 = M^2$ | virtuality of the photon, dimuon invariant mass |
| $\mathbf{q}_T, q_T = \mathbf{q}_T $ | transverse (w.r.t. \hat{z}_{TF}) component of \mathbf{q} , where $q = (q_0, \mathbf{q})$ |
| $x_a = \frac{q^2}{2P_a \cdot q}$ | beam hadron Bjorken variable |
| $x_b = \frac{q^2}{2P_b \cdot q}$ | target nucleon Bjorken variable |
| $x_F = x_a - x_b$ | Feynman variable |
| ϕ_S | the angle between \mathbf{S}_T and \mathbf{q}_T (Fig. 1.10(a)) |
| θ, ϕ | polar and azimuthal angle of l^- in CS frame (Fig. 1.10(b)) |

Table 1.2: Drell–Yan process: notations.

where

$$\lambda = \frac{F_U^1 - F_U^2}{F_U^1 + F_U^2} \quad \mu = \frac{F_U^{\cos\phi}}{F_U^1 + F_U^2} \quad \nu = \frac{2F_U^{\cos 2\phi}}{F_U^1 + F_U^2}. \quad (1.83)$$

The so-called Lam–Tung relation [42, 43]

$$\lambda + 2\nu = 1 \quad (1.84)$$

holds exactly at $\mathcal{O}(\alpha_s)$ in the standard collinear QCD framework and even at $\mathcal{O}(\alpha_s^2)$ the numerical violation is rather small [25]. Deviations from the Lam–Tung relation were observed at CERN [44, 45] and Fermilab [46] in negative pion-induced Drell–Yan reactions. In particular, large values of the amplitude of the $\cos 2\phi$ modulation of the cross-section were measured. A non-zero Boer–Mulders function of quarks might account for the effect [47]. No significant violation was observed in pd and pp Drell–Yan [48, 49], which does not contradict the explanation by the Boer–Mulders function, as the antiquarks are coming from the sea in this case, while in the $\pi^- A$ Drell–Yan valence antiquarks dominate.

Recently, a next-to-leading order perturbative QCD simulations of the λ and ν coefficients were compared to a wide range of experiments [50]. The high-energy collider data, including those from the Tevatron $p\bar{p}$ collider, were found to be in a very good agreement with the simulations. Even the fixed-target $\pi^- A$ measurements are reproduced fairly well, leaving only a small room for the Boer–Mulders effect. Clearly, the data from new fixed-target experiments, such as COMPASS and SeaQuest [51], will be relevant in resolving the issue.

1.3.1 Structure functions in the TMD approach

The parton model representation of the Drell–Yan hadronic tensor is shown in Fig. 1.9(b). The structure functions of Eq. (1.79) in the LO QCD and TMD factorisation at leading twist [25] can be written as

$$F_U^1 = \mathcal{C} \left[f_{1,a} f_{1,b} \right], \quad (1.85)$$

$$F_U^2 = F_U^{\cos\phi} = F_T^2 = F_T^{\cos(\phi \pm \phi_S)} = 0, \quad (1.86)$$

$$F_U^{\cos\phi} = \mathcal{C} \left[\frac{2(\mathbf{q}_T \cdot \mathbf{k}_{aT})(\mathbf{q}_T \cdot \mathbf{k}_{bT}) - q_T^2(\mathbf{k}_{aT} \cdot \mathbf{k}_{bT})}{q_T^2 M_a M_b} h_{1,a}^\perp h_{1,b}^\perp \right], \quad (1.87)$$

$$F_T^1 = F_T^{\sin\phi_S} = -\mathcal{C} \left[\frac{\mathbf{q}_T \cdot \mathbf{k}_{bT}}{q_T M_b} f_{1,a} f_{1T,b}^\perp \right] \quad (1.88)$$

$$F_T^{\sin(2\phi + \phi_S)} = -\mathcal{C} \left[\left(\frac{(\mathbf{q}_T \cdot \mathbf{k}_{bT}) [2(\mathbf{q}_T \cdot \mathbf{k}_{aT})(\mathbf{q}_T \cdot \mathbf{k}_{bT}) - q_T^2(\mathbf{k}_{aT} \cdot \mathbf{k}_{bT})]}{q_T^3 M_a M_b^2} \right) \right] \quad (1.89)$$

$$- \frac{\mathbf{k}_{bT}^2 (\mathbf{q}_T \cdot \mathbf{k}_{aT})}{2q_T M_a M_b^2} h_{1,a}^\perp h_{1T,b}^\perp \right], \quad (1.90)$$

$$F_T^{\sin(2\phi - \phi_S)} = -\mathcal{C} \left[\frac{\mathbf{q}_T \cdot \mathbf{k}_{aT}}{q_T M_a} h_{1,a}^\perp h_{1,b}^\perp \right]. \quad (1.91)$$

From now on we stay with this approximation. We use $F_T^{\sin\phi_S}$ instead of F_T^1 in order to make the notation more intuitive with superscripts, which correspond to

the azimuthal modulations. In fact, in Ref. [25] $F_T^{\sin \phi_S}$ is defined slightly differently than F_T^1 , but their definitions coincide in the leading order approximation, where F_T^2 can be neglected. We also use the Siverson function sign convention defined in Sec. 1.2.1.

\mathcal{C} indicates a convolution of two TMD PDFs f_a and f_b over the intrinsic transverse momenta of quarks \mathbf{k}_{aT} and \mathbf{k}_{bT} , which is defined as

$$\begin{aligned} \mathcal{C}[w(\mathbf{k}_{aT}, \mathbf{k}_{bT}) f_a f_b] &= \frac{1}{N_c} \sum_q e_q^2 \int d^2 \mathbf{k}_{aT} d^2 \mathbf{k}_{bT} \delta^{(2)}(\mathbf{q}_T - \mathbf{k}_{aT} - \mathbf{k}_{bT}) \\ &\times w(\mathbf{k}_{aT}, \mathbf{k}_{bT}) \left[f_a^{\bar{q}}(x_a, \mathbf{k}_{aT}^2) f_b^q(x_b, \mathbf{k}_{bT}^2) + f_a^q(x_a, \mathbf{k}_{aT}^2) f_b^{\bar{q}}(x_b, \mathbf{k}_{bT}^2) \right], \end{aligned} \quad (1.92)$$

where N_c is the number of colours. Apart from $x_{a,b}$, which in the TMD approach are the fractions of the parent hadron momenta carried by the quarks, and the momenta $k_{a,bT}^2$, the TMD PDFs depend also on the QCD scale, represented by Q^2 , which is not written explicitly.

As was stated before, the structure functions do not depend on the azimuthal angle of \mathbf{q}_T . Looking at Eq. (1.92) it is not obvious, as \mathbf{q}_T appears at the right-hand side. However, the dependence on the azimuthal angle of \mathbf{q}_T is removed thanks to the integration over \mathbf{k}_{aT} and \mathbf{k}_{bT} and the result depends only on the modulus q_T . To see it explicitly we make a small exercise. First note in Eq. (1.85–1.91) that $w(\mathbf{k}_{aT}, \mathbf{k}_{bT})$, in fact, does not depend on \mathbf{k}_{aT} and \mathbf{k}_{bT} , but on $\mathbf{k}_{aT} \cdot \mathbf{k}_{bT}$, $\mathbf{q}_T \cdot \mathbf{k}_{aT}$, $\mathbf{q}_T \cdot \mathbf{k}_{bT}$, q_T^2 , and \mathbf{k}_{bT}^2 . Second, we write (we omit the dependence of the PDFs on x)

$$\begin{aligned} F_X^Y &= \mathcal{C} \left[w(\mathbf{k}_{aT}, \mathbf{k}_{bT}) f_a^{\bar{q}}(\mathbf{k}_{aT}^2) f_b^q(\mathbf{k}_{bT}^2) \right] = \int d^2 \mathbf{k}_{aT} d^2 \mathbf{k}_{bT} \delta^{(2)}(\mathbf{q}_T - \mathbf{k}_{aT} - \mathbf{k}_{bT}) \\ &\times w(\mathbf{k}_{aT} \cdot \mathbf{k}_{bT}, \mathbf{q}_T \cdot \mathbf{k}_{aT}, \mathbf{q}_T \cdot \mathbf{k}_{bT}, q_T^2, \mathbf{k}_{bT}^2) f_a^{\bar{q}}(\mathbf{k}_{aT}^2) f_b^q(\mathbf{k}_{bT}^2) \\ &= \int d^2 \mathbf{k}_{bT} w(\mathbf{k}_{bT}^2 - \mathbf{k}_{bT} \cdot \mathbf{q}_T, \mathbf{q}_T \cdot \mathbf{k}_{bT} - q_T^2, \mathbf{q}_T \cdot \mathbf{k}_{bT}, q_T^2, \mathbf{k}_{bT}^2) \\ &\times f_a^{\bar{q}}(\mathbf{k}_{bT}^2 + q_T^2 - 2\mathbf{k}_{bT} \cdot \mathbf{q}_T) f_b^q(\mathbf{k}_{bT}^2). \end{aligned} \quad (1.93)$$

We can see that the integrand depends only on \mathbf{k}_{bT}^2 , q_T^2 , and $\mathbf{q}_T \cdot \mathbf{k}_{bT}$. The scalar product gives $\mathbf{q}_T \cdot \mathbf{k}_{bT} = k_{bT} q_T \cos(\phi_{\mathbf{k}_{bT}} - \phi_{\mathbf{q}_T})$. The azimuthal angle $\phi_{\mathbf{k}_{bT}}$ of \mathbf{k}_{bT} is, however, integrated over from 0 to 2π . Therefore, if we replace \mathbf{q}_T with $\mathbf{q}'_T = (q_T \cos \psi, q_T \sin \psi)$, where ψ is an arbitrary azimuthal angle, nothing changes. The difference between ψ and $\phi_{\mathbf{q}_T}$ can be absorbed in substitution $\phi_{\mathbf{k}_{bT}} = \phi'_{\mathbf{k}_{bT}} + \psi - \phi_{\mathbf{q}_T}$, which does not change the result of the integral over the 2π interval.

Omitting the modulations F_U^2 , $F_U^{\cos \phi}$, F_T^2 , and $F_T^{\cos(\phi \pm \phi_S)}$, which vanish in our approximation, and using Eq. (1.81), the cross-section given in Eq. (1.79) simplifies to

$$\begin{aligned} \frac{d\sigma_{DY}}{dx_a dx_b dq_T^2 d\phi_S d\cos\theta d\phi} &= C_0 \left\{ (1 + \cos^2 \theta) F_U^1 + \sin^2 \theta \cos 2\phi F_U^{\cos 2\phi} \right. \\ &+ |S_T| \left[(1 + \cos^2 \theta) \sin \phi_S F_T^{\sin \phi_S} \right. \\ &+ \sin^2 \theta \sin(2\phi + \phi_S) F_T^{\sin(2\phi + \phi_S)} \\ &+ \left. \left. \sin^2 \theta \sin(2\phi - \phi_S) F_T^{\sin(2\phi - \phi_S)} \right] \right\}. \end{aligned} \quad (1.94)$$

1.3.2 Standard azimuthal asymmetries

The azimuthal modulations, which stand in front of the structure functions in both SIDIS and Drell–Yan cross-sections, are orthogonal to each other. Since the structure functions do not depend on the azimuthal angles, one can get them by a multi-dimensional fit of the measured cross-section. Alternatively, to get a particular structure function one can integrate the cross-section over the azimuthal angles with a weight equal to the azimuthal modulation of this structure function as will be spelled out here and in Sec. 3.3.1. For future convenience, let us examine the simple integrated (i.e. integrated with weight equal to one) Drell–Yan cross-section,

$$\begin{aligned} \frac{d\sigma_{\text{DY}}}{dx_a dx_b dq_T^2 d\cos\theta} &= \int d\phi d\phi_S \frac{d\sigma_{\text{DY}}}{S} dx_a dx_b dq_T^2 d\phi_S d\Omega \\ &= 2\pi C_0(1 + \cos^2\theta) F_U^1(x_a, x_b, q_T^2). \end{aligned} \quad (1.95)$$

All the modulations vanish in the integration over the azimuthal angles. Integrating further over $\cos\theta$ brings in factor $\int_{-1}^1 d\cos\theta (1 + \cos^2\theta) = 8/3$. However, in experiments the distribution of $(1 + \cos^2\theta)$ usually enters convoluted with acceptance in the integral. The amplitude of the Sivers modulation can be extracted by integration of the cross-section in Eq. (1.94) with the weight $\sin\phi_S$.

$$\begin{aligned} \frac{d\sigma_{\text{DY}}^{\sin\phi_S}}{dx_a dx_b dq_T^2 d\cos\theta} &= \int d\phi d\phi_S \sin\phi_S \frac{d\sigma_{\text{DY}}}{dx_a dx_b dq_T^2 d\phi_S d\Omega} \\ &= \pi C_0(1 + \cos^2\theta) |S_T| F_T^{\sin\phi_S}(x_a, x_b, q_T^2). \end{aligned} \quad (1.96)$$

As in the SIDIS case, it is convenient to define asymmetries as the relative measure of the azimuthal modulation amplitudes, which simplify into ratios of the structure functions $A_X^Y = F_X^Y/F_U^1$. The cross-section given in Eq. (1.94) in terms of asymmetries is

$$\begin{aligned} \frac{d\sigma_{\text{DY}}}{dx_a dx_b dq_T^2 d\phi_S d\cos\theta d\phi} &= C_0(1 + \cos^2\theta) F_U^1 \left\{ 1 + D_{\cos 2\phi}(\theta) \cos 2\phi A_U^{\cos 2\phi} \right. \\ &\quad + |S_T| \left[D_{\sin\phi_S}(\theta) \sin\phi_S A_T^{\sin\phi_S} \right. \\ &\quad \quad + D_{\sin(2\phi+\phi_S)}(\theta) \sin(2\phi + \phi_S) A_T^{\sin(2\phi+\phi_S)} \\ &\quad \quad \left. \left. + D_{\sin(2\phi-\phi_S)}(\theta) \sin(2\phi - \phi_S) A_T^{\sin(2\phi-\phi_S)} \right] \right\}, \end{aligned} \quad (1.97)$$

where we have defined the kinematic factors

$$D_{\sin\phi_S}(\theta) = 1, \quad D_{\cos 2\phi}(\theta) = D_{\sin(2\phi\pm\phi_S)}(\theta) = \frac{\sin^2\theta}{1 + \cos^2\theta}. \quad (1.98)$$

The asymmetries due to the target transverse polarisation are called TSAs and can be extracted using the cross-sections integrated with appropriate weights,

$$A_T^Y(x_a, x_b, q_T) = \frac{2}{\bar{D}_Y |S_T|} \frac{\sigma_{\text{DY}}^Y(x_a, x_b, q_T)}{\sigma_{\text{DY}}(x_a, x_b, q_T)}, \quad (1.99)$$

where the integrated cross-section $\sigma_{\text{DY}}(x_a, x_b, q_{\text{T}})$ is obtained from Eq. (1.95) by integrating over $\cos \theta$, the $\sigma_{\text{DY}}^{\text{Y}}(x_a, x_b, q_{\text{T}})$ from Eq. (1.96). The integrated factors \tilde{D}_{Y} are defined as

$$\tilde{D}_{\sin \phi_{\text{S}}} = 1, \quad \tilde{D}_{\cos 2\phi} = \tilde{D}_{\sin(2\phi \pm \phi_{\text{S}})} = \frac{\int d \cos \theta \sin^2 \theta}{\int d \cos \theta (1 + \cos^2 \theta)}. \quad (1.100)$$

In the case of an ideal acceptance in θ the ratio of the integrals gives $D_{\cos 2\phi} = D_{\sin(2\phi \pm \phi_{\text{S}})} = \frac{4/3}{8/3} = 1/2$. In practice it is better to calculate the integrals from the data. To get an equation analogical to Eq. (1.99) for the unpolarised asymmetry $A_{\text{U}}^{\cos 2\phi}$, we just need to replace $|S_{\text{T}}|$ with 1 on its right hand side.

As was explained in Sec. 1.2.2 for the Sivers asymmetry in SIDIS, one needs to be careful when some of the variables are integrated over. There is no problem for q_{T} , as C_0 does not depend on it. For instance, the expression for an asymmetry as a function of x_b is

$$A_X^{\text{Y}}(x_b) = \frac{\int dx_a dq_{\text{T}} C_0(x_a, x_b) F_X^{\text{Y}}(x_a, x_b, q_{\text{T}})}{\int dx_a dq_{\text{T}} C_0(x_a, x_b) F_{\text{U}}^1(x_a, x_b, q_{\text{T}})} = \frac{\int dx_a C_0(x_a, x_b) F_X^{\text{Y}}(x_a, x_b)}{\int dx_a C_0(x_a, x_b) F_{\text{U}}^1(x_a, x_b)}, \quad (1.101)$$

where the integrals are implicitly weighted by the experimental acceptance. In fact, one faces the problem even with a fully differential cross-section, as the bin width is always finite. We ignore this effect throughout the text and instead of an integral over a variable we consider the asymmetry at the mean value of the variable in question, e.g. $A_X^{\text{Y}}(x_b, \langle x_a \rangle)$.

In the case of the target spin independent modulation $\cos 2\phi$ an acceptance correction is mandatory, but the TSAs, as we show in Sec. 3.3.1, can be extracted even without it if the target polarisation can be reversed and certain assumptions are made. For future use, we simplify the cross-section by keeping it differential only in the angle $\Phi = \phi_{\text{S}}$, $2\phi \pm \phi_{\text{S}}$ of the modulation of interest. From Eq. (1.97) and (1.100) we obtain after the appropriate integrations

$$\sigma_{\text{DY}}(x_a, x_b, q_{\text{T}}, \Phi) = \frac{d\sigma_{\text{DY}}}{dx_a dx_b dq_{\text{T}}^2 d\Phi} \propto 1 + |S_{\text{T}}| \tilde{D}_{\sin \Phi} \sin \Phi A_{\text{T}}^{\sin \Phi}. \quad (1.102)$$

1.4 Present knowledge of the PDFs

In this Section we briefly summarise the current experimental knowledge of the PDFs. As the collinear number density and helicity are rather well established, the emphasis is given on the transverse-spin-dependent distributions and especially on the TMDs.

1.4.1 Collinear PDFs

A great wealth of data over a large kinematic domain exists constraining the spin-independent collinear PDFs of quarks and gluons. They come from fixed-target experiments (mostly DIS and Drell–Yan processes), the HERA ep collider (e.g. DIS, lepton production of heavy quarks and of jets), the Tevatron $p\bar{p}$ collider, and the LHC pp collider (e.g. production of jets, electroweak bosons, Drell–Yan lepton pairs, photons) [52]. The data are fitted globally by several groups using

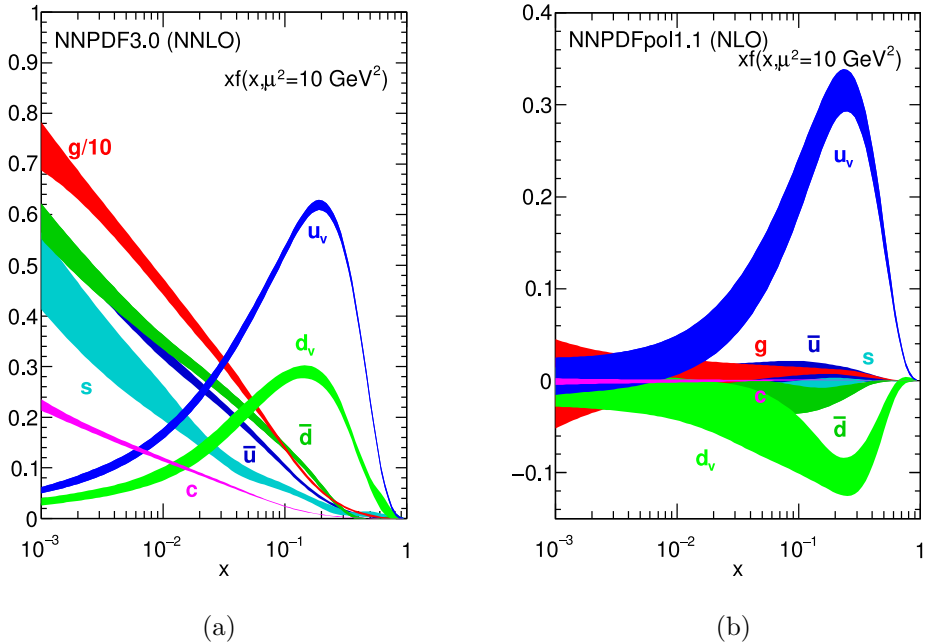


Figure 1.11: Results of a recent global fit of the collinear PDFs by the NNPDF group: (a) number density and (b) helicity. The scale is $10 \text{ (GeV}/c)^2$, the figures are from Ref. [52].

collinear evolution and calculation of the hard underlying processes in next-to-leading order or even next-to-next-to-leading order. An example from the NNPDF group is shown in Fig. 1.11(a).

The helicity PDFs are less constrained, especially those of gluons and sea quarks. Most of the available data are coming from fixed-target DIS, especially from COMPASS and JLab experiments. The flavour separation can be achieved using SIDIS (accompanied by the knowledge of FFs, usually from e^+e^- annihilation) and open charm production in DIS. Besides that, there are data from the longitudinally polarised pp scattering at RHIC. Recent global analyses come from [53]: the DSSV group [54] (DIS, SIDIS, pp), the NNPDF group [55] (DIS, pp), and the JAM group [56] (DIS, SIDIS). An example is shown in Fig. 1.11(b).

The least known is the transversity PDF, owing to its chirally-odd nature as explained in Sec. 1.1.3. The first evidence of this elusive PDF has been given only in 2005 by HERMES [57] and COMPASS [58], which have measured the $\sin(\phi_h + \phi_S + \pi)$ modulation in the SIDIS reactions $e^- p^\uparrow \rightarrow e^- \pi^\pm X$ and $\mu^+ d^\uparrow \rightarrow \mu^+ h^\pm X$, respectively. The amplitude of the modulation is called Collins asymmetry, as it is induced by the transversity PDF coupled to Collins fragmentation function introduced in Sec. 1.2.1. The asymmetry has been found to be of about the same magnitude and opposite sign for π^+ and for π^- production on proton target and compatible with zero for production of hadrons of both charges on deuteron target due to cancellation between u and d quarks. To extract the transversity distribution from the SIDIS data the Collins FF needed to be determined. This input has been provided by the Belle collaboration, which has measured azimuthal

asymmetries in the distribution of two almost back-to-back hadrons in e^+e^- annihilation [59]. Finally, the transversity has been extracted for the first time from a simultaneous analysis of the SIDIS and e^+e^- data [60].

A caveat of the extractions of transversity from the single-particle-inclusive DIS is its reliance on the TMD framework, despite the transversity being a collinear quantity. In particular a convolution over transverse momenta appears in the expression of the Collins asymmetry and, because of the very different energies of the DIS and the e^+e^- experiments, the method is sensitive to the TMD FF evolution, which is not completely understood. These problems are absent in the production of hadron pairs with small invariant mass in SIDIS. In this case, the transversity is coupled to a chiral-odd dihadron fragmentation function $H_1^{\perp q}$, which describes the correlation between the transverse polarisation of the fragmenting quark and the azimuthal orientation of the plane containing the momenta of the detected hadron pair. Contrary to the Collins FF, this effect survives after integration over single quark transverse momenta and can be analysed in the collinear factorisation scheme. On top of that, similar approach can be applied even to the two-hadron inclusive production in $pp^\uparrow \rightarrow \pi^+\pi^-X$ at RHIC. The first collinear extraction of transversity has been done using HERMES and Belle data [61].

Later, additional data have been made available. In particular, the SIDIS data on proton target from COMPASS showed clear signals in both the Collins asymmetry [62] and di-hadron [63] channels. The high statistics collected by COMPASS made possible a point-by-point determination of the transversity distributions from both channels, carried out in a recent analysis [64]. The extraction, which uses also the e^+e^- annihilation data, is based only on simple assumptions and does not use any parametrisation of the transversity PDF. The transversity PDFs extracted from the Collins and dihadron asymmetries are very much the same. The remarkable similarity between the Collins asymmetry for positive hadrons and the di-hadron asymmetry, shown in Fig. 1.12(a), lead to further phenomenological analysis and to the conclusion that both are driven by the same elementary mechanism [65]. As is illustrated on Fig. 1.12(b) and (c) the measured asymmetries have been recently successfully reproduced in a Monte Carlo simulation [66, 67] based on string fragmentation (Lund Symmetric Model [68]) with transverse polarisation of quarks taken into account via a quantum version of the 3P_0 mechanism [69].

In addition, the Collins asymmetry has been measured with a ^3He target at Jefferson Lab (JLab). More electron-positron annihilation data from Belle and BaBar experiments have been published. Both the Collins asymmetry [70–73] and the dihadron asymmetry [74] based extractions have been revisited. Results from the di-hadron inclusive production from STAR experiment at RHIC collider have been very recently added to the collinear analysis [53], making it the first truly global one.

Several recent extractions of the transversity distribution are compared in Fig. 1.13. It is worth noting that the uncertainty of the d quark transversity is considerably larger than that of the u-quark and often constrained by the Soffer bound. This fact has motivated the COMPASS Collaboration to propose a new SIDIS data taking with a transversely polarized deuteron target [75].

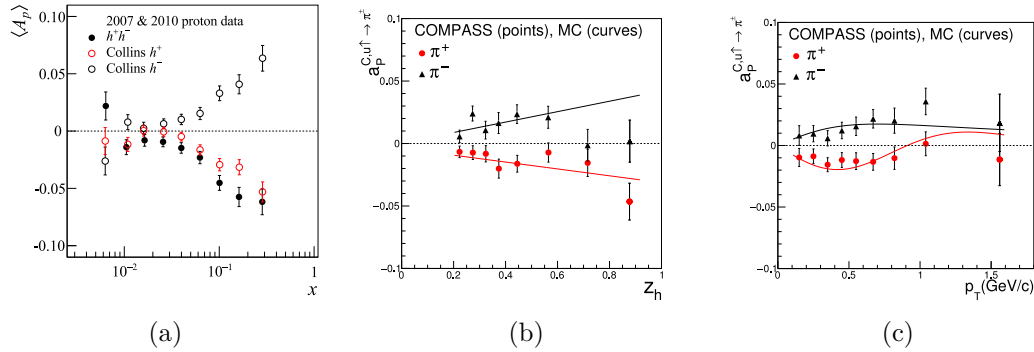


Figure 1.12: (a) Comparison of the Collins and di-hadron asymmetries measured by COMPASS [63]. (b, c) Comparison of the string fragmentation simulation with the measured Collins asymmetry [67].

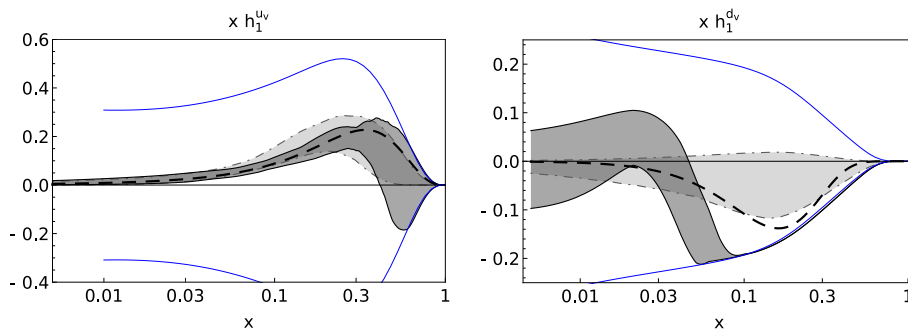


Figure 1.13: The u (left) and d (right) valence quark transversity PDFs at $Q^2 = 2.4 \text{ (GeV}/c)^2$. The darker band indicates the collinear extraction [74]. The lighter band and the thick dashed line are extractions from the Collins effect from Ref. [70] and [72], respectively. The blue curves indicate the Soffer bound. The figure is from Ref. [74].

1.4.2 Transverse momentum dependent PDFs

The basic matter is of course the unpolarised TMD PDF and the TMD FF, which are necessary to extract e.g. the Sivers function and several groups are working in this field. An effort towards the first truly global analysis of the unpolarised TMDs has started recently with an analysis of SIDIS (COMPASS, HERMES), Drell–Yan (E 288, E 605), and Z production (D0, CDF II) transverse momentum distribution results [76]. The e^+e^- annihilation data, which could bring a cleaner information on the FFs, are missing so far, but their addition is foreseen in the future. Other data are expected as well, in particular COMPASS is expected to measure the \mathbf{P}_{HT} -dependent multiplicities of charged hadrons produced in SIDIS off a liquid hydrogen Target. A large effort is ongoing, but in the following we focus on the transverse-spin-dependent functions, especially on the Sivers PDF.

The first clear evidence for a nonzero TMD PDF that has no collinear counterpart was the measurement of the Sivers asymmetry on proton at HERMES [57], done on the same data that revealed the transversity through the Collins asymmetry. The asymmetry is induced by the Sivers function [9] coupled to the unpolarised TMD FF. The asymmetry was found to be compatible with zero on deuteron target by COMPASS [58]. The results were immediately used to extract the Sivers function, a review of these early works can be found in Ref. [77].

Later on, COMPASS measured the asymmetry on proton target finding at its larger energy a clear signal for positive hadrons [78, 79]. The experiment on polarised ^3He at JLab has also measured the Sivers asymmetry [80]. Unlike in the Collins case, the magnitude of the Sivers asymmetry at COMPASS is somewhat smaller than the one measured by HERMES [81]. This has been interpreted as first evidence for scale evolution the average Q^2 of COMPASS being larger by a factor of 3–4 at large x , where the asymmetry is large and definitely different from zero.

Several Sivers function extractions, which combine the available SIDIS data, have been done. Often the works include also predictions for the Sivers asymmetries in hadron–hadron processes, where the function is predicted to bear opposite sign (Sec. 1.1.5), e.g. in Ref. [82], using the DGLAP evolution of the collinear part of the function, or Ref. [83–85], using the TMD evolution. An example of a fit result is shown in Fig. 1.14.

An extraction of the Sivers function $f_{1\text{T}}^\perp$, from the COMPASS Sivers asymmetry data for pions and kaons, is shown in Fig. 1.15 from Ref. [24]. The method, which relies on some simple assumptions, is based on a combined analysis of both the proton and deuteron asymmetry data measured by COMPASS. Although a Gaussian form of the \mathbf{k}_{T}^2 -dependence is assumed for the $f_{1\text{T}}^\perp$ in order to factorise them from the fragmentation functions, no parametrisation is employed for the x -dependence, making the extraction essentially parameter-free. This point-to-point extraction compares well with the other determinations of the Sivers function like that of Ref. [83], which is also shown in the same figure.

The Sivers asymmetry has been recently measured in hadron–hadron interactions in attempts to test the change of sign. The STAR experiment at RHIC has published [86] Sivers asymmetry measured in $pp^\uparrow \rightarrow W^\pm X$ and $pp^\uparrow \rightarrow Z^0 X$, showing a hint towards the sign change. The results are shown in Fig. 1.16 together with two theoretical predictions. The scale of the experiment is very far from the SIDIS fixed-target experiments, making the predictions difficult due to possible strong Q^2 evolution effects. Indeed, some evolution scenarios predict

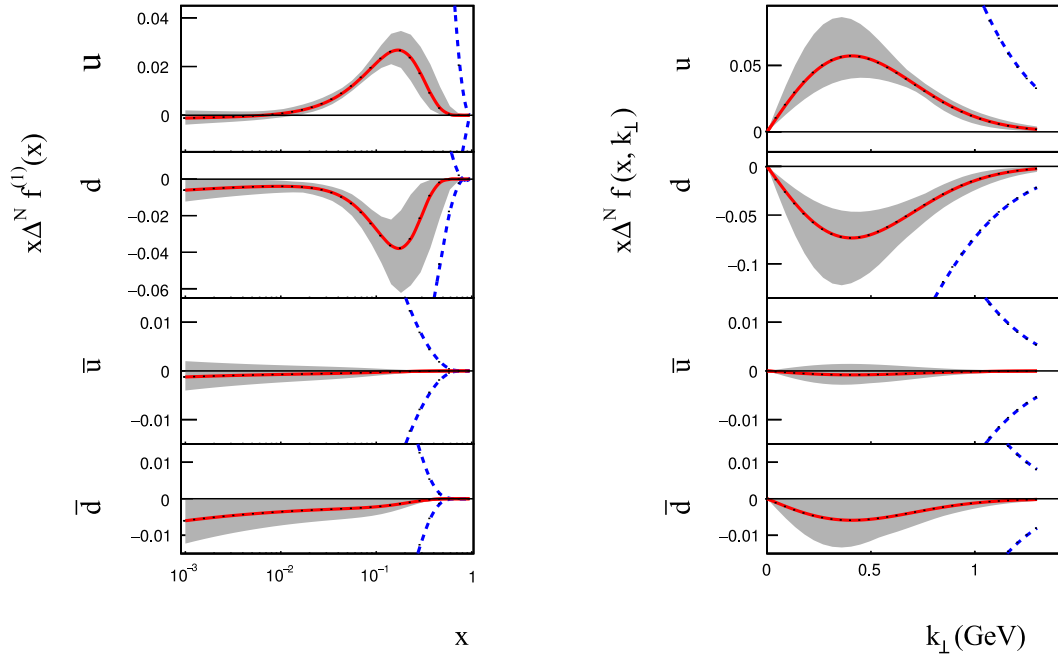


Figure 1.14: The first k_T^2 -moment of the Sivers function at $Q^2 = 2.4 (\text{GeV}/c)^2$, extracted from HERMES, COMPASS and JLab data versus x (left) and k_T (right) [82]. The solid red lines correspond to the best fits, the shaded band to the estimated 95 % confidence levels, and the dashed lines to the positivity bounds.

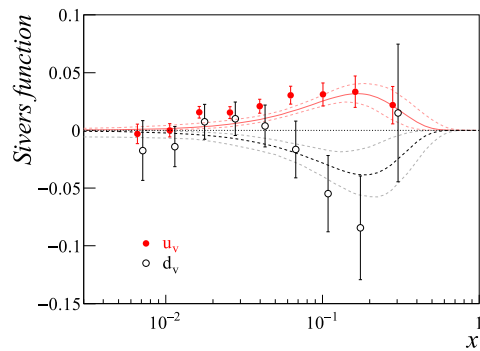


Figure 1.15: The first k_T^2 -moment of the Sivers function from the point-by-point analysis [24] of COMPASS data, compared to the extraction from Ref. [83].

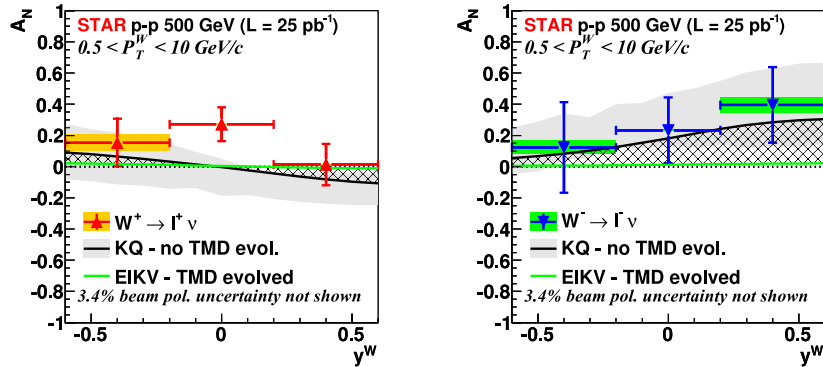


Figure 1.16: The Siverts asymmetries measured in W^\pm at STAR [86], compared to theoretical predictions KQ [87] and EIKV [84]. The large differences between the predictions and their uncertainties come mostly from the TMD evolution.

only very small asymmetries, below the experimental precision, at RHIC energies [84, 85]. The new, much larger, data set that has been collected in 2016 will allow to clarify the issue.

In 2015, COMPASS has measured for the first time the Siverts asymmetry in the Drell–Yan process with transversely polarised target $\pi^- p^\uparrow \rightarrow \mu^- \mu^+ X$. The results [88] are described in Sec. 5.1. A complementary analysis of the asymmetry weighted with the virtual photon transverse momentum is the main topic of this thesis and is presented in Chap. 5 and 6. New data should be taken in 2018, promising to more than double the sample. The advantage of COMPASS is that the Q^2 of its SIDIS and Drell–Yan measurements are rather close. Moreover, COMPASS has published a new multi-differential analysis aimed at the comparison between SIDIS and Drell–Yan processes [89]. All the eight asymmetries expected in the SIDIS model-independent cross-section have been extracted in four regions of the photon virtuality Q^2 corresponding to the four regions of the dimuon mass $M = \sqrt{Q^2}$ used in the analyses of the COMPASS Drell–Yan measurement. In the highest Q^2 range, which coincides with the background-free region for the Drell–Yan measurement, the SIDIS Siverts asymmetry for positive hadrons is significantly positive. This allows for a direct comparison of the nucleon TMD PDFs extracted from these two complementary measurements, and in particular to test the change of sign of the Siverts function without the necessity of applying Q^2 evolution corrections to the measured asymmetries.

COMPASS has explored all structure functions accessible in the transversely polarised SIDIS and, apart from the Siverts and Collins effects, has observed signals for the $A_{LT}^{\cos(\phi_h - \phi_s)}$ and $A_{UT}^{\sin \phi_s}$ asymmetries (see e.g. [90]). The other asymmetries have been found consistent with zero. The two nonzero ones are related to the worm gear PDF g_{1T} and to higher-twist PDFs, respectively.

Considering the gluon transverse-spin-dependent TMDs, only the asymmetries that may be linked the Siverts function have been studied so far. Even in this case, the data are not abundant and suffer from model or data analysis related assumptions. The COMPASS measurement of the high- P_{hT} hadron pair production in SIDIS [30, 31] has been mentioned in Sec. 1.2.3. It has shown a signal of

a Siverson-like asymmetry negative by about three standard deviations. The new measurement of the J/ψ Siverson-like asymmetry is described in Chap. 4. Information on the gluon Siverson distribution has been obtained by PHENIX collaboration, which has measured open heavy flavour production in pp^\uparrow collisions at RHIC [91] observing no clear evidence for a nonzero gluon Siverson PDF.

1.5 Disentangling the convolution by transverse momentum weighting

To access the TMD PDFs from the standard asymmetries one needs to handle the convolutions over the partonic transverse momenta both in SIDIS (see Eq. (1.66)) and in Drell–Yan (Eq. (1.92)). This can be easily done for the constant terms $F_{UU,T}$ in SIDIS and F_U^1 in Drell–Yan by integration over the transverse momentum. In the case of the other modulations the integral can not be solved and strong assumptions are usually made. However, it has been shown [92–94], that the convolution in SIDIS can be disentangled if the cross-section is properly weighted. Of course, some assumptions are needed in this case too. The same principle can be applied to Drell–Yan [95–98].

In the following, we demonstrate the principle of the weighted Siverson asymmetry in SIDIS and we work out in more detail the weighted asymmetries accessible in Drell–Yan with transversely polarised target.

1.5.1 Weighted Siverson asymmetry in SIDISs

In the case of the structure function $F_{UU,T}$ the convolution (1.66) can be easily solved by integration over \mathbf{P}_{hT} ,

$$\begin{aligned} F_{UU,T}(x, z) &= \int d^2\mathbf{P}_{hT} \mathcal{C} \left[f_1(x, \mathbf{k}_T^2) D_1(z, \mathbf{p}_\perp^2) \right] \\ &= x \sum_q e_q^2 \int d^2\mathbf{P}_{hT} d^2\mathbf{k}_T d^2\mathbf{p}_\perp \delta^{(2)}(\mathbf{p}_\perp + z\mathbf{k}_T - \mathbf{P}_{hT}) \\ &\quad \times f_1^q(x, \mathbf{k}_T^2) D_1^q(z, \mathbf{p}_\perp^2) = x \sum_q e_q^2 f_1^q(x) D_1^q(z). \end{aligned} \quad (1.103)$$

First we have changed the order of the integrations, used the Dirac delta function to trivially solve the integral over \mathbf{P}_{hT} , and finally employed the definition of the integrated PDF $f_1(x) = \int d^2\mathbf{k}_T f_1(x, \mathbf{k}_T^2)$ and FF $D_1(z) = \int d^2\mathbf{p}_\perp D_1(z, \mathbf{p}_\perp^2)$.

This approach does not work for the other structure functions, because of the kinematic factors $w(\mathbf{k}_T, \mathbf{p}_\perp)$ in the convolution. The solution is to assume that the TMD PDF (or FF) factorises into a collinear x (or z) dependent part and a \mathbf{k}_T (or \mathbf{p}_\perp) dependent part. In particular the Gaussian model is a simple and popular choice, e.g. the Siverson function and the unpolarised FF are written as

$$f_{1T}^\perp(x, \mathbf{k}_T^2) = f_{1T}^\perp(x) \frac{e^{-\mathbf{k}_T^2 / \langle \mathbf{k}_T^2 \rangle_{\text{Siv}}}}{\pi \langle \mathbf{k}_T^2 \rangle_{\text{Siv}}} \quad D_1(x, \mathbf{p}_\perp^2) = D_1(z) \frac{e^{-\mathbf{p}_\perp^2 / \langle \mathbf{p}_\perp^2 \rangle}}{\pi \langle \mathbf{p}_\perp^2 \rangle}. \quad (1.104)$$

Assuming flavour-independent Gaussian widths $\langle \mathbf{k}_T^2 \rangle_{\text{Siv}}$, $\langle \mathbf{p}_\perp^2 \rangle$, the structure function $F_{UT,T}^{\text{sin}(\phi_h - \phi_S)}$ can be expressed as

$$F_{UT,T}^{\text{sin}(\phi_h - \phi_S)}(x, z) = a_G x \sum_q e_q^2 f_{1T}^{\perp q(1)}(x) D_1^q(z), \quad (1.105)$$

where

$$a_G = \frac{\sqrt{\pi}M}{\sqrt{\langle \mathbf{k}_T^2 \rangle_{\text{Siv}} + \langle \mathbf{p}_\perp^2 \rangle / z^2}} \quad (1.106)$$

and $f_{1T}^{\perp q(1)}$ is the first \mathbf{k}_T^2 -moment of the Siverson function. In general, the n -th moment of a PDF is defined as

$$f^{(n)}(x) = \int d^2 \mathbf{k}_T \left(\frac{\mathbf{k}_T^2}{2M^2} \right)^n f(x, \mathbf{k}_T^2), \quad (1.107)$$

where M is the mass of the nucleon.

An alternative way is weighting with powers of transverse momentum [92–94]. For example, integrating the structure function $F_{\text{UT},\text{T}}^{\sin(\phi_h - \phi_s)}$ with weight $P_{\text{hT}}/(zM)$ yields a simple result, similar to the case of $F_{\text{UU},\text{T}}$,

$$\int d^2 \mathbf{P}_{\text{hT}} \frac{P_{\text{hT}}}{zM} F_{\text{UT},\text{T}}^{\sin(\phi_h - \phi_s)}(x, z) = 2x \sum_q e_q^2 f_{1T}^{\perp q(1)}(x) D_1^q(z). \quad (1.108)$$

The calculations to obtain this result are explained in the analogous case of Drell–Yan structure functions in the next section.

We define the $P_{\text{hT}}/(zM)$ -weighted Siverson asymmetry as

$$A_{\text{UT},\text{T}}^{\sin(\phi_h - \phi_s) \frac{P_{\text{hT}}}{zM}} = \frac{\int d^2 \mathbf{P}_{\text{hT}} \frac{P_{\text{hT}}}{zM} F_{\text{UT},\text{T}}^{\sin(\phi_h - \phi_s)}(x, z)}{\int d^2 \mathbf{P}_{\text{hT}} F_{\text{UU},\text{T}}(x, z)}. \quad (1.109)$$

Using the previous results, the interpretation of the asymmetry in the TMD factorisation is obvious:

$$A_{\text{UT},\text{T}}^{\sin(\phi_h - \phi_s) \frac{P_{\text{hT}}}{zM}} = 2 \frac{\sum_q e_q^2 x f_{1T}^{\perp q(1)}(x) D_1^q(z)}{\sum_q e_q^2 x f_1^q(x) D_1^q(z)}. \quad (1.110)$$

The methods of weighted asymmetry measurement are described in Sec. 3.3.

1.5.2 Weighting with q_T in Drell–Yan

Similarly to SIDIS, the convolution can be removed in the case of F_U^1 by integration over \mathbf{q}_T . Using Eq. (1.85) and (1.92), one finds

$$\begin{aligned} \int d^2 \mathbf{q}_T F_U^1 &= \int d^2 \mathbf{q}_T \frac{1}{N_c} \sum_q e_q^2 \int d^2 \mathbf{k}_{aT} d^2 \mathbf{k}_{bT} \delta^{(2)}(\mathbf{q}_T - \mathbf{k}_{aT} - \mathbf{k}_{bT}) \\ &\quad \times \left[f_{1,a}^{\bar{q}}(x_a, \mathbf{k}_{aT}^2) f_{1,b}^q(x_b, \mathbf{k}_{bT}^2) + f_{1,a}^q(x_a, \mathbf{k}_{aT}^2) f_{1,b}^{\bar{q}}(x_b, \mathbf{k}_{bT}^2) \right] \\ &= \frac{1}{N_c} \sum_q e_q^2 \left[f_{1,a}^q(x_a) f_{1,a}^{\bar{q}}(x_b) + (q \leftrightarrow \bar{q}) \right]. \end{aligned} \quad (1.111)$$

However, as in SIDIS, this does not work for the other structure functions. The Gaussian model is widely used in Drell–Yan as well. We follow the transverse momentum weighted approach, which was first developed for SIDIS. Later, it was used for Drell–Yan [95–97] too. As we are going to show, it is only the presence of $q_T = |\mathbf{q}_T|$ in the denominator of w , what prevents the trivial integration. It is possible to bypass the problem of the convolution by integration with a weight, which is chosen such that the q_T in the denominator is cancelled. Additional factors are in some cases added to the weight to obtain more elegant results.

Sivers function induced structure function

The integral of the structure function $F_T^{\sin \phi_S}$ over \mathbf{q}_T yields a simple result when it is weighted with q_T/M_b . First, we again use the delta function to solve the integral over \mathbf{q}_T ,

$$\begin{aligned} \int d^2 \mathbf{q}_T \frac{q_T}{M_b} F_T^{\sin \phi_S} &= - \int d^2 \mathbf{q}_T \frac{q_T}{M_b} \mathcal{C} \left[\frac{\mathbf{q}_T \cdot \mathbf{k}_{bT}}{q_T M_b} f_{1,a} f_{1T,b}^\perp \right] \\ &= - \sum_q e_q^2 \int d^2 \mathbf{k}_{aT} d^2 \mathbf{k}_{bT} \frac{(\mathbf{k}_{aT} + \mathbf{k}_{bT}) \cdot \mathbf{k}_{bT}}{N_c M_b^2} \\ &\quad \times \left[f_{1,a}^{\bar{q}}(x_a, \mathbf{k}_{aT}^2) f_{1T,b}^{\perp q}(x_b, \mathbf{k}_{bT}^2) + (q \leftrightarrow \bar{q}) \right]. \end{aligned} \quad (1.112)$$

Thanks to the weight, the q_T in the denominator is cancelled. Second, we realise that only terms even in \mathbf{k}_T can contribute,

$$\int_{-\infty}^{\infty} d^2 \mathbf{k}_{aT} (\mathbf{k}_{aT} \cdot \mathbf{k}_{bT}) f(\mathbf{k}_{aT}^2) = 0. \quad (1.113)$$

Finally, we utilise definitions of the integrated PDF and the first moment of a PDF (1.107) and we obtain

$$\int d^2 \mathbf{q}_T \frac{q_T}{M_b} F_T^{\sin \phi_S} = - \frac{2}{N_c} \sum_q e_q^2 \left[f_{1,a}^{\bar{q}}(x_a) f_{1T,b}^{\perp(1)q}(x_b) + (q \leftrightarrow \bar{q}) \right]. \quad (1.114)$$

In this way we directly get the first \mathbf{k}_T^2 -moment of the Sivers function of the target hadron times the unpolarised PDF of the beam hadron.

Transversity and Boer–Mulders function induced structure functions

The expression for $F_T^{\sin(2\phi - \phi_S)}$ is very similar to the one for Sivers, so we easily find

$$\begin{aligned} \int d^2 \mathbf{q}_T \frac{q_T}{M_a} F_T^{\sin(2\phi - \phi_S)} &= \int d^2 \mathbf{q}_T \frac{q_T}{M_a} \mathcal{C} \left[\frac{\mathbf{q}_T \cdot \mathbf{k}_{aT}}{q_T M_a} h_{1,a}^\perp h_{1,b} \right] \\ &= - \sum_q e_q^2 \int d^2 \mathbf{k}_{aT} d^2 \mathbf{k}_{bT} \frac{(\mathbf{k}_{aT} + \mathbf{k}_{bT}) \cdot \mathbf{k}_{aT}}{N_c M_a^2} \\ &\quad \times \left[h_{1,a}^{\perp \bar{q}}(x_a, \mathbf{k}_{aT}^2) h_{1,b}^q(x_b, \mathbf{k}_{bT}^2) + (q \leftrightarrow \bar{q}) \right] \\ &= - \frac{2}{N_c} \sum_q e_q^2 \left[h_{1,a}^{\perp(1)\bar{q}}(x_a) h_{1,b}^q(x_b) + (q \leftrightarrow \bar{q}) \right] \end{aligned} \quad (1.115)$$

The same reasoning applies also to the unpolarised structure function $F_U^{\cos 2\phi}$. In this case the proper weight is $\frac{q_T^2}{4M_a M_b}$,

$$\begin{aligned} \int d^2 \mathbf{q}_T \frac{q_T^2}{4M_a M_b} F_U^{\cos 2\phi} &= \int d^2 \mathbf{q}_T \frac{q_T^2}{4M_a M_b} \\ &\quad \times \mathcal{C} \left[\frac{2(\mathbf{q}_T \cdot \mathbf{k}_{aT})(\mathbf{q}_T \cdot \mathbf{k}_{bT}) - q_T^2(\mathbf{k}_{aT} \cdot \mathbf{k}_{bT})}{q_T^2 M_a M_b} h_{1,a}^\perp h_{1,b}^\perp \right]. \end{aligned} \quad (1.116)$$

After the integration over \mathbf{q}_T with the delta function the numerator becomes

$$\begin{aligned} & 2(\mathbf{k}_{aT} + \mathbf{k}_{bT}) \cdot \mathbf{k}_{aT} (\mathbf{k}_{aT} + \mathbf{k}_{bT}) \cdot \mathbf{k}_{bT} - (\mathbf{k}_{aT} + \mathbf{k}_{bT})^2 \mathbf{k}_{aT} \cdot \mathbf{k}_{bT} \\ & = 2\mathbf{k}_{aT}^2 \mathbf{k}_{bT}^2 + (\mathbf{k}_{aT}^2 + \mathbf{k}_{bT}^2) \mathbf{k}_{aT} \cdot \mathbf{k}_{bT}. \end{aligned} \quad (1.117)$$

Putting this result back in the full expression we remember that only terms even in \mathbf{k}_{aT} and \mathbf{k}_{bT} can contribute in the integral. Finally,

$$\begin{aligned} \int d^2 \mathbf{q}_T \frac{q_T^2}{4M_a M_b} F_U^{\cos 2\phi} &= - \sum_q e_q^2 \int d^2 \mathbf{k}_{aT} d^2 \mathbf{k}_{bT} \frac{2\mathbf{k}_{aT}^2 \mathbf{k}_{bT}^2 + (\mathbf{k}_{aT}^2 + \mathbf{k}_{bT}^2) \mathbf{k}_{aT} \cdot \mathbf{k}_{bT}}{4M_a^2 M_b^2} \\ &\quad \times \left[h_{1,a}^{\perp(1)\bar{q}}(x_a, \mathbf{k}_{aT}^2) h_{1,b}^{\perp(1)q}(x_b, \mathbf{k}_{bT}^2) + (q \leftrightarrow \bar{q}) \right] \\ &= \frac{2}{N_c} \sum_q e_q^2 \left[h_{1,a}^{\perp(1)\bar{q}}(x_a) h_{1,b}^{\perp(1)q}(x_b) + (q \leftrightarrow \bar{q}) \right]. \end{aligned} \quad (1.118)$$

We can see that the structure function $F_T^{\sin(2\phi-\phi_S)}$ gives access to the transversity of the target hadron times the first moment of the Boer–Mulders PDF of the beam hadron, and the structure function $F_U^{\cos 2\phi}$ could give information on the product of the first moments of the Boer–Mulders PDF of the two hadrons.

Pretzelosity-induced structure function

The case of $F_T^{\sin(2\phi+\phi_S)}$ is more complicated.

$$\begin{aligned} \int d^2 \mathbf{q}_T \frac{q_T^3}{2M_a M_b^2} F_T^{\sin(2\phi+\phi_S)} &= - \sum_q e_q^2 \int d^2 \mathbf{q}_T d^2 \mathbf{k}_{aT} d^2 \mathbf{k}_{bT} \\ &\quad \times \frac{2(\mathbf{q}_T \cdot \mathbf{k}_{bT}) \left[2(\mathbf{q}_T \cdot \mathbf{k}_{aT})(\mathbf{q}_T \cdot \mathbf{k}_{bT}) - q_T^2 (\mathbf{k}_{aT} \cdot \mathbf{k}_{bT}) \right] - q_T^2 \mathbf{k}_{bT}^2 (\mathbf{q}_T \cdot \mathbf{k}_{aT})}{4M_a^2 M_b^4} \\ &\quad \times \delta^{(2)}(\mathbf{q}_T - \mathbf{k}_{aT} - \mathbf{k}_{bT}) \left[h_{1,a}^{\perp\bar{q}}(x_a, \mathbf{k}_{aT}^2) h_{1,b}^{\perp q}(x_b, \mathbf{k}_{bT}^2) + (q \leftrightarrow \bar{q}) \right]. \end{aligned} \quad (1.119)$$

First we integrate over \mathbf{q}_T using the delta function. To simplify the numerator, we change notation $\mathbf{k}_{aT} = \mathbf{a}$, $\mathbf{k}_{bT} = \mathbf{b}$. Note, that after the first integration we have $\mathbf{q}_T = \mathbf{a} + \mathbf{b}$. We mark the numerator as $D(\mathbf{a}, \mathbf{b}) = 2[(\mathbf{a} + \mathbf{b}) \cdot \mathbf{b}] B(\mathbf{a}, \mathbf{b}) - C(\mathbf{a}, \mathbf{b})$.

$$\begin{aligned} B &= \left[2(\mathbf{a} + \mathbf{b}) \cdot \mathbf{a} (\mathbf{a} + \mathbf{b}) \cdot \mathbf{b} - (\mathbf{a} + \mathbf{b})^2 \mathbf{a} \cdot \mathbf{b} \right] = \left[2a^2 b^2 + (a^2 + b^2) \mathbf{a} \cdot \mathbf{b} \right] \\ C &= (\mathbf{a} + \mathbf{b})^2 b^2 (\mathbf{a} + \mathbf{b}) \cdot \mathbf{a} = b^2 \left[a^4 + (a^2 + b^2) \mathbf{a} \cdot \mathbf{b} + a^2 b^2 + 2(\mathbf{a} \cdot \mathbf{b})^2 \right] \\ D &= 2[(\mathbf{a} + \mathbf{b}) \cdot \mathbf{b}] B - C = a^2 b^4 - a^4 b^2 + 5a^2 b^2 \mathbf{a} \cdot \mathbf{b} + 2a^2 (\mathbf{a} \cdot \mathbf{b})^2 \end{aligned} \quad (1.120)$$

From the previous we know that $a^2 b^2 \mathbf{a} \cdot \mathbf{b}$, the third term in D , gives zero in the integration, because it is odd in \mathbf{a} and \mathbf{b} . To evaluate the contribution of the last term $2a^2 (\mathbf{a} \cdot \mathbf{b})^2$ we note that

$$\int_{-\infty}^{\infty} d^2 \mathbf{a} a_i^2 f(a^2) = \frac{1}{2} \int_{-\infty}^{\infty} d^2 \mathbf{a} a^2 f(a^2), \quad (1.121)$$

where $i = 1, 2$ and $\mathbf{a} = (a_1, a_2)$. Therefore,

$$\int_{-\infty}^{\infty} d^2 \mathbf{a} d^2 \mathbf{b} (\mathbf{a} \cdot \mathbf{b})^2 f(a^2) g(b^2) = \frac{1}{2} \int_{-\infty}^{\infty} d^2 \mathbf{a} d^2 \mathbf{b} a^2 b^2 f(a^2) g(b^2) \quad (1.122)$$

and we find that

$$\int_{-\infty}^{\infty} d^2\mathbf{a} d^2\mathbf{b} D f(a^2) g(b^2) = \int_{-\infty}^{\infty} d^2\mathbf{a} d^2\mathbf{b} a^2 b^4 f(a^2) g(b^2) \quad (1.123)$$

Finally we can come back to the structure function

$$\int d^2\mathbf{q}_T \frac{q_T^3}{2M_a M_b^2} F_T^{\sin(2\phi+\phi_S)} = -\frac{2}{N_c} \sum_q e_q^2 \left[h_{1,a}^{\perp(1)\bar{q}}(x_a) h_{1T,b}^{\perp(2)q}(x_b) + (q \leftrightarrow \bar{q}) \right]. \quad (1.124)$$

The structure function $F_T^{\sin(2\phi+\phi_S)}$ gives access to the second moment of pretzelosity of the target hadron times the first moment of the Boer–Mulders PDF of the beam hadron.

Transverse momentum weighted asymmetries

To summarise, the q_T -weighted integrals of the structure functions are

$$\int d^2\mathbf{q}_T F_U^1 = \frac{1}{N_c} \sum_q e_q^2 \left[f_1^{\bar{q}}(x_a) f_1^q(x_b) + (q \leftrightarrow \bar{q}) \right] \quad (1.125)$$

$$\int d^2\mathbf{q}_T \frac{q_T^2}{4M_a M_b} F_U^{\cos 2\phi} = \frac{2}{N_c} \sum_q e_q^2 \left[h_{1,a}^{\perp(1)\bar{q}}(x_a) h_{1,b}^{\perp(1)q}(x_b) + (q \leftrightarrow \bar{q}) \right], \quad (1.126)$$

$$\int d^2\mathbf{q}_T \frac{q_T}{M_b} F_T^{\sin \phi_S} = -\frac{2}{N_c} \sum_q e_q^2 \left[f_{1,a}^{\bar{q}}(x_a) f_{1T,b}^{\perp(1)q}(x_b) + (q \leftrightarrow \bar{q}) \right], \quad (1.127)$$

$$\int d^2\mathbf{q}_T \frac{q_T^3}{2M_a M_b^2} F_T^{\sin(2\phi+\phi_S)} = -\frac{2}{N_c} \sum_q e_q^2 \left[h_{1,a}^{\perp(1)\bar{q}}(x_a) h_{1T,b}^{\perp(2)q}(x_b) + (q \leftrightarrow \bar{q}) \right], \quad (1.128)$$

$$\int d^2\mathbf{q}_T \frac{q_T}{M_a} F_T^{\sin(2\phi-\phi_S)} = -\frac{2}{N_c} \sum_q e_q^2 \left[h_{1,a}^{\perp(1)\bar{q}}(x_a) h_{1,b}^q(x_b) + (q \leftrightarrow \bar{q}) \right]. \quad (1.129)$$

We define the weighted asymmetry as

$$A_X^{YW_Y}(x_a, x_b) = \frac{\int d^2\mathbf{q}_T W_Y F_X^Y}{\int d^2\mathbf{q}_T F_U^1}, \quad (1.130)$$

where W_Y is the weight corresponding to the modulation Y in Eq. (1.125–1.129). In the TMD approach it is straightforward to interpret the weighted asymmetry using the aforementioned equations. The weighted asymmetries defined here are the same as in the references [95–98] (up to a factor of 4 in the case of [96, 97]). For example, in the important case of the weighted Sivers asymmetry it is

$$A_T^{\sin \phi_S \frac{q_T}{M_b}} = \frac{\int d^2\mathbf{q}_T \frac{q_T}{M_b} F_T^{\sin \phi_S}}{\int d^2\mathbf{q}_T F_U^1} = -2 \frac{\sum_q e_q^2 \left[f_{1,a}^{\bar{q}}(x_a) f_{1T,b}^{\perp(1)q}(x_b) + (q \leftrightarrow \bar{q}) \right]}{\sum_q e_q^2 \left[f_1^{\bar{q}}(x_a) f_1^q(x_b) + (q \leftrightarrow \bar{q}) \right]}. \quad (1.131)$$

Another interesting example is the weighted asymmetry

$$A_T^{\sin(2\phi-\phi_S) \frac{q_T}{M_a}} = -2 \frac{\sum_q e_q^2 \left[h_{1,a}^{\perp(1)\bar{q}}(x_a) h_{1,b}^q(x_b) + (q \leftrightarrow \bar{q}) \right]}{\sum_q e_q^2 \left[f_1^{\bar{q}}(x_a) f_1^q(x_b) + (q \leftrightarrow \bar{q}) \right]}. \quad (1.132)$$

As in the SIDIS case, the methods to measure the spin-dependent weighted asymmetries in Drell–Yan are described in Sec. 3.3. To that end, we will need two expressions. The first is the denominator $\int d^2\mathbf{q}_T F_U^1$, which is common to all the weighted asymmetries. We integrate the cross-section (1.94) over q_T^2 , ϕ_S , and ϕ as

$$\begin{aligned} \frac{d\sigma_{\text{DY}}}{dx_a dx_b d\cos\theta} &= C_0(1 + \cos^2\theta) \int dq_T^2 d\phi_S d\phi \left\{ F_U^1 \right. \\ &\quad \left. + D_{\cos 2\phi} \cos 2\phi F_U^{\cos 2\phi} + |S_T| \left[\sin \phi_S F_T^{\sin \phi_S} + \dots \right] \right\} \quad (1.133) \\ &= 4\pi C_0(1 + \cos^2\theta) \int dq_T^2 d\phi_S F_U^1 \\ &= 4\pi C_0(1 + \cos^2\theta) \int d^2\mathbf{q}_T F_U^1. \end{aligned}$$

The polarisation-dependent terms have vanished in the integration over ϕ and ϕ_S . In the last step, we have used the fact that \mathbf{q}_T can be expressed in the target spin frame as $\mathbf{q}_T = (q_T \cos \phi_S, q_T \sin \phi_S)$, as explained in Sec. 1.3.1. Therefore, we have been able to write $dq_T^2 d\phi_S = 2d^2\mathbf{q}_T$.

The second expression needed is for the numerator $\int d^2\mathbf{q}_T W_{\sin \Phi} F_T^{\sin \Phi}$, where $\Phi = \phi_S, 2\phi \pm \phi_S$. To obtain it, we do the substitution $\phi_S = \Phi, \phi_S = \Phi - 2\phi$, or $\phi_S = 2\phi - \Phi$, according to the modulation of interest. Then we integrate with the appropriate weight $W_{\sin \Phi}$ over the azimuthal angle ϕ and over q_T^2 , eliminating the $\cos 2\phi$ modulation and the two spin-dependent ones, except $\sin \Phi$:

$$\begin{aligned} \frac{d\sigma_{\text{DY}}^{W_{\sin \Phi}}}{dx_a dx_b d\cos\theta d\Phi} &= \int dq_T^2 d\phi W_{\sin \Phi} \frac{d\sigma_{\text{DY}}^{W_{\sin \Phi}}}{dx_a dx_b d\cos\theta d\Phi dq_T^2 d\phi} \\ &= 2C_0(1 + \cos^2\theta) \left[\int d^2\mathbf{q}'_T W_{\sin \Phi} F_U^1 \right. \\ &\quad \left. + D_{\sin \Phi}(\theta) |S_T| \sin \Phi \int d^2\mathbf{q}'_T W_{\sin \Phi} F_T^{\sin \Phi} \right]. \quad (1.134) \end{aligned}$$

We have written $dq_T^2 d\phi = d^2\mathbf{q}'_T$, where $\mathbf{q}'_T = (q_T \cos \phi, q_T \sin \phi)$. As explained in Sec. 1.3.1, \mathbf{q}'_T may be inserted instead of \mathbf{q}_T into Eq. (1.88–1.91) with the equations remaining valid, and consequently into Eq. (1.127–1.129) as well. Therefore, the numerator of the weighted asymmetry of interest is the amplitude of the $\sin \Phi$ modulation in Eq. (1.134).

2. The COMPASS experiment

The COMPASS collaboration has set up an experimental facility in the North area of CERN and since 2002 carries on a series of fixed target experiments for various high energy physics channels [99]. In 2012, the physics data-taking entered a second phase (COMPASS II) expanding further the original scientific goals [100]. From its start, COMPASS was designed as a multi-purpose apparatus. The main points of interest are nucleon structure studies, hadron spectroscopy and studies of chiral dynamics. This thesis is focused on the first; from the rest let me just single out extensive studies of light meson spectrum (e.g. [101]) and measurements of pion polarisability by scattering of pions in the nuclear Coulomb field [102].

In the first phase of COMPASS (2002–2011), the spin structure of nucleons was studied in DIS and SIDIS processes on longitudinally polarised targets $\vec{\mu}^+ \vec{N} \rightarrow \mu^+ X$ and $\vec{\mu}^+ \vec{N} \rightarrow \mu^+ hX$ focusing on helicity distributions of quarks [103] and gluons [28, 29, 34] and in SIDIS on transversely polarised targets $\mu^+ N^\uparrow \rightarrow \mu^+ hX$ to investigate the transverse spin and transverse momentum structure of the nucleon [58, 79, 104].

In the COMPASS II phase the knowledge of the nucleon structure is deepened further. In 2015 COMPASS collected data on Drell–Yan reaction with transversely polarised target $\pi^- p^\uparrow \rightarrow \mu^+ \mu^- X$, which, combined with the earlier SIDIS measurements, as is discussed in Chap. 1, provides the important test of TMD universality. A different way to the understanding of the nucleon structure leads via exclusive reactions like deep virtual compton scattering (DVCS) $\mu^\pm p \rightarrow \mu^\pm p \gamma$, which was measured at COMPASS in 2016 and 2017.

In this chapter, the COMPASS apparatus as it was used in the 2015 Drell–Yan data taking is described. The polarised target is discussed in detail, the other parts are merely briefly introduced. Comprehensive information can be found in Ref. [105, 106]. In the description, we point out differences with respect to the SIDIS data taking in 2010. The two setups were very similar, the main differences being: the presence of a hadron absorber in the Drell–Yan setup, which in addition leads to the shift of the target position in upstream direction; the trigger settings (a hard-scattered single muon in SIDIS, a muon pair in Drell–Yan); a new drift chamber in place of an old straw detector; and a new data acquisition system. The general aspects of event reconstruction and data analysis are described at the end of this chapter.

2.1 Beamline and target area

COMPASS makes use of a secondary beam of hadrons (mainly π or p) with energy up to 280 GeV/c, or a tertiary μ beam with energy up to 190 GeV/c. The hadron beam is produced by a slow extraction of the super proton synchrotron (SPS) proton beam of typically $2\text{--}3 \times 10^{13}$ protons per pulse over a period of about 5–10 s (the so-called “spill”), which subsequently hits a beryllium target producing secondary hadrons. Various thicknesses of the production target can be chosen to match the required the secondary beam intensity. The secondary hadrons are sent to the experimental hall via a 1 km long beamline. The momentum and angular distributions of the beam can be tuned by magnets and collimators. The beam is

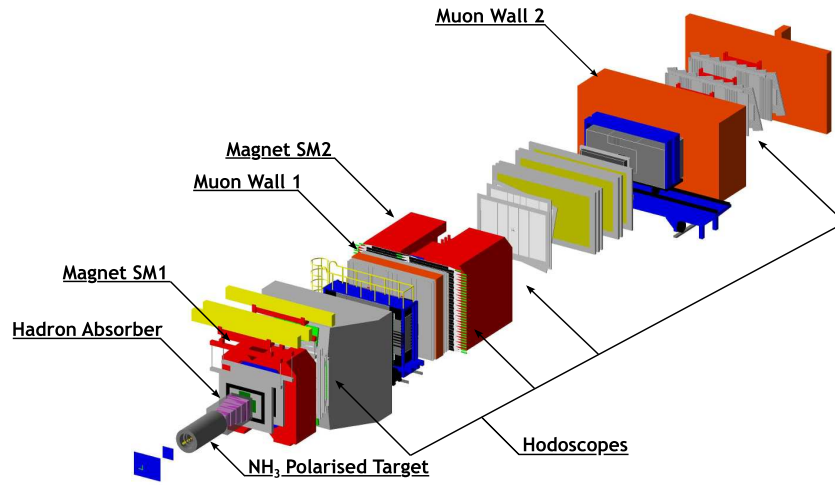


Figure 2.1: An artistic view of the COMPASS setup for the Drell–Yan programme, with labelled key components. The SIDIS setup is shown in Fig. 2.2. It differs mainly in the absence of the hadron absorber.

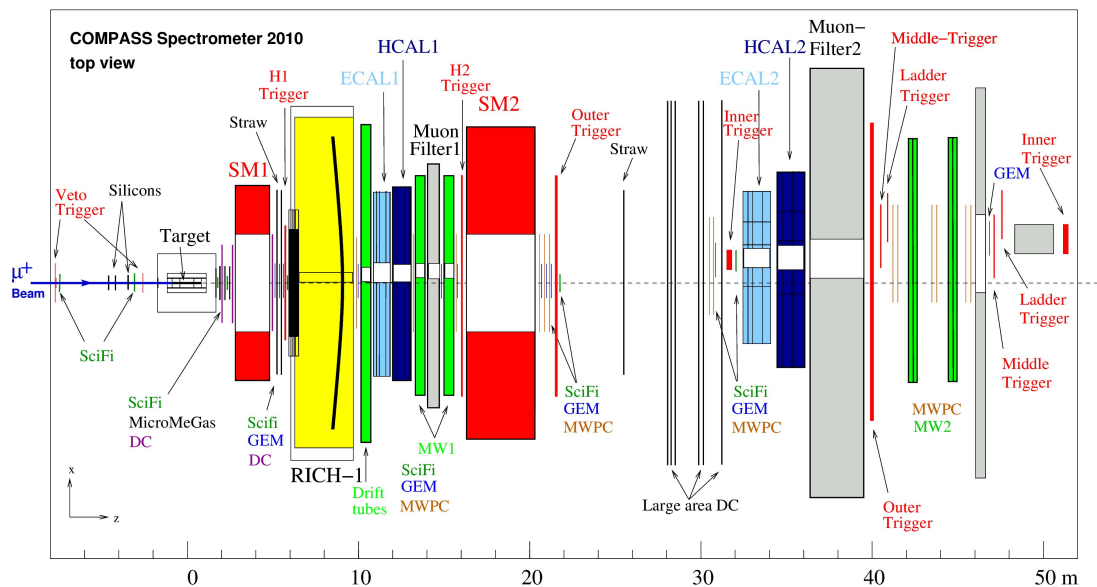


Figure 2.2: Top view of the COMPASS setup for the data-taking with muon beam in 2010. The vertical scale is arbitrary and indicates only the relative detector sizes.

accompanied by a halo, consisting mainly of muons. The negative hadron beam contains mostly pions, with admixture of kaons, antiprotons and other hadrons (the fractions depend on the beam momentum; at 190 GeV/c there are about 95 % π^- , 4.5 % K^- , and 0.5 % \bar{p} [105]). In the positive beam protons prevail, making up about 70 % at 190 GeV/c. Two differential Cherenkov counters can be used for hadron beam particle identification [106]. However, while they were successfully used in the hadron spectroscopy programme, their time resolution is not sufficient to effectively tag particles in the high-intensity beam needed for the Drell–Yan programme. An upgrade is ongoing to improve their performance in the upcoming 2018 Drell–Yan data-taking.

The muon beam comes from weak decay of pions and kaons, which makes it naturally longitudinally polarised. In the muon beam mode, 9 thick absorbers are placed in the beamline to remove the hadron component. Positive muon beam can reach intensities up to $10^8 \mu/s$, while negative one is available with lower intensities. In order to maximise the flux, the momentum spread as defined by the beam optics is relatively large and can reach 5 % [105]. Measurement of the momentum of each individual muon is therefore needed to determine the reaction kinematics precisely. This is done by the beam momentum station (BMS), which consists of a series of bending magnets surrounded by six scintillator hodoscopes. The momentum is measured with a precision better than 1 %. The beam polarisation as well as the intensity depends on the fraction of the decaying hadron momentum transferred to the muon. The beam line is usually tuned to $p_\mu/p_\pi \approx 0.9$, which maximises the flux and leads to about 80 % polarisation [107].

The arrangement of the target region differs according to the various programmes. A large solid-state polarised target, described in detail in Sec. 2.2, is used for SIDIS and Drell–Yan measurements. A 2.5 m long liquid-hydrogen target together with a recoil proton detector installed around it were used for the DVCS programme, while various solid state nuclear targets were used in the hadron spectroscopy measurements [106].

The setup for the the Drell–Yan program is shown in Fig. 2.1. The Drell–Yan reaction has a relatively low counting rate, especially in the mass range above the J/ψ peak. Therefore, a beam with the highest available intensity of about $10^8 \pi/s$ has been used, being limited mainly by radioprotection requirements. COMPASS had never used such intense hadron beam before. A carefully designed hadron absorber with a tungsten beam plug has been placed right downstream of the polarised target to lower detector occupancies and radiation levels. However, the muons going through the absorber experience multiple scattering, which reduces the resolution of the spectrometer.

The SIDIS setup of 2010 is shown in Fig. 2.2. It differed mostly in the absence of the hadron absorber allowing for the target to be placed more downstream.

2.2 The polarised target

The measurements of the TSAs in SIDIS and Drell–Yan reactions require a target with a large number of polarised nucleons. COMPASS uses NH_3 as polarised proton target material. The material was doped by electron beam irradiation with typically 10^{-3} – 10^{-4} free radicals per nucleus [108]. The hydrogen nuclei can reach polarisation $P = 0.8$ – 0.9 with dynamic nuclear polarisation (DNP) method

and their fraction in the NH_3 , which is roughly equal to the polarisation dilution factor f_D , is 0.176. Therefore, it has a high figure of merit $\propto P^2 f_D^2$, which makes it an optimal choice for COMPASS-like facilities [109]. The radiation hardness of the doped ammonia is an additional factor, very important for the Drell–Yan experiment, since it was estimated that the target material would get a dose of about 20 kGy in 220 days of running [108].

During the DNP procedure, the target material is irradiated with high intensity microwaves (≈ 70 GHz), while it needs to stay at temperatures lower than 1 K. In addition, the DNP requires high magnetic field (typically several Tesla), homogeneous at the level of 10^{-5} . The core of the COMPASS polarised target system is a superconducting magnet, designed and built for this experimental facility, which consists of a 2.5 T solenoid, about 1.4 m long, complemented with saddle coils, which can provide a 0.63 T field in the transverse vertical direction (see Sec. 2.2.1). The high and homogeneous magnetic field would be difficult to achieve in transverse polarisation mode, so after the target material reaches desired polarisation in longitudinal magnetic field, the DNP is switched off and the target material is rapidly cooled below 100 mK to reach the so-called “frozen spin” regime. At this temperature the relaxation time of the polarisation increases to more than 1 000 hours — a sufficient time for the experiments. Then the magnetic field can be rotated to the transverse direction. The cooling is provided by a ^3He – ^4He dilution refrigerator (see Sec. 2.2.2). The polarisation measurement is done by continuous-wave nuclear magnetic resonance (NMR) system, outlined in Sec. 2.2.5.

The target system is shown in Fig. 2.3. About 1 kg of the target material in the form of small beads is loaded in cylindrical, perforated target cells, placed on the beam axis. In the 2010 SIDIS run, the target was divided into three cells, the upstream and downstream being 30 cm long, and the central 60 cm long. In the Drell–Yan measurement the accuracy of the vertex reconstruction was expected to be worse than in the SIDIS runs, so two cells were utilised, each cell 55 cm long, 4 cm in diameter, and separated by a 20 cm gap. The cells are surrounded by the mixing chamber of the dilution cryostat, microwave cavity, and the magnet. The main part of the dilution refrigerator is indicated by the number 8 in Fig. 2.3 and the rest stays in the big turret. The other turrets contain magnet subsystems: liquid nitrogen connection for pre-cooling, current leads, cryocooler, and liquid He supply.

Further information about the target system can be found in Ref. [105] and the details of the 2015 setup in Ref. [108, 110, 111].

2.2.1 The superconducting magnet

The large-aperture superconducting target magnet has been put into operation in 2006 [112]. It is 2 350 mm long and its large aperture with 638 mm in diameter is essential for the large forward acceptance of the COMPASS spectrometer, which is 180 mrad in the polar angle. The magnet contains a superconducting solenoid coil complemented by 16 superconducting shim coils that produces a 2.5 T field parallel to the beam axis with homogeneity better than 10^{-5} over the volume of the target cells. The longitudinal field is used for the DNP. In addition, there is a superconducting dipole saddle coil capable of producing 0.63 T transverse holding

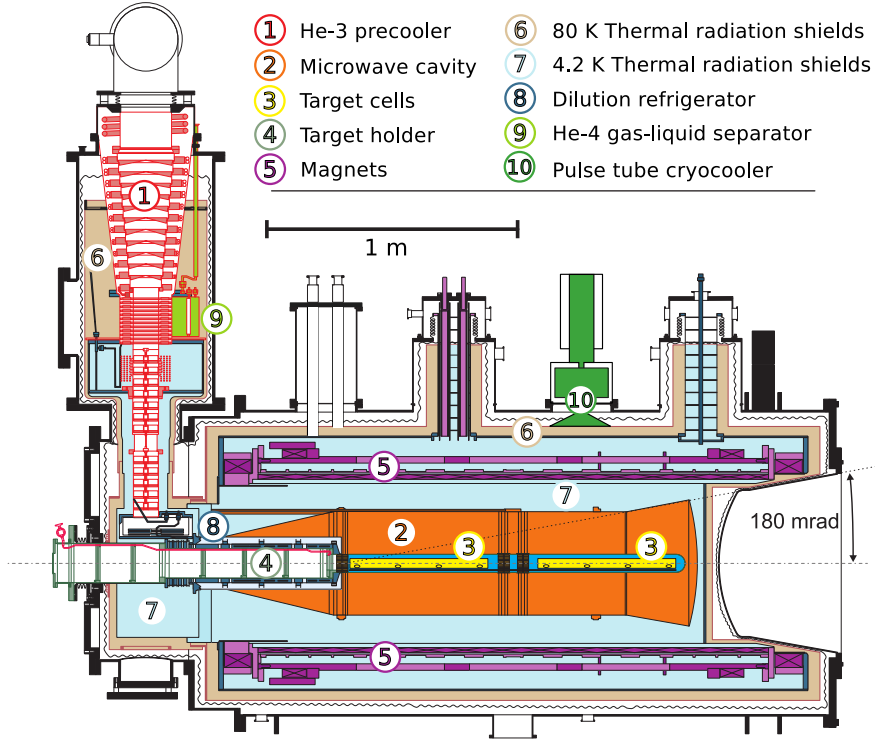


Figure 2.3: The polarised target system in 2015. The beam enters from the left-hand side and its path is denoted as the fine dashed line. It passes through two oppositely-polarised cells filled with polarised material (in yellow). The cells are surrounded by the refrigerator mixing chamber (in cyan), microwave cavity for the DNP (in orange), and by the magnet with its cryostat.

field. Combination of the two coils can be used in the frozen-spin mode to rotate the polarisation from the longitudinal to transverse direction, or to rotate it by 180° . Such operation is relatively fast (about 30 minutes) as compared to a DNP polarisation reversal, which takes at least 24 h. This is a great advantage for runs with longitudinally polarised target. For the transverse runs it is not possible because the beamline would have to be re-adjusted in order to compensate the effect of the reversed dipole field on the beam, and the DNP polarisation reversal is a must.

Between 2011 and 2015 the magnet underwent a general refurbishment by the CERN magnet team. Shorts on two shim coils were repaired and several design weaknesses were addressed to improve safety and lower service costs. A pulse tube cryocooler for cooling of thermal screens was added. The magnet cryostat was instrumented by new temperature sensors and quench detection. CERN UNICOS [113] is used for monitoring and control of the magnet. Apart from a local terminal, the measured values are accessible via DIP service [114] over LAN for the COMPASS detector control system (DCS) as well as for remotely-connected magnet experts, if needed. The connectivity is illustrated in Fig. 2.5. [108]

2.2.2 The dilution cryostat

A diagram of operation of the ^3He - ^4He dilution cryostat is shown in Fig. 2.4. The cooling mechanism is based on different properties of the two quantum liquids.

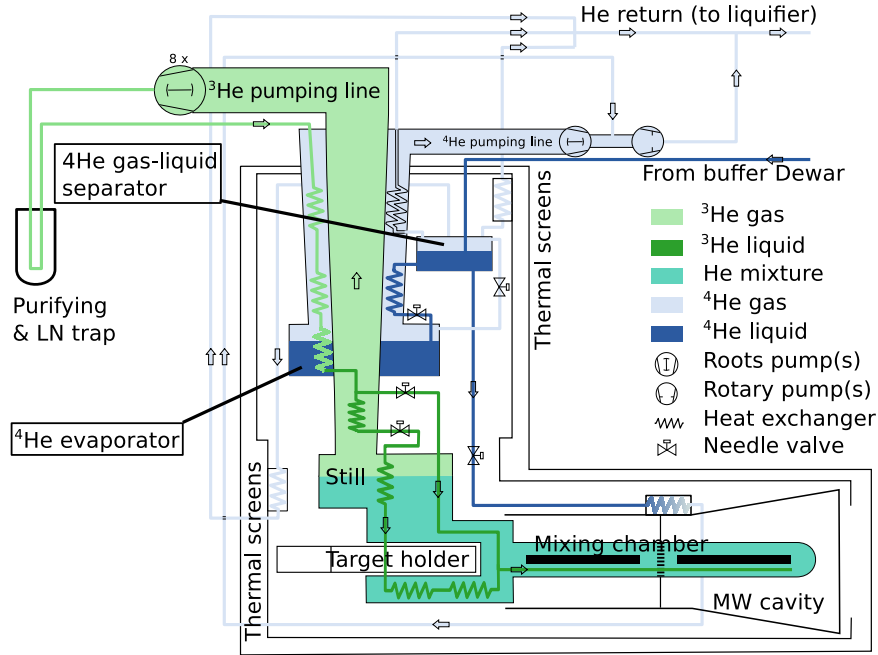


Figure 2.4: A scheme of operation of the polarised target dilution refrigerator. The closed inner loop containing the helium mixture is shown in green. Additional cooling of thermal screens and pre-cooling of the returning mixture is provided by liquid ^4He , denoted in blue.

When the helium mixture is cooled below certain temperature¹, the mixture dissociates into a ^3He -concentrated and diluted phase. When the concentration of ^3He in the diluted phase is artificially lowered, atoms of ^3He cross the boundary between the two phases, and the mixture cools down. This part is analogous to cooling by evaporation, and takes place in the mixing chamber. The ^3He can be efficiently removed from the diluted phase by pumping the vapours in the still, as it is lighter than ^4He , so it evaporates more easily. The removed ^3He gas flows back into the mixing chamber through a series of heat exchangers, where it is cooled down, so the heat input into the mixing chamber is minimised. [115]

Large mixing chamber about 1.6 m long and 7 cm in diameter is needed to contain the target cells. About 9000 l of He gas mixture with 10–15% of ^3He is used for operation of the refrigerator. The pumping of the ^3He -rich vapour is done by 8 Pfeiffer roots blowers in series. The compressed gas goes through activated-charcoal filters at room and liquid nitrogen temperatures to remove impurities. The gas returns to the mixing chamber through pre-cooler and series of flattened stainless steel tubes and sintered copper heat exchangers.

The ^3He flow rate and thus the cooling power is controlled with an electric heater placed on the bottom of the still. In the frozen-spin mode the still temperature is about 1.0 K and pressure 0.42 mbar with flow of 0.07 g/s and 0.2 mbar roots inlet pressure [108]. Temperatures below 50 mK were measured in the mixing chamber without beam and with beam of about $10^8 \mu\text{s}$, which corresponds to an estimated heat input of 1 mW [116]. In 2015 with the hadron beam of similar intensity the temperature was about 30–40 mK higher [108]. In the DNP mode the cooling power is about 350 mW at 0.3 K with about 3 times higher ^3He flow

¹Below 0.9 K, depending on the concentration of ^3He .

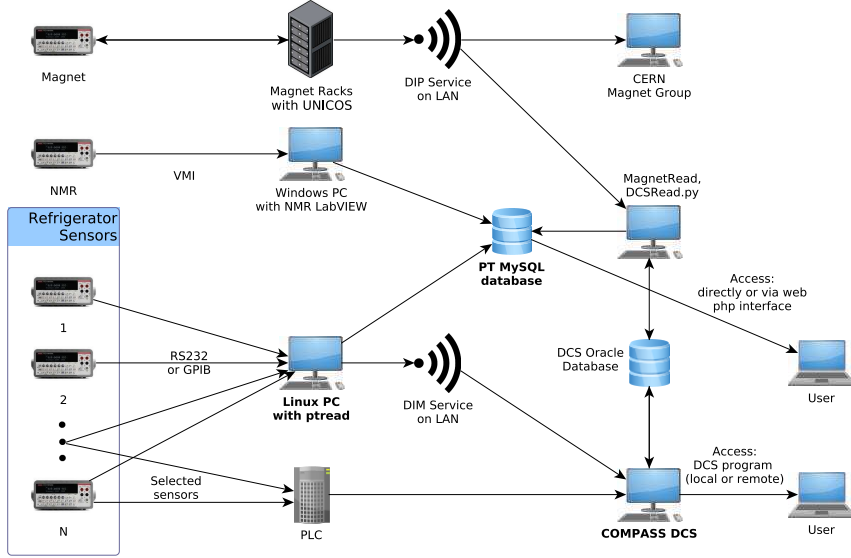


Figure 2.5: Scheme of polarised target remote monitoring: The magnet is monitored and controlled by UNICOS. The NMR measurements are done by a LabVIEW program, and are saved to databases. The dilution cryostat is monitored by *pthread*. In parallel, important parameters are read by a power-failure-protected PLC.

rate [116].

In addition to the circulating mixture the cryostat consumes about 15–20 l/h of liquid ^4He for the ^3He -precooler and cooling of thermal screens [116]. The precooler includes ^4He evaporator at 1.4 K pumped by a roots blower and a rotary pump [108].

To monitor the operation, the cryostat is instrumented by more than 30 thermometers. Temperatures above 4 K are measured by diode thermometers connected to a Lakeshore LS 218 temperature monitor. The dilution chamber, where much lower temperatures are reached, is instrumented by 3 RuO and 3 Speer resistive thermometers read by low-noise Picowatt AVS 46 and AVS 47 resistance bridges. The thermal equilibrium calibration of the NMR system requires very precise temperature measurement at about 1 K, which is provided by a ^3He vapour pressure thermometer.

2.2.3 Monitoring of the dilution cryostat

From the 2015 data-taking on, the control-room is no longer in the experimental hall itself, but in an office building, which is about 500 m away. As a consequence, the polarised target systems needed a better remote monitoring. Before, the dilution cryostat had been monitored by a LabVIEW [117] program, running on a dedicated computer in the control-room. Several critical parameters had been read in parallel by a programmable logic controller (PLC), powered from a source protected from power-failures. The PLC had been connected to the DCS.

The polarised target group had decided to replace the LabVIEW-based cryostat monitoring with a new, more robust, Linux-based software, which would make all parameters accessible for the DCS. Of course, the power failure insensitive

PLC solution remained in place, operating in parallel with this new system. A programme package *ptread* was developed by J. Koivuniemi and the author of this thesis. It consists of two background processes, *ptread.pl* and *ptdimserv*. The former periodically initiates reading of the sensors (thermometers, pressure gauges etc.) by simple instrumental drivers scripts [118], sends the measured values via socket to the latter program, and optionally calls scripts writing the values to SQL databases. Both the main program and the drivers are written in Perl.

The *ptdimserv* program acts as an interface between *ptread.pl* and the DCS. The communication with the former is done via a socket connection. To make the measured values available for the DCS, it maintains a Distributed information management (DIM) server [119], which is a way of communication used by many COMPASS subsystems. The role played by *ptread* in the monitoring of the target systems is shown in Fig. 2.5. The system was successfully used in 2015. The availability of the monitoring in the DCS was beneficial for the data-taking shifts as well as for the target experts, who in addition could access directly the databases. In addition to the dilution cryostat, *ptread* monitors also the operation of the DNP.

2.2.4 Nuclear polarisation

When a particle with spin I is subjected to a magnetic field B , the Zeeman interaction forms a set of $2I+1$ sub-levels separated by energy $\hbar\omega$. The $\omega_I = -\gamma B$ is called Larmor frequency of the particle. The gyromagnetic ratio γ is a distinct property of the particle². An ensemble of such particles can be described by polarisation

$$P = \langle I_z \rangle / I = n^+ - n^-, \quad (2.1)$$

where n^\pm are fractions of the total number of spins oriented parallel and anti-parallel to the magnetic field. In thermal equilibrium at temperature T , the polarisation is given by Brillouin function, which in the case of ^1H nuclei with $I = 1/2$ has the simple form

$$P_{\text{TE}} = \tanh \frac{\hbar\gamma B}{2k_{\text{B}}T}, \quad (2.2)$$

k_{B} being the Boltzmann constant. Since the gyromagnetic ratio of an electron is three orders of magnitude larger than that of proton,

$$\frac{\gamma_{\text{e}}}{2\pi} \doteq 28.025 \text{ GHz/T} \qquad \frac{\gamma_{\text{p}}}{2\pi} \doteq 42.577 \text{ MHz/T}, \quad (2.3)$$

the polarisation of ^1H nuclei in NH_3 in 2.5 T magnetic field and at 1 K is about 0.25 %, while the polarisation of the electrons in the $\dot{\text{N}}\text{H}_3$ radicals is almost 100 %. Reaching considerable polarisation in currently achievable magnetic fields would require very low temperatures, which would in turn cause extremely slow thermal exchange between atomic lattice and the nuclear spins in almost all insulators, making the polarisation to take weeks or longer to establish. On the other hand, this approach works well for many metals, where the relaxation is faster (and

²For an electron — a Dirac particle — it is $\gamma_{\text{e}} = g_{\text{e}}\mu_{\text{B}}/\hbar \approx 2\mu_{\text{B}}/\hbar$. For composite systems like nucleons or nuclei its calculation is a challenge.

DNP impossible), especially in para- and ferro-magnets, where the external field is amplified, and the nuclei experience fields as high as 100 T [120].

The method of DNP can be phenomenologically described as follows: a small amount of paramagnetic impurities is introduced³ into a dielectric insulator containing the nuclei of interest. The material is put into a static magnetic field, where the Larmor frequencies are ω_A and ω_e for the nuclei and electrons of the paramagnetic centres respectively. Finally, the material is subjected to an additional oscillating magnetic field with frequency $\omega = \omega_e + \delta$, where $\delta \approx \omega_A \ll \omega_e$. For the typical static fields in the order of 1 T the frequency ω is in the microwave region, while ω_A is in the radiofrequency region, as can be seen from Eq. (2.3). The procedure can lead to a strong enhancement of the nuclear polarisation, up to the levels close to the polarisation of the electrons, i.e. 100%. When $\delta < 0$, the polarisation is positive, when $\delta > 0$ it is negative.

The word dynamic in the name of the method refers to the fact that the system of nuclear spins polarised by DNP is not in thermal equilibrium with the lattice. If the oscillating field is switched off, the polarisation exponentially approaches the value given by Eq. (2.2). The paramagnetic centres, necessary for the DNP, speed up the relaxation. However, at sufficiently low temperature the relaxation time can be in the order of weeks or months. It is worth noting, that the negative polarisation of nuclear spins is not possible in the thermal equilibrium, as it means that the higher energy states (spins anti-parallel to the field) are more populated than the lower ones, which corresponds to a negative temperature.

Two popular theories, describing the mechanism of the DNP, exist — the solid-state effect and the equal spin temperature theory. The former assumes no interaction between the paramagnetic centres, which may be valid for very low concentrations of the impurities, and describes the effect as simultaneous flips of pairs of electron and nuclear spins. The latter on the contrary assumes strong interaction and describes the polarisation as a cooling of an electronic spin-spin interaction thermal reservoir, thermally connected with the system of nuclear spins [109, 120].

On the COMPASS polarised target, the DNP is applied in 2.5 T field of the target solenoid. Two extended interaction oscillators (EIOs) provide the microwave field at two frequencies 70 ± 0.1 GHz to simultaneously polarise the two target cells in the opposite directions. The water-cooled EIOs provide power of 20 W, which can be regulated using custom-made attenuators. The microwaves are lead to the experimental area and into the target cryostat through about 15 m long waveguides, losing 6–8 dB on the way. They are connected to a copper cavity (number 2 in Fig 2.3), divided into two compartments by a microwave stopper [108].

The frequency and the power of the microwaves are fine-tuned during the DNP. They are monitored by two EIP-548-B Phase Matrix frequency counters (for the two cells) and by a multimeter connected to Millitech DET-12-RPFW0 diode, which measures the microwave power. The frequency counters and the multimeter are read by the program *ptread* described in Sec. 2.2.3.

³By chemical doping or, like in the case of COMPASS NH₃ target, by irradiation [109].

2.2.5 Polarisation measurement and target operation

A continuous-wave NMR system with 10 coils provides measurement of the polarisation in the two target cells. In the Drell–Yan data taking, four rectangular coils ($5 \times 1.1 \text{ cm}^2$) are placed on the surface of the target cells, two are inside [108]. In the SIDIS data-taking, all 10 coils were placed outside the cells. The polarisation of the nuclei changes the absorption part of the coil inductance in a narrow region around the nuclear Larmor frequency (106.4 MHz for ^1H in 2.5 T field). The integral of the absorption peak is proportional to the polarisation. The frequency is swept in 600 kHz window around the ^1H Larmor frequency by the PTS250 synthesiser. The resonance effect is measured by a series-tuned Q-meter circuit, followed by an offset-subtraction and signal amplification circuit on Yalecard. [121] The signal is digitised by a 32-channel 16-bit A/D-converter in the National Instruments PXI crate. The data acquisition and control of the sweep is done in a LabVIEW program [108].

The constant of proportionality between the integral of the NMR signal and the polarisation is determined by measuring the NMR signal in the thermal equilibrium state at several temperatures. In that case the polarisation is given by Eq. (2.2). ^1H nuclei in any material close to the coils contribute to the thermal equilibrium signal. However, their polarisation is not enhanced by the DNP. This background is determined by the NMR measurement with empty target cells. In the past (including the 2010 run), the background had been found to be about 30 % due to hydrogen contained in the polyamide target cells. For the 2015 data-taking, new hydrogen-free target cells made of polychlorotrifluoroethylene have been produced, reducing the background to 5 %. [111]

During the SIDIS data taking in 2010, the target was operated in the same way during 12 periods, usually a week long. Each of them consisted of two subperiods, characterised by opposite polarisation in each cell. In a period, first the polarisation was built up (opposite in the two target cells) and measured in the 2.5 T field longitudinal with respect to the beam. Subsequently, the target material was cooled down to about 60 mK and the polarisation was rotated by the solenoid and dipole magnets to the transverse direction and the physics data taking started. The physics data were acquired during the first subperiod. At the end of the subperiod, the polarisation was rotated to the longitudinal direction to be measured, as the NMR circuits and coil positions are optimised for measurement in the 2.5 T longitudinal field and can not operate in the transverse mode. The decay of the polarisation between the two measurements was interpolated by an exponential function [111]

$$P(t) = P_{\text{TE}} + P_0 e^{-t/\tau}, \quad (2.4)$$

where the relaxation time τ characterises the rate of the polarisation loss. Before the beginning of the second subperiod, the polarisation was built up again in the opposite direction by the DNP with changed microwave frequencies in the three cells. Between the second subperiod and the beginning of the following period the polarisation was usually preserved or topped up to save time. The values of the maximum polarisation, the average polarisation over the data-taking are summarised in Tab. 2.1. As can be seen they slightly depend on the target cell and polarity.

| cell | polarity | maximum P [%] | τ with beam on [h] |
|---------|----------|--------------------|-----------------------------|
| up | + | 85.5 ± 2.7 | $(7.0 \pm 1.7) \times 10^3$ |
| | - | 84.8 ± 2.6 | |
| central | + | 84.2 ± 1.2 | $(5.7 \pm 0.7) \times 10^3$ |
| | - | 84.3 ± 1.2 | |
| down | + | 85.4 ± 1.3 | $(5.7 \pm 1.2) \times 10^3$ |
| | - | 85.4 ± 1.3 | |

Table 2.1: Target polarisation in 2010 [122]. The average polarisation over the whole year was about 80 %.

| cell | polarity | maximum P [%] | average P over data-taking [%] | τ with beam on [h] | τ with beam off [h] |
|------|----------|--------------------|-------------------------------------|----------------------------|-----------------------------|
| up | + | 82.7 | 74.2 | 1.4×10^3 | 3.6×10^3 |
| | - | 86.0 | 71.4 | 1.2×10^3 | 2.9×10^3 |
| down | + | 79.3 | 69.2 | 1.0×10^3 | 4.9×10^3 |
| | - | 77.8 | 67.0 | 0.74×10^3 | 1.7×10^3 |

Table 2.2: Target polarisation in 2015 [111].

In the 2015 data-taking, the target was operated in a similar way, but with 9 two-week-long periods. Polarisation loss of about 1 % was observed in the rotation [111]. The characteristics of the run are summarised in Tab. 2.2. They are difficult to interpret, as there are several effects at play. During the beam on, the relaxation time is clearly shorter due to the heat introduced by the beam. Moreover, it is shorter in the downstream cell, which may be due to stronger flux of secondary hadrons. This systematic difference between the cells is not observed in measurements without beam. The maximum polarisation reached in the two cells might be different, because it depends on the homogeneity of the magnetic field and of the microwave power.

2.3 Spectrometer

Because of its challenging and wide physics focus, the COMPASS spectrometer was designed to offer large angular and momentum acceptance, including tracking from extremely small polar angles up to 180 mrad and particle identification [105, 106]. The setup used in 2010 for SIDIS measurements is shown in Fig. 2.2. The setup for the 2015 Drell–Yan run, shown in Fig. 2.1, was similar. It did not include the silicon trackers; the target was moved upstream to make room for the hadron absorber; and the straw tube detector at $Z \approx 25$ m was replaced by a new drift chamber.

The spectrometer is divided in two stages built around two large horizontal-bending dipole magnets SM1 and SM2 with bending power 1 Tm and 5 Tm, respectively, shown in red in Fig. 2.2. The stages are called large angle spectrometer (LAS) and small angle spectrometer (SAS), and each is equipped with

tracking detectors, an electromagnetic calorimeter, a hadronic calorimeter and a muon filter. In addition, there is a ring imaging Cherenkov (RICH) detector for charged hadron identification in the LAS.

2.3.1 Tracking

Detection of charged particle tracks at small polar angles requires good time resolution and radiation hardness, as the rates are very high. In the vicinity of the beam scintillating fibres (SciFi) read out by multi-anode photomultipliers are used. They have spatial resolution $\sigma_s \approx 130 \mu\text{m}$ and time resolution $\sigma_t \approx 0.4 \text{ ns}$ [105]. In the data-taking with muon beam, they were complemented with silicon microstrip detectors, which bring an excellent spatial resolution ($\sigma_s \approx 7 \mu\text{m}$, $\sigma_t \approx 1.6 \text{ ns}$ [106]).

At slightly larger angles the tracks are recorded by micro-pattern gaseous detectors (11 GEMs and 3 Micromegas), characterised by high spatial resolution and low material budget. Central dead zones with 5 cm diameter protect them from the non-interacting beam. A GEM detector consists of two parallel electrodes and several thin (about $50 \mu\text{m}$) polyimide foils cladded on both sides with copper. The foils are itched with microscopic holes and a potential difference of about 100 V is applied on their two sides. The avalanche multiplication of primary electrons induced by the passing charged particles takes place in the holes, the electric field of the two electrodes collects the electrons and guides them to the next stage, until they are finally detected by a readout anode segmented in two perpendicular layers of strips. The detectors have active area of $31 \times 31 \text{ cm}^2$ and resolutions $\sigma_s \approx 70 \mu\text{m}$, $\sigma_t \approx 12 \text{ ns}$ [105]. In 2008, smaller ($10 \times 10 \text{ cm}^2$) GEM detectors with pixelised readout in the central part and no dead zone were added to the setup to replace some of the SciFis, lowering the material budget [106].

The Micromegas detectors have a parallel-plate electrode structure as well. The space between the electrodes is divided by a metallic micro-mesh in two parts: a conversion gap with a moderate electric field, and a narrow (about $100 \mu\text{m}$) amplification gap with a high field. The mesh captures most of the positive ions created in the amplification gap and the small size of the gap reduces transverse diffusion of the electrons. Thus high rate capability is obtained. COMPASS was the first high-energy experiment to employ this technology. Each chamber has an active area of $40 \times 40 \text{ cm}^2$ with a central deadzone (5 cm diameter). The resolutions are $\sigma_s \approx 90 \mu\text{m}$, $\sigma_t \approx 9 \text{ ns}$ [105]. As the detectors are positioned in the fringe fields of the target and SM1 magnets, the spatial resolution is lowered due to the Lorentz force on the electrons down to $110\text{--}145 \mu\text{m}$, depending on the readout strip orientation [106]. Between 2010 and 2015, some stations have were upgraded to pixelised readout in their central parts.

At larger angles multi-wire proportional chambers (MWPCs), drift chambers and drift tube detectors are used. The MWPCs take care of the large area tracking in the SAS. They have active areas of about $180 \times 100 \text{ cm}^2$ with a $16\text{--}22 \text{ cm}$ diameter dead zone and resolution $\sigma_s \approx 1.6 \text{ mm}$. In drift chambers, the drift time of the avalanche to the anode wire is measured in addition to the charge collected, improving the spatial resolution. Several types of them are in the setup. Three are installed in LAS with active areas of $180 \times 127 \text{ cm}^2$, 30 cm diameter dead zone, and $\sigma_s \approx 110 \mu\text{m}$ in the horizontal direction and $\sigma_s \approx 170 \mu\text{m}$ in the vertical one

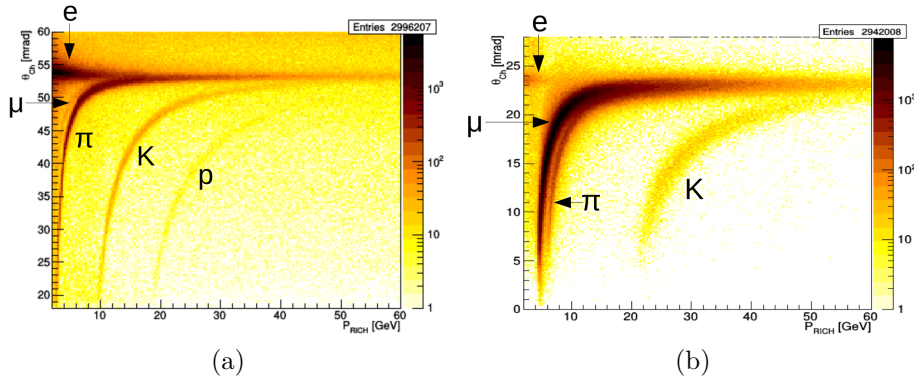


Figure 2.6: The Cherenkov angle versus the particle momentum with the nominal radiator gas C_4F_{10} and minimal-maintenance gas N_2 , which was used in the Drell–Yan run, when the hadron tagging was not needed.

(due to the SM1 fringe field) [105]. Two large ones, covering $248 \times 208 \text{ cm}^2$, are positioned in the SAS. One of them was produced only before the 2015 run to replace an ageing straw tube detector. Finally, six large area drift chambers with an active area of $5 \times 2.5 \text{ m}^2$ and less fine resolution of about 0.5 mm are used also in the SAS.

Straw tube detectors (only one in 2015) play in the setup the same role as the drift chambers. They consist of so-called straw drift tubes with 6–9 mm in diameter and an anode wire in the center. The aluminium-cladded inner wall of the tube serves as a cathode. The active area is about $3.2 \times 2.8 \text{ m}^2$ with a $20 \times 20 \text{ cm}$ physical central hole. The resolution is about $190 \mu\text{m}$. Another very large area detector consisting of mini drift tubes is positioned downstream of the RICH, matching its angular acceptance. It helps to measure the momentum of particles detected in the RICH. It has an active area of about $5 \times 4 \text{ m}^2$ with a $1 \times 0.5 \text{ m}^2$ central hole and resolution of about 1 mm .

2.3.2 Particle identification and calorimetry

The identification of muons is based on their material-penetration capability. There are two dedicated stations consisting of an absorber, preceded and followed by tracking stations (Mun Walls). They are located downstream of the calorimeters, which already absorb most hadrons. In the LAS, the detection is done by eight planes of squared mini drift tubes with resolution of 3 mm . The 60 cm thick absorber is made of iron. The station covers an area of $4.8 \times 4.1 \text{ m}^2$ with a central hole of $1.4 \times 0.9 \text{ m}^2$, which matches the angular acceptance of the SAS. The second station is installed at the very end of the SAS. The absorber is a 2.4 m thick concrete wall. The tracking upstream of the wall is done by the SAS tracker system, while downstream of the wall there is a dedicated steel drift tube detector with $\sigma_s = 0.6\text{--}0.9 \text{ mm}$.

The RICH detector can distinguish hadron species in certain momentum range. It is based on the Cherenkov effect – the radiation of light by charged particles travelling faster than the speed of light in a medium. The Cherenkov photons are emitted under a certain angle with respect to the particle track, which de-

depends on the relative velocity β of the particle and the refractive index n of the medium, $\cos\theta_{\text{Ch}} = 1/(n\beta)$. Thus measuring the angle, the particle velocity is determined. As the momentum p is known from the spectrometer, particle mass can be calculated, if $p > m/\sqrt{1-n^2}$. At high momenta, the angle saturates at the same value for all masses. COMPASS uses C_4F_{10} gas as the radiator medium, which has the refractive index $n - 1 = 1.5 \times 10^{-3}$ for 7 eV photons. This leads to hadron identification in a range from the Cherenkov threshold, which is 1.5, 10, and 18 GeV/ c for π , K, and p, respectively, up to about 40 GeV/ c . The measured correlation of the angle and the particle momentum is shown in Fig. 2.6(a), illustrating this. Fig. 2.6(b) demonstrates how the situation changes with a different refractive index $n - 1 \approx 0.3 \times 10^{-3}$. It is from 2015, when the RICH was filled with N_2 , as its use in Drell–Yan data analysis was not foreseen. For an optimal exploitation of all the available information for the hadron identification, the reconstruction software assigns a likelihood of being a pion, kaon, proton, electron, or background to each track with a signal in the RICH. The radiator gas is kept in an 80 m³ volume, which is large enough to cover the angular acceptance of the LAS. A thin-wall pipe is mounted in the center to let the non-interacting beam pass without light emission. The Cherenkov light is reflected by a mirror system towards photodetectors, positioned outside of the spectrometer acceptance. In the lower-occupancy outer part, the photons are detected by MWPCs equipped with CsI-coated photocathodes, which are sensitive to ultra-violet light. The inner part is instrumented with multi-anode photomultipliers coupled to fused silica lens telescopes, which offer an excellent time resolution of less than 1 ns and high-rate capability [106]. Recently, one third of the MWPCs was replaced by novel micro-pattern detectors, which are more resistant to discharges and can thus operate at higher gain [123].

The electromagnetic calorimeter in the LAS (ECAL1) is made of 1 500 lead-glass modules. The high energetic photons and electrons entering the modules create an electromagnetic shower. Scintillation light produced by the shower particles is detected by photomultipliers. The other electromagnetic calorimeter (ECAL2) positioned in the SAS is in part also build with the lead glass blocks as well, while for the remaining part shashlik modules alternating lead and scintillator layers are used. In total it consists of 2 972 blocks and its resolution is about $\sigma(E)/E \approx 0.06/\sqrt{E} + 0.02$ with the energy E in the units of GeV/ c^2 [105]. Both calorimeters are calibrated using a 40 GeV/ c electron beam. The time stability of the calibration is ensured by a LED or laser monitoring systems. The calibration is further improved in the offline analysis, when the $\pi^0 \rightarrow \gamma\gamma$ decays are used as a reference. As a result, the resolution for the π^0 mass is about 4.6 MeV/ c^2 [106].

The two hadronic calorimeters (HCAL1,2) have lower spatial granularity and consist of 480 and 220 modules. Each module has alternating layers of iron and scintillator plates. The resolution is about $\sigma(E)/E \approx 0.7/\sqrt{E} + 0.05$ with the energy E in the units of GeV/ c^2 [105].

2.3.3 Trigger

The purpose of the trigger system is to provide a signal for the readout electronics to record an event. The decision is made based on signals from scintillating hodoscopes or energy deposited in the calorimeters. Veto hodoscopes are situated

upstream from the target, surrounding the beam. They prevent contamination of the recorded events with halo tracks. Some of the trigger hodoscopes are positioned downstream of the hadron absorbers to provide the muon triggers, which are important both in the SIDIS (triggering on scattered muons) and Drell–Yan (triggering on dimuon production) data-takings, and are described in the following.

The fact that the muon originated in an interaction in the target region is checked using two techniques: target-pointing in the vertical plane (as the spectrometer magnets change only the horizontal component of particle momenta) and energy loss, which utilises the fact that the muons originated in the interactions have smaller momentum as compared to the beam or halo particles and thus are deflected more in the spectrometer magnetic field. To determine the polar angle in the vertical (target pointing) or horizontal (energy loss) direction, two stations with hodoscope slabs are needed. All allowed coincidences of signals from the slabs in the two stations are encoded in the so-called trigger matrix. The trigger fires when an allowed coincidence occurs (and if there is no veto signal). Such a pair of hodoscope stations forms a trigger system.

In the SIDIS data-taking, several triggers have been set up to single out the events with a scattered muon in the kinematical regions of interest. They are: the Inner Trigger, Ladder Trigger, middle trigger (MT), outer trigger (OT), and large angle spectrometer trigger (LAST). All of them but LAST are positioned in the SAS. In the Drell–Yan data-taking, the 2μ trigger was used. It selects events with 2 muon tracks, which roughly point to the target. This is achieved by a combination of two single-muon triggers, namely a coincidence of 2 LAST, LAST + OT, or LAST + MT is required.

2.4 Data acquisition and detector control

Each experiment needs to read, process, and store data — the activities known altogether as data acquisition (DAQ). The process starts with the front-end electronics, which reads raw signals from the detectors, and digitises and sends them further if a trigger signal arrives. The data are transmitted using the S-Link protocol on a passive optical network, optionally via data concentrator modules, to event builders. They combine the data originating in the same trigger, label them properly, and store the data on disks. The approximately 250 000 channels of the spectrometer are read out with a trigger rate up to 50 kHz during the beam extraction time with an average event size of about 36 kB.

After 12 years of successful operation, it became difficult to maintain the original DAQ based on PCI technology (the system is described in Ref. [106]). It was decided to design a new and modern system of event building, DAQ monitoring, and control for the ambitious physics program of the COMPASS II. While the old DAQ utilised an event building based on distributed computers on a high-speed network, the new system developed mostly in 2013 and 2014 uses field-programmable gate arrays (FPGAs), which allow the event building algorithm to be encoded in the hardware [124]. The new system has been found faster, more compact and, once initial problems were dealt with, more reliable. The system owes its reliability mostly to consistency checks applied on the data at each stage. Thus the data blocks with front-end or transmission errors are dropped

on their way and a decodable data structure is always preserved, which enables the readout computers to recognise and localise the origin of errors present in the data stream.

COMPASS detector control system (DCS) provides a centralised access to slow-varying parameters of almost all parts of the experimental apparatus. The DCS is based on a commercial SCADA (Supervisory Controls and Data Acquisition system), called PVSS; and it is used on daily basis by both data-taking shift crews and detector experts. Its two main roles are recording of the data-taking conditions and alerting the shift-crews in the event of technical problems.

3. Measurement of the transverse spin asymmetries

In the following, the way from the collected raw data to the final TSAs is described. First we briefly introduce the event reconstruction and the data selection features that are common to both the J/ψ and Drell–Yan analyses. Finally, we describe how the TSAs are extracted utilising the acceptance cancellation.

3.1 Event reconstruction

The reconstruction of the collected events (also called production) is done on a computational farm using an object-oriented package called CORAL (COMPASS reconstruction and analysis) [105, 106, 125]. The input for CORAL are the raw data from the detectors or the output from the COMPASS Monte Carlo simulation ComGeant [105], based on Geant 3, or the more recent TGeant [126], based on Geant 4. In addition, position and calibration parameters of the detectors need to be provided, as well as magnetic field and material maps. The software fits charged particle tracks and interaction vertices, reconstructs RICH patterns, calculates number of radiation lengths passed by the particles in the spectrometer, and associates tracks to calorimetric clusters. CORAL produces ROOT [127, 128] histograms, mostly used for detector studies, and the so-called mini data summary tapes (mDSTs), which contain all the information in the reconstructed events. The mDSTs are ROOT Trees containing objects defined by the package PHAST (Physics analysis software tools) [106, 129], used in further physics analyses.

In CORAL the tracks of the final-state particles are reconstructed in three steps. First, straight segments are searched for in the three regions free from magnetic fields and from large amounts of dense materials. In the second step, called bridging, the straight segments are connected over the magnets and absorbers. Finally, the best track parameters are found in a fitting procedure based on a Kalman filter. [105]

During the reconstruction, the connection of groups of reconstructed tracks into vertices is attempted. There are two kinds of vertices – primary and secondary. The primary vertex reconstruction starts with the calculation of the points of closest approach between one beam track and all outgoing tracks. A set of tracks with these points reasonably close to each other are analysed further. An inverse Kalman fit is performed to get the vertex position and tracks contributing too much to the χ^2 of the fit are excluded from the vertex. In the reconstruction of the secondary vertices the two-body decays of neutral particles are taken into account. All pairs of oppositely-charged tracks are searched for a possible decay position.

Several primary and secondary vertices may be reconstructed in an event. The same track can be connected to more than one vertex, the selection of the best option is done in at the physics analysis stage. To this end, PHAST offers a function for the best primary vertex determination. As it is optimised for SIDIS, it returns the vertex with the scattered muon and the highest number of other outgoing tracks.

3.2 Data selection

The collected data are checked for stability in time. In particular, occasionally there is a spill with bad extraction and thus containing a spike in intensity or other irregularities. In addition, some detector may have problems for a certain period of time. The stability and quality checks are done on several levels. First, the occupancies, multiplicities, and other detector characteristics are studied. If an unstable detector is identified, especially if the problems are concentrated in one subperiod only, it can be excluded from the reconstruction. Second, the so-called macro variables (like the number of reconstructed vertices or muon tracks per event) are monitored. Finally, a set of relevant kinematic distributions (different from the ones used for the results) is monitored on a run-by-run basis¹. The choice of the variables and distributions can be different for different physics analysis. The outliers spills and runs identified in the checks are registered in the so-called bad spills list to be rejected in the physics analyses.

In the 2010 data, 2–5% of the collected events were rejected by the macro variables monitoring and an additional 6% were rejected based on the kinematic distributions. In the Drell–Yan analysis, about 15% of the data were rejected based on the macro variables and about 2% based on the distributions. In general, the rejection rates differ a lot between the periods.

The physics analysis is done utilising PHAST. The collected events are filtered in order to suppress the background, which may be either of physical origin or combinatorial. Usually, the event selection contains the following steps: the requirement for a physics trigger signal, i.e. scattered muon trigger in SIDIS and dimuon trigger in Drell–Yan; selection of the best primary vertex of the event; requirements on the track reconstruction, usually the reduced χ^2 of the track fit must be smaller than 10; and the cut on the vertex position, which should lie in the target cells. The muon selection is based on the number of radiation lengths crossed by the track (usually 30), complemented with the requirements on the first and last measured point. The first one should be upstream from the SM1 magnet to ensure a precise momentum measurement, while the last one should be downstream from the first muon filter. Other selection steps are included and tuned for each analysis.

3.3 Extraction of transverse spin asymmetries

Precise measurement of azimuthal distribution of final state particles requires either a precise description of the experimental acceptance or a clever trick to cancel the acceptance. The former requires a very good knowledge of the geometry of the setup and of the efficiency of the various detectors during the data taking, and a Monte Carlo simulation in order to calculate and correct for the acceptance. The latter is possible in the measurement of target polarisation dependent asymmetries, if the target polarisation can be frequently reversed. Doing so, the spectrometer effectively turns into its mirror image, cancelling the azimuthal acceptance. With a target containing oppositely-polarised cells that are illuminated by the beam at the same time the impact of possible variation of

¹An uninterrupted run lasts 200 spills.

the acceptance in time can be reduced. Such variation can be caused e.g. by a detector plane, which breaks at some point and takes several hours to be repaired.

COMPASS implements the acceptance cancellation using several methods. The so-called “double ratio method” of TSA measurement [130] and a similar method, which works for the weighted TSA, are presented in the following. They have been used for the analyses described in this thesis. The “standard” un-weighted TSA published by COMPASS are measured by the extended maximum likelihood method [131]. It is also briefly described in the following, but its use in the case of signal plus background and for the weighted asymmetries is not straightforward.

3.3.1 Conventional TSAs

In Sec. 1.2.2 and 1.3.2 we have introduced the TSAs in SIDIS and Drell–Yan processes. The starting point is the one-azimuthal-angle-differential cross-section in a given kinematic bin, given in Eq. (1.71) and Eq. (1.102), respectively. Both have the form

$$\sigma(\Phi) = \sigma_0 + |\mathbf{S}_T| \sigma_\Phi \sin \Phi, \quad (3.1)$$

where Φ is the relevant azimuthal angle. It could be $\phi_h - \phi_S$ in SIDIS and ϕ_S , $\phi + \phi_S$ or $\phi - \phi_S$ in Drell–Yan.

Measuring the TSA $A_T^{\sin \Phi} = \sigma_\Phi / \sigma_0$ means extracting the amplitude of the modulation. It can be done by integrating the cross-section over Φ weighted with $\sin \Phi$. In practice, weighting the cross-section means summing the weights of events in a particular kinematic bin, instead of just counting the number of events in that bin. We label the weighted cross-section with the weight in superscript. For example, for the Sivers asymmetry in SIDIS the denominator is obtained by integration of Eq. (1.71) over $\phi_h - \phi_S$, getting

$$\sigma_{\text{SIDIS}}(x, y, z, \mathbf{P}_{hT}^2) = 2\pi C(x, y) F_{\text{UU},T}. \quad (3.2)$$

The numerator is obtained integrating the same cross-section with weight $\sin(\phi_h - \phi_S)$ and reads

$$\sigma_{\text{SIDIS}}^{\sin(\phi_h - \phi_S)}(x, y, z, \mathbf{P}_{hT}^2) = \pi |\mathbf{S}_T| C(x, y) F_{\text{UT},T}^{\sin(\phi_h - \phi_S)}(x, z, \mathbf{P}_{hT}^2). \quad (3.3)$$

Thanks to the weight, only the Sivers term survives the integration. Finally, the Sivers asymmetry can be written as

$$A_{\text{UT},T}^{\sin(\phi_h - \phi_S)} = \frac{F_{\text{UT},T}^{\sin(\phi_h - \phi_S)}}{F_{\text{UU},T}} = \frac{2}{|\mathbf{S}_T|} \frac{\sigma_{\text{SIDIS}}^{\sin(\phi_h - \phi_S)}(x, y, z, \mathbf{P}_{hT}^2)}{\sigma_{\text{SIDIS}}(x, y, z, \mathbf{P}_{hT}^2)}. \quad (3.4)$$

The TSAs in Drell–Yan can be measured in the same way. However, this method assumes constant acceptance as a function of the azimuthal angle Φ . If this is not the case, the result is affected by systematic errors.

Simple ratio method

If the target polarisation can be rotated² by 180°, the acceptance problem can be avoided by measuring in each kinematic bin the ratio

$$R(\Phi) = \frac{b_{\downarrow}N_{\uparrow}(\Phi) - b_{\uparrow}N_{\downarrow}(\Phi)}{b_{\downarrow}N_{\uparrow}(\Phi) + b_{\uparrow}N_{\downarrow}(\Phi)} = \frac{b_{\downarrow}b_{\uparrow}a_{\uparrow}(\Phi)\sigma(\Phi) - b_{\uparrow}b_{\downarrow}a_{\downarrow}(\Phi)\sigma(\Phi + \pi)}{b_{\downarrow}b_{\uparrow}a_{\uparrow}(\Phi)\sigma(\Phi) + b_{\uparrow}b_{\downarrow}a_{\downarrow}(\Phi)\sigma(\Phi + \pi)}, \quad (3.5)$$

where $N_{\uparrow,\downarrow}$ are the event counts (number of events in the given bin) in the subperiods with the target polarisation oriented up or down, $b_{\uparrow,\downarrow}$ and $a_{\uparrow,\downarrow}$ are the integrated beam flux and the acceptance in the two subperiods. Clearly the beam fluxes cancel and if the acceptance is the same in the two subperiods, we obtain

$$R(\Phi) = \frac{\sigma(\Phi) - \sigma(\Phi + \pi)}{\sigma(\Phi) + \sigma(\Phi + \pi)} = \tilde{D}_X \langle S_T \rangle A_X^{\sin \Phi}(\dots) \sin \Phi, \quad (3.6)$$

where $\langle S_T \rangle$ is the average polarisation in the kinematic bin, the two cells and subperiods, and \tilde{D}_X is the integrated factor depending on the process and modulation. It is unity in the case of the Siverson asymmetry in SIDIS. For Drell–Yan the factors are defined in Eq. (1.100) and they can be calculated from the data as

$$\tilde{D}_{\phi_S} = 1, \quad \tilde{D}_{(2\phi \pm \phi_S)} = \frac{\int d \cos \theta a(\theta) \sin^2 \theta}{\int d \cos \theta a(\theta) (1 + \cos^2 \theta)} = \frac{1 - \langle \cos^2 \theta \rangle}{1 + \langle \cos^2 \theta \rangle}, \quad (3.7)$$

where $a(\theta)$ is the acceptance in θ and the averaging is done like for $\langle S_T \rangle$.

Thus, the ratio enables to cancel the acceptance $a(\Phi)$ in each Φ -bin separately. Of course, we need to assume factorisation of the acceptance $a(\Phi, \theta) = a(\Phi)a(\theta)$. Also, counts from the two subperiods, divided by the spin reversal, need to be normalised and this is not always easy.

Double ratio method

The acceptance and beam flux variation in time can be dealt with, if the target has two oppositely polarised cells $c = U, D$ and the data are taken in two subperiods $p = 1, 2$ with spin configurations of the cells $\uparrow\downarrow, \downarrow\uparrow$, as done in COMPASS, see Sec. 2.2.5. We define the so-called “double ratio”

$$R_D(\Phi) = \frac{N_{U1}(\Phi)N_{D2}(\Phi)}{N_{D1}(\Phi)N_{U2}(\Phi)} = \frac{b_{U1}a_{U1}(\Phi)\sigma(\Phi)b_{D2}a_{D2}(\Phi)\sigma(\Phi)}{b_{D1}a_{D1}(\Phi)\sigma(\Phi + \pi)b_{U2}a_{U2}(\Phi)\sigma(\Phi + \pi)}. \quad (3.8)$$

Requesting that the beam track extrapolation crosses both cells, we obtain cancellation of the beam fluxes:

$$\frac{b_{U1}b_{D2}}{b_{D1}b_{U2}} = 1. \quad (3.9)$$

Also, assuming that the ratio of the acceptances of the two target cells does not change between the subperiods, namely if the so-called reasonable assumption

$$\frac{a_{U1}(\Phi)a_{D2}(\Phi)}{a_{D1}(\Phi)a_{U2}(\Phi)} = 1 \quad (3.10)$$

²We express the target polarisation angle after the rotation as $\phi_S + \pi$.

holds, the double ratio simplifies to:

$$R_D(\Phi) = \frac{\sigma(\Phi)\sigma(\Phi)}{\sigma(\Phi + \pi)\sigma(\Phi + \pi)} \approx 1 + 4\tilde{D}_X \langle S_T \rangle A_X^{\sin \Phi} \sin \Phi. \quad (3.11)$$

The approximate equality holds for small “raw asymmetries” $\langle S_T \rangle A_X^{\sin \Phi}$, which is our case. The double ratio is calculated in several (typically 8 or 16) bins in Φ and fitted with the function $p_0 + p_1 \sin \Phi$. A small correction due to the finite (but constant) bin width is applied, because the mean values of the expected distribution in the bins are slightly different from the values at the bin centre. Therefore, in the bin i with width $\Delta\Phi$ and centre at Φ_i the expected event yield is

$$\bar{R}_D(\Phi_i) = \frac{1}{\Delta\Phi} \int_{\Phi_i - \frac{\Delta\Phi}{2}}^{\Phi_i + \frac{\Delta\Phi}{2}} d\varphi R_D(\varphi) = \frac{2}{\Delta\Phi} \sin \frac{\Delta\Phi}{2} R_D(\Phi_i). \quad (3.12)$$

The statistical uncertainty of the ratio is calculated by the standard error-propagation formula, assuming Poissonian errors of the bin populations, and reads

$$\sigma_{R_D}^2 = \frac{1}{N_{U1}} + \frac{1}{N_{U2}} + \frac{1}{N_{D1}} + \frac{1}{N_{D2}}. \quad (3.13)$$

Here, the expectation value of R_D is taken equal to 1 to reduce the bias in the case of very low statistics.

Extended maximum likelihood method

The published TSAs on proton in both SIDIS and Drell–Yan have been extracted using the extended maximum likelihood method. It is based on the description of the expected event distribution as a convolution of the cross-section and acceptance, both suitably parametrised. For each event, the likelihood of its occurrence given certain values of the parameters is calculated. A numerical minimisation finds the set of parameters, which maximises the overall likelihood of the whole data set. To take advantage of the acceptance cancellation, events from each subperiod and cell are treated as a subset with accordingly defined azimuthal angles. All the asymmetries are included in the parameters of the cross-section and are thus extracted simultaneously, as explained in Ref. [132].

The results of this method are always cross-checked with the results of the double ratio method finding small differences, with residuals centered at zero. The main advantages are the simultaneous extraction of all the modulations and the absence of binning, which makes it very stable even in the case of low statistics. In spite of this, it has not been used in this work for the measurement of the J/ψ Sivvers-like asymmetry and of the weighted TSAs. As already mentioned, its use in these cases is not straightforward.

3.3.2 Weighted TSA

The transverse-momentum-weighted TSAs have been defined in Sec. 1.5 as

$$A_X^{YW_Y} = \frac{\int d^2\mathbf{q}_T W_Y F_X^Y}{\int d^2\mathbf{q}_T F_U}. \quad (3.14)$$

The denominator can be easily obtained from the cross-section Eq. (3.1). To get the numerator, we need the same cross-section, but weighted with the appropriate weight $W_{\sin\Phi}$, which can be schematically written as

$$\sigma^{W_{\sin\Phi}}(\Phi) = \sigma_0^{W_{\sin\Phi}} + |\mathbf{S}_T| \sigma_{\Phi}^{W_{\sin\Phi}} \sin\Phi. \quad (3.15)$$

For example, comparing this expression with Eq. (1.134) we obtain in the case of Drell–Yan: $\sigma_{\Phi}^{W_{\sin\Phi}} \propto \int d^2\mathbf{q}_T W_{\sin\Phi} F_U^{\sin\Phi}$. In SIDIS, the situation is analogous. To summarize, one has to weight only the spin-dependent part of the cross-section and divide it with the unweighted spin-independent part. This is quite easy in principle. In fact, using the same approach as in Eq. (3.4) we obtain for Drell–Yan

$$A_T^{\sin\Phi} W_{\sin\Phi} = \frac{\int d^2\mathbf{q}_T W_{\sin\Phi} F_T^{\sin\Phi}}{\int d^2\mathbf{q}_T F_U^1} = \frac{2}{\tilde{D}_{\sin\Phi} |\mathbf{S}_T|} \frac{\sigma_{\text{DY}}^{\sin\Phi}(x_a, x_b, q_T^2)}{\sigma_{\text{DY}}(x_a, x_b, q_T^2)}. \quad (3.16)$$

Practically, this method has the same disadvantages described in the case of the conventional TSAs.

Modified simple ratio method

Like for the conventional TSAs, it is beneficial to utilise the target polarisation reversal. In that case the weighted asymmetry can be obtained from the ratio

$$\begin{aligned} R^W(\Phi) &= \frac{b_{\downarrow} N_{\uparrow}^W(\Phi) - b_{\uparrow} N_{\downarrow}^W(\Phi)}{b_{\downarrow} N_{\uparrow}(\Phi) + b_{\uparrow} N_{\downarrow}(\Phi)} = \frac{\sigma^W(\Phi) - \sigma^W(\Phi + \pi)}{\sigma(\Phi) + \sigma(\Phi + \pi)} \\ &= \tilde{D}_{\sin\Phi} \langle S_T \rangle A_X^{\sin\Phi W} \sin\Phi. \end{aligned} \quad (3.17)$$

where $N_{\uparrow,\downarrow}^W$ are the weighted event counts, i.e. sums of event weights in each bin. We use the shorthand notation $W = W_{\sin\Phi}$ from now on. Like for the conventional simple ratio, the acceptance is cancelled in each Φ bin. The disadvantages are the same as well.

As we will use this simple extraction method to check the statistical uncertainties of the weighted asymmetries, we show here the expression for the uncertainty, obtained by the usual error propagation method:

$$\sigma_{R^W}^2(\Phi) = \frac{b_{\downarrow}^2 \sigma_{N_{\uparrow}^W}^2(\Phi) + b_{\uparrow}^2 \sigma_{N_{\downarrow}^W}^2(\Phi) + [R^W(\Phi)]^2 \times [b_{\downarrow}^2 N_{\uparrow}(\Phi) + b_{\uparrow}^2 N_{\downarrow}(\Phi)]}{[b_{\downarrow} N_{\uparrow}(\Phi) + b_{\uparrow} N_{\downarrow}(\Phi)]^2} \quad (3.18)$$

where $\sigma_{N_{\uparrow,\downarrow}^W}^2(\Phi) = \sum_i W_i^2(\Phi)$ are the sums of squared weights in each bin. In practice, we observed that they give the dominant contribution to the error.

Modified double ratio method

A combination of normal and weighted event counts from two oppositely polarised target cells and two subperiods with reversed polarisation, similar to the double ratio, can be constructed to avoid beam normalisation and to take into possible account changes in the acceptances. The “modified double ratio” is

$$R_{\text{DM}}^W(\Phi) = \frac{N_{\text{U1}}^W N_{\text{D2}}^W - N_{\text{U2}}^W N_{\text{D1}}^W}{\sqrt{(N_{\text{U1}}^W N_{\text{D2}}^W + N_{\text{U2}}^W N_{\text{D1}}^W)(N_{\text{U1}} N_{\text{D2}} + N_{\text{U2}} N_{\text{D1}})}} \quad (3.19)$$

Under the conditions similar to the standard double ratio, namely the reasonable assumption for the ratio of the acceptances of Eq. (3.10) and small raw asymmetry, we obtain

$$R_{\text{DM}}^W(\Phi) \approx 2 \tilde{D}_{\sin \Phi} \langle S_T \rangle A_X^{\sin \Phi W} \sin \Phi. \quad (3.20)$$

The statistical uncertainty of the modified double ratio is

$$\sigma_{R_{\text{DM}}^W}^2 = \frac{\sum_{c,p} \sigma_{N_{cp}}^2}{\sum_{c,p} N_{cp}} \times \frac{4(N_{U1}N_{D2}N_{U2}N_{D1})^2}{(N_{U1}N_{D2} + N_{U2}N_{D1})^4} \times \sum_{c,p} \frac{1}{N_{cp}}, \quad (3.21)$$

where the sums are over the cells $c = U, D$ and the subperiods $p = 1, 2$. The weighted TSA is obtained by a fit of the modified double ratios, taking into account the finite bin width through the correction explained in Eq. (3.12)

3.4 Polarisation dilution effects

Several effects need to be taken into account to calculate the transverse component of the nucleon spin $\langle S_T \rangle$. First, not all ^1H nuclei are oriented in the right direction. In the 2015 data analysis, the target polarisation $P(t, Z_{\text{vert}})$ is calculated for each event using the event time. An exponential decay of the polarisation in time is assumed (Sec. 2.2.5). A linear interpolation between the nearest NMR coils gives the polarisation at the position of the vertex of origin along the target. For the 2010 SIDIS data there was no evidence of polarisation dependence on the vertex position, so an average over the coils was used.

The second effect is the composition of the target material, discussed in Sec. 2.2. In fact, in the target region we have NH_3 , He of the cooling bath, and other nuclei in the support structures. Because of that, the unpolarised part of the measured cross-section arises from a mixture of H and other nuclei A . On the other hand, the polarised part comes only from H. Dilution factor f_D is used to correct the asymmetries as if the unpolarised part came from the pure H as well and it is given by

$$f_D = \frac{n_{\text{H}}\sigma_{\text{H}}}{n_{\text{H}}\sigma_{\text{H}} + \sum_A n_A\sigma_A}, \quad (3.22)$$

where $n_{p,A}$ is the number of H or A in a unit of target volume and $\sigma_{p,A}$ is the unpolarised cross section of the studied reaction on H or A . For each event, the dilution factor is obtained from a table of pre-calculated values of f_D , as a function of several kinematic variables. The dilution factor for SIDIS has been used already in many COMPASS publications, e.g. [79]. The dilution factor for Drell–Yan has been used in Ref. [88]. The composition of the target has been measured by the target group and the cross-sections calculated in a parton-level Monte Carlo program MCFM [133], adapted to accommodate a pion beam and validated against E 615 πW Drell–Yan cross-section measurements [134]. Nuclear effects were taken into account via PDF correction factors extracted by the EKS group [135] and checked against E 772 πA data [136]. The average value of f_D in the Drell–Yan data is shown on Fig. 3.1. There is a mild linear dependence on q_T .

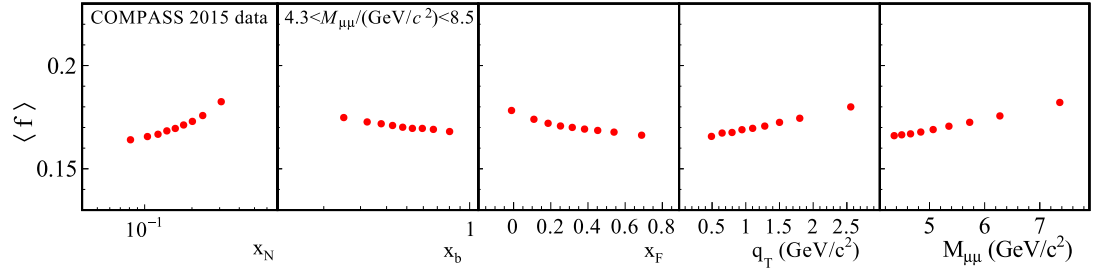


Figure 3.1: The average depolarisation factor in the Drell–Yan data as the function of several kinematic variables.

The polarisation and dilution factor are calculated event-by-event and averaged over the data-taking period, and finally the nucleon polarisation is

$$\langle S_T \rangle = \langle P \rangle \langle f_D \rangle. \quad (3.23)$$

4. Sivers-like asymmetry in the J/ψ leptonproduction

This chapter is dedicated to the measurement of the Sivers-like asymmetry in J/ψ production in scattering of muons off transversely polarised protons

$$\mu^+(l) + p(P, S) \rightarrow \mu^+(l') + J/\psi(P_h) + X, \quad (4.1)$$

described in Sec. 1.2. The J/ψ 's are identified via their decay into muons, looking for $2\mu^+ + 1\mu^-$ in the final state. Since the dominant mechanism of the J/ψ production can be different depending on the fraction of available energy z , the asymmetry has been measured in two z -intervals $0.3 < z < 0.95$ and $0.95 < z < 1.05$. We utilise the SIDIS formalism and apart from the standard SIDIS variables, defined in Sec. 1.2, we define:

- The decay muon momenta l^+ and l^- , leading to $P_h = l^+ + l^-$.
- The invariant mass of the dimuon $M_{\mu\mu} = |P_h^2|$.
- The J/ψ rapidity $y_R = \frac{1}{2} \ln \left(\frac{P_h^0 + P_h^3}{P_h^0 - P_h^3} \right)$ in the μp center-of-mass frame with the z -axis pointing along the incident muon momentum.
- The so-called missing energy of the undetected system $E_{\text{miss}} = \frac{M_X^2 - M_p^2}{2M_p} = E - E' - E_h + \frac{(q - P_h)^2}{2M_p}$.

4.1 Event selection

This new and exploratory measurement has been done using the data collected in 2010 with the 160 GeV/c μ^+ beam and transversely polarised NH_3 target. The data production is the same used for the published Collins, Sivers, and di-hadron asymmetries [62, 63, 78], for which numerous systematic studies and data quality checks have been performed. In particular, the same list of bad spills has been used.

An already pre-selected data sample, which contains only events with best primary vertex (see Sec. 3.1) and at least two μ^+ and one μ^- outgoing tracks from the vertex, has been utilised. A particle is identified as a muon at this stage, if it has crossed more than 15 radiation lengths in the spectrometer. The pre-selection has been checked using one data taking period. The effects of the selection on the number of events in this period is shown in Tab. 4.1.

The events have been further filtered. The additional cuts are:

1. The beam track is reconstructed with $\chi^2/N_{\text{df}} < 10$.
2. The beam μ momentum \mathbf{l} is measured in the BMS and $|\mathbf{l}| \in [140, 180]$ GeV/c.
3. The beam track extrapolation crosses both the most upstream and the most downstream end of the target cells.

| Cut | Events | Absolute ratio | Relative ratio |
|-----------------|---------------|-----------------------|-----------------------|
| All events | 2 798 242 560 | 1.000 | 1.000 |
| Best PV exists | 2 786 434 304 | 0.996 | 0.996 |
| $2\mu^+ 1\mu^-$ | 77 217 | 27.6×10^{-6} | 27.7×10^{-6} |
| Bad-spills list | 69 715 | 24.9×10^{-6} | 0.903 |

Table 4.1: The effect of cuts in the pre-selection shown for the period W33.

| Cut | Events | Absolute ratio | Relative ratio |
|---|---------|-----------------------|-----------------------|
| All preselected events | 839 450 | 1.000 | 1.000 |
| Beam track $\chi^2/n_{\text{df}} < 10$ | 827 424 | 0.986 | 0.986 |
| $ \mathbf{l} \in [140, 180] \text{ GeV}/c$ | 770 421 | 0.918 | 0.931 |
| Beam traj. cros. PT ends | 739 818 | 0.881 | 0.960 |
| μ -ID: X/X_0 and Z_{last} checks | 483 940 | 0.576 | 0.654 |
| Muon track $\chi^2/n_{\text{df}} < 10$ | 480 726 | 0.573 | 0.993 |
| Vertex in target cells | 397 536 | 0.474 | 0.827 |
| Both muon combinations | 795 072 | 1.000 | 1.000 |
| $z \in [0.3, 1.05]$ | 736 264 | 0.877 | 0.926 |
| $M_{\mu\mu} \in [2.999, 3.239] \text{ GeV}/c^2$ | 8 026 | 9.56×10^{-3} | 10.9×10^{-3} |
| $M_{\mu\mu}$ in the side-bands | 4 784 | 5.70×10^{-3} | 6.50×10^{-3} |

Table 4.2: Effect of cuts on event selection from the pre-selected events stage down to the invariant mass cut.

4. A more strict muon identification, requiring more than 30 radiation lengths crossed and the last detection point downstream from the first muon filter.
5. The outgoing μ tracks are reconstructed with $\chi^2/N_{\text{df}} < 10$.
6. The primary vertex is inside the target cells.

Since it is not possible to tell which one of the two μ^+ comes from the J/ψ decay and which one is the scattered beam muon, both combinations are used. For each combination the kinematic variables Q^2 , x , z and $M_{\mu\mu}$ are calculated. In the analysis at this stage, we have a total of 795×10^3 dimuons. The variable z is then asked to be in one of the two bins, $0.3 < z < 0.95$, or $0.95 < z < 1.05$, where the lowest boundary corresponds to the minimum measured value. The distribution of the invariant mass of the pairs is shown in Fig. 4.1 We require the mass to belong to one of two sets:

1. signal band with $M_{\mu\mu} \in [2.999, 3.239] \text{ GeV}/c^2$, corresponding approximately to $M_{J/\psi} \pm 2\sigma$, where $M_{J/\psi}$ and σ are parameters of the invariant mass fit;
2. side-bands with $M_{\mu\mu} \in [2.579, 2.939] \cup [3.299, 3.659] \text{ GeV}/c^2$, used to evaluate the background.

This is the most selective cut, as can be seen in Tab. 4.2, where the effect of all cuts is shown. In total, there are 8.0×10^3 events in the signal band and 4.8×10^3 events in the side bands. Even if the process $\mu^+ + N \rightarrow \mu^+ + J/\psi + X$ is very rare, the background is very small.

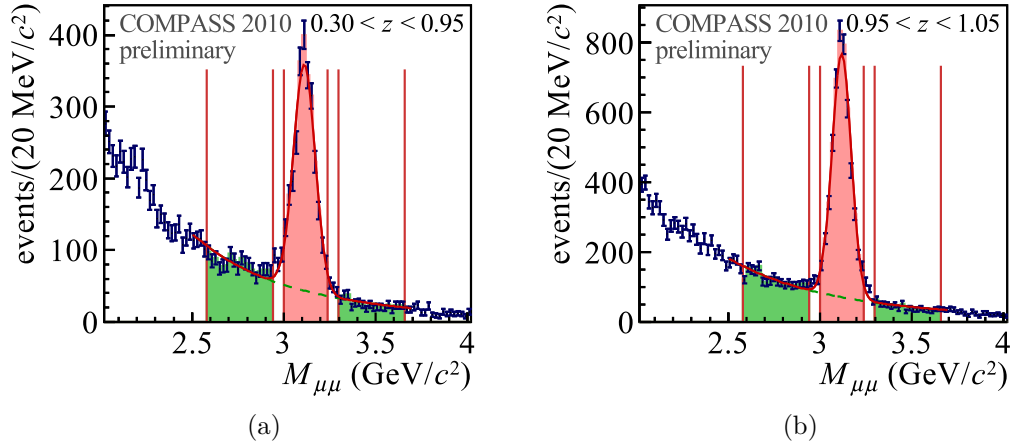


Figure 4.1: Dimuon invariant mass in the low (a) and high (b) z -intervals. The boundaries of the side-bands and the signal band are denoted by vertical red lines. The red and the dotted green lines are the results of the fit.

| | A | μ [GeV/ c^2] | σ [GeV/ c^2] | B | C | $N_{\text{sig}}/N_{\text{bg}}$ |
|--------------|-------|---------------------|------------------------|--------|------|--------------------------------|
| 1st z -bin | 2 340 | 3.11 | 0.059 | 10 000 | -4.8 | 4.31 |
| 2nd z -bin | 4 550 | 3.12 | 0.052 | 10 000 | -4.3 | 5.25 |

Table 4.3: Parameters of the invariant mass fits.

4.2 Kinematic distributions

The invariant mass distributions shown in Fig. 4.1 were fitted using a normal (Gaussian) distribution plus background of the form

$$\frac{A}{w} N(M_{\mu\mu}, \mu, \sigma) + B (M_{\mu\mu})^C, \quad (4.2)$$

where A , μ , σ , B and C are free parameters and w is the bin width. The results of the fit are shown in Fig. 4.1 by the red (total) and dotted green (background) curves. The parameter values obtained from the fits are given in Tab. 4.3. In the table, $N_{\text{sig}}/N_{\text{bg}}$ is the ratio of the number of signal and background events in the signal band. They are obtained from integrals of the signal and background terms of Eq. (4.2) using the best fit parameters from Tab. 4.3. As a result, there are about 2 240 J/ψ events in the signal band for $0.3 < z < 0.95$ and 4 450 events for $0.95 < z < 1.05$.

All the other distributions shown in Fig. 4.2–4.6 have the background subtracted assuming the distributions in the side-bands have the same shape as the distributions of the background. For example, the background-subtracted Bjorken x distribution of the signal events is obtained from

$$\frac{dN_{\text{sig}}}{dx}(x) = \frac{dN}{dx}(x) - \frac{N_{\text{bg}}}{N_{\text{side}}} \times \frac{dN_{\text{side}}}{dx}(x), \quad (4.3)$$

where $\frac{dN_{\text{side}}}{dx}(x)$ is the Bjorken x distribution for the side-band events and $\frac{dN}{dx}(x)$

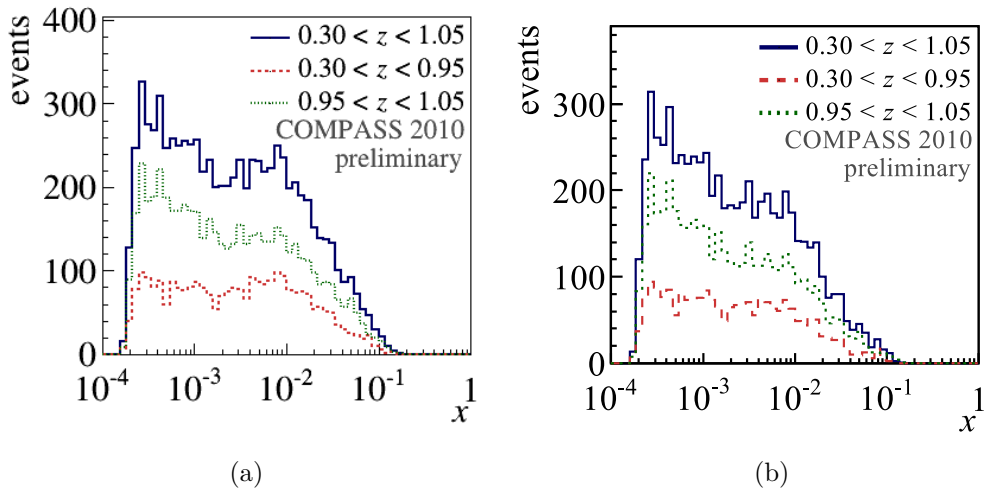


Figure 4.2: Bjorken x distributions before (a) and after (b) the background subtraction.

is the measured distribution. The number of background events N_{bg} , which normalises the sideband distribution, is determined as described above. The number of side-band events N_{side} is counted directly.

The particular case of the Bjorken x is plotted in Fig. 4.2, showing a change in the shape of the distribution after the subtraction. The other distributions have very similar shapes before and after the subtraction, so only the latter are shown. The primary vertex distribution with the three physical target cells visible is shown in Fig. 4.3(a). The cells with the same polarisation direction are shown in red and green. The Bjorken x and Q^2 correlation is illustrated in Fig. 4.3(b). Both are notably lower than in SIDIS, where the cut $Q^2 > 1 (\text{GeV}/c)^2$ is usually imposed. The distributions of the invariant z , with the two integration ranges denoted, is plotted in Fig. 4.4(a). The distribution has a peak at $z = 1$ and a tail towards smaller values. This structure translates into a peak in the missing energy distribution, shown in Fig. 4.4(b). The J/ψ momentum in the γ^*N frame and its transverse component are plotted in Fig. 4.5.

The J/ψ rapidity in the μN frame y_R , plotted in Fig. 4.6(a) for comparison with Ref. [37, 40], can be related to the fraction x_g of the nucleon momentum carried by the struck gluon assuming the PGF mechanism [37],

$$x_g = \frac{M_{\mu\mu} e^{-y_R}}{\sqrt{s}}. \quad (4.4)$$

Its distribution is shown in Fig. 4.6(b). The mean values of selected kinematic variables can be found in Table 4.4.

4.3 The asymmetry calculation

The data from 2010 are divided into 12 periods, each consisting of two sub-periods with the opposite target polarity (Sec. 2.2.5). This data structure is treated in two ways. In the simpler one all the sub-periods with the same polarisation

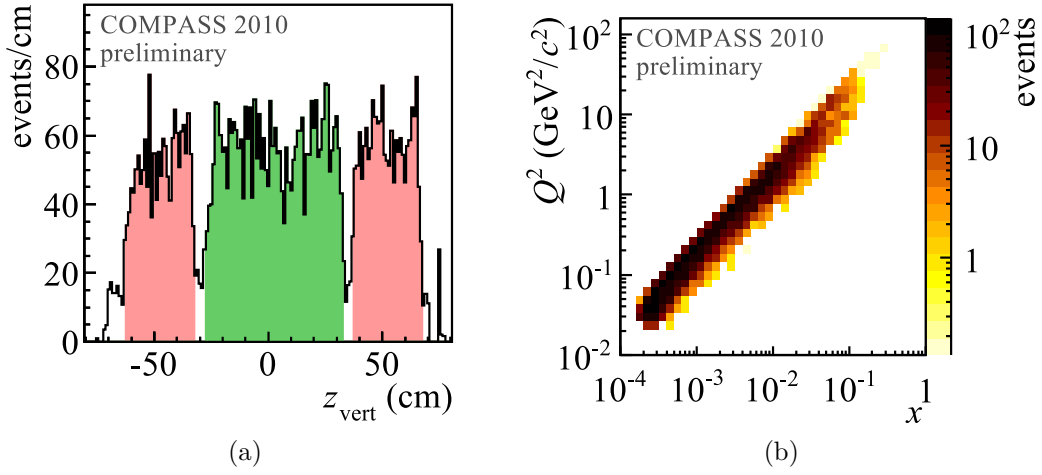


Figure 4.3: (a) The primary vertex distribution. (b) The Bjorken x versus Q^2 distribution.

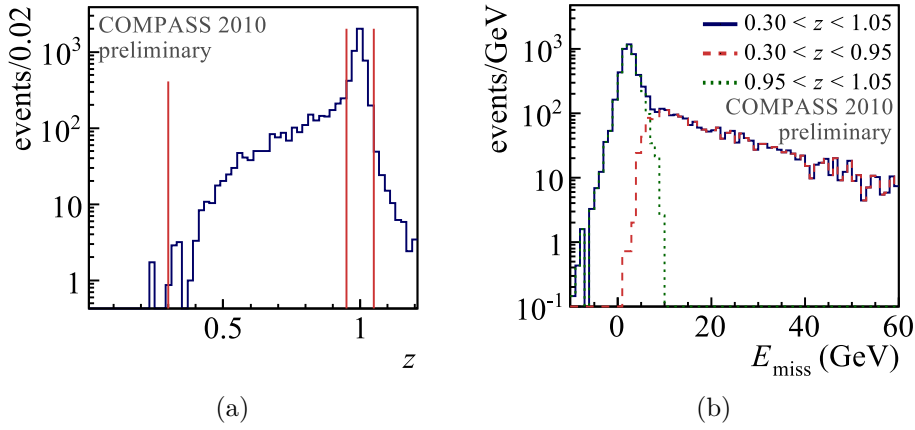


Figure 4.4: The z distribution (a) with the red lines denoting the integration ranges; and the missing energy (b).

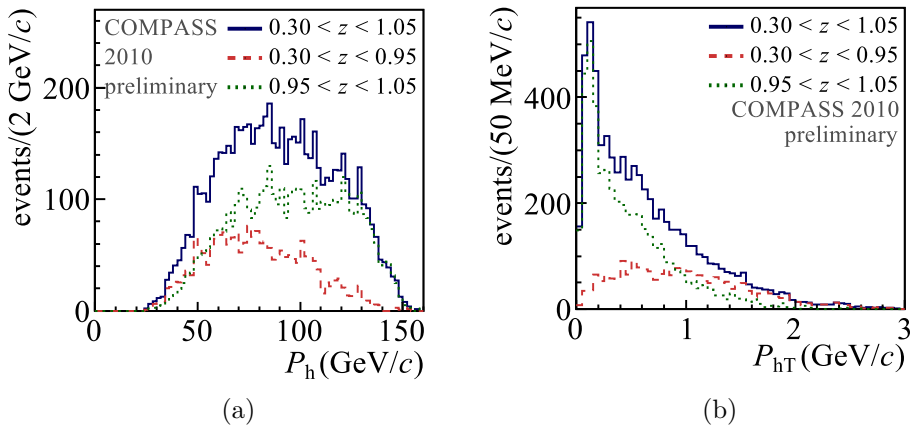


Figure 4.5: J/ψ momentum (a) and its transverse component (b).

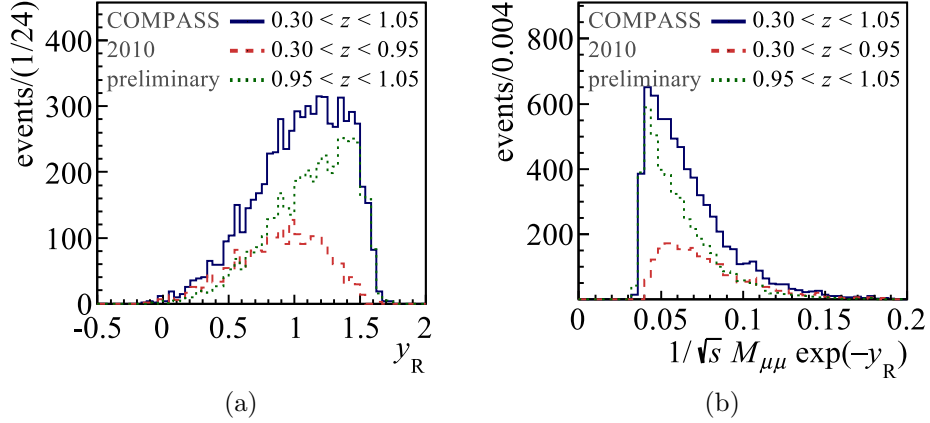


Figure 4.6: (a) The J/ψ rapidity in the μN frame. (b) The gluon longitudinal momentum fraction calculated from it.

| | $\langle z \rangle$ | $\langle x \rangle$ | $\langle Q^2 \rangle$ [GeV ² /c ²] | $\langle y_R \rangle$ | $\langle \mathbf{P}_{hT} \rangle$ [GeV/c] |
|--------------|---------------------|---------------------|---|-----------------------|---|
| 1st z -bin | 0.79 | 0.0064 | 1.14 | 0.89 | 0.96 |
| 2nd z -bin | 1.00 | 0.0063 | 1.11 | 1.13 | 0.46 |

Table 4.4: The mean values of selected kinematic variables, evaluated after the background subtraction.

are combined so the whole 2010 run is treated as one period. It is indicated as “combined” in the following. In the second one, “weighted mean” in the following, the asymmetry is calculated period-by-period and then an error-weighted mean is calculated

$$\langle A \rangle = \frac{\sum_{i=1}^n A_i \sigma_i^{-2}}{\sum_{i=1}^n \sigma_i^{-2}} \quad \sigma_{\langle A \rangle}^2 = \frac{1}{\sum_{i=1}^n \sigma_i^{-2}} \times \frac{1}{n-1} \sum_{i=1}^n \frac{(A_i - \langle A \rangle)^2}{\sigma_i^2}, \quad (4.5)$$

where n stands for the number of periods. The second term in the uncertainty formula takes into account possible underestimation of σ_i . The advantage of this method is that it does not require a balanced statistics or stable conditions over the whole year. It also allows to check the consistency of the asymmetry values measured in the different periods of data taking, an important test of systematic effects. The disadvantage is that in each period the extraction is performed on smaller event sample, which could cause problems. Despite that we prefer the latter method. In both cases, the asymmetry is extracted using the double ratio method (Sec. 3.3.1). To minimise the impact of the low statistics the ϕ_{Siv} range is divided in just 8 bins.

The extraction is done both in the signal band and in the side bands. The results of the combined and weighted mean methods are given in Tab. 4.5. Note that they are the so-called raw asymmetries, i.e. not corrected for the target composition and finite polarisation (Sec. 3.4). The agreement between the two methods is good, except the asymmetry in side-bands for the lower z interval. The asymmetries from the signal band extracted from the 12 periods, the weighted

| | | $z \in [0.3, 0.95]$ | | $z \in [0.95, 1.05]$ | |
|---------------|-------------|-------------------------------|--------------|-------------------------------|--------------|
| | | $A_{\text{Siv}}^{\text{raw}}$ | σ_A | $A_{\text{Siv}}^{\text{raw}}$ | σ_A |
| Weighted mean | Signal band | -0.010 | 0.031 | -0.034 | 0.018 |
| | Side bands | -0.025 | 0.031 | -0.030 | 0.024 |
| Combined | Signal band | -0.020 | 0.031 | -0.028 | 0.021 |
| | Side bands | 0.036 | 0.029 | -0.016 | 0.030 |

Table 4.5: The raw asymmetry obtained with the two different procedures.

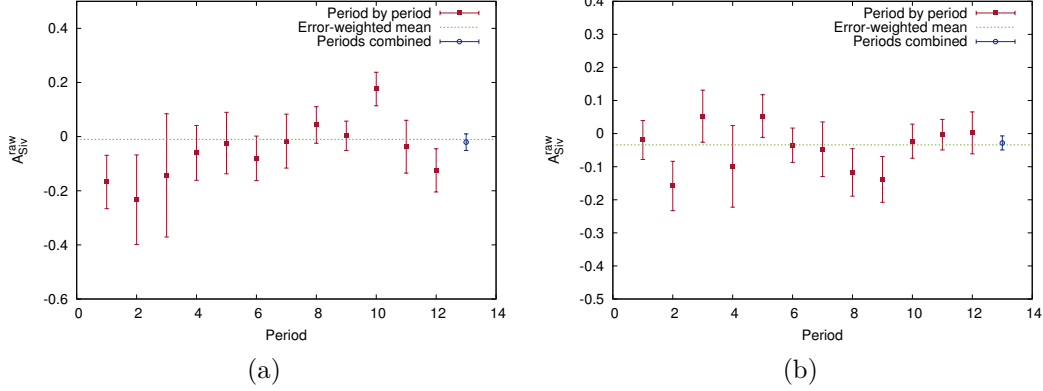


Figure 4.7: The raw asymmetries from all periods, their weighted mean and the asymmetry calculated from the combined periods for $0.3 < z < 0.95$ (a) and $0.95 < z < 1.05$ (b).

mean, and the asymmetry extracted from the combined periods are shown in Fig. 4.7. All the plotted results are compatible. The weighted mean results are used in the following.

4.4 Background-corrected asymmetries

The asymmetry measured in the signal band $A_{\text{Siv}}^{\text{raw}}$ gets contribution from the real asymmetry $A_{\text{Siv}}^{\text{raw}}|_{\text{sig}}$ and from the asymmetry of the background $A_{\text{Siv}}^{\text{raw}}|_{\text{bg}}$, weighted by ratios of event counts

$$A_{\text{Siv}}^{\text{raw}} = \frac{N_{\text{sig}}}{N_{\text{tot}}} A_{\text{Siv}}^{\text{raw}}|_{\text{sig}} + \frac{N_{\text{bg}}}{N_{\text{tot}}} A_{\text{Siv}}^{\text{raw}}|_{\text{bg}}. \quad (4.6)$$

Then one can proceed by two ways:

1. If one assumes the asymmetry of the background to be zero, the real asymmetry of the signal is

$$A_{\text{Siv}}^{\text{raw}}|_{\text{sig}} = \frac{N_{\text{tot}}}{N_{\text{sig}}} A_{\text{Siv}}^{\text{raw}}. \quad (4.7)$$

In this model, the background just dilutes the asymmetry of the signal. The asymmetry measured in the side-bands is indeed consistent with this assumption.

| | $z \in [0.3, 0.95]$ | | $z \in [0.95, 1.05]$ | |
|------------------------|-------------------------------|-------------|-------------------------------|-------------|
| | $A_{\text{Siv}}^{\text{raw}}$ | σ_A | $A_{\text{Siv}}^{\text{raw}}$ | σ_A |
| Dilution | -0.012 | 0.038 | -0.040 | 0.021 |
| Subtraction | -0.006 | 0.039 | -0.034 | 0.021 |
| | A_{Siv}^p | σ_A | A_{Siv}^p | σ_A |
| Final asymmetry | -0.05 | 0.33 | -0.28 | 0.18 |

Table 4.6: The raw Sivers-like asymmetry from the two methods of background correction and the final asymmetry, after the correction for the dilution factor and target polarisation.

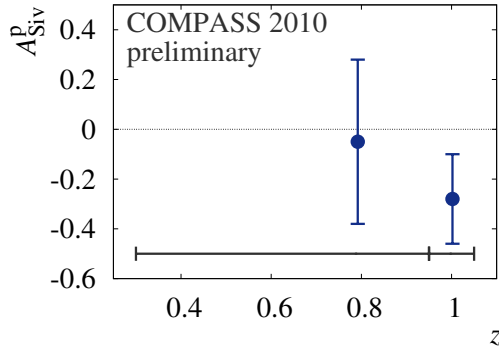


Figure 4.8: The final Sivers-like asymmetry in J/ψ leptonproduction on proton target, the horizontal grey lines indicate the integration ranges.

- Another option is to assume that the background asymmetry is the same as the side-band asymmetry. Then one can subtract it:

$$A_{\text{Siv}}^{\text{raw}}|_{\text{sig}} = \frac{N_{\text{tot}}}{N_{\text{sig}}} A_{\text{Siv}}^{\text{raw}} - \frac{N_{\text{bg}}}{N_{\text{sig}}} A_{\text{Siv}}^{\text{raw}}|_{\text{side}}. \quad (4.8)$$

In both cases one utilises the number of signal and background events given in 4.3. The errors of the numbers of events are considered to be small with respect to the errors of the asymmetries and are not taken into account when propagating the errors through Eq. (4.7, 4.8).

Both the dilution compensation and the background subtraction procedures have been applied on the weighted means, as the background is not expected to change over the year and the signal-to-background ratio can be measured more accurately using the bigger data sample. The results of both methods are shown in Tab. 4.6. They are consistent and do not differ much from the uncorrected result, which is expected taking into account the low background level. In the following, we use the results of the background subtraction method.

4.5 Results and discussion

The actual Sivers-like asymmetry $A_{\text{UT,T}}^{\sin(\phi_h - \phi_S)} = A_{\text{Siv}}$ can be obtained dividing the raw asymmetry by the average target polarisation P and the dilution factor

f (Sec. 3.4), which has the mean value $\langle f \rangle = 0.15$. During the data taking the average polarisation varied in the range 77–82%, but if we simply take the average value of 80% (over all events), the systematic uncertainty coming from this approximation is negligible as compared to the asymmetry uncertainty. The final results for the Sivers-like asymmetries are given in Tab. 4.6 and Fig. 4.8. They have been presented at conferences and published in the proceedings [137].

The process of interest is very rare, so it is not surprising that the final asymmetries have large statistical uncertainty. With the whole 2010 transverse run data, after the background subtraction, one is left with 2 240 and 4 450 events in the two z -bins.

The Sivers-like asymmetry is found to be compatible with zero in the lower z bin and with a slight preference for negative value in the higher z bin. As discussed in Sec. 1.2.4, the latter case corresponds to the range of the PGF-based models from Ref. [21, 37, 40], which predict negative asymmetry¹ with magnitude of about 0.05–0.2. The relative uncertainty of the measurement is, however, large as compared to the available estimates of the asymmetry.

Only limited improvements of the precision could come analysing all the existing proton and deuteron COMPASS data. A new run with the transversely polarised deuteron target, proposed for the year 2021, could allow for larger improvement. Precise measurements will be performed at the future Electron–Ion Collider. With more statistics, it would be also possible to address the questions regarding the fraction of J/ψ 's originating from the PGF. In the higher z bin a diffractive contribution is expected, while the lower z bin could contain resolved photon processes and J/ψ 's formed by the colour singlet mechanism (the hard gluon carrying away the missing fraction of the available energy). A future improvement of this exploratory study could be achieved utilising cuts to control the diffractive component (e.g. to look on the mass of the undetected system W or on the number of tracks reconstructed from the vertex).

In addition, one could look into other azimuthal modulations, including the target-spin-independent ones and those, depending on the the orientation of the J/ψ decay plane. The latter could help to restrict the J/ψ production models and possibly show hints of gluonic Boer–Mulders function [21]. The measurements of J/ψ lepto- or photoproduction are relatively rare. The existing ones are e.g. [138–140].

¹In fact, in the first two references it is positive, but only due to conventions, as the z -axis direction is the opposite.

5. Drell–Yan data analysis

In 2015, COMPASS has measured the Drell–Yan process using a 190 GeV/ c negative pion beam and a transversely polarised proton target. The main motivation of the measurement was to test the fundamental prediction of the opposite sign of the T-odd Sivers function in the Drell–Yan reaction with respect to SIDIS. The other two LO TSA introduced in Sec. 1.3 could be accessed in parallel. Besides the TSAs, the data are relevant also for studies of the spin-independent azimuthal modulations, nuclear effects and other things. The choice of the π^- beam and p target was done in order to maximise the cross-section, since they contain \bar{u} and u valence quarks. As we shall see, this simplifies the interpretation of the measured asymmetries. The beam energy was set in order to optimise the acceptance of the spectrometer in the target valence region, where the the SIDIS measurements had demonstrated the Sivers function reaches maximum. Also, the Q^2 ranges of the Drell–Yan and SIDIS measurements are similar, an important point in order to minimise the uncertainties due to the TMD evolution in the comparison of the results.

The Drell–Yan process is described in Sec. 1.3 for hadrons a (here π^-) and b (here the nucleon N). The reaction is

$$\pi^-(P_\pi) + N(P_N, S) \rightarrow \mu^-(l^-) + \mu^+(l^+) + X. \quad (5.1)$$

The solid NH_3 target, described in Sec. 2.2, has been used. It has a high fraction of H nuclei transversely polarised. As discussed in Sec. 3.4, the asymmetries are corrected by the dilution factor, so they can be understood as being measured on protons.

In this section, we first briefly describe the measurement of the published standard TSAs and comment the results. Then, the original work for the measurement of the weighted TSAs is presented in detail. The interpretation of the measured weighted asymmetries is discussed in Chap. 6.

5.1 Measurement of the standard TSAs

In the data analysis, first all the pairs of muon tracks, which are oppositely charged and come from a primary vertex with an incoming pion, are identified. The track is considered a muon, if it has crossed more than 30 radiation lengths of material along the spectrometer (after the main hadron absorber). The transverse momentum of the dimuon q_T is required to be in the range $0.4 \text{ GeV}/c < q_T < 5 \text{ GeV}/c$. The lower limit ensures good resolution in the azimuthal angles and the upper one cuts the tail of the q_T -distribution, as will be discussed in Sec. 5.2.1. Finally, the primary vertex is required to be in one of the target cells.

The distribution of $Q^2 = M^2$ versus the reconstructed Bjorken scaling variable x_N of the nucleon for the events passing the cuts is shown in Fig. 5.1(a). There are four mass ranges denoted by horizontal dashed lines and the J/ψ peak is visible in one of them in the central part of the plot. As can be noticed, both the J/ψ and the highest-mass regions correspond to the valence region of the nucleon.

The mass spectrum is shown in Fig. 5.1(b). The J/ψ peak is visible, with a shoulder from the $\psi(2S)$ resonance. The contributions to the spectrum are

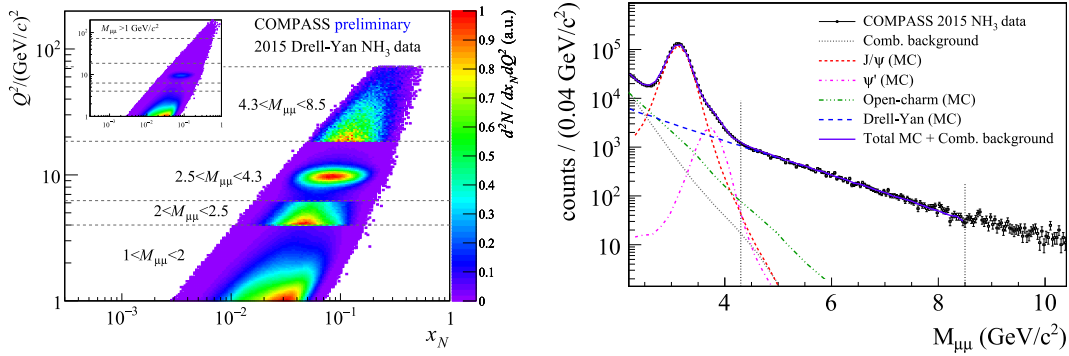


Figure 5.1: (a) The x_N versus Q^2 distribution of the dimuons. (b) The invariant mass distribution with Drell–Yan, charmonia production, open-charm processes, and combinatorial background contributions indicated by the curves [88].

evaluated in a MC simulation, where the hard physics processes are simulated by Pythia8 event generator [141], the propagation of the particles through the COMPASS setup is taken care of by TGeant, and the data are reconstructed by CORAL. The Drell–Yan process is shown by the dashed blue line, the charmonia by the dotted red and magenta curves, and the semi-muonic open-charm decays is shown by the green dash–dotted line. In addition, the combinatorial background originating mainly from the decay of the beam pions is determined using like-sign muon pairs in the real data as $N_{\mu^+\mu^-} = 2\sqrt{N_{\mu^+\mu^+}N_{\mu^-\mu^-}}$. The normalisations of the contributions are simultaneously fitted to the measured invariant mass distribution, except the combinatorial component, which is kept fixed. The spectrum is well described by the fit. As can be seen, the highest-mass region, $M > 4.3 \text{ GeV}/c^2$ as indicated by the vertical line, is almost background-free. For the analysis, we use this range, namely $4.3 \text{ GeV}/c^2 < M < 8.5 \text{ GeV}/c^2$. The lower limit is chosen to exclude the charmonia tails and the higher one avoids the contribution from the Υ resonances. In this range, the estimated contamination is below 4%.

The sample consists of 35×10^3 dimuons after the selection. The TSAs are extracted using the extended maximum likelihood method in three kinematic bins of the variables x_π , x_N , x_F and q_T , always integrating over the other variables. The dilution and depolarisation factors are calculated event-by-event and weight the asymmetries, unlike in the double ratio method (see Sec. 3.3.1), where an average over the period and cell is used. It has been checked that the values obtained with the double ratio method are compatible. For the target polarisation an average value over the data-taking period is used. In the evaluation of the depolarisation factors the approximation for the $\cos^2\theta$ azimuthal modulation amplitude $\lambda = 1$ is used leading to an overall normalisation uncertainty smaller than 5%. The extracted asymmetries are checked for various systematic effects. The main contribution to the systematic uncertainty is a possible variation of the experimental conditions within each period, which is evaluated using various types of “false asymmetries” (see Sec. 5.2.3). The resulting systematic uncertainty is at the level of 0.7 times the statistical one. In addition, there are normalisation uncertainties of about 5% from the polarisation measurement and about 8% from

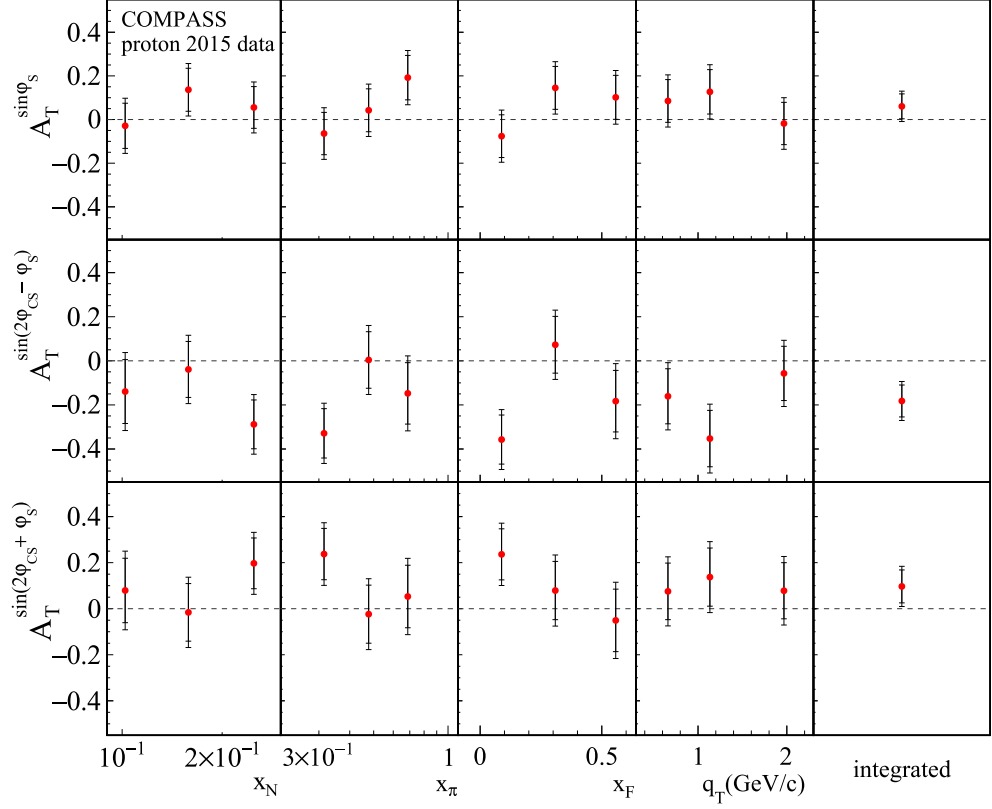


Figure 5.2: The TSAs $A_T^{\sin\phi_S}$ (first row), $A_T^{\sin(2\phi-\phi_S)}$ (second row), and $A_T^{\sin(2\phi+\phi_S)}$ (third row) in bins of x_N , x_π , x_F , q_T , and integrated, measured in the Drell–Yan process at COMPASS [88]. The error bars indicate both statistical and systematic errors. The lepton angles in the Collins–Soper frame θ and ϕ are denoted θ_{CS} and ϕ_{CS} in the figure.

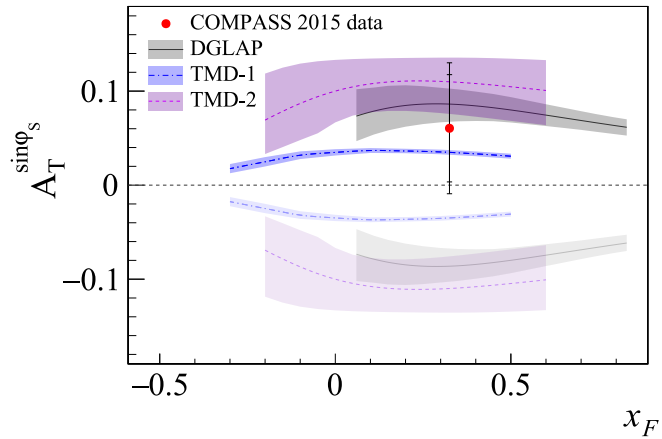


Figure 5.3: The Siverts asymmetry measured in the Drell–Yan process at COMPASS [88] compared to theoretical predictions (DGLAP [82], TMD-1 [84], TMD-2 [85]). Assuming the change of sign between SIDIS and Drell–Yan, the positive value of the asymmetry is expected.

the dilution factor calculation.

The results for the three leading order TSAs are shown in Fig. 5.2. No clear trends are visible in the three-bin plots. The average Sivers asymmetry $A_T^{\sin\phi_S}$ is found to be positive by about one standard deviation. In Fig. 5.3 it is compared with three theoretical predictions, which differ mainly in the Q^2 evolution framework used. The positive value predictions shown in darker colours take into account the predicted change of sign of the Sivers function (see Sec. 1.1.5), the negative, shown in lighter colours, do not. The measured value seems to favour the sign-change hypothesis, however, the statistical uncertainty is too large to conclude.

The average asymmetry $A_T^{\sin(2\phi-\phi_S)}$, which in the TMD framework corresponds to the convolution of the transversity TMD PDF of the proton and of the Boer–Mulders TMD PDF of the pion, is measured to be negative by about two standard deviations. Together with the $A_T^{\sin(2\phi+\phi_S)}$ TSA, which can be linked to the convolution of the pretzelosity TMD PDF of the proton and of the Boer–Mulders function of the pion, it could be used to obtain information on the Boer–Mulders function, including the determination of its sign. This is at variance with the spin-independent asymmetry $A_U^{\cos 2\phi}$, which is the convolution of two Boer–Mulders functions, and thus is sensitive only to the relative sign of the function in proton and pion.

5.2 Measurement of the weighted TSAs

In this section, the measurement of the three q_T -weighted asymmetries corresponding to the standard TSAs introduced above is described. They are the asymmetries $A_T^{\sin\phi_S q_T/M_N}$, $A_T^{\sin(2\phi+\phi_S) q_T^3/(2M_\pi M_N^2)}$, and $A_T^{\sin(2\phi-\phi_S) q_T/M_\pi}$, where $\frac{q_T}{M_N}$, $\frac{q_T^3}{2M_\pi M_N^2}$, and $\frac{q_T}{M_\pi}$ are the weights to be used. The main points of the data analysis, which is very similar to the one used for the standard TSAs, are described. The asymmetries are extracted from the data using the modified double ratio method, introduced in Sec. 3.3.2. The results are discussed in more detail in the next chapter.

5.2.1 Event selection for the weighted TSAs

The sample has been collected in nine periods (denoted W07–W15) of data taking. The target had two oppositely-polarised cells. Each data-taking period was divided into two subperiods, and the polarisation was reversed in each cell between the subperiods, as explained in Sec. 2.2.5. The event selection is almost identical to the published TSA measurement.

Selection steps

The main selection steps are the following:

1. Identified muons are selected, i.e. tracks that crossed more than 30 radiation lengths in the spectrometer (excluding the absorber), with a common primary vertex and invariant mass $M > 1.5 \text{ GeV}/c^2$.

| Cut | events |
|---|-------------|
| 1 Preselection | 143 420 272 |
| 2 Bad spills list | 116 794 968 |
| 3 Opposite signs | 73 609 944 |
| 4 Two muon trigger, validated | 36 640 268 |
| 5 Muon track quality | 35 856 244 |
| 6 $ \Delta t < 5$ ns | 32 074 224 |
| 7 $4.3 \text{ GeV}/c^2 < M < 8.5 \text{ GeV}/c^2$ | 138 255 |
| 8 $l^- + l^+ < 190 \text{ GeV}/c$ | 137 954 |
| 9 $l_{\text{T}}^{\pm} < 7 \text{ GeV}/c$ | 137 812 |
| 10 Primary vertex in the target cells | 39 088 |

Table 5.1: Event counts for the q_{T} -weighted TSAs event selection from all 9 data-taking periods of the year 2015.

2. The spill and run must have passed stability checks. We use the same lists of bad spills as in the standard analysis.
3. The two muons have opposite charge.
4. A validated 2μ -trigger.
5. Quality of the reconstructed muon tracks: track $\chi^2/n_{\text{df}} < 10$, with the point of first detection upstream from the first magnet $Z_{\text{first}} < 300$ cm and the point of last detection downstream from muon filter $Z_{\text{last}} > 1500$ cm.
6. The mean muon track time difference $|\Delta t|$ has to be < 5 ns.
7. The muon pair invariant mass cut $M \in [4.3; 8.5] \text{ GeV}/c^2$.
8. Energy of the dimuon $l^- + l^+ < 190 \text{ GeV}/c$ is required.
9. The transverse component of the muon momenta (in the laboratory frame) must be $l_{\text{T}}^{\pm} < 7 \text{ GeV}/c$.
10. The longitudinal and radial position of the primary vertex must be in the target cells $Z_{\text{vert}} \in [-294.5, -239.3] \cup [-219.5, -164.3] \text{ cm}$ and $R_{\text{vert}} < 1.9 \text{ cm}$.

The corresponding reduction of the number of events is given in Tab. 5.1. Several selection steps are discussed in more detail in the following. In particular, we pay attention to the only selection step that differs between the standard and q_{T} -weighted TSAs — the cut on q_{T} . In the standard TSA analysis it is required to be between 0.4 and 5 GeV/c. In the case of the q_{T} -weighted TSAs, the integration over the full q_{T} range, where the cross-section is nonzero, is essential, even if the effect of on the result is marginal, as we will show. In addition, the target cut and Δt cut are illustrated in Fig. 5.4.

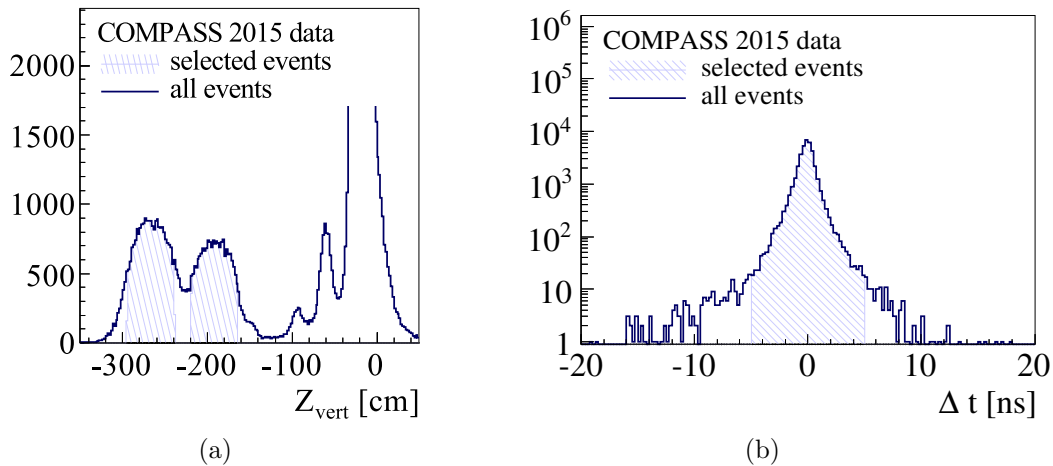


Figure 5.4: Illustration of the event selection: (a) Vertex position along the target, (b) time difference between the two muons. The distribution labelled “all events” is obtained with all cuts applied except the cut in question.

2μ trigger and trigger validation

As described in Sec. 2.3, the 2μ trigger selects events with two muon tracks, which roughly point to the target. This is achieved by a coincidence of two single-muon triggers. Originally, it was defined as a coincidence of 2 LASTs, LAST + OT, or LAST + MT. Each trigger ensures the target-pointing of the track by requiring hits in two hodoscopes. However, it was shown that the events that trigger LAST+MT are mostly combinatorial background, induced by muons coming from the beam pion decay. Therefore, the trigger selection has been modified and we require 2LAST or LAST + OT to be activated, and LAST + MT not activated.

The purpose of the trigger validation is to test if at least one of the 2μ triggers that actually fired is compatible with those that could have been activated by the two reconstructed muon tracks. First, one checks to which pairs of hodoscopes the two tracks point to using the PHAST functions for track extrapolation and the description of the active areas of the hodoscopes planes. The cut is passed if at least one of the 2μ triggers that actually fired is compatible with the pairs of hodoscopes crossed by the two tracks. For example, if only the 2LAST has been activated, each track must cross a pair of LAST hodoscopes.

Selection of the dimuon and the vertex

All possible pairs of tracks, reconstructed by the COMPASS reconstruction program CORAL, identified as muons in an event are considered. For each pair, the primary vertices are identified. For a single pair of tracks more than one vertex might have been reconstructed differing in the list of tracks that are associated to them. To select the best one, we use the same criterion as in the published TSA analysis [88], which is as follows: if one of the vertices is marked as the best primary vertex of the event by PHAST (Sec. 3.1), we use that one. Otherwise, the vertex with the smallest χ^2 is used.

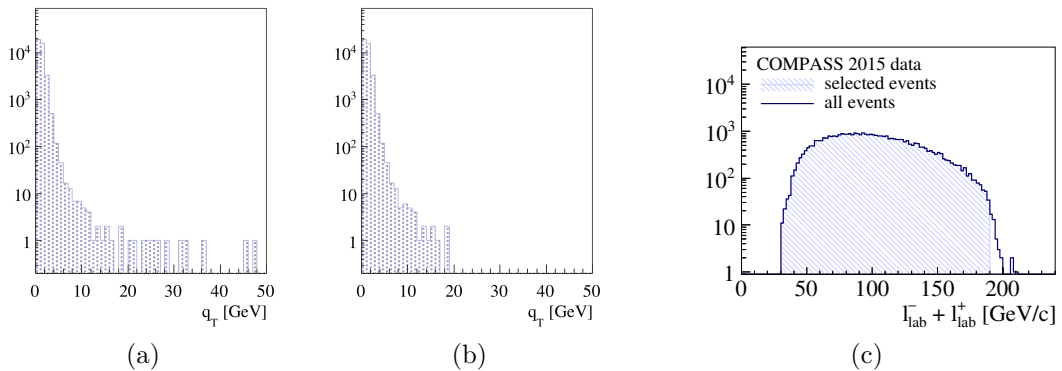


Figure 5.5: (a) The q_T distribution, (b) the q_T distribution with the cut on the sum of muon momenta $l_{\text{lab}}^- + l_{\text{lab}}^+ < 190 \text{ GeV}/c$, (c) the distribution of $l_{\text{lab}}^- + l_{\text{lab}}^+$. The distribution labelled “all events” is obtained with all cuts applied except the cut in question.

Note that nothing forbids that more than one muon pair with a common primary vertex in one event is used in the analysis. In practice such cases do not occur in the selected mass range.

High q_T events

In the standard TSA analysis, a cut $q_T \in [0.4; 5] \text{ GeV}/c$ has been used. In the case of the q_T -weighted TSAs, the integration over the full q_T range, where the cross-section is nonzero, is needed. The low- q_T events, which have been rejected from the TSA analysis for their lower resolution in azimuthal angles, enter with small weight in the q_T -weighted analysis and their influence on the result is marginal. This is shown on Fig. 5.6, where blue circles correspond the event sample of the standard TSA analysis and blue triangles to our final selection.

As can be seen in Fig. 5.5(a), when the high- q_T cut is removed, a very long tail of the q_T distribution appears. It contains only a tiny portion of the statistics, 124 events are gained when we allow $q_T > 5 \text{ GeV}/c$. Because of the rarity of such events, they have only small impact on the asymmetries. However, they do influence the statistical error of the $2\phi + \phi_S$ asymmetry, which grows due to the large weight of these events that is proportional to q_T^3 . This is also illustrated in Fig. 5.6, where the weighted asymmetries extracted from event samples with the cut $q_T < 5 \text{ GeV}/c$ and without it are shown as blue circles and red squares, respectively.

Looking at Fig. 5.5(a), a violation of the energy conservation in the tail is apparent, thus we impose a cut on the sum of the magnitudes of the momenta of the two muons $l^- + l^+ < 190 \text{ GeV}/c$, which restricts the energy of the dimuon to be smaller than the energy available in the initial state (neglecting the beam momentum spread of several GeV/c and masses of μ , π , and p). The cut, illustrated in Fig. 5.5(c), reduces the tail, as shown in Fig. 5.5(b).

Even after the momentum sum cut the q_T distribution reaches rather high values. Inspecting various distributions of the high- q_T events we find out that the distribution of the interaction vertex position, shown in Fig. 5.7(a), differs

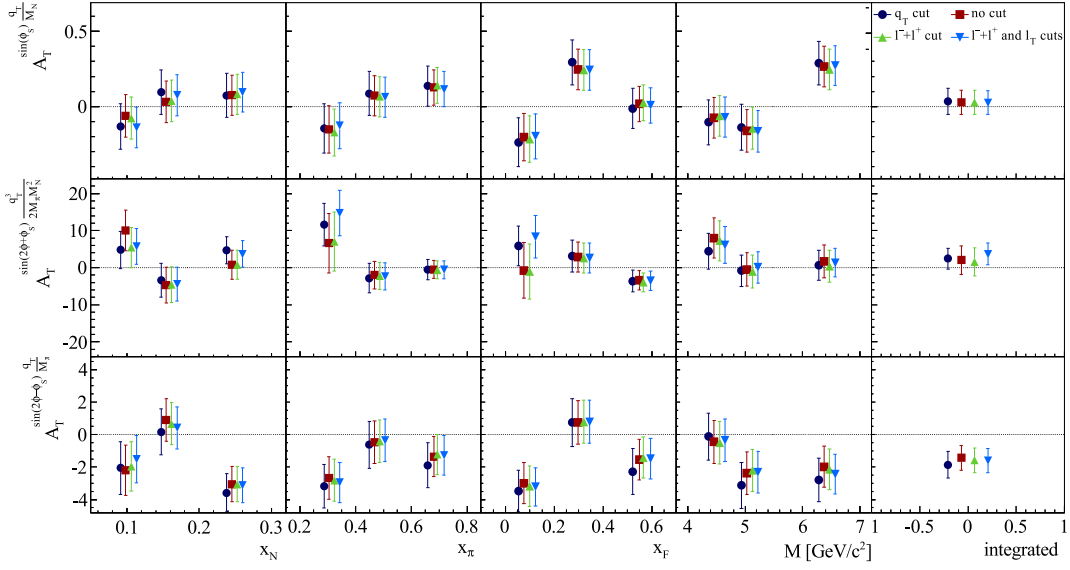


Figure 5.6: The q_T -weighted TSA extracted from the data samples with the following differences in cuts with respect to the final selection: $q_T \in [0.4; 5]$ GeV/ c and no cuts on muon momenta (the same cuts as in the TSA analysis, here blue circles); without the cuts on muon momenta (red squares); without cut on l_T^\pm (green triangles); all compared to the final selection (blue triangles). For the red and green points the high- q_T tail is present, causing the statistical errors of the $2\phi + \phi_S$ asymmetry to slightly grow. The effect is visible in the low x_π and x_F bins, because these variables are anti-correlated with q_T .

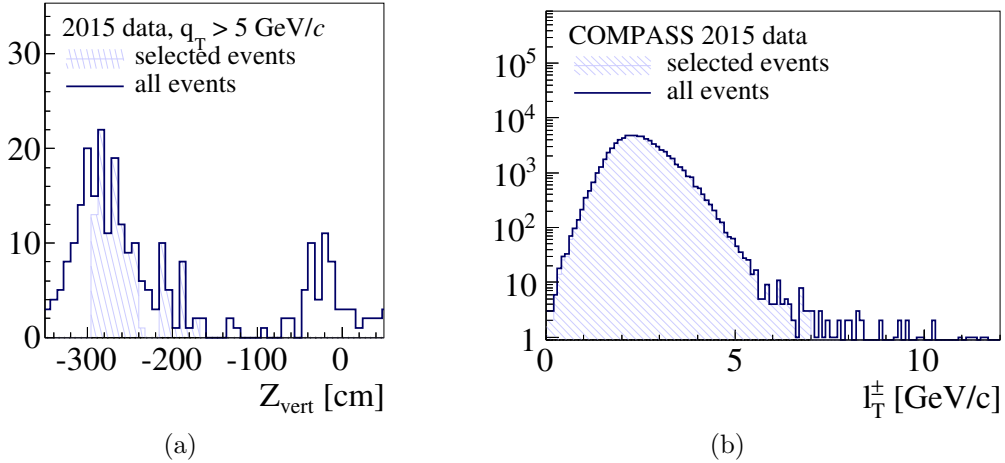


Figure 5.7: (a) Vertex position along the target for all selected events and for those with $q_T > 5$ GeV/ c . All cuts except l_T^\pm and Z_{vert} have been applied. (b) The cut on muon transverse momentum in the laboratory frame l_T^\pm . The distribution labelled “all events” is obtained with all cuts applied except the one in question.

| x_N | x_π | x_F | M [GeV/ c^2] |
|-------|---------|-------|-------------------|
| 0.00 | 0.00 | -1.00 | 4.30 |
| 0.13 | 0.40 | 0.21 | 4.75 |
| 0.19 | 0.56 | 0.41 | 5.50 |
| 1.00 | 1.00 | 1.00 | 8.50 |

Table 5.2: Bin limits.

significantly from the Z_{vert} distribution of the overall sample (Fig. 5.4(a) for the comparison). Namely, most of the events come from the very upstream end of the upstream cell and a few of them originate in the absorber (at $Z_{\text{vert}} \in [-80; 0]$ cm). This distribution gives us some confidence, that the events are not genuine physics events, but badly reconstructed events or combinatorial background.

We have tested several methods of rejection of these events. We consider a cut on transverse momentum of each muon in the laboratory frame $l_{\text{T}}^\pm < 7$ GeV/ c to be the best option (Fig. 5.7(b)). In Fig. 5.8(a) and 5.8(b) we show the correlation of l_{T}^\pm and q_{T} . For each event there are two points corresponding to the transverse momenta of the two muons. For large q_{T} , there is always one muon with low and one with large l_{T} . We believe, that this is another hint towards the reconstruction problem, as if events are generated in TGeant MC simulation of the COMPASS apparatus with q_{T} generated up to 9 GeV/ c , the distribution of l_{T}^\pm is flat for a given $q_{\text{T}} \in [5; 9]$ GeV/ c . This is shown in Fig. 5.8(d). For large q_{T} where no events were generated, we observe a similar tail as in the real data. However, it is small despite the MC sample being about six times larger than the real data sample. The MC simulation is discussed in more detail in Sec. 5.2.3. The distributions of q_{T} after all cuts have been applied are shown in Fig. 5.9. The effect of the two muon momentum cuts on the measured weighted asymmetry is shown in Fig. 5.6.

Binning

We measure the asymmetries in one combined bin (referred to as integrated) and in three bins in four variables (x_N , x_π , x_F and M). We use the same binning as in the analysis of the standard TSAs, which is summarised in the Table 5.2. Of course we do not divide q_{T} into bins.

Distributions of the fractions of parton longitudinal momenta x_π and x_N are shown in Fig. 5.10(a). We can see that both are in the valence region, but x_π spreads over wider range. The distribution of the Feynman variable $x_F = x_\pi - x_N$ is shown in Fig. 5.10(b). Selected correlations of the bin variables and of q_{T} versus x_π is shown in Fig. 5.11.

5.2.2 Measurement of the asymmetries

The q_{T} -weighted TSAs are calculated as is outlined in Sec. 3.3.2. We use eight bins in the azimuthal angle Φ . The fit is carried out by a ROOT graph-fitting function. The dilution factor was obtained from a table of pre-calculated $f_{\text{D}}(M, q_{\text{T}}, x_N)$, used already in the analysis of the standard TSAs. The event migration between the target cells, coming from the event reconstruction, was taken into account by

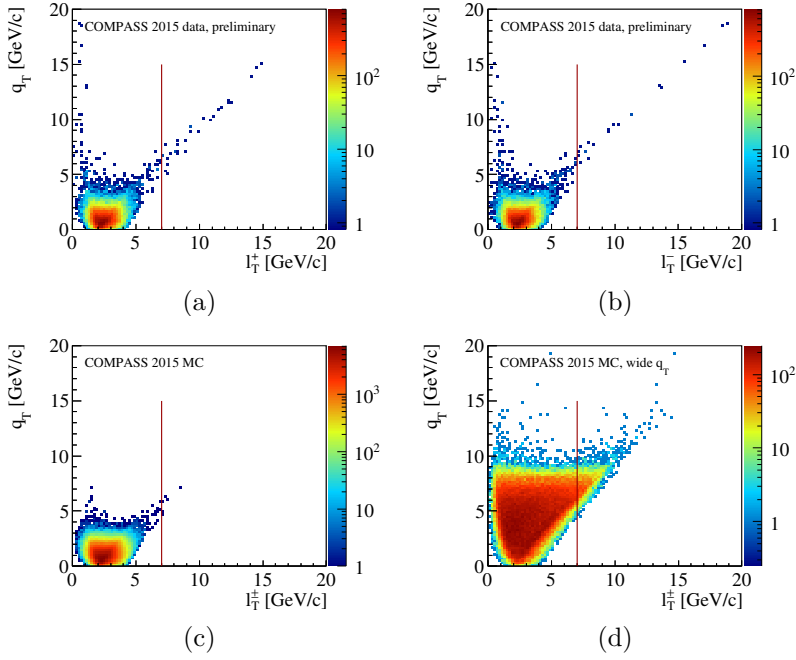


Figure 5.8: Correlation of q_T and l_T^\pm for real data, positive (a) and negative (b) muons; and for MC data generated with a realistic (c) and artificially widened (d) q_T distributions. All cuts except the l_T^\pm , (denoted by the red lines) are applied.

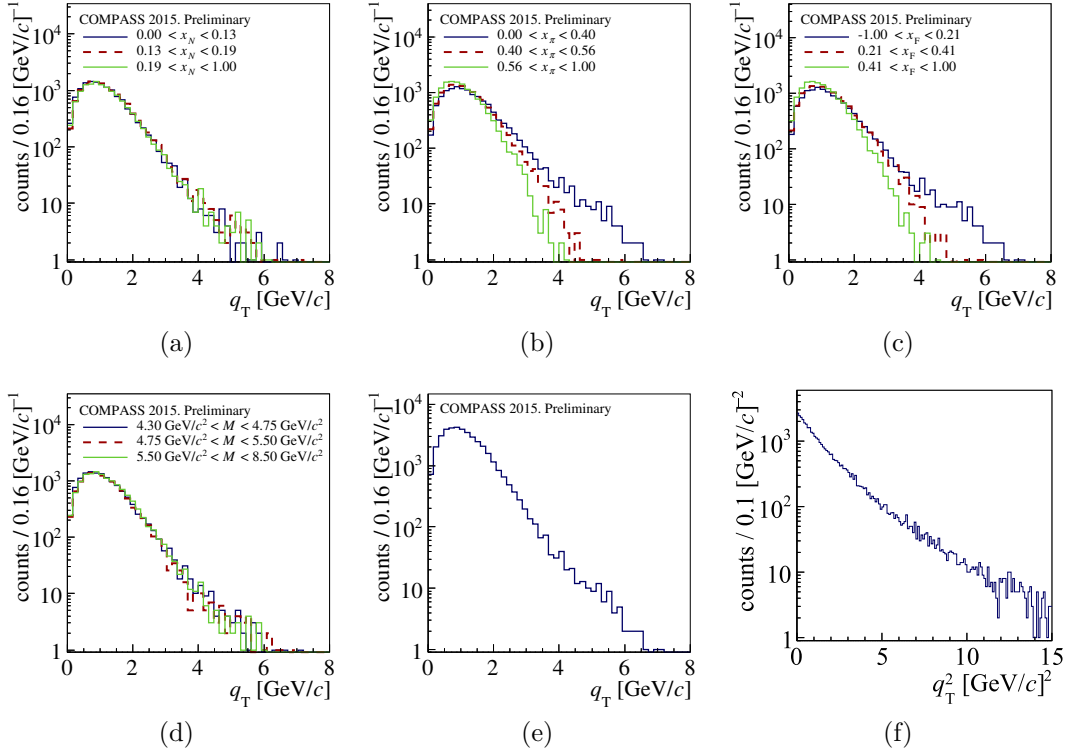


Figure 5.9: Distribution of the virtual photon momentum in the target frame q_T in the kinematic bins and in the bins combined, where q_T^2 is shown as well. All selection cuts are applied.

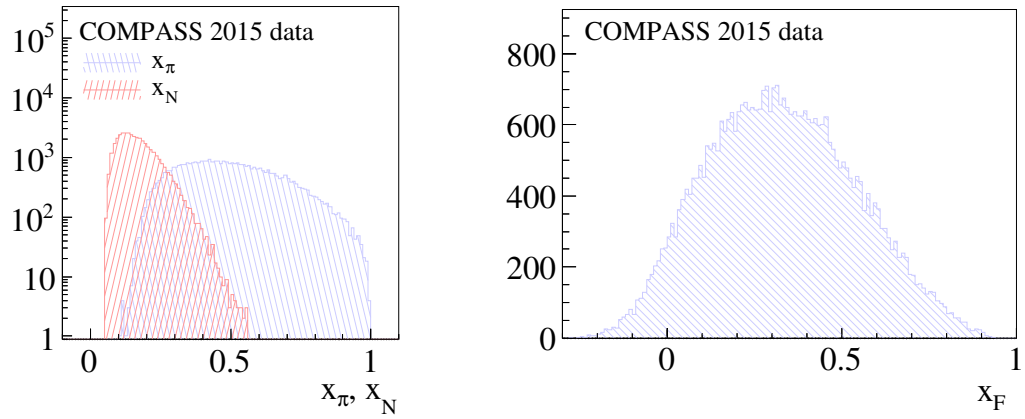


Figure 5.10: Distributions of the variables x_N and x_π (a) and of the Feynman variable $x_F = x_\pi - x_N$ (b).

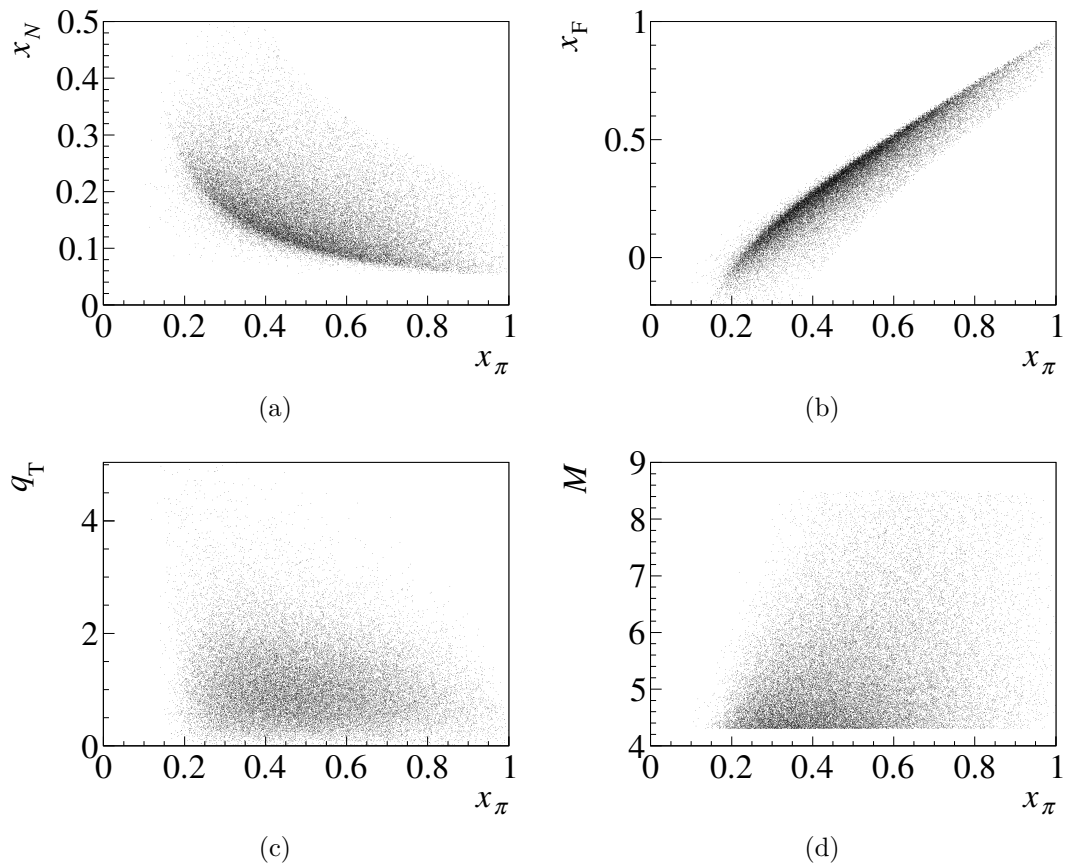


Figure 5.11: Correlations of kinematic variables with x_π : (a) x_N , (b) x_F , (c) q_T , and (d) M .

multiplying the dilution factor of the events originating from the upstream cell by a correction factor 0.95, which is

$$c_U = r_{U \rightarrow U} - r_{D \rightarrow U}, \quad (5.2)$$

where $r_{c_2 \rightarrow c_1}$ is the fraction of events originating from cell c_2 and being reconstructed in c_1 . It corrects for both the events that are lost from c_1 and for those that enter from c_2 with opposite polarisation. It is obtained from the TGeant MC simulation of the full COMPASS setup. In the case of the downstream cell, the correction factor is 0.91.

The asymmetry is extracted in each of the nine data-taking periods separately to minimise effects of acceptance changes over time. The final asymmetries A are obtained as statistically-weighted averages of the asymmetries in the periods A_i ($i = W07 \dots W15$)

$$A = \frac{\sum_i A_i \sigma_i^{-2}}{\sum_i \sigma_i^{-2}}, \quad \sigma^2 = \frac{1}{\sum_i \sigma_i^{-2}}, \quad (5.3)$$

where σ is the statistical uncertainty¹ of A . The compatibility of the periods is discussed in the Sec. 5.2.3. The results are shown in Fig. 5.12. Note, that x_π and x_F are highly correlated, as shown in Fig. 5.11b.

The error-bars give only the statistical uncertainties. The systematic ones are estimated in Sec. 5.2.3. The standard published TSAs multiplied by the mean value of each weight are shown in the same figure for comparison. In the case of Siverts asymmetry $A_T^{\sin \phi_S q_T / M_N}$ (top row, weight $W = \frac{q_T}{M_N}$) and transversity-induced asymmetry $A_T^{\sin(2\phi - \phi_S) q_T / M_\pi}$ (bottom row, weight $W = \frac{q_T}{M_\pi}$) the two are very similar. The error of the weighted asymmetry is always slightly larger than the error of the corresponding standard one times the mean weight. That is expected and the reason is the weighting of the events. One can imagine an extreme example: if weight one was assigned to one half of the sample and weight zero to the other one, the resulting error would be larger by a factor of $\sqrt{2}$. In reality, the factor depends on the distribution of the weight. In the case of the remaining pretzelosity-induced asymmetry $A_T^{\sin(2\phi + \phi_S) q_T^3 / (2M_\pi M_N^2)}$ (middle row, weight $W = \frac{q_T^3}{2M_\pi M_N^2}$) we can see a large difference both in the size and in the error. The distribution of q_T , shown in Fig. 5.9, contains many entries with $q_T < 0.5 \text{ GeV}/c$ and several with $q_T > 5 \text{ GeV}/c$, which means that the distribution of the weight extends at least over three orders of magnitude. The mean value of the weight is about 15 and its dependence on the kinematic variables is mild, except for x_π (and x_F). The average values of the weights in the kinematic bins are shown in Fig. 5.13.

5.2.3 Systematic uncertainty

We have performed several tests to estimate systematic uncertainty due to experimental effects: check of the statistical compatibility of asymmetries measured in the nine periods, test of the acceptance cancellation, and study of the effect of a finite resolution in q_T .

¹For the sake of brevity, we denote the statistical uncertainty as σ . Only when it appears in formulas together with the systematic one, we use σ_{stat} , σ_{syst} .

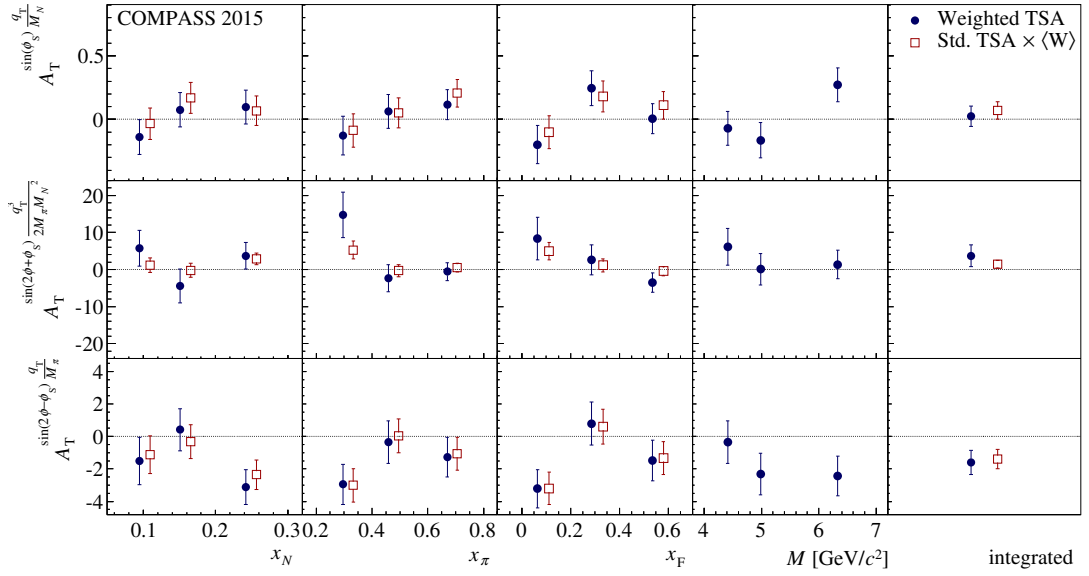


Figure 5.12: The q_T -weighted TSAs $A_T^{\sin \phi_S q_T / M_N}$ (top), $A_T^{\sin(2\phi+\phi_S) q_T^3 / (2M_\pi M_N^2)}$ (middle), and $A_T^{\sin(2\phi-\phi_S) q_T / M_\pi}$ (bottom) from the 2015 Drell–Yan run (blue circles). Each asymmetry is a statistically-weighted average over the nine data-taking periods. The standard published TSAs scaled with the mean values of the weights are shown for comparison (open red squares). The error-bars denote only the statistical uncertainty.

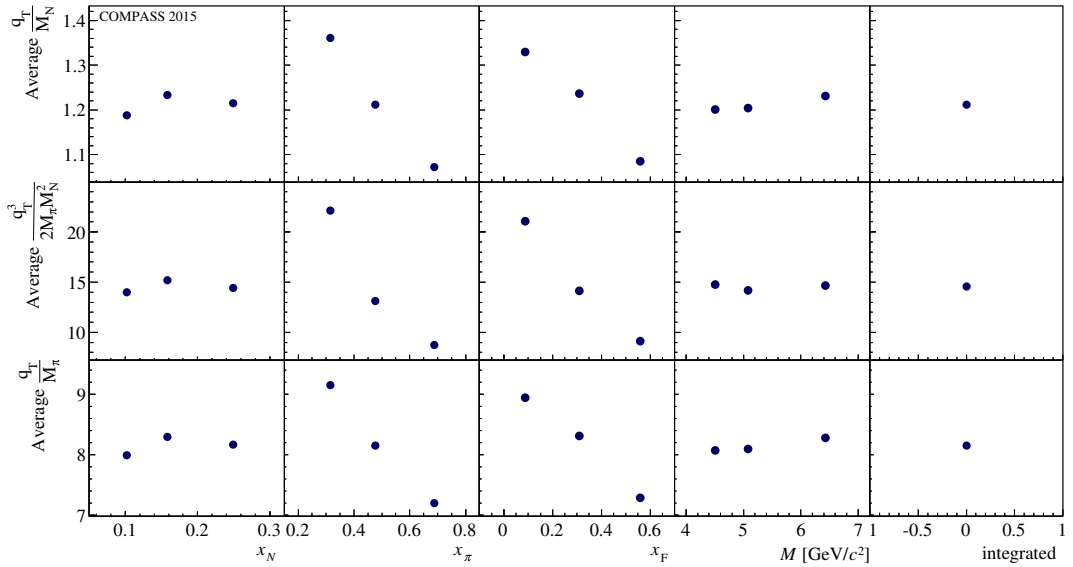


Figure 5.13: The mean values of the weights in the kinematic bins.

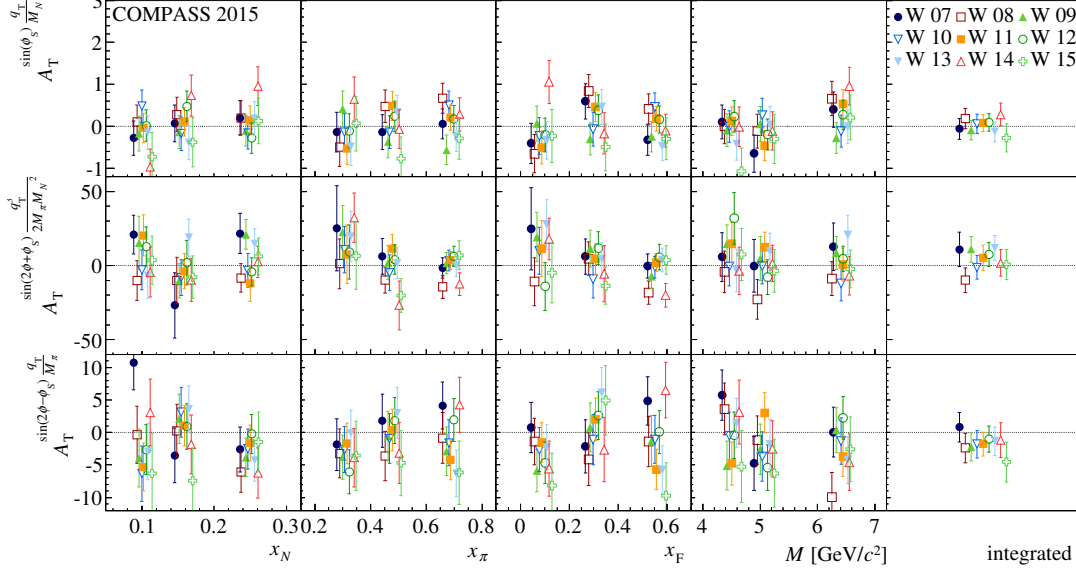


Figure 5.14: The q_T -weighted TSAs in each of the nine periods of data-taking. The abscissa of the points is shifted to improve readability.

Compatibility of the periods

The asymmetries measured in the nine periods of data-taking are shown in Fig. 5.14. We check the compatibility of the periods using two methods. First, we have looked at histograms of the normalised differences (“pulls”) ΔA_i for each asymmetry in each kinematic bin. The pulls are defined as

$$\Delta A_i = \frac{A_i - A}{\sqrt{\sigma_i^2 - \sigma^2}}. \quad (5.4)$$

If A_i are normally distributed, ΔA_i should be also normally distributed with mean equal to zero and width equal to one (or smaller). We have fitted them with normal distributions for each asymmetry and binning variable separately and we have found all the distribution widths smaller than 1.02, as can be seen in Fig. 5.15.

Second, we have calculated the reduced χ^2 of the weighted averages.

$$\frac{\chi^2}{n_{\text{df}}} = \frac{1}{n_{\text{per}} - 1} \sum_i \frac{(A_i - A)^2}{\sigma_i^2}. \quad (5.5)$$

They are plotted in Fig. 5.16. They lay around or below one, with three exceptions that reach value of about 1.6, which gives a significance level of about 20%. From the two tests, we conclude that the results per week are well compatible, and we assume that the contribution to the total systematic uncertainty from this source is negligible.

Acceptance cancellation tests

In Fig. 5.17 we show our result for the weighted TSAs compared to the result extracted using the modified simple ratio method introduced in Sec. 3.3.2. As

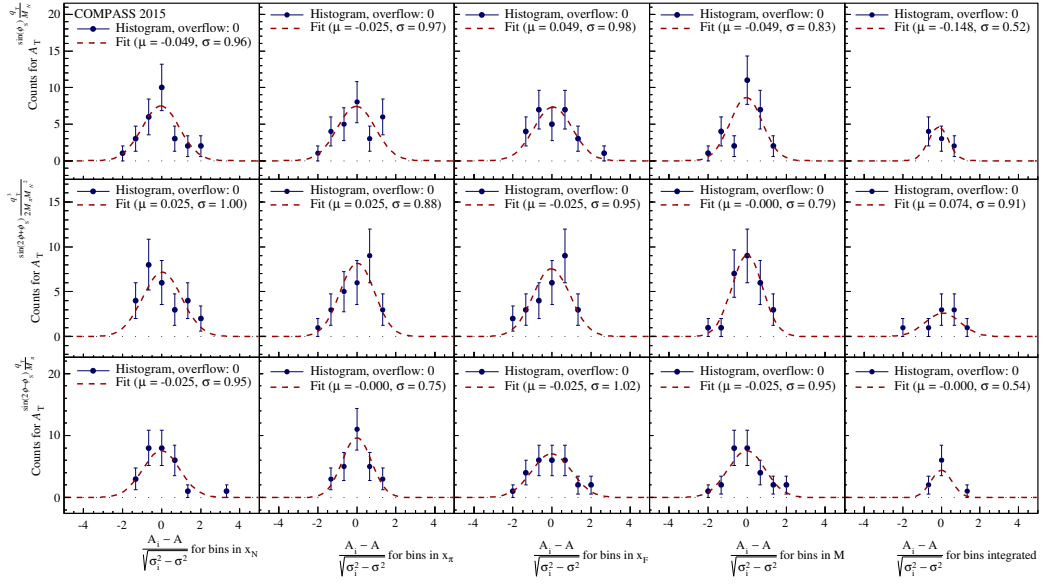


Figure 5.15: Pulls for the q_T -weighted TSAs in the nine periods of 2015, fitted with normal distributions. Each histogram has nine times the number of bins entries. All Gaussian widths are smaller than 1.02.

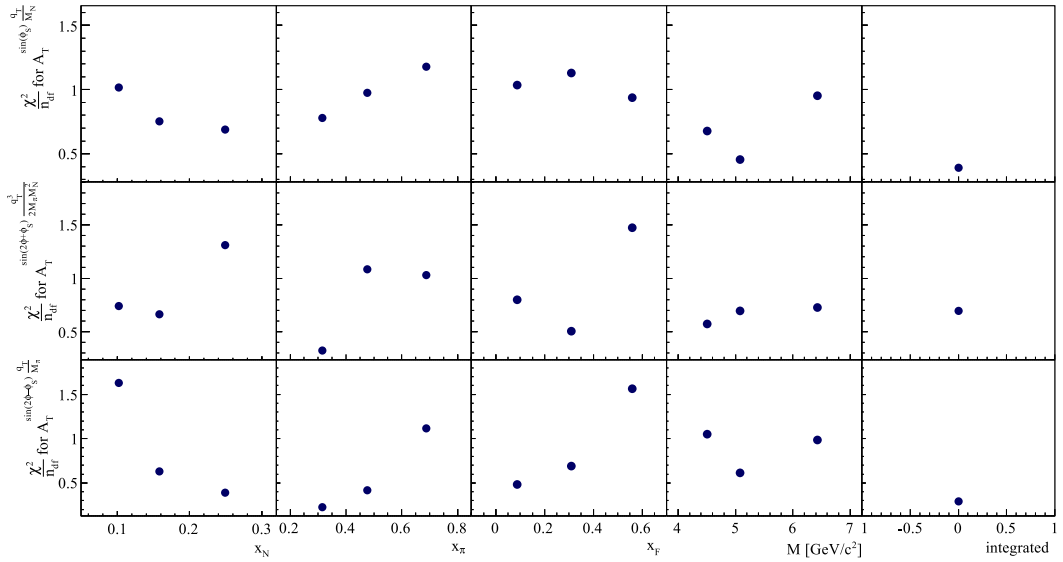


Figure 5.16: The reduced χ^2 of the error-weighted averages of the asymmetries over the nine periods.

explained there, this method does not provide as good acceptance cancellation as the modified double ratio method. However, the results are almost the same, indicating that the spectrometer was stable during the run. In addition, it is a check of the double ratio uncertainty calculation, which is not straightforward.

To test the acceptance cancellation in the modified double ratio, we mix the data in such a way that the physics asymmetries cancel. The only source left for any azimuthal modulation in that case is the apparatus. We mix randomly the events between the two subperiods in each data-taking period. The average polarisation in each subperiod and target cell has to be very small, as the statistics is reasonably balanced between the subperiods. Therefore, the weighted TSA must be close to zero. The randomised data are treated the same as the normal one, and asymmetries are extracted. A different mixing is done between the target cells. Each target cell is divided into two halves, which are then combined forming “inner” and “outer” cells. The average polarisation in each such cell is close to zero in this case and it is expected to cancel in the modified double ratio. Again, the asymmetries are extracted treating the modified data as the normal one. The “false asymmetries” obtained in the two tests are shown in Fig. 5.18.

Analysing the false asymmetries, one faces the question to what extent their nonzero value can be attributed on one hand to statistical fluctuations and on the other hand to real systematic effects. We adopt here the approach similar to earlier COMPASS analyses. For each false asymmetry FA, bin, and data-taking period i we take

$$\begin{aligned} \left(\frac{\sigma_{\text{syst}}}{\sigma_{\text{stat}}}\right)_i &= 0 && \text{if } |\text{FA}_i| < 0.68 \sigma_{\text{stat},i}, \\ \left(\frac{\sigma_{\text{syst}}}{\sigma_{\text{stat}}}\right)_i &= \sqrt{(\text{FA}_i)^2 / \sigma_{\text{stat},i}^2 - 0.68^2} && \text{otherwise.} \end{aligned} \quad (5.6)$$

If the only sources of FA_i are statistical fluctuations, they are normally distributed around zero with width $\sigma_{\text{stat},i}$. The probability, that $|\text{FA}_i| > 0.68 \sigma_{\text{stat},i}$ is then 50%. Using the Eq. (5.6), we conservatively assume that such a case is an indication of a possible systematic effect. The systematic error of the statistically weighted average of the asymmetries over the data-taking periods is obtained as a statistically weighted average of the systematic errors over the periods

$$\frac{\sigma_{\text{syst}}}{\sigma_{\text{stat}}} = \frac{\sum_i \left(\frac{\sigma_{\text{syst}}}{\sigma_{\text{stat}}}\right)_i \sigma_{\text{stat},i}^{-2}}{\sum_i \sigma_{\text{stat},i}^{-2}}. \quad (5.7)$$

This quantity for the two false asymmetries is plotted in Fig. 5.19. At each point, we use the greater of the two values, and finally we make an average over kinematic bins. We do not add them in quadrature, since the false asymmetries are not completely independent. Note that this is an estimation of the upper limit of the systematic effect.

Effects of a finite q_T resolution

It has been observed, as is illustrated in Fig. 5.20(b), that when the acceptance is evaluated in MC in bins of q_T , it rises towards high q_T . This result has been obtained with Pythia 6 event generator [142], set up to pure Drell–Yan process with

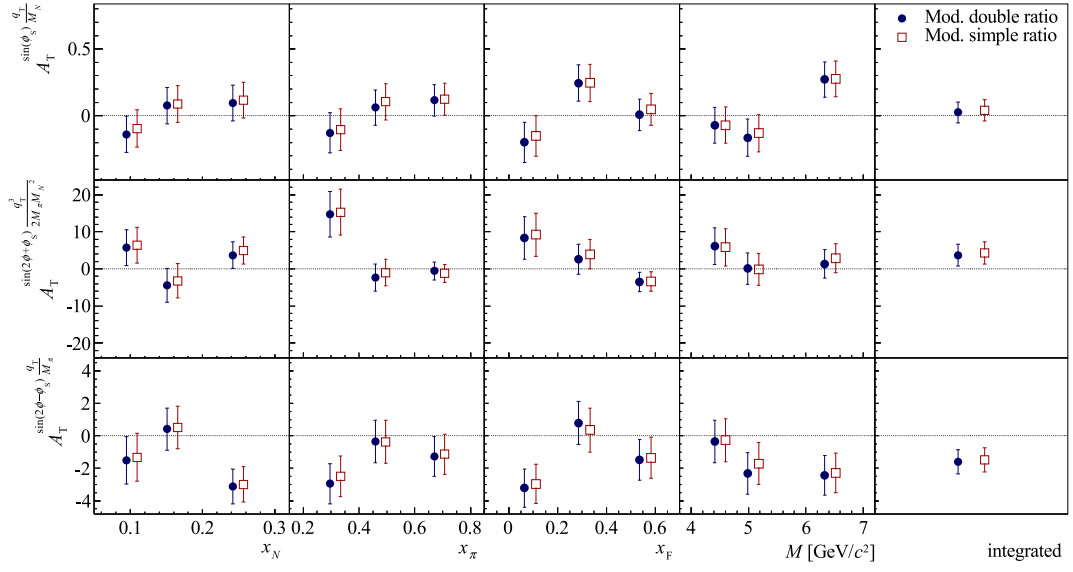


Figure 5.17: The q_T -weighted TSAs extracted with the modified simple ratio (open squares) and our standard modified double ratio (closed points) methods.

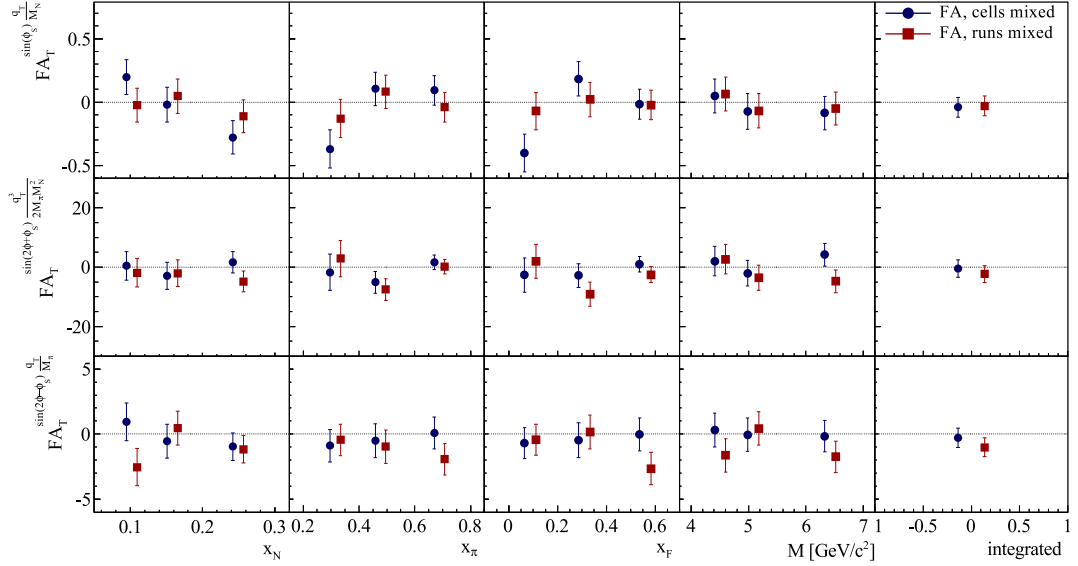


Figure 5.18: The so-called false asymmetries obtained combining differently the target cells (left points) and mixing randomly the events (right points).

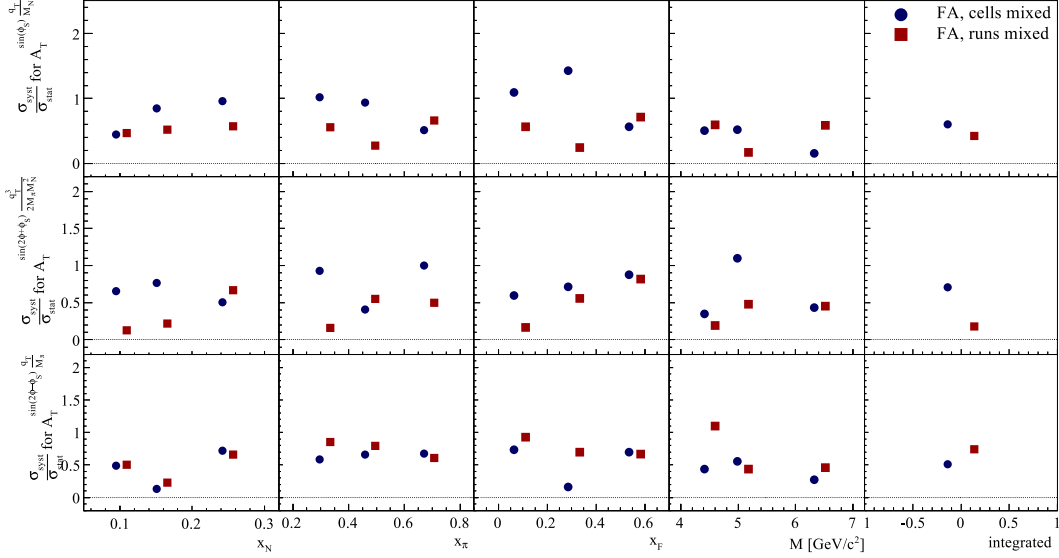


Figure 5.19: The systematic uncertainty estimated from the false asymmetries. The larger value is used for each point.

intrinsic partonic transverse momentum k_T normally distributed with a realistic width of $0.9 \text{ GeV}/c$. The transport of the generated particles through the spectrometer and the detector response were simulated using TGeant COMPASS setup simulation [126] and CORAL. However, when a different settings of the generator have been used, namely when the generated q_T distribution has been made wider, the acceptance has appeared flat. The two generated q_T distributions are shown in Fig. 5.20(a). The use of the wider one (in red) leads to the acceptance shown in Fig. 5.20(c). Such behaviour can be explained by a migration effect: the measured q_T is smeared by the resolution, which has been determined from the MC to be about $0.1\text{--}0.14 \text{ GeV}/c$. When the smearing is applied to a steeply-decreasing distribution, such as the blue histogram in Fig. 5.20(a), the events migrate down the slope much more often than up, creating a less steep distribution with a longer tail. The ratio of the smeared distribution over the original one is therefore rising.

Having observed the migration effect on the q_T distribution, we have to check how is the q_T -weighted asymmetry affected. The migration towards higher q_T means a systematic shift of our weight. To recover the true distribution we utilise a histogram unfolding method based on a Bayesian approach [143], which is suitable for multi-dimensional distributions and arbitrary binning of both generated and reconstructed quantities, which are called causes and effects respectively. In our case we aim to obtain a histogram of $q_{T,\text{true}}$ with n_{true} bins. We call cause C_i the occurrence of an event in the bin $i = 1, 2, \dots, n_{\text{true}}$. In addition to the physics causes we take into account also the background as a special cause C_0 . The outcome of the measurement is for us a histogram of the reconstructed $q_{T,\text{rec}}$ with n_{rec} bins. The presence of an event in the j th bin is called the effect E_j . Note, that the ranges and numbers of bins may differ for the true and reconstructed distributions. In fact, it is natural to expect that the experimentally smeared distribution might require a broader range.

Let us assume we know the initial probabilities of the causes $P(C_i)$ (i.e. the

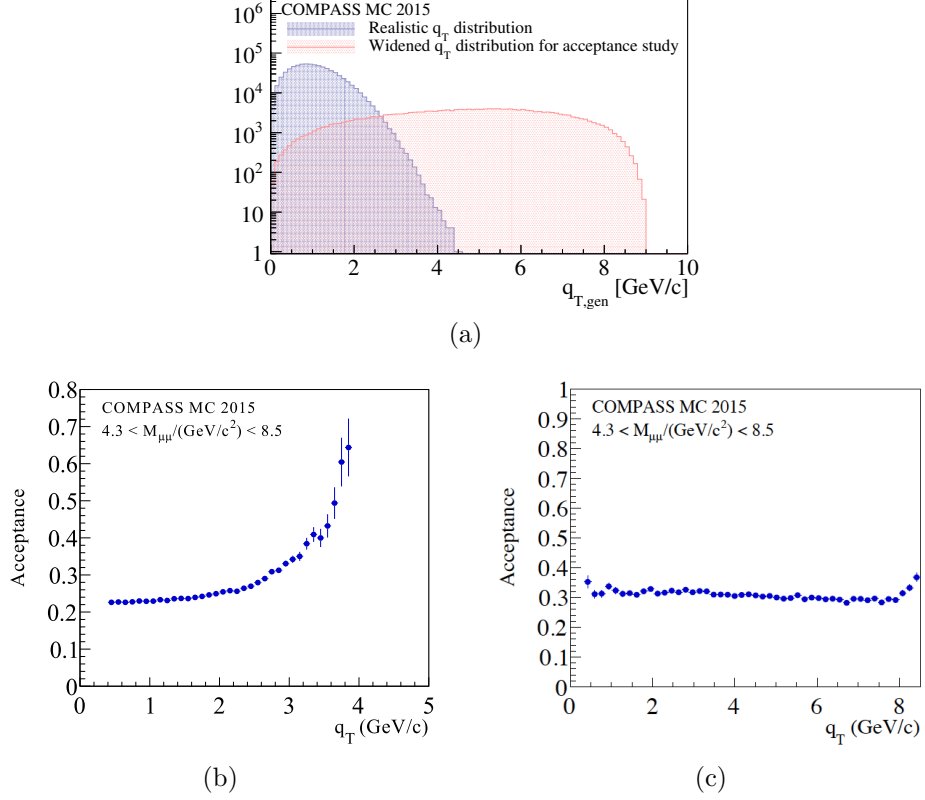


Figure 5.20: (a) Distributions of the generated q_T obtained from the TGeant MC with different event generator settings. The blue distribution is similar to the real data. (b, c) The acceptance as obtained using the realistic and wide q_T distribution (in blue and red on panel (a)). Clearly, the acceptance depends strongly on the distribution shape.

true q_T distribution) and the conditional probability of the i th cause to produce the j th effect $P(E_j|C_i)$. Then we can use the Bayes formula

$$P(C_i|E_j) = \frac{P(E_j|C_i)P(C_i)}{\sum_{k=0}^{n_{\text{true}}} P(E_j|C_k)P(C_k)} \quad (5.8)$$

to evaluate the improvement of our knowledge of $P(C_i)$ given the observation of E_j . The formula says: if we observe a single event in the j th bin, the probability that the true q_T has lied in the i th bin is proportional to the probability of the cause times the probability of the cause to produce the effect.

Having observed $n(E_j)$ events in the j th bin of $q_{T,\text{rec.}}$, we calculate the expected number of events for the causes (in the $q_{T,\text{true}}$ bins)

$$\hat{n}(C_i)|_{\text{obs.}} = \frac{1}{\epsilon_i} \sum_{j=1}^{n_{\text{rec.}}} n(E_j)P(C_i|E_j). \quad \epsilon_i = \sum_{k=1}^{n_{\text{rec.}}} P(E_k|C_i), \quad (5.9)$$

where ϵ_i is the overall efficiency of detection of the cause C_i . The estimated numbers of events can be used to calculate the probability of the causes

$$\hat{P}(C_i) = P(C_i|n(E)) = \frac{\hat{n}(C_i)}{\sum_{i=1}^{n_{\text{true}}} \hat{n}(C_i)}, \quad (5.10)$$

and these we finally insert instead of the initial probabilities $P(C_i)$ into Eq. (5.8) and the whole process is repeated. A criterion for the last iteration is a χ^2 comparison of $n(C_i) = P(C_i)N_{\text{obs}}$ and $\hat{n}(C_i)$

$$\frac{\chi^2}{n_{\text{true}}} = \frac{2}{n_{\text{true}}} \sum_{i=0}^{n_{\text{true}}} \frac{[n(C_i) - \hat{n}(C_i)]^2}{n(C_i) + \hat{n}(C_i)} \quad \text{for } n(C_i) + \hat{n}(C_i) > 0 \quad (5.11)$$

or simply a maximum number of iterations. Both need to be adjusted depending on the distributions, size of the sample etc.

The initial distribution $P(C_i)$ used in the first iteration has no influence on the final unfolded distribution, so we use a uniform distribution for simplicity. The probabilities $P(E_j|C_i)$ are evaluated using a Monte Carlo simulation. Note, that they are independent on the shape of the true distribution, they describe purely the response of the spectrometer, reconstruction, and the selection cuts on a given input C_i . Therefore, it is better to use an artificial distribution of generated q_T , that covers reasonably well all the hypothetical causes, rather than a distribution based on the simulation of the underlying physics process. Thus we utilise both samples of Monte Carlo data mentioned before, the realistic $q_{T,\text{gen}}$ distribution, shown in Fig. 5.20(a) in blue, and the artificially widened $q_{T,\text{gen}}$ distribution, shown on the same Figure in red. The first one provides good statistics in the low q_T range, while the latter in the high range. We subject the generated data to the same selection as the real data and fill the muon pairs into a two-dimensional histogram $n_{\text{gen.}}(E_j, C_i)$ shown in Fig. 5.21, which apart from events generated in bin i of $q_{T,\text{gen}}$ and reconstructed in bin j of $q_{T,\text{true}}$ contains in the underflow bins also the events generated but not reconstructed and those reconstructed but not generated². No systematic distortion from the diagonal is visible, in line with our expectation that the migration is not due to a systematic problem in the apparatus, but only due to the smearing combined with a steep slope of the distribution.

To cope with statistical fluctuations in the distribution tail, which tend to amplify in the iterations, we smooth the $P(C_i)$ distribution at each step except the last one in the range $q_T > 2 \text{ GeV}/c$. This is in line with the Bayesian approach, as the $P(C_i)$ is our expectation, which should be free from fluctuations. To determine the weighted asymmetries we need to know the unfolded q_T event-by-event, which is not possible with the distribution unfolding method. However, for a given $q_{T,\text{rec.}} \in E_j$ the method provides us with the probabilities $P(C_i|E_j)$, so we can tell which $q_{T,\text{true}}$ are likely. For our estimation of the effect, we utilise a simple method of randomly changing q_T according to the probability. For simplicity we do not recalculate variables correlated with q_T , such as θ , x_π or x_F .

We use the MC sample with the realistic generated q_T distribution to test the unfolding. The generated, reconstructed, and unfolded distributions are compared in Fig. 5.21(b). One particular realisation of this reshuffling is shown in Fig. 5.22(a). One can notice the different ratios for the unfolded and reshuffled distributions over the true one. While the distribution unfolding compensates also for the overall acceptance (although not perfectly, as can be noticed), the event-by-event unfolding only changes the q_T . Both the unfolded and reshuffled distributions agree with the generated one better than the reconstructed one,

²These are mostly events generated out of our mass range, but reconstructed in it, there are also combinations of uncorrelated tracks etc.

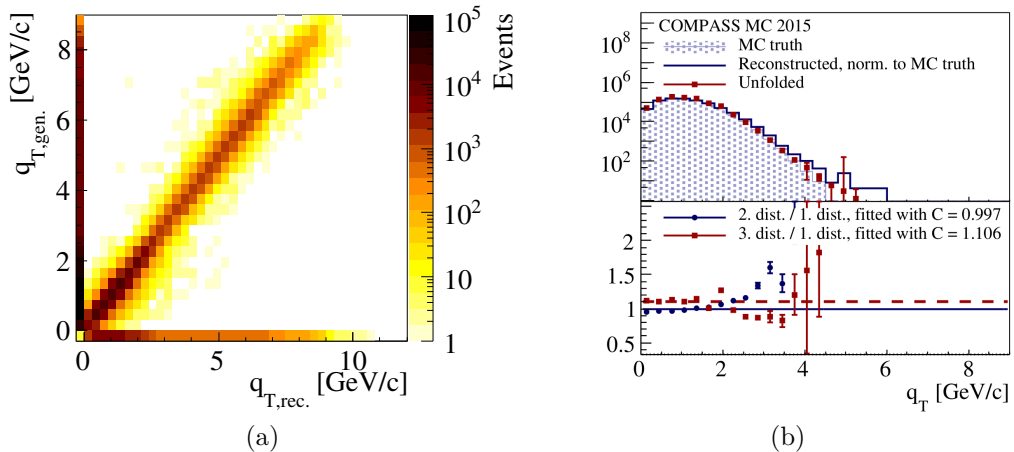


Figure 5.21: (a) Distribution of the generated and reconstructed q_T , including the underflow bins with mis-reconstructed events. (b) The unfolded distribution compared with the Monte Carlo truth and the reconstructed distribution, normalised to the MC truth.

where the migration effect is clearly visible. In Fig. 5.22(b) we show the resolution before and after the event-by-event unfolding. The resolution before is asymmetric. The resolution after is broader, but symmetric. This might look disappointing, but it is actually expected. As the resolution-induced migration is random, it is impossible to know event-wise what the true shifts should be. The method can not improve the resolution, it can only remove, or decrease, the bias.

In the real data, we determine the unfolded distribution, which is shown in Fig. 5.23, and the unfolding matrix $P(C_i|E_j)$ from the full data sample. After that, we use the unfolding matrix for the event-by-event reshuffling, which we apply to each data-taking period separately. We apply it to the whole sample as well, to compare it better with the normally-unfolded one, as shown in Fig. 5.24(a) for 50 particular realisations (replicas) of the random procedure. We can see that, unlike in the MC test, the event-by-event unfolded distribution is different from the normally unfolded one and lies somewhere between it and the reconstructed one. We are not sure what is the reason. However, a systematic shift to lower q_T is still visible. One can see it in Fig. 5.24(b) as well.

To see the impact of the smoothing, we carry out the event-by-event unfolding without the smoothing step and with it, using the same random number generator seed for the reshuffling of the q_T . The result is shown in Fig. 5.23. To evaluate how much is the procedure sensitive to the particular random series we generate 1 000 replicas and we extract the weighted asymmetries from the unfolded data from all of them. As can be seen in Fig. 5.25 and 5.26, the effect is small. For the weighted Siverts asymmetry and for the $2\phi - \phi_S$ asymmetry it is negligible. In the case of the weighted q_T^3 -weighted $2\phi + \phi_S$ asymmetry the difference is up to 30 % of the statistical uncertainty and is most pronounced in the first bins of x_π and x_F (as they are anti-correlated with q_T).

We evaluate the contribution of this test to the systematic error as a difference

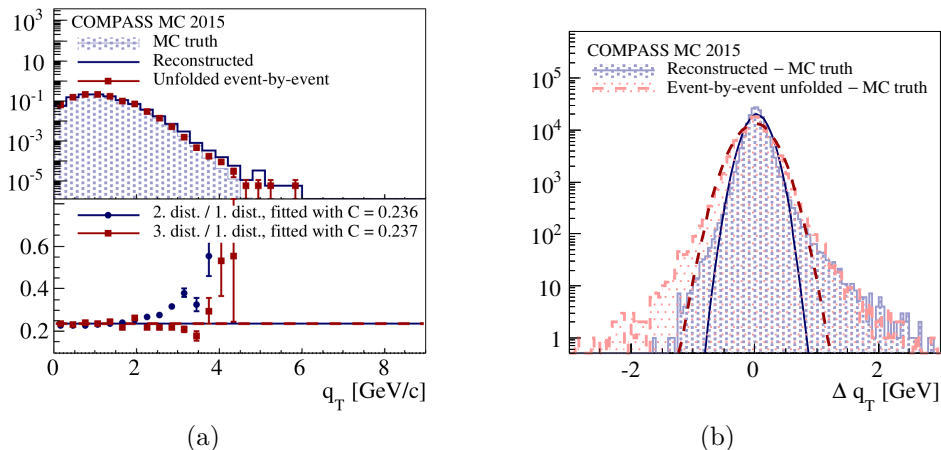


Figure 5.22: (a) The event-by-event unfolded distribution compared with the Monte Carlo truth and the measured distribution. (b) The resolution before (in blue) and after (in red) the event-by-event unfolding. Note, that after the unfolding the peak is broader, but symmetric.

between the asymmetry of the normal sample and the mean asymmetry of the unfolded replicas in each kinematic bin., since we expect them to be the same, as the sample and the extracted quantity are the same. We define

$$\sigma_{\text{syst}} = |A - \langle A_{\text{unf}} \rangle|. \quad (5.12)$$

The values of $\sigma_{\text{syst}}/\sigma_{\text{stat}}$ due to the q_T smearing are plotted in Fig. 5.27, together with the contribution of the false asymmetries to the systematic uncertainty. As can be seen, the contribution is smaller and can be neglected.

Background

Three main sources of background have been singled out for the standard TSA analysis [88, 100]: charmonia resonances, open-charm processes (D meson decay with the production of muons) and combinatorial background, as described in Sec. 5.1. The level of the contamination in the mass range $M \in [4.3; 8.5] \text{ GeV}/c^2$, used in the analysis, has been found to be below 4%. Most of the background is concentrated in the first bin in M . Since the event selection has been only slightly changed between the weighted and standard TSA analysis, we assume the contamination to be at a similar level.

The total systematic uncertainty

The main source of the estimated systematic uncertainty are the false asymmetries. We take the average of this uncertainty over the kinematic bins to reduce the statistical fluctuation. The q_T migration, estimated by the unfolding, can be safely neglected, as can be seen in Fig. 5.27. Two other possible systematic effects have been studied and found negligible: the impact of the number of bins in the azimuthal angles and of the q_T cut removal and its substitution by cuts on muon momenta. As a conclusion, the overall systematic uncertainty is estimated

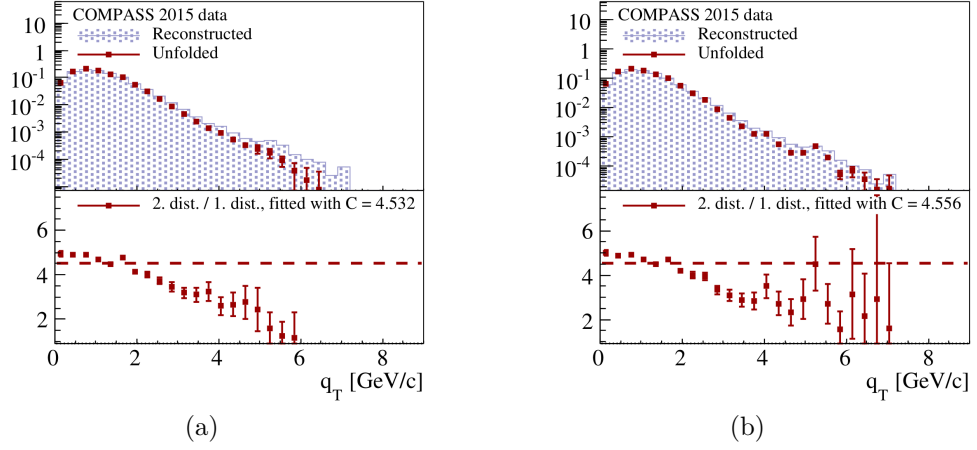


Figure 5.23: The unfolded distribution obtained with (a) and without (b) smoothing from the real data.

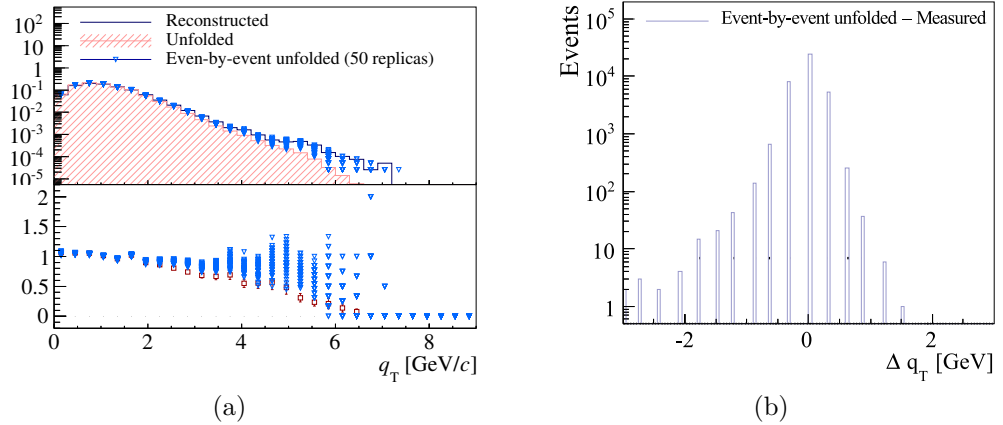


Figure 5.24: (a) 50 replicas of the event-by-event unfolding in the real data, compared to the reconstructed and to the unfolded distributions. (b) The shifts of q_T introduced in the event-by-event unfolding.

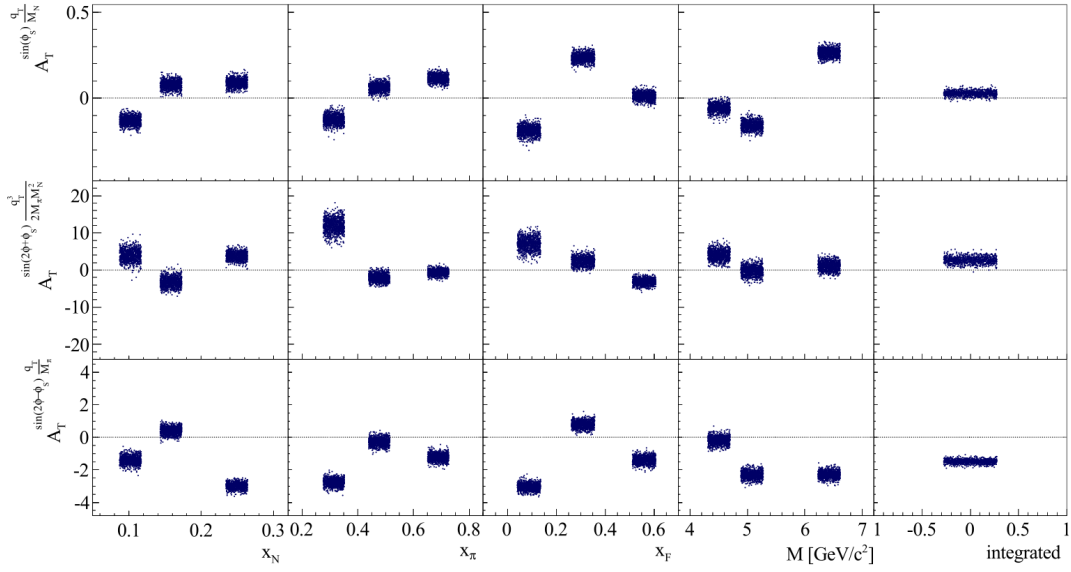


Figure 5.25: The q_T -weighted TSAs, extracted from the 1 000 replicas of the event-by-event unfolded data (abscissa of the points is shifted, statistical uncertainty is not shown).

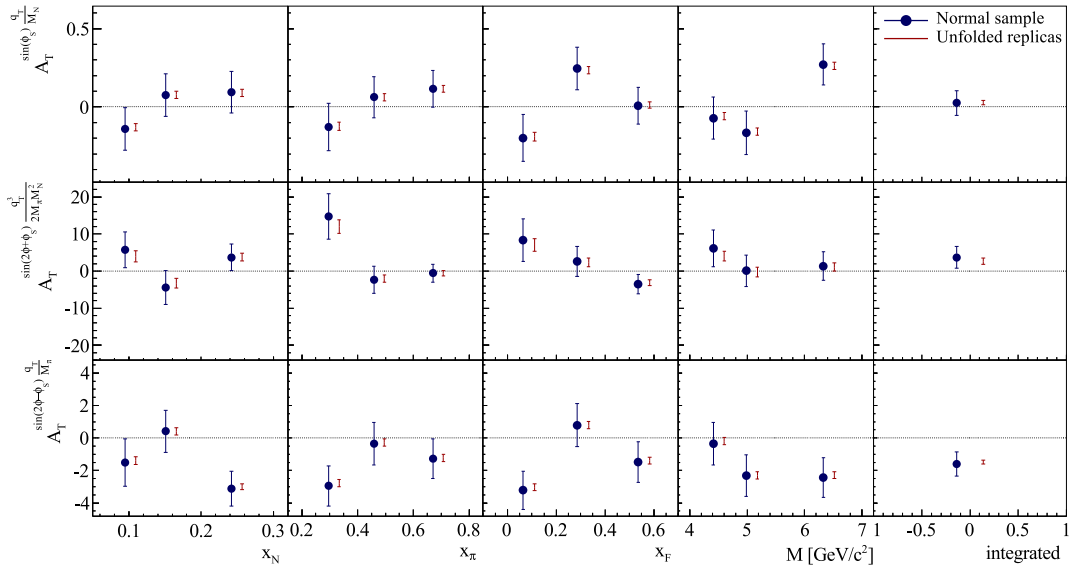


Figure 5.26: The q_T -weighted TSAs, extracted from the normal sample and from the event-by-event unfolded data. 1 000 replicas of the event-by-event unfolding have been generated, the mean and RMS is shown. The difference between the normal sample and the mean of the replicas is used as an estimate of the systematic uncertainty coming from the q_T smearing.

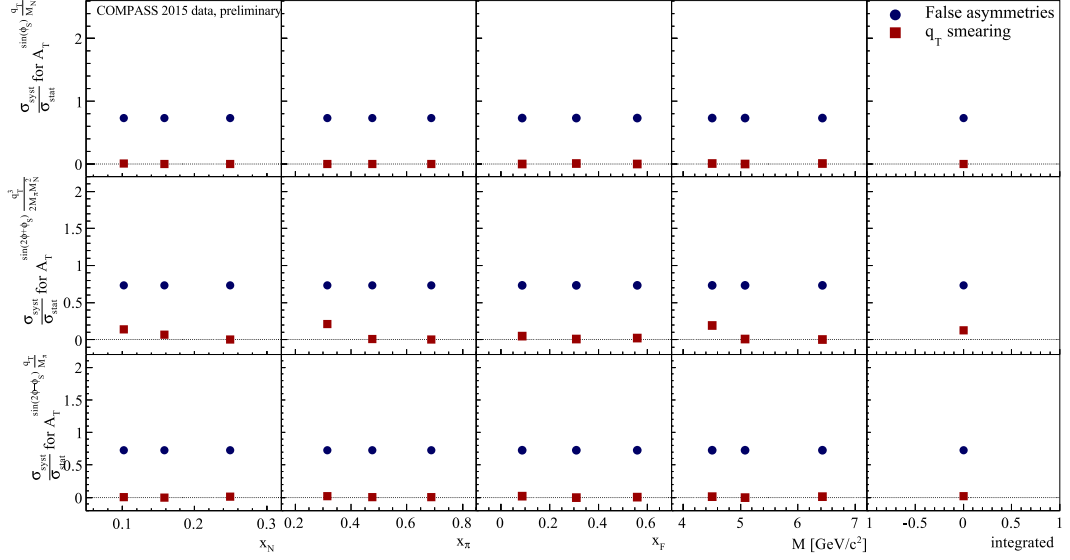


Figure 5.27: The two contributions to the systematic error: false asymmetries (averaged over kinematic bins), and q_T smearing, estimated by the unfolding.

to be about $0.7\sigma_{\text{stat.}}$. In addition, there are normalisation uncertainties of about 5% from the polarisation measurement and about 8% from the dilution factor calculation, which are present in the standard TSA analysis as well.

6. Results and interpretation of the weighted asymmetries

In this chapter we discuss the interpretation of the new results on the transverse-momentum-weighted TSAs measured in the Drell–Yan process, as described in Chap. 5. First we utilise a simplified scenario in Sec. 6.1, then we concentrate on the Siverson asymmetry. For this purpose, we extract the first k_T^2 -moments of the u and d quark Siverson functions from the weighted asymmetries measured in SIDIS at COMPASS. This work, described in Sec. 6.2, is interesting also by itself, since it is the first extraction from this recent measurement. Finally, the result is used to calculate the projection for the weighted Siverson asymmetry in the Drell–Yan process assuming the change of sign of the Siverson function.

6.1 Weighted TSAs in Drell–Yan

In Chapter 5, the first measurement of q_T -weighted TSAs in Drell–Yan process has been described. The results for the asymmetries are presented in three bins in four kinematic variables x_N , x_π , x_F and M , and integrated over the covered kinematic range in Fig. 6.1. The integrated results are given in Tab. 6.1, together with the mean values of selected kinematic variables. The error-bars denote the statistical uncertainty, the shaded areas the systematic one. In addition, there are normalisation uncertainties of about 5% from the polarisation measurement and about 8% from the dilution factor calculation.

Before we discuss the asymmetries, it is interesting to look at the measured distribution of the virtual photon transverse momentum q_T and compare it with the Gaussian model. A summary of various experimental results on the intrinsic transverse momenta in SIDIS and Drell–Yan reactions, and their comparison with the Gaussian model, can be found in Ref. [144]. We have extracted $\langle q_T^2 \rangle$ from the Drell–Yan data in several ways. The values are given in Tab. 6.2. In Fig. 6.2 we show the q_T -distribution as it is measured (a) and after the unfolding procedure (b). The unfolding method, which apart from bin-to-bin migration corrects also for the overall acceptance, is described in Sec. 5.2.3. The curves are fits with the function

$$\frac{d\sigma_{DY}}{dq_T} = \frac{C q_T e^{-q_T^2/\langle q_T^2 \rangle}}{\langle q_T^2 \rangle}, \quad (6.1)$$

where C and $\langle q_T^2 \rangle$ are the free parameters. As can be seen, the fits approximately describe both distributions below about 3 GeV/c with the fitted values of $\langle q_T^2 \rangle = 1.79$ and $1.59 (\text{GeV}/c)^2$ for the measured and the unfolded distributions, respectively. The values are in good agreement with the averages calculated directly from the q_T^2 distributions, which are $\langle q_T^2 \rangle = 1.77$ and $1.66 (\text{GeV}/c)^2$. Finally, the mean value of q_T^2 has been evaluated from the mean value of q_T using the Gaussian model relation

$$\langle q_T^2 \rangle = \frac{4}{\pi} \langle q_T \rangle^2. \quad (6.2)$$

They are also shown in Tab. 6.2. Our results are similar to the E615 results [46], which were obtained with a 256 GeV/c π^- beam and W target, and which were

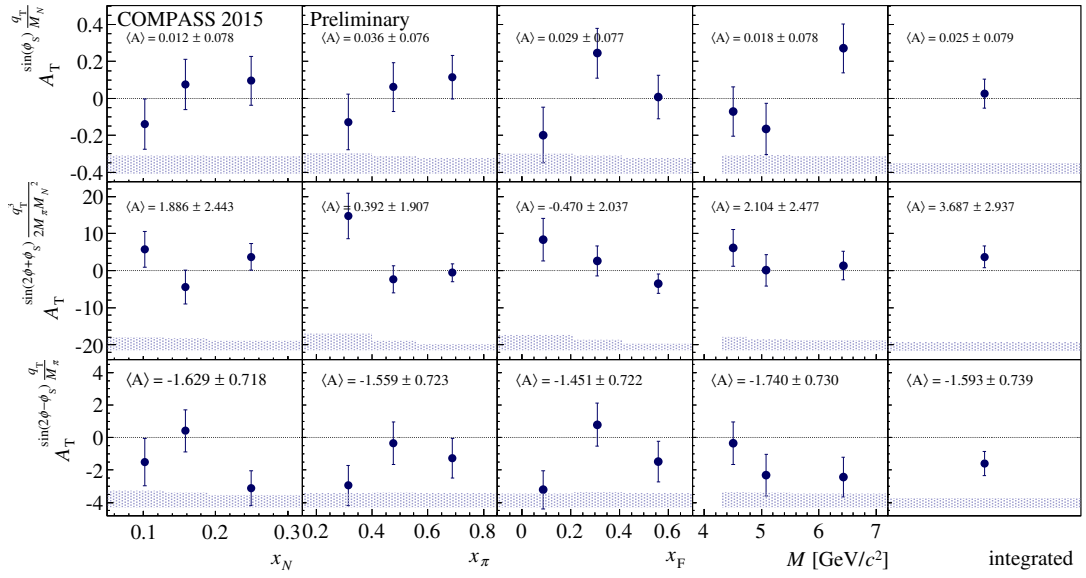


Figure 6.1: The q_T -weighted TSAs from the 2015 Drell–Yan run.

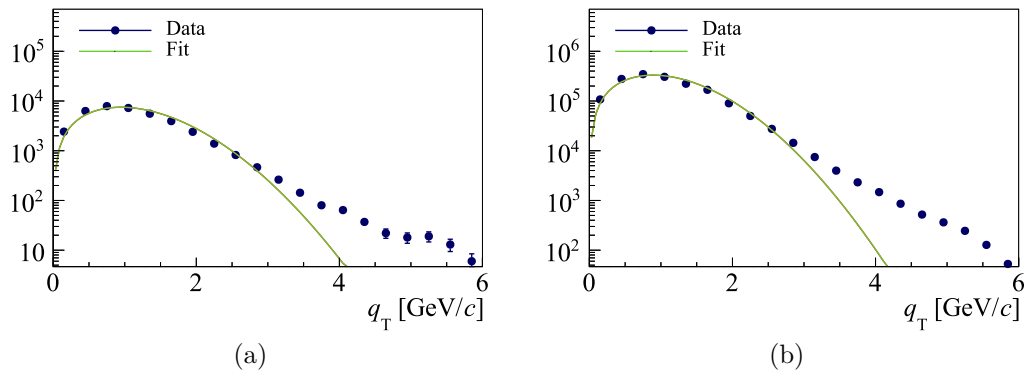


Figure 6.2: The measured (a) and unfolded (b) distribution of q_T , fitted with a Gaussian function.

| | | | | | |
|---|-------------------|-------------------------|--------|-------------------------------------|------------------------|
| $A_T^{\sin\phi_S \frac{q_T}{M_N}}$ | 0.025 ± 0.079 | $\langle x_N \rangle$ | 0.17 | $\langle q_T \rangle$ | $1.14 \text{ GeV}/c$ |
| $A_T^{\sin(2\phi-\phi_S) \frac{q_T}{M_\pi}}$ | -1.59 ± 0.74 | $\langle x_\pi \rangle$ | 0.50 | $\langle q_T^{\text{unf.}} \rangle$ | $1.10 \text{ GeV}/c$ |
| $A_T^{\sin(2\phi+\phi_S) \frac{q_T^3}{2M_\pi M_N^2}}$ | 3.7 ± 2.9 | $\langle x_F \rangle$ | 0.33 | $\langle Q^2 \rangle$ | $29 \text{ (GeV}/c)^2$ |

Table 6.1: The q_T -weighted TSAs in Drell–Yan process and the average values of selected kinematic variables. The uncertainties are statistical only. For q_T , the values before and after distribution unfolding are shown.

| | $\langle q_T^2 \rangle [\text{GeV}/c]^2$ | $\langle q_T^2 \rangle_{\text{fit}} [\text{GeV}/c]^2$ | $\frac{4}{\pi} \langle q_T \rangle^2 [\text{GeV}/c]^2$ |
|-----------------------|--|---|--|
| Measured distribution | 1.77 | 1.79 | 1.65 |
| Unfolded distribution | 1.66 | 1.59 | 1.54 |

Table 6.2: The average q_T^2 calculated from the data by three methods.

discussed in Ref. [144]. Namely, keeping in mind the relation $\langle q_T^2 \rangle = \langle k_{\pi_T}^2 \rangle + \langle k_{p_T}^2 \rangle$, valid in the Gaussian model, we find the values $\langle k_{p_T}^2 \rangle = 0.7 \text{ GeV}/c$ and $\langle k_{\pi_T}^2 \rangle = 1.0 \text{ GeV}/c$ [144] to be in agreement with our data. To conclude, the discrepancies from the Gaussian model are visible, in particular at large q_T , however, it describes reasonably well the bulk of the data at $q_T < 3 \text{ GeV}/c$.

Among the measured weighted TSAs the Sivers asymmetry has presently a special role and is discussed in detail in Sec. 6.2 and 6.3. Here we concentrate on the other two asymmetries.

The $A_T^{\sin(2\phi+\phi_S) \frac{q_T^3}{2M_\pi M_N^2}}$ weighted asymmetry can be interpreted in terms of the products of the first \mathbf{k}_T^2 -moment of the Boer–Mulders PDF of the pion $h_{1,\pi}^{\perp(1)}$ and of the second moment of the pretzelosity PDF of the proton $h_{1T,p}^{\perp(2)}$, which are both presently unknown. As our experiment explores the valence region of both the p and the π^- , we can neglect the sea quarks contributions in Eq. (1.128) and write

$$A_T^{\sin(2\phi+\phi_S) \frac{q_T^3}{2M_\pi M_N^2}} \approx -2 \frac{h_{1,\pi}^{\perp(1)\bar{u}} h_{1T,p}^{\perp(2)u}}{f_{1,\pi}^{\bar{u}} f_{1,p}^u}. \quad (6.3)$$

Since the asymmetry has been measured to be about one standard deviation from zero, the only conclusion that we can make is that there is no evidence, with the present statistics, for non-zero values of both the valence Boer–Mulders function of pion and pretzelosity PDF of proton.

The $A_T^{\sin(2\phi-\phi_S) \frac{q_T}{M_\pi}}$ weighted asymmetry can be related to products of the transversity PDF of the proton $h_{1,p}$ and the first \mathbf{k}_T^2 -moment of the Boer–Mulders PDFs of the pion $h_{1,\pi}^{\perp(1)}$. Neglecting the sea quarks, 1.129 becomes simply

$$A_T^{\sin(2\phi-\phi_S) \frac{q_T}{M_\pi}} \approx -2 \frac{h_{1,\pi}^{\perp(1)\bar{u}} h_{1,p}^u}{f_{1,\pi}^{\bar{u}} f_{1,p}^u} \quad (6.4)$$

Our result, a negative value about two standard deviation from zero, gives a hint for a non-vanishing Boer–Mulders PDF of the pion, since $h_{1,p}^u$ has been found different from zero from SIDIS data. To get information on $h_{1,p}^u$, we use the

extraction from Collins and dihadron asymmetries in SIDIS [64], selecting the three highest bins in Bjorken x , which correspond to the x_N range explored in our Drell–Yan experiment, and to a mean Q^2 smaller by a factor less than two. The average value extracted from the Collins asymmetry in the three bins is $h_{1,p}^u = 0.15$.

The u quark unpolarised PDF of proton $f_{1,p}^u$ is well known and we take it from the CTEQ 5D parametrisation [145]. Its average value over our x_N range is $f_{1,p}^u = 0.58$. Inserting the numbers in Eq. (6.4), we obtain

$$\frac{h_{1,\pi}^{\perp(1)\bar{u}}}{f_{1,\pi}^{\bar{u}}} = 3.1 \pm 1.4. \quad (6.5)$$

To have a straightforward interpretation of the result, we assume the Boer–Mulders function to be proportional to the unpolarised PDF. For simplicity, we employ the Gaussian model for the k_T -dependent part of the PDF and we write

$$h_{1,\pi}^{\perp\bar{u}}(x_\pi, k_{\pi T}^2) = C_{\text{BM}} f_{1,\pi}^{\bar{u}}(x_\pi, k_{\pi T}^2) = C_{\text{BM}} f_{1,\pi}^{\bar{u}}(x_\pi) \frac{e^{-k_{\pi T}^2/\langle k_{\pi T}^2 \rangle}}{\langle k_{\pi T}^2 \rangle}, \quad (6.6)$$

where the constant C_{BM} is constrained by the positivity requirement. Using the definition of the first moment given in Eq. (1.107), we obtain

$$h_{1,\pi}^{\perp(1)\bar{u}}(x_\pi) = \int d^2\mathbf{k}_{\pi T} \frac{k_{\pi T}^2}{2M_\pi^2} C_{\text{BM}} f_{1,\pi}^{\bar{u}}(x_\pi) \frac{e^{-k_{\pi T}^2/\langle k_{\pi T}^2 \rangle}}{\langle k_{\pi T}^2 \rangle} = \frac{C_{\text{BM}} \langle k_{\pi T}^2 \rangle}{2M_\pi^2} f_{1,\pi}^{\bar{u}}(x_\pi). \quad (6.7)$$

In the model, our result from Eq. (6.5) yields $C_{\text{BM}} \langle k_{\pi T}^2 \rangle = 0.12 \pm 0.05$. Using the value $\langle k_{\pi T}^2 \rangle = 1.0 \text{ GeV}/c$ introduced before, we obtain the relative magnitude of the valence Boer–Mulders distribution in pion to be

$$C_{\text{BM}} = 0.12 \pm 0.05, \quad (6.8)$$

where the error is obtained only by propagation of the statistical uncertainty our measurement, not taking into account the model assumptions.

6.2 Siverson function from SIDIS data

Recently, COMPASS has measured the P_{hT}/z -weighted Siverson asymmetry in SIDIS for positively and negatively charged hadrons using the data collected in 2010 [23, 146]. As shown in Sec. 1.5, the convolutions over transverse momenta that complicate the interpretation of the TSAs are not present in these asymmetries, which are given by

$$A_{\text{UT,T}}^{\sin(\phi_h - \phi_S) \frac{P_{\text{hT}}}{zM}} = 2 \frac{\sum_q e_q^2 x f_{1T}^{\perp q(1)}(x) D_1^q(z)}{\sum_q e_q^2 x f_1^q(x) D_1^q(z)}. \quad (6.9)$$

This makes the extraction of the Siverson function from these asymmetries much easier, as we will see.

The asymmetry has been measured in the same nine bins of the Bjorken x and z used for the standard Siverson asymmetry measurement [78]. The DIS events and the final state hadrons have been selected performing the same cuts, namely:

$$0.004 < x < 0.7, \quad Q^2 > 1 \text{ (GeV}/c)^2, \quad W > 5 \text{ GeV}/c, \quad (6.10)$$

$$0.1 < y < 0.9, \quad P_{\text{hT}} > 0.1 \text{ GeV}/c, \quad z > 0.2. \quad (6.11)$$

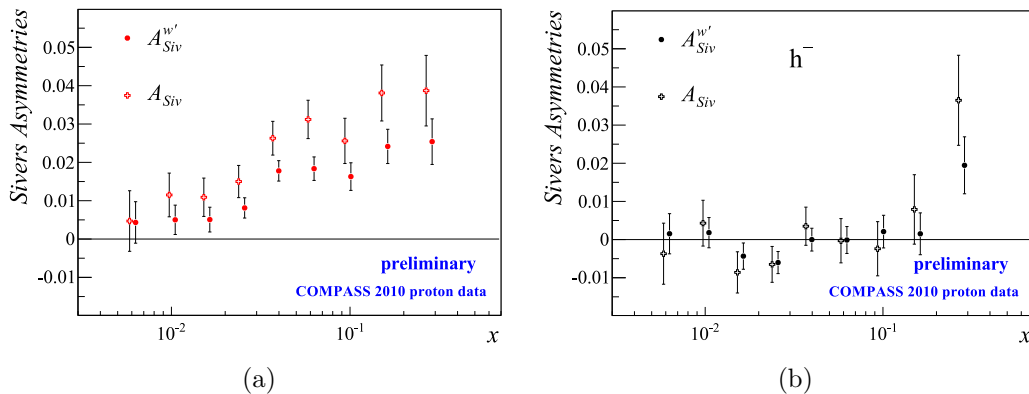


Figure 6.3: The full dots denote the P_{hT}/z -weighted Siverson asymmetries in SIDIS off polarised proton target for production of positive (a) and negative (b) hadrons [23]. The empty crosses are the standard asymmetries extracted from the same event sample [28].

The asymmetry has been measured using the modified double ratio method, described in Sec. 3.3.2. The results are shown in Fig. 6.3, where the standard Siverson asymmetries are also plotted.

Assuming the u-quark dominance in the production of positive hadrons, in other words, neglecting the unfavoured fragmentation, the FFs in Eq. (6.9) in the numerator and denominator cancel and the asymmetry becomes

$$A_{UT,T,h^+}^{\sin(\phi_h - \phi_S) \frac{P_{hT}}{zM_p}}(x, z) = 2 \frac{f_{1T,p}^{\perp(1)u}(x)}{f_{1,p}^u(x)}, \quad (6.12)$$

providing a direct measurement of the u-quark Siverson function first \mathbf{k}_T^2 -moment. Note, that for the negative hadrons there is no such cancellation. The u-quark dominance approximation in SIDIS is, however, not needed and using both positive and negative hadron asymmetries, one can access both the u and d quark Siverson functions, as is shown in the following.

In the extraction, we loosely follow the path outlined in Ref. [95], where the preliminary weighted Siverson asymmetries from HERMES [147] were used to estimate the q_T -weighted Siverson asymmetry expected in Drell–Yan experiments. More specifically, we introduce a suitable parametrisation for the first \mathbf{k}_T^2 -moments of the u and d valence quark Siverson function, use known values for the unpolarised PDFs and FFs, and we estimate the parameters fitting the weighted asymmetries.

In writing explicitly the denominator of the weighted asymmetry, which is polarisation-independent, we only consider u, d, and s quarks and the corresponding antiquarks within the proton. We also assume vanishing Siverson function of sea quarks. Under these assumptions we obtain from Eq. (6.9)

$$A_{UT,T,h^\pm}^{\sin(\phi_h - \phi_S) \frac{P_{hT}}{zM}}(x, Q^2) = 2 \frac{\frac{4}{9} f_{1T}^{\perp(1)u}(x, Q^2) \tilde{D}_{1,u}^{h^\pm}(Q^2) + \frac{1}{9} f_{1T}^{\perp(1)d}(x, Q^2) \tilde{D}_{1,d}^{h^\pm}(Q^2)}{\sum_q e_q^2 f_1^q(x, Q^2) \tilde{D}_{1,q}^{h^\pm}(Q^2)}, \quad (6.13)$$

where

$$\tilde{D}_{1,q}^{h^\pm}(Q^2) = \int_{0.2}^1 dz D_{1,q}^{h^\pm}(z, Q^2) \quad (6.14)$$

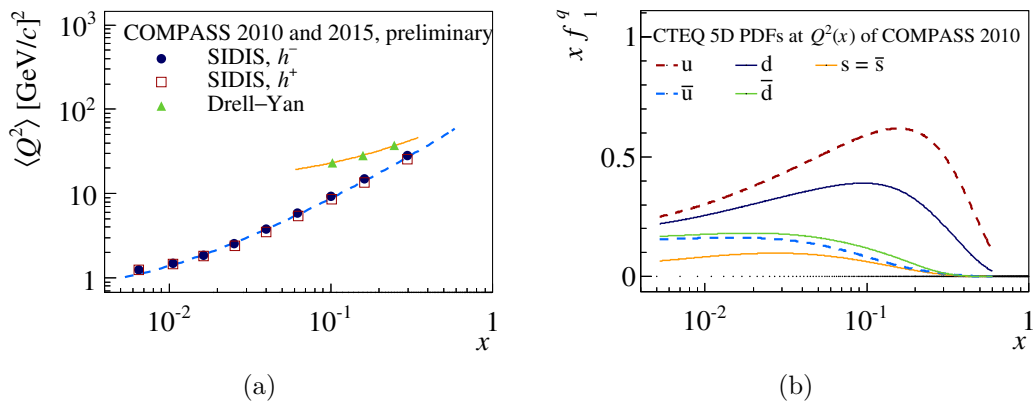


Figure 6.4: (a) Mean value Q^2 versus x for SIDIS and Drell-Yan events. (b) The unpolarised PDFs from Ref. [145] as a function of x at $Q^2 = Q_{\text{SIDIS}}^2(x)$.

Both the unpolarised PDFs and FFs can be taken from global fits, leaving only two unknowns — the Siversons functions of u and d quarks.

As in Ref. [24], we take into account the Q^2 evolution of f_1^q and D_{1,h^\pm}^q , using their values at the average Q^2 of the data shown in Fig. 6.4(a) as a function of x . We parametrise the $\langle Q^2 \rangle$, averaged over h^+ and h^- , by a second order polynomial

$$Q_{\text{SIDIS}}^2 = \alpha + \beta x + \gamma x^2, \quad (6.15)$$

the best fitted parameters being

$$\alpha = 0.60 \pm 0.04 \text{ (GeV}/c)^2 \quad \beta = 78.0 \pm 0.9 \text{ (GeV}/c)^2 \quad \gamma = 35 \pm 3 \text{ (GeV}/c)^2. \quad (6.16)$$

For the unpolarised PDFs we utilise the results of the CTEQ 5D global fit [145], implemented in the LHAPDF library [148–150]¹. The functions $f_1^q(x, Q_{\text{SIDIS}}^2)$ are plotted in Fig. 6.4(b).

Charged hadron fragmentation functions are taken from the results of the DSS 07 LO global fit [151], implemented by the authors into a dynamic library. The fragmentation functions for h^+ versus z at $Q^2 = 1$ are shown in Fig. 6.5(a). The functions $\tilde{D}_{1,q}^{h^\pm}(Q^2)$ have been obtained integrating numerically the FFs over z from 0.2 to 1 at Q_{SIDIS}^2 corresponding to each x value. The results for h^+ are plotted in Fig. 6.5(b).

For the u and d quark first moments of the Siversons function we use the parametrisation

$$x f_{1T}^{+(1)q}(x) = a_q x^{b_q} (1-x)^{c_q}. \quad (6.17)$$

The P_{hT}/z -weighted Siversons asymmetries in SIDIS for positive and negative hadrons measured in the 9 x -bins have been simultaneously fitted with Eq. (6.13) minimising the square residuals using the Minuit minimiser of ROOT. The fit results are shown in Fig. 6.6 together with the measured asymmetries. The fit curve describes the data well, as can be seen also from the reduced χ^2 of the fit, which is 0.9. The best set of parameters is

¹More specifically, we use a table file from LHAPDF 5.9.1 library [148], migrated to LHAPDF 6.2.0 [149, 150].

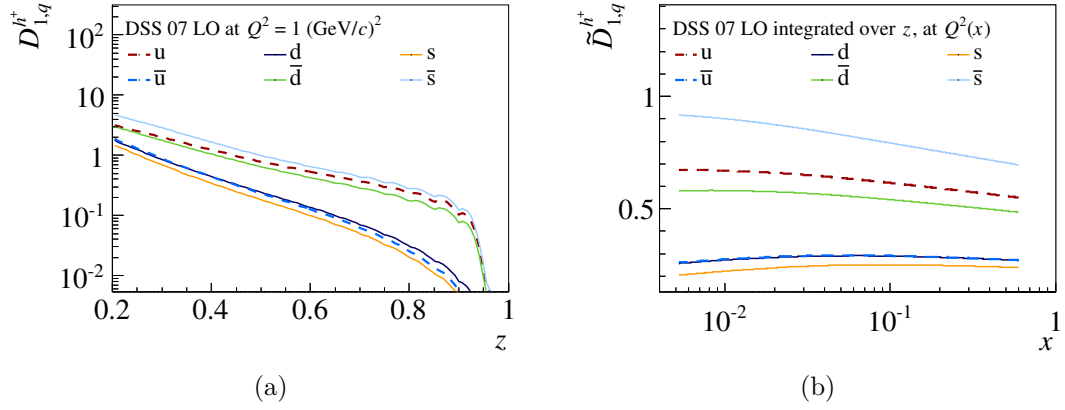


Figure 6.5: Positively charged hadron unpolarised FFs from Ref. [151] versus z , at fixed $Q^2 = 1 \text{ (GeV/c)}^2$ (a) and integrated over z , at $Q^2 = Q_{\text{SIDIS}}^2(x)$ (b).

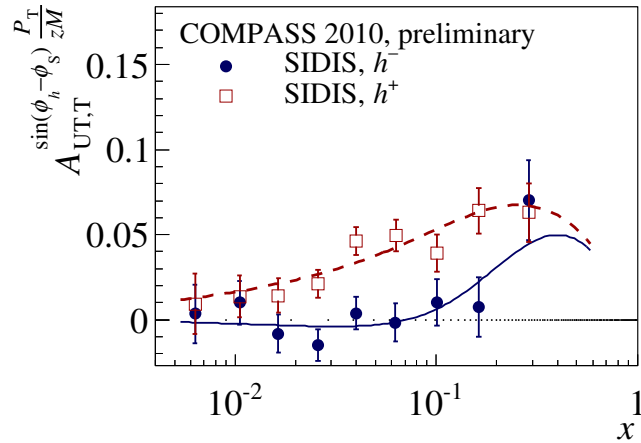


Figure 6.6: Fit of the P_{hT}/z -weighted Siverts asymmetries [23].

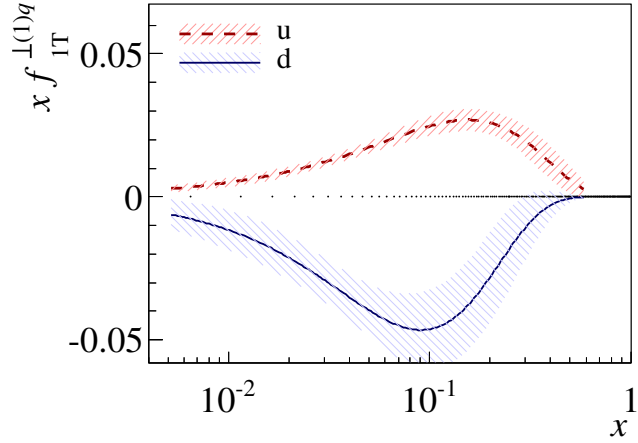


Figure 6.7: The resulting first k_T^2 -moment of the Siverts PDF as a function of x and $Q^2 = Q_{\text{SIDIS}}^2(x)$. The error-bands correspond to 1σ statistical uncertainty.

$$a_u = 0.31 \pm 0.25, \quad b_u = 0.90 \pm 0.23, \quad c_u = 4.7 \pm 1.9, \quad (6.18)$$

$$a_d = -1.4 \pm 2.5, \quad b_d = 1.06 \pm 0.50, \quad c_d = 10.9 \pm 5.8. \quad (6.19)$$

The correlation coefficients of the parameters are

| | a_u | b_u | c_u | a_d | b_d | c_d | |
|-------|-------|-------|-------|-------|-------|-------|--------|
| a_u | 1.00 | 0.98 | 0.92 | -0.62 | 0.63 | 0.38 | |
| b_u | 0.98 | 1.00 | 0.87 | -0.60 | 0.64 | 0.34 | |
| c_u | 0.92 | 0.87 | 1.00 | -0.61 | 0.58 | 0.51 | (6.20) |
| a_d | -0.62 | -0.60 | -0.61 | 1.00 | -0.98 | -0.85 | |
| b_d | 0.63 | 0.64 | 0.58 | -0.98 | 1.00 | 0.78 | |
| c_d | 0.38 | 0.34 | 0.51 | -0.85 | 0.78 | 1.00 | |

The uncertainties have been calculated using the statistical errors and correlations of the fitted parameters, and the simple error propagation formula

$$\begin{aligned} \sigma_{\text{Siv},q}^2(x) = & \left(\frac{\partial f_{1T}^{\perp(1)q}}{\partial a_q} \right)^2 \sigma_{a_q}^2 + \left(\frac{\partial f_{1T}^{\perp(1)q}}{\partial b_q} \right)^2 \sigma_{b_q}^2 + \left(\frac{\partial f_{1T}^{\perp(1)q}}{\partial c_q} \right)^2 \sigma_{c_q}^2 \\ & + 2 \frac{\partial f_{1T}^{\perp(1)q}}{\partial a_q} \frac{\partial f_{1T}^{\perp(1)q}}{\partial b_q} \text{cov}(a_q, b_q) + 2 \frac{\partial f_{1T}^{\perp(1)q}}{\partial a_q} \frac{\partial f_{1T}^{\perp(1)q}}{\partial c_q} \text{cov}(a_q, c_q) \\ & + 2 \frac{\partial f_{1T}^{\perp(1)q}}{\partial b_q} \frac{\partial f_{1T}^{\perp(1)q}}{\partial c_q} \text{cov}(b_q, c_q), \end{aligned} \quad (6.21)$$

where the partial derivatives are $\frac{\partial f_{1T}^{\perp(1)q}}{\partial a_q} = \frac{1}{a_q} f_{1T}^{\perp(1)q}(x)$, $\frac{\partial f_{1T}^{\perp(1)q}}{\partial b_q} = \ln x f_{1T}^{\perp(1)q}(x)$, and $\frac{\partial f_{1T}^{\perp(1)q}}{\partial c_q} = \ln(1-x) f_{1T}^{\perp(1)q}(x)$.

The Siverts functions $f_{1T}^{\perp(1)}$ corresponding to the fitted parameters is plotted in Fig. 6.7. This is the first time that the u and d Siverts functions are independently determined from the weighted TSAs, avoiding all the problems related to the convolution over the transverse momenta. The shape as well as the absolute

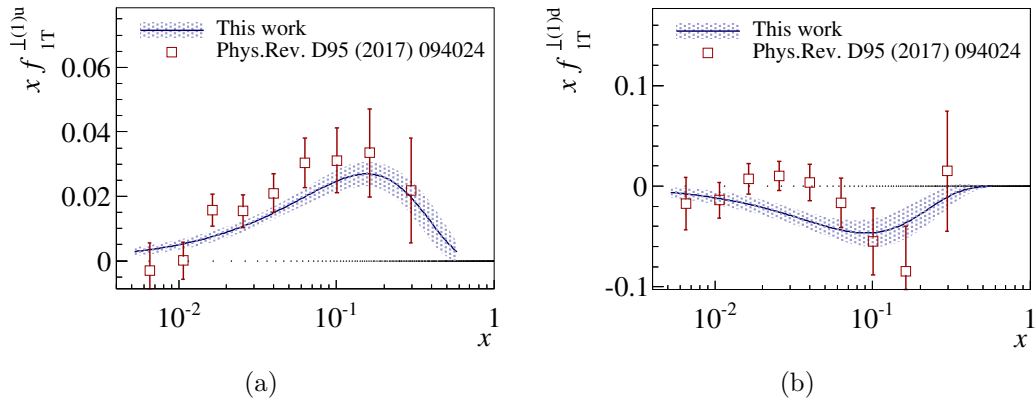


Figure 6.8: Comparison of the results with the point-by-point extraction from standard Siverts asymmetries from the same data and using the same choices of PDFs and FFs [24].

values are quite close to the values obtained from standard asymmetries as can be seen on Fig. 6.8, where our extraction is compared with the point-by-point extraction of Ref. [24]. In both extractions the functions do not correspond to a given fixed Q^2 , but on the measured one, which depends on x according to Eq. (6.15) or Fig. 6.4(a). The method is promising, in particular more could be done having a comparable sample of deuteron target data.

The 1σ error bands shown in the plots seem rather narrow, but it must be reminded that they correspond to the statistical uncertainty on our relatively rigid parametrisation of the Siverts functions. In addition, the uncertainties of the PDFs and FFs have not been taken into account. In the following, we show the impact of our choices of PDF and FF sets on the Siverts functions.

Several alternative choices of PDF sets compared in Fig. 6.9 have been tested. The differences of the extracted $f_{1T}^{\perp(1)}$ are small, they lie within the statistical error of the fit, except at small x as shown in Fig. 6.10.

We have compared our results obtained with the FFs from DSS07 LO with the results obtained DSS07 NLO and with the Kretzer FFs [155]. The integrated FFs are shown in Fig. 6.11 and the impact on the Siverts functions is shown in Fig. 6.12. In this case the differences are larger, of the order of 1σ or more.

We have also looked at the differences when the FFs were integrated over z to obtain $\tilde{D}_{1,q}^{h^\pm}(Q^2)$, as we did for our results, and when they were evaluated at the mean z considering the dependence of $\langle z \rangle$ on x . Since the FFs both appear in the numerator and denominator of the asymmetry, also in this case, the impact is smaller than the statistical error of the fit, as shown in Fig. 6.13.

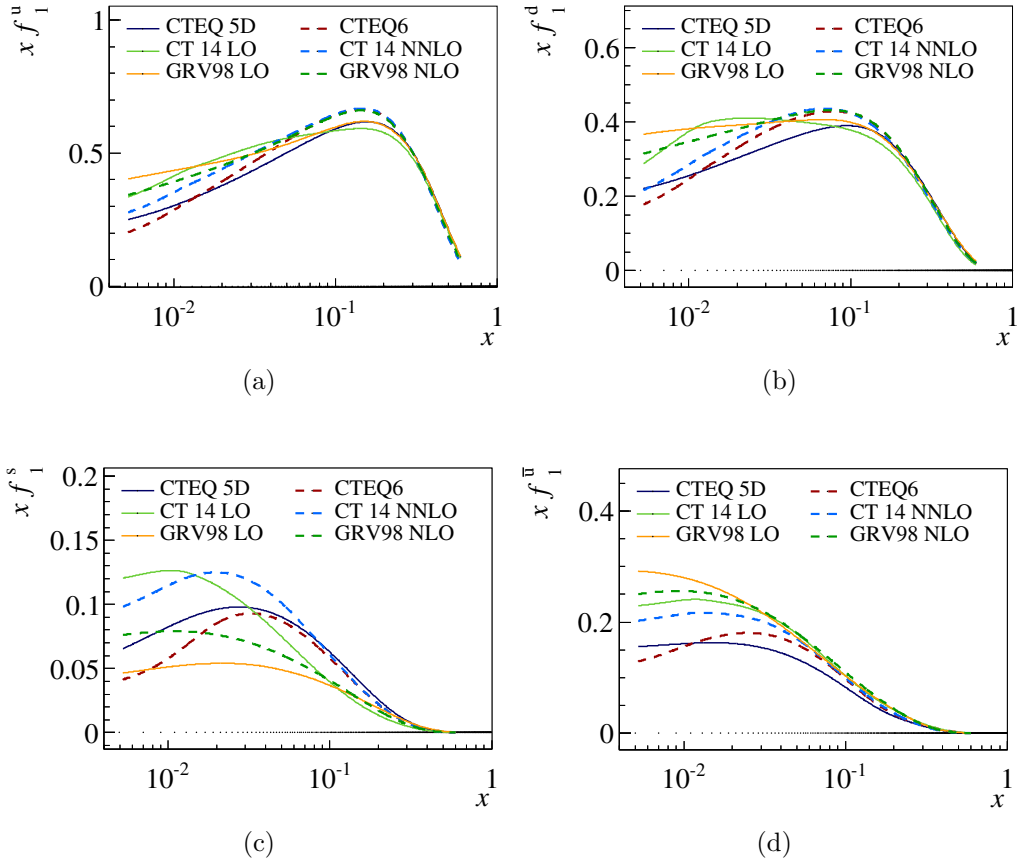


Figure 6.9: PDFs for u , d , s , and \bar{u} from different parametrisations: CTEQ 6 [152], CT 14 [153], and GRV 98 [154].

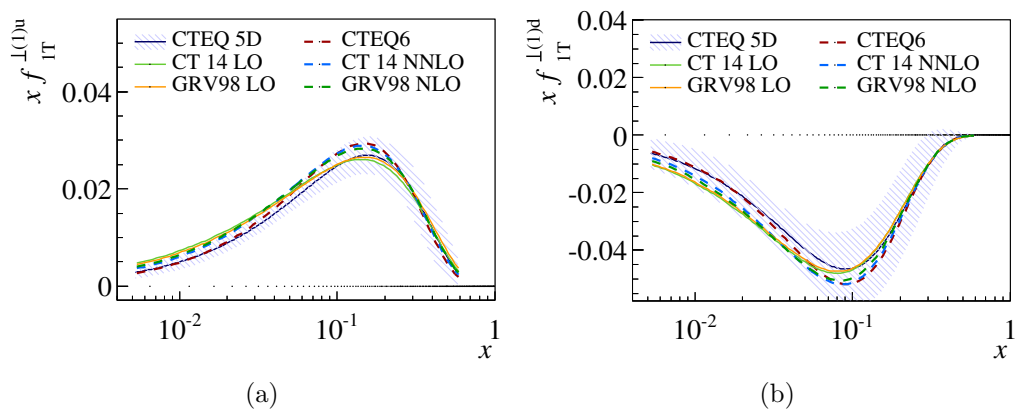


Figure 6.10: The impact of the PDF set choice on the Siviers functions.

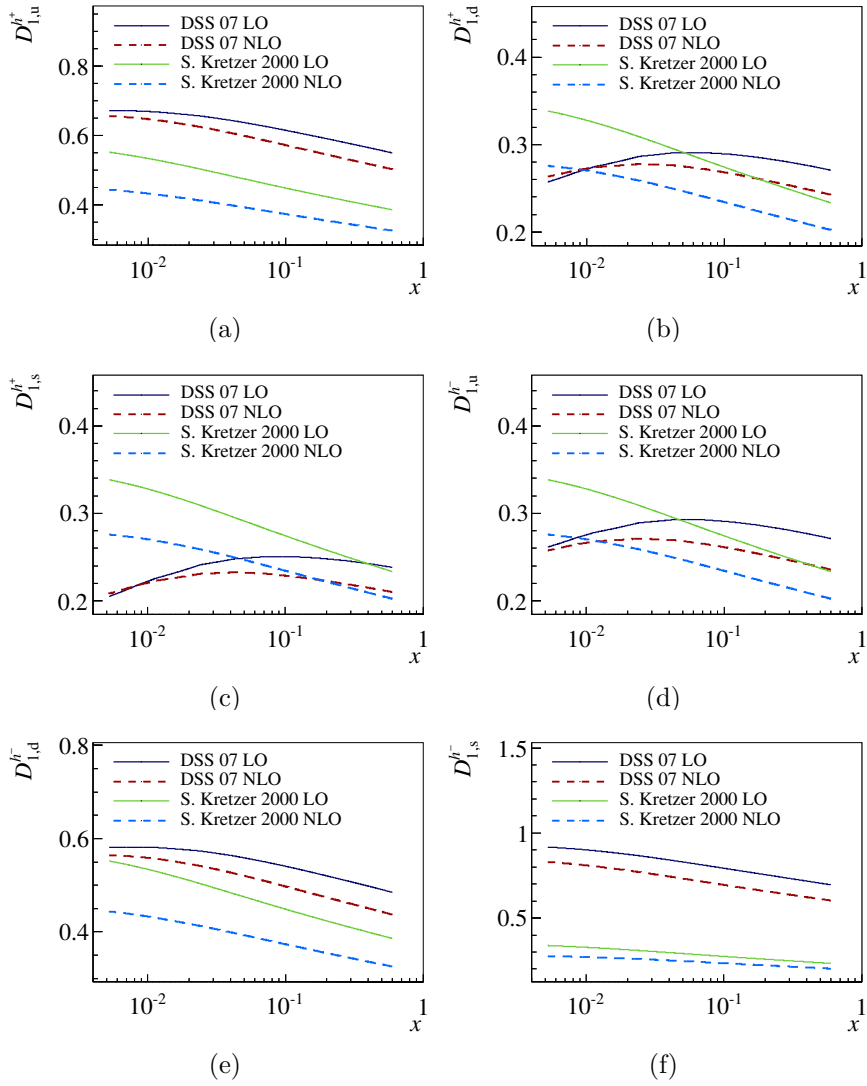


Figure 6.11: FFs from different parametrisations: DSS [151] and Kretzer [155].

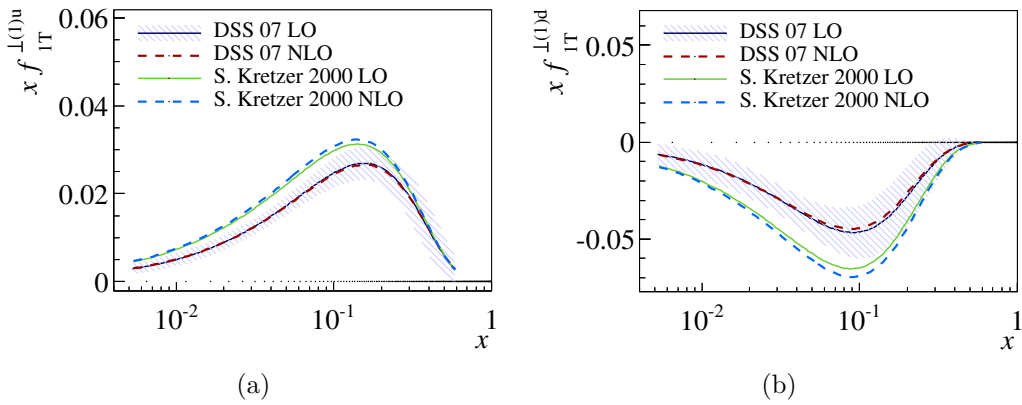


Figure 6.12: The impact of the FF set choice on the Siverts functions.

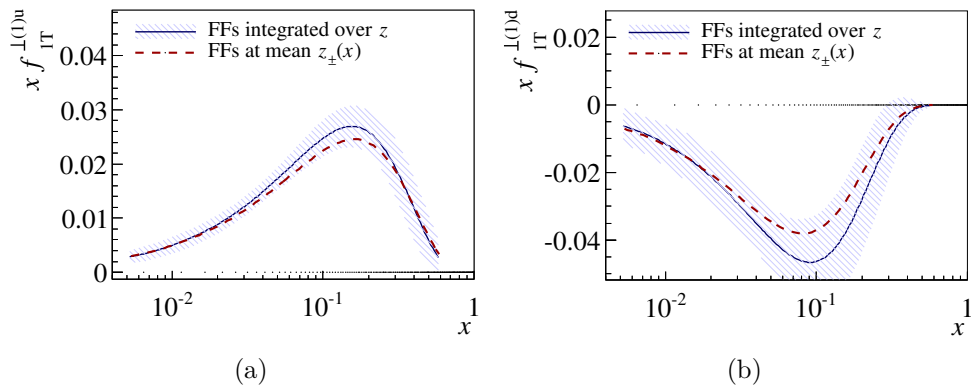


Figure 6.13: The impact of different treatment of the FFs — instead of integration over z , they are taken at $z = z_{\pm}(x)$.

6.3 Projection for the weighted Siverts TSA in Drell–Yan

To compare the SIDIS and Drell–Yan weighted asymmetries, it is necessary to clarify the sign conventions. In SIDIS, we describe the reaction in the γ^*N frame using the Siverts angle $\phi_h - \phi_S$, defined in Sec. 1.2. The target frame of the Drell–Yan reaction and the Siverts angle ϕ_S are defined in Sec. 1.3. The direction of the Siverts angles in the two reference frames is opposite, as is illustrated in Fig. 6.14. With this convention and with the predicted change of sign of the Siverts function $f_{1T}^{\perp q}|_{\text{DY}} = -f_{1T}^{\perp q}|_{\text{SIDIS}}$, we expect to observe the same sign of the Siverts asymmetry of measured in SIDIS and Drell–Yan processes. Of course, this statement is valid only if the same quark flavour is dominant in both processes, which is the case for $\ell p^\uparrow \rightarrow \ell' h^+ X$ and $\pi^- p^\uparrow \rightarrow \ell^+ \ell^- X$.

The TMD expression of the weighted asymmetry in Drell–Yan is given in Eq. (1.131). We can neglect in the sum over flavours the terms, which contain sea PDFs, and Eq. (1.131) simplifies to

$$A_T^{\sin \phi_S \frac{q_T}{M_p}}(x_\pi, x_N) = -2 \frac{f_{1T,p}^{\perp(1)u}(x_N)}{f_{1,p}^u(x_N)} = 2 \frac{f_{1T,p}^{\perp(1)u}(x_N)|_{\text{SIDIS}}}{f_{1,p}^u(x_N, Q^2)}, \quad (6.22)$$

since our experiment covers the valence region of both pion and nucleon. The advantage is the cancellation of the pion PDFs, which are not very well known. Here, x_N denotes the fraction of target nucleon momentum, carried by the struck parton, so that we can identify it with the Bjorken x of SIDIS.

Neglecting the evolution effects between the Q^2 scales of the two experiments and using Eq. (6.12), we can directly compare the two asymmetries, as we do in Fig. 6.15. The Drell–Yan data point is compatible with all the hypotheses of sign-change, zero asymmetry, and no sign-change. The vast difference in the size of the statistical error-bars illustrates well the much smaller cross-section of the Drell–Yan process.

Having extracted the first moment of the Siverts function, we can do more, namely calculate the expected weighted Siverts asymmetry in Drell–Yan as func-

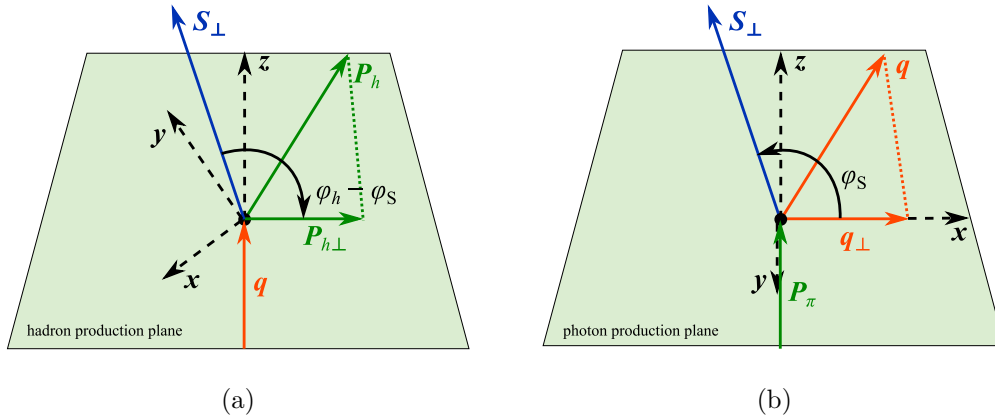


Figure 6.14: Sivers angles as they are defined in the γ^*N frame of SIDIS (a) and in the target frame of Drell–Yan (b) when looking along the z axis direction. The angles have opposite orientations, thus if the sign of the Sivers function is changed between the processes, the sign of the Sivers asymmetry would be the same.

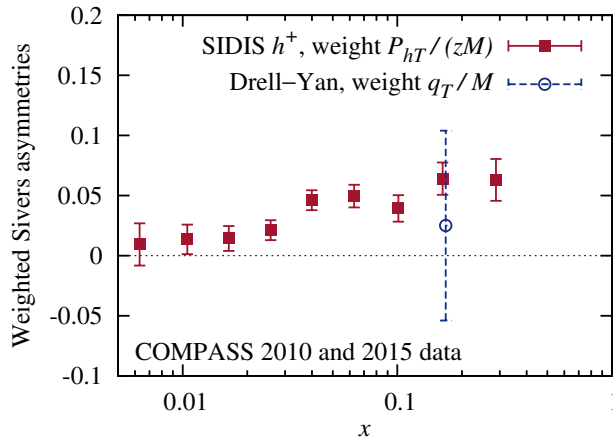


Figure 6.15: The direct comparison of the transverse-momentum-weighted Sivers asymmetries measured in SIDIS $\mu p^\uparrow \rightarrow \mu'/h^+ X$ [23] and Drell–Yan $\pi^- p^\uparrow \rightarrow \mu^+ \mu^- X$ (this work) processes at COMPASS. Positive asymmetry in Drell–Yan is expected based on the sign change prediction. Only statistical errors are shown.

tion of x_N . We use the same unpolarised PDF as in SIDIS, taken at $Q^2 = Q_{\text{DY}}^2(x_N)$, which is obtained from the mean Q^2 of the events used in the Drell–Yan measurement. The $\langle Q^2 \rangle$ values in the three x_N -bins are shown in Fig. 6.4(a) together with the parametrisation

$$Q_{\text{DY}}^2(x_N) = \alpha' + \beta' x_N, \quad \alpha' = 13.7 \pm 0.4, \quad \beta' = 90 \pm 2 \quad (6.23)$$

and with the values of $\langle Q^2 \rangle$ for the SIDIS events. The difference is up to a factor of 2.7. We do not consider any evolution of the Siversons function first moment between the kinematics of the two experiments. The calculated weighted Siversons asymmetry in Drell–Yan is shown in Fig. 6.16 and it has already been shown at conferences [156]. As can be seen, it is almost constant over the measured x_N -range and its mean value of 0.085 is in agreement with the central value of the calculations of Ref. [82], indicated by DGLAP in Fig. 5.3. The error bands give the statistical uncertainty. In addition, several tests have been done to evaluate the effect of our assumptions.

We test an alternative parametrisation of the Siversons first moment, namely

$$x f_{1\text{T}}^{\perp(1)q}(x, Q^2) = a_q x^{b_q} (1-x)^{c_q} x f_1^q(x, Q^2). \quad (6.24)$$

It contains the unpolarised PDF, which can alter the function shape, but we found that it is not the case and the difference between the Siversons functions extracted with this parametrisation and with our standard one is very small. In addition, f_1^q in the parametrisation induces a collinear Q^2 dependency of the Siversons function, which can have an effect on the Drell–Yan projection. However, the unpolarised PDFs are very similar at $Q_{\text{SIDIS}}^2(x)$ and $Q_{\text{DY}}^2(x)$ in the explored valence region, as illustrated in Fig. 6.19. As a result, the effect on the asymmetry is negligible.

To estimate the effect of neglecting the sea quarks to get Eq. (6.22), we have used a different expression, which takes into account the sea quarks as well,

$$A_{\text{T}}^{\sin \phi_{\text{S}} \frac{q_{\text{T}}}{M_{\text{p}}}}(x_N) = 2 \frac{\frac{4}{9} f_{1\text{T},\text{p}}^{\perp(1)\text{u}}(x_N) f_{1,\pi^-}^{\bar{\text{u}}}(x_\pi) + \frac{1}{9} f_{1\text{T},\text{p}}^{\perp(1)\text{d}}(x_N) f_{1,\pi^-}^{\bar{\text{d}}}(x_\pi)}{\sum_{q=\text{u,d,\bar{u},\bar{d}}} e_q^2 f_{1,\text{p}}^q(x_N) f_{1,\pi^-}^q(x_\pi)}. \quad (6.25)$$

The unpolarised PDFs of pion are taken from GRV-PI parametrisation [157], implemented in the LHAPDF 6 library. They are shown in Fig. 6.17(a). We take the pion PDF at $\langle x_\pi \rangle = 0.5$ and $Q^2 = Q_{\text{DY}}^2(x_N)$. The effect on the weighted Siversons asymmetry is shown in Fig. 6.17(b). The difference rises towards smaller x , but in our kinematic range it stays within the statistical uncertainty. As a result, the valence approximation is justified and the uncertainty coming from the pion PDFs cancels in the weighted Siversons asymmetry, as claimed in Eq. (6.22). Note, that a priori this is not the case in the standard asymmetry, where the functions appear in convolution over the transverse momenta.

The radiative \mathbf{k}_{T} -broadening has been considered as well. It is known that the width of the q_{T} distribution measured in Drell–Yan depends on the centre-of-mass energy squared s . Similar dependency was observed between the distributions of P_{hT} measured in SIDIS at different s . The effect can be explained as intrinsic momentum broadening due to gluon radiation [144]. The COMPASS SIDIS data have $s \approx 300 (\text{GeV})^2$, while the Drell–Yan experiment was done at $s = 357 (\text{GeV})^2$. In Ref. [144], the broadening is approximated by a linear function of s , giving

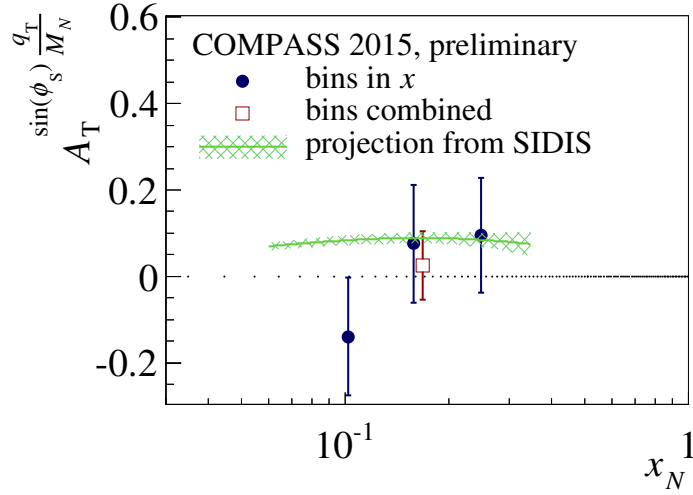


Figure 6.16: The q_T -weighted Siverts asymmetry in Drell–Yan reaction measured in the 2015 data, and the projection based on the P_{hT}/z -weighted Siverts asymmetry in SIDIS.

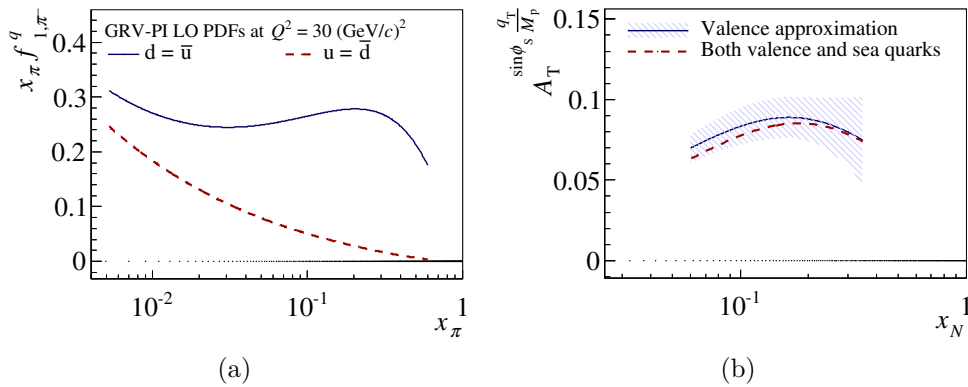


Figure 6.17: (a) Pion PDFs from the GRV-PI parametrisation [157]. (b) The continuous line shows the q_T -weighted Siverts asymmetry in Drell–Yan using Eq. (6.22). The dashed line shows the result obtained using Eq. (6.25).

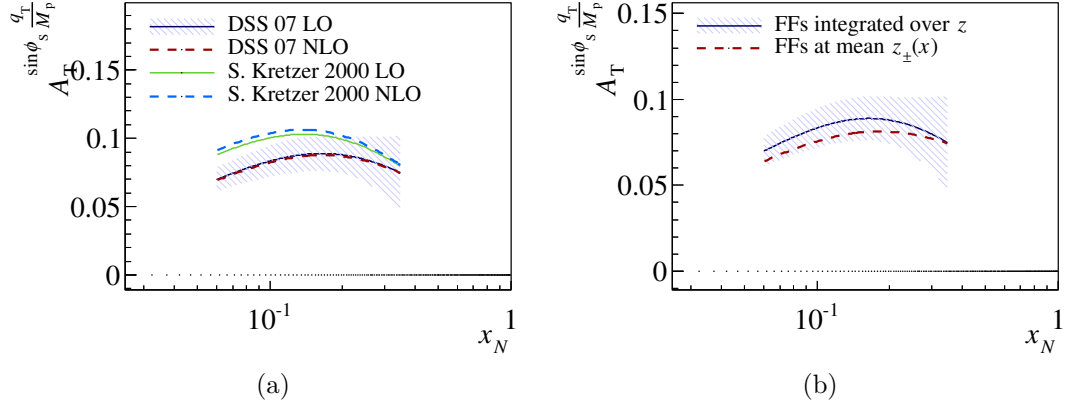


Figure 6.18: The impact of the FF-related choices made in the Siverson function extraction on the Drell–Yan projection. (a) Alternative FF sets: DSS [151] and Kretzer [155]. (b) FFs integrated over z and taken at $z = z_{\pm}(x)$.

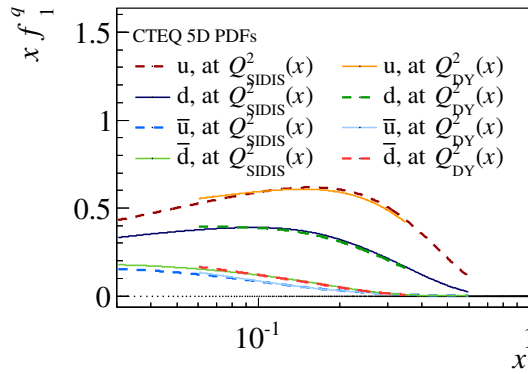


Figure 6.19: The unpolarised PDFs at $Q_{\text{SIDIS}}^2(x)$ and $Q_{\text{DY}}^2(x)$ in the valence region.

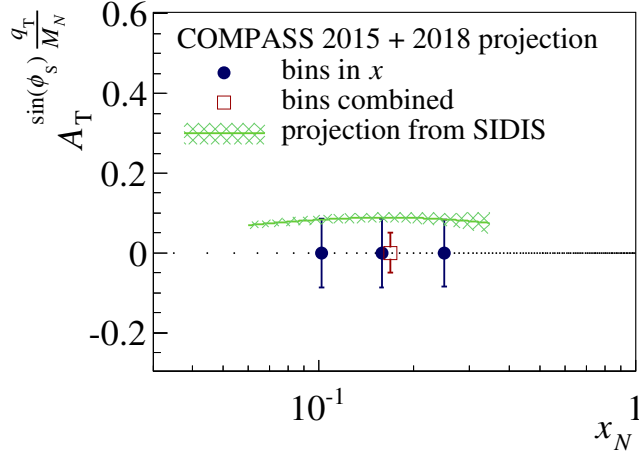


Figure 6.20: The same projection as in Fig. 6.16, but for the foreseen combined analysis of 2015 and 2018 data. Only the statistical uncertainties are shown.

$\langle \mathbf{k}_T^2 \rangle_{s=300 \text{ GeV}^2} - \langle \mathbf{k}_T^2 \rangle_{s=357 \text{ GeV}^2} = 0.04 (\text{GeV}/c)^2$. Thus, the impact of this effect is not expected to be large.

Finally, all the relevant variations seen in the systematic tests on the extracted first moment of the Sivers function, described in Sec. 6.2, have been propagated to the calculated Sivers asymmetry in Drell–Yan. Namely, the effects due to the choice of FF set and to the calculation of $\tilde{D}_{1,q}^{h^\pm}(Q^2)$. They are shown in Fig. 6.18. The differences are comparable to the statistical uncertainty, the larger one coming from the FF set variation.

To conclude, although the expected asymmetry is slightly larger than the one observed in positive hadron production in SIDIS, the Drell–Yan data point is still compatible with all the hypotheses of sign-change, zero asymmetry, and no sign-change. The result is less significant than the standard Sivers asymmetry measured by COMPASS (shown in Fig. 5.3). The reason is the smaller size of the measured asymmetry towards higher q_T which can be noticed in the plot for three bins in q_T . However, it is hard to say if this decrease has any physical meaning or if it is just a statistical fluctuation.

COMPASS is carrying out a second Drell–Yan run in 2018. A projection for combined analysis of the two runs is shown in Fig. 6.20, assuming the statistics in 2018 to be 1.5 times larger than in 2015. That is a conservative estimate, as much shorter commissioning of the apparatus and significantly better data taking stability are expected. In the combined analysis, the prospect to test the sign-change hypothesis is more realistic.

Conclusion

The transverse spin and transverse momentum dependent structure (the so-called 3D structure) of the nucleon is a relatively new and very exciting field of hadronic physics, which is being investigated by a world-wide community involving both theoreticians and experimentalists of several laboratories. Information on the 3D structure is encoded in the transverse momentum dependent (TMD) parton distributions, recently introduced as an extension to the parton model. The new transverse spin asymmetries (TSAs), measured since 2005 in SIDIS by the COMPASS and HERMES experiments, have demonstrated that the transversity distribution, as well as the Sivers function, the most famous of the TMD PDFs, and the Collins TMD fragmentation function, are different from zero. Together with the evidence of the non-zero Collins FF coming from Belle e^+e^- experiment, they constitute a strong support for the TMD framework and they have stimulated further theoretical and experimental developments.

On the theory side, one can quote studies of the TMD factorisation in various processes, their QCD evolution and their universality. In particular, the Sivers functions, already extracted from SIDIS data, are expected to have an equal magnitude and opposite sign in SIDIS and Drell–Yan processes. An experimental verification of this sign change is a critical test for the TMD framework. On the experimental side, new measurements are being performed and proposed at COMPASS, RHIC, and FNAL. At Jefferson Lab, an upgrade raising the beam energy to $12 \text{ GeV}/c^2$ has been just finished, and a new Electron–ion collider (EIC), which would significantly extend the frontiers of the field, is being proposed.

In this context, COMPASS has given and is continuing to bring relevant contributions to the understanding of the hadron structure. This work is part of this effort and is focused on two specific topics: the gluon Sivers function, accessed in J/ψ leptonproduction, and the study of the Drell–Yan process in $\pi^- p^\uparrow \rightarrow \mu^- \mu^+ X$, which is the central part of the work.

Sivers-like asymmetry in J/ψ leptonproduction

The open questions of the experimental TMD physics include also the TMD PDFs of sea quarks and gluons. Among the transverse-spin-dependent TMDs of gluons, only the Sivers function has been experimentally accessed so far. PHENIX has measured an asymmetry compatible with zero in open heavy flavour production in pp^\uparrow collisions, however, the interpretation is difficult. COMPASS has studied hadron pair production in SIDIS on transversely polarised protons and deuterons $\mu N^\uparrow \rightarrow \mu' 2hX$, finding a clearly negative signal for a Sivers-like asymmetry. In this thesis, a complementary channel, namely the J/ψ production, has been studied using the same data.

In lepton–nucleon scattering, the sub-leading hard process of photon–gluon fusion (PGF) $\gamma^* g \rightarrow q\bar{q}$ gives access to the distribution of gluons. The main problem in utilising the PGF is the background consisting of the leading process $\gamma^* q \rightarrow q$ and the QCD Compton process $\gamma^* q \rightarrow qg$. The background can be reduced by selecting hadron pairs with large transverse momentum or hadrons containing heavy quarks in the final state. Thus the leptonproduction of J/ψ on transversely polarised protons has been proposed as a probe for the gluon Sivers

function.

In this work, this process has been studied in two bins of the diquark energy fraction z passed to the J/ψ . The Sivers-like asymmetry, measured for the first time in this process, is -0.05 ± 0.33 at $z < 0.95$ and -0.28 ± 0.18 at $z > 0.95$. The negative value of the asymmetry is in line with the dihadron measurement and with the model predictions. The relative uncertainty of the measurement is, however, large. Questions remain regarding the fraction of J/ψ 's originating from the PGF. In particular, in the higher z bin a diffractive contribution is expected. A future improvement of this exploratory study could be achieved utilising cuts to control the diffractive component. However, more data are needed for this purpose. The available COMPASS data would not bring a significant improvement, but a new high-statistics run with deuteron target is foreseen in 2021. In the event of such re-analysis, one could look in addition into other azimuthal modulations, including the target-spin-independent ones and those, depending on the the orientation of the J/ψ decay plane. The latter could help to restrict the J/ψ production models and possibly show hints of gluonic Boer–Mulders function. Obviously, these studies could be done with much more statistics at the future EIC.

Transverse-momentum-weighted asymmetries in Drell–Yan process

Concerning the sign change of the Sivers function, STAR experiment has measured a Sivers asymmetry in $pp^\uparrow \rightarrow W^\pm X$ and $pp^\uparrow \rightarrow Z^0 X$, hinting towards the sign change. However, the predictions for the asymmetry strongly depend on the scale evolution scenarios. COMPASS has measured the Sivers asymmetry in the Drell–Yan reaction with a transversely polarised target, $\pi^- p^\uparrow \rightarrow \mu^- \mu^+ X$. The measured asymmetry is positive by one standard deviation, pointing towards the sign change as well. In this work, a new approach consisting in the measurement of the transverse-momentum-weighted TSAs has been used. In the extraction of the TMD PDFs from the measured asymmetries one faces the problem of the convolution over parton intrinsic transverse momenta \mathbf{k}_T , which can be overcome by employing a certain functional form of the \mathbf{k}_T -dependent part of the TMD PDF or by weighting of the spin-dependent part of the cross-section with appropriate powers of the outgoing particle transverse momentum. In the Drell–Yan process, the weights contain the dimuon transverse momentum q_T .

Apart from the q_T -weighted Sivers asymmetry, which was the main objective, the other two leading-twist TSA have been measured from the COMPASS 2015 Drell–Yan data as well. The asymmetry $A_T^{\sin(2\phi+\phi_S)q_T^3/(2M_\pi M_N^2)}$ is interpreted in terms of products of the first \mathbf{k}_T^2 -moment of the Boer–Mulders PDF of the pion and of the second moment of the pretzelosity PDF of the proton. We have obtained the value $A_T^{\sin(2\phi+\phi_S)q_T^3/(2M_\pi M_N^2)} = 3.7 \pm 2.9$ (stat.) ± 2.0 (syst.). This asymmetry depends on two almost unknown TMD PDFs and the result gives no clear evidence for non-zero values.

In the TMD framework, the asymmetry $A_T^{\sin(2\phi-\phi_S)q_T/M_\pi}$ is related to products of the transversity PDF of the proton $h_{1,p}(x_N)$ and of the first \mathbf{k}_T^2 -moment of the Boer–Mulders PDF of the pion $h_{1,\pi}^{\perp(1)}(x_\pi)$. The measured value is $A_T^{\sin(2\phi-\phi_S)q_T/M_\pi} = -1.59 \pm 0.74$ (stat.) ± 0.52 (syst.). Using this result and the transversity distribution extracted from Collins and dihadron asymmetries in SIDIS, we have ob-

tained $h_{1,\pi}^{\perp(1)\bar{u}}/f_{1,\pi}^{\bar{u}} = 3.1 \pm 1.4$. Assuming in addition the Boer–Mulders function to be proportional to the unpolarised TMD PDF $f_{1,\pi}^{\bar{u}}(x_\pi, k_{\pi T}^2)$ and employing the Gaussian model for the \mathbf{k}_T^2 -dependent part of $f_{1,\pi}^{\bar{u}}$, we have derived $h_{1,\pi}^{\perp(1)\bar{u}}(x_\pi, k_{\pi T}^2) = (0.12 \pm 0.05)f_{1,\pi}^{\bar{u}}(x_\pi, k_{\pi T}^2)$.

The measured value of the weighted Siverts asymmetry is $A_T^{\sin \phi_S q_T/M_N} = 0.025 \pm 0.079$ (stat.) ± 0.055 (syst.), which, compared with the expected value given in the following, is well compatible with all the hypotheses of sign-change, zero asymmetry, and no sign-change. The result is less significant than the standard Siverts asymmetry measured by COMPASS, which can be understood as a decrease of the asymmetry towards higher q_T . However, it is hard to say if this decrease has any physical meaning or if it is just a statistical fluctuation.

Having measured the Drell–Yan weighted Siverts asymmetry, it is natural to compare it with the value predicted in the TMD framework. We have done it utilising the Siverts function extracted from the transverse-momentum-weighted Siverts asymmetries measured in SIDIS. In SIDIS, the P_{hT} -weighted asymmetries are related to products of \mathbf{k}_T^2 -moments of the TMD PDFs and FFs, not to their convolutions. Recently, COMPASS has measured the P_{hT}/z -weighted Siverts asymmetries on protons. In this thesis, the asymmetries are fitted using parametrisations of the first \mathbf{k}_T^2 -moments of the valence quark Siverts function. Thus the first moments of the Siverts function versus x are extracted at Q^2 values of the experiment, which depend on x . This is the first time that the u and d Siverts functions are determined from the weighted TSAs, exploiting their straightforward interpretation and avoiding all the problems related to the convolution over the transverse momenta. The result, compatible with previous Siverts function extractions, is utilised to get a projection for Drell–Yan in a direct way. No evolution is considered, as the Q^2 of the two measurements are different by a factor less than three. The predicted value of the q_T -weighted Siverts asymmetry in Drell–Yan averaged over the available kinematic range is about 0.085 ± 0.015 , where the uncertainty is just statistical. Several tests have been made in order to estimate the systematic uncertainty finding differences of at most 0.02, i.e. at the level of the statistical uncertainty.

The method of weighted asymmetries has proved itself to be useful, as it offers straightforward interpretations of the measured quantities in the TMD framework. A second COMPASS Drell–Yan run is taking place in 2018, when a sample at least 1.5 times larger than the present one is expected to be collected. Given the calculation of the value of the weighted Siverts asymmetry obtained here, in the combined analysis of the two runs the prospect to test the hypothesis of the sign-change of the Siverts function looks quite realistic.

Bibliography

- [1] V. Barone, A. Drago, and P. G. Ratcliffe. Transverse polarisation of quarks in hadrons. *Phys. Rept.*, 359, 1–168, 2002. doi: [10.1016/S0370-1573\(01\)00051-5](https://doi.org/10.1016/S0370-1573(01)00051-5), [arXiv:hep-ph/0104283](https://arxiv.org/abs/hep-ph/0104283) [hep-ph].
- [2] J. Chýla. *Quarks, partons and Quantum Chromodynamics*. Published online, 2009. URL <http://www-hep2.fzu.cz/~chyla/lectures/text.pdf>.
- [3] E. D. Bloom et al. High-Energy Inelastic e p Scattering at 6-Degrees and 10-Degrees. *Phys. Rev. Lett.*, 23, 930–934, 1969. doi: [10.1103/PhysRevLett.23.930](https://doi.org/10.1103/PhysRevLett.23.930).
- [4] Martin Breidenbach et al. Observed Behavior of Highly Inelastic electron-Proton Scattering. *Phys. Rev. Lett.*, 23, 935–939, 1969. doi: [10.1103/PhysRevLett.23.935](https://doi.org/10.1103/PhysRevLett.23.935).
- [5] J. D. Bjorken and E. A. Paschos. Inelastic Electron Proton and gamma Proton Scattering, and the Structure of the Nucleon. *Phys. Rev.*, 185, 1975–1982, 1969. doi: [10.1103/PhysRev.185.1975](https://doi.org/10.1103/PhysRev.185.1975).
- [6] J. P. Ralston and D. E. Soper. Production of Dimuons from High-Energy Polarized Proton Proton Collisions. *Nucl. Phys.*, B152, 109, 1979. doi: [10.1016/0550-3213\(79\)90082-8](https://doi.org/10.1016/0550-3213(79)90082-8).
- [7] J. C. Collins. Fragmentation of transversely polarized quarks probed in transverse momentum distributions. *Nucl. Phys.*, B396, 161–182, 1993. doi: [10.1016/0550-3213\(93\)90262-N](https://doi.org/10.1016/0550-3213(93)90262-N), [arXiv:hep-ph/9208213](https://arxiv.org/abs/hep-ph/9208213) [hep-ph].
- [8] J. Soffer. Positivity constraints for spin dependent parton distributions. *Phys. Rev. Lett.*, 74, 1292–1294, 1995. doi: [10.1103/PhysRevLett.74.1292](https://doi.org/10.1103/PhysRevLett.74.1292), [arXiv:hep-ph/9409254](https://arxiv.org/abs/hep-ph/9409254) [hep-ph].
- [9] D. W. Sivers. Single Spin Production Asymmetries from the Hard Scattering of Point-Like Constituents. *Phys. Rev.*, D41, 83, 1990. doi: [10.1103/PhysRevD.41.83](https://doi.org/10.1103/PhysRevD.41.83).
- [10] M. Burkardt, C. A. Miller, and W. D. Nowak. Spin-polarized high-energy scattering of charged leptons on nucleons. *Rept. Prog. Phys.*, 73, 016201, 2010. doi: [10.1088/0034-4885/73/1/016201](https://doi.org/10.1088/0034-4885/73/1/016201), [arXiv:0812.2208](https://arxiv.org/abs/0812.2208) [hep-ph].
- [11] J. C. Collins. Leading twist single transverse-spin asymmetries: Drell–Yan and deep inelastic scattering. *Phys. Lett.*, B536, 43–48, 2002. doi: [10.1016/S0370-2693\(02\)01819-1](https://doi.org/10.1016/S0370-2693(02)01819-1), [arXiv:hep-ph/0204004](https://arxiv.org/abs/hep-ph/0204004) [hep-ph].
- [12] M. Burkardt. Chromodynamic lensing and transverse single spin asymmetries. *Nucl. Phys.*, A735, 185–199, 2004. doi: [10.1016/j.nuclphysa.2004.02.008](https://doi.org/10.1016/j.nuclphysa.2004.02.008), [arXiv:hep-ph/0302144](https://arxiv.org/abs/hep-ph/0302144) [hep-ph].
- [13] V. N. Gribov and L. N. Lipatov. Deep inelastic e p scattering in perturbation theory. *Sov. J. Nucl. Phys.*, 15, 438–450, 1972. [*Yad. Fiz.*15,781(1972)].

- [14] G. Altarelli and G. Parisi. Asymptotic Freedom in Parton Language. *Nucl. Phys.*, B126, 298–318, 1977. doi: [10.1016/0550-3213\(77\)90384-4](https://doi.org/10.1016/0550-3213(77)90384-4).
- [15] Y. L. Dokshitzer. Calculation of the Structure Functions for Deep Inelastic Scattering and e^+e^- Annihilation by Perturbation Theory in Quantum Chromodynamics. *Sov. Phys. JETP*, 46, 641–653, 1977. [*Zh. Eksp. Teor. Fiz.*73,1216(1977)].
- [16] S. M. Aybat and T. C. Rogers. TMD Parton Distribution and Fragmentation Functions with QCD Evolution. *Phys. Rev.*, D83, 114042, 2011. doi: [10.1103/PhysRevD.83.114042](https://doi.org/10.1103/PhysRevD.83.114042), [arXiv:1101.5057](https://arxiv.org/abs/1101.5057) [[hep-ph](#)].
- [17] S. J. Brodsky, D. S. Hwang, and I. Schmidt. Final state interactions and single spin asymmetries in semiinclusive deep inelastic scattering. *Phys. Lett.*, B530, 99–107, 2002. doi: [10.1016/S0370-2693\(02\)01320-5](https://doi.org/10.1016/S0370-2693(02)01320-5), [arXiv:hep-ph/0201296](https://arxiv.org/abs/hep-ph/0201296) [[hep-ph](#)].
- [18] D. Boer, P. J. Mulders, C. Pisano, and J. Zhou. Asymmetries in Heavy Quark Pair and Dijet Production at an EIC. *JHEP*, 08, 001, 2016. doi: [10.1007/JHEP08\(2016\)001](https://doi.org/10.1007/JHEP08(2016)001), [arXiv:1605.07934](https://arxiv.org/abs/1605.07934) [[hep-ph](#)].
- [19] D. Boer, C. Lorcé, C. Pisano, and J. Zhou. The gluon Sivers distribution: status and future prospects. *Adv. High Energy Phys.*, 2015, 371396, 2015. doi: [10.1155/2015/371396](https://doi.org/10.1155/2015/371396), [arXiv:1504.04332](https://arxiv.org/abs/1504.04332) [[hep-ph](#)].
- [20] U. D’Alesio, F. Murgia, and C. Pisano. Towards a first estimate of the gluon Sivers function from A_N data in pp collisions at RHIC. *JHEP*, 09, 119, 2015. doi: [10.1007/JHEP09\(2015\)119](https://doi.org/10.1007/JHEP09(2015)119), [arXiv:1506.03078](https://arxiv.org/abs/1506.03078) [[hep-ph](#)].
- [21] A. Mukherjee and S. Rajesh. J/ψ Production in Polarized and Unpolarized ep Collision and Sivers and $\cos 2\phi$ Asymmetries. 2016, [arXiv:1609.05596](https://arxiv.org/abs/1609.05596) [[hep-ph](#)].
- [22] A. Bacchetta et al. Semi-inclusive deep inelastic scattering at small transverse momentum. *J. High Energy Phys.*, 02, 093, 2007. doi: [10.1088/1126-6708/2007/02/093](https://doi.org/10.1088/1126-6708/2007/02/093), [arXiv:hep-ph/0611265](https://arxiv.org/abs/hep-ph/0611265).
- [23] F. Bradamante (COMPASS Coll.). COMPASS measurement of the P_T weighted Sivers asymmetry. In *Proceedings of the 22nd International Spin Symposium, Urbana-Champaign, USA*, 2017, [arXiv:1702.00621](https://arxiv.org/abs/1702.00621) [[hep-ex](#)].
- [24] A. Martin, F. Bradamante, and V. Barone. Direct extraction of the Sivers distributions from spin asymmetries in pion and kaon lepton production. *Phys. Rev.*, D95(9), 094024, 2017. doi: [10.1103/PhysRevD.95.094024](https://doi.org/10.1103/PhysRevD.95.094024), [arXiv:1701.08283](https://arxiv.org/abs/1701.08283) [[hep-ph](#)].
- [25] S. Arnold, A. Metz, and M. Schlegel. Dilepton production from polarized hadron hadron collisions. *Phys. Rev.*, D79, 034005, 2009. doi: [10.1103/PhysRevD.79.034005](https://doi.org/10.1103/PhysRevD.79.034005), [arXiv:0809.2262](https://arxiv.org/abs/0809.2262) [[hep-ph](#)].

- [26] A. Bacchetta, U. D’Alesio, M. Diehl, and C. A. Miller. Single-spin asymmetries: The Trento conventions. *Phys. Rev.*, D70, 117504, 2004. doi: [10.1103/PhysRevD.70.117504](https://doi.org/10.1103/PhysRevD.70.117504), [arXiv:hep-ph/0410050](https://arxiv.org/abs/hep-ph/0410050) [hep-ph].
- [27] B. Adeva et al. (Spin Muon Coll.). Spin asymmetries for events with high $p(T)$ hadrons in DIS and an evaluation of the gluon polarization. *Phys. Rev.*, D70, 012002, 2004. doi: [10.1103/PhysRevD.70.012002](https://doi.org/10.1103/PhysRevD.70.012002), [arXiv:hep-ex/0402010](https://arxiv.org/abs/hep-ex/0402010) [hep-ex].
- [28] C. Adolph et al. (COMPASS Coll.). Leading order determination of the gluon polarisation from DIS events with high- p_T hadron pairs. *Phys. Lett.*, B718, 922–930, 2013. doi: [10.1016/j.physletb.2012.11.056](https://doi.org/10.1016/j.physletb.2012.11.056), [arXiv:1202.4064](https://arxiv.org/abs/1202.4064) [hep-ex].
- [29] C. Adolph et al. (COMPASS Coll.). Leading-order determination of the gluon polarisation from semi-inclusive deep inelastic scattering data. *Eur. Phys. J.*, C77(4), 209, 2017. doi: [10.1140/epjc/s10052-017-4716-x](https://doi.org/10.1140/epjc/s10052-017-4716-x), [arXiv:1512.05053](https://arxiv.org/abs/1512.05053) [hep-ex].
- [30] C. Adolph et al. (COMPASS Coll.). First measurement of the Sivers asymmetry for gluons using SIDIS data. *Phys. Lett.*, B772, 854–864, 2017. doi: [10.1016/j.physletb.2017.07.018](https://doi.org/10.1016/j.physletb.2017.07.018), [arXiv:1701.02453](https://arxiv.org/abs/1701.02453) [hep-ex].
- [31] A. Szabelski. *The gluon contribution to the Sivers effect measurement at the COMPASS experiment*. PhD thesis, National Centre of Nuclear Research, Warsaw, Poland, 2016. URL http://wwwcompass.cern.ch/compass/publications/theses/2016_phd_szabelski.pdf.
- [32] G. Altarelli and G. G. Ross. The Anomalous Gluon Contribution to Polarized Lepton Production. *Phys. Lett.*, B212, 391–396, 1988. doi: [10.1016/0370-2693\(88\)91335-4](https://doi.org/10.1016/0370-2693(88)91335-4).
- [33] M. Glück and E. Reya. Spin Dependent Parton Distributions in Polarized Deep Inelastic Lepton Nucleon Scattering. *Z. Phys.*, C39, 569, 1988. doi: [10.1007/BF01555989](https://doi.org/10.1007/BF01555989).
- [34] C. Adolph et al. (COMPASS Coll.). Leading and Next-to-Leading Order Gluon Polarization in the Nucleon and Longitudinal Double Spin Asymmetries from Open Charm Muoproduction. *Phys. Rev.*, D87(5), 052018, 2013. doi: [10.1103/PhysRevD.87.052018](https://doi.org/10.1103/PhysRevD.87.052018), [arXiv:1211.6849](https://arxiv.org/abs/1211.6849) [hep-ex].
- [35] E. Braaten and S. Fleming. Color octet fragmentation and the psi-prime surplus at the Tevatron. *Phys. Rev. Lett.*, 74, 3327–3330, 1995. doi: [10.1103/PhysRevLett.74.3327](https://doi.org/10.1103/PhysRevLett.74.3327), [arXiv:hep-ph/9411365](https://arxiv.org/abs/hep-ph/9411365) [hep-ph].
- [36] J. Amundson, O. Eboli, E. Gregores, and F. Halzen. Colorless states in perturbative QCD: Charmonium and rapidity gaps. *Phys. Lett.*, B372, 127–132, 1996. doi: [10.1016/0370-2693\(96\)00035-4](https://doi.org/10.1016/0370-2693(96)00035-4), [arXiv:hep-ph/9512248](https://arxiv.org/abs/hep-ph/9512248) [hep-ph].

- [37] R. M. Godbole, A. Misra, A. Mukherjee, and V. S. Rawoot. Siverts Effect and Transverse Single Spin Asymmetry in $e+p^\dagger \rightarrow e+J/\psi+X$. *Phys. Rev.*, D85, 094013, 2012. doi: [10.1103/PhysRevD.85.094013](https://doi.org/10.1103/PhysRevD.85.094013), [arXiv:1201.1066](https://arxiv.org/abs/1201.1066) [hep-ph].
- [38] G. T. Bodwin, E. Braaten, and G. P. Lepage. Rigorous QCD analysis of inclusive annihilation and production of heavy quarkonium. *Phys. Rev.*, D51, 1125–1171, 1995. doi: [10.1103/PhysRevD.55.5853](https://doi.org/10.1103/PhysRevD.55.5853), [10.1103/PhysRevD.51.1125](https://doi.org/10.1103/PhysRevD.51.1125), [arXiv:hep-ph/9407339](https://arxiv.org/abs/hep-ph/9407339) [hep-ph]. [Erratum: *Phys. Rev. D*55,5853(1997)].
- [39] M. Cacciari and M. Krämer. Color octet contributions to J/ψ photoproduction. *Phys. Rev. Lett.*, 76, 4128–4131, 1996. doi: [10.1103/PhysRevLett.76.4128](https://doi.org/10.1103/PhysRevLett.76.4128), [arXiv:hep-ph/9601276](https://arxiv.org/abs/hep-ph/9601276) [hep-ph].
- [40] R. M. Godbole, A. Misra, A. Mukherjee, and V. S. Rawoot. Transverse Single Spin Asymmetry in $e+p^\dagger \rightarrow e+J/\psi+X$ and Transverse Momentum Dependent Evolution of the Siverts Function. *Phys. Rev.*, D88(1), 014029, 2013. doi: [10.1103/PhysRevD.88.014029](https://doi.org/10.1103/PhysRevD.88.014029), [arXiv:1304.2584](https://arxiv.org/abs/1304.2584) [hep-ph].
- [41] S. D. Drell and T.-M. Yan. Massive Lepton Pair Production in Hadron-Hadron Collisions at High-Energies. *Phys. Rev. Lett.*, 25, 316–320, 1970. doi: [10.1103/PhysRevLett.25.316](https://doi.org/10.1103/PhysRevLett.25.316). [Erratum: *Phys. Rev. Lett.*25,902(1970)].
- [42] C. S. Lam and W.-K. Tung. A Systematic Approach to Inclusive Lepton Pair Production in Hadronic Collisions. *Phys. Rev.*, D18, 2447, 1978. doi: [10.1103/PhysRevD.18.2447](https://doi.org/10.1103/PhysRevD.18.2447).
- [43] C. S. Lam and W.-K. Tung. A Parton Model Relation Sans QCD Modifications in Lepton Pair Productions. *Phys. Rev.*, D21, 2712, 1980. doi: [10.1103/PhysRevD.21.2712](https://doi.org/10.1103/PhysRevD.21.2712).
- [44] S. Falciano et al. (NA10 Coll.). Angular Distributions of Muon Pairs Produced by 194-GeV/c Negative Pions. *Z. Phys.*, C31, 513, 1986. doi: [10.1007/BF01551072](https://doi.org/10.1007/BF01551072).
- [45] M. Guanziroli et al. (NA10 Coll.). Angular Distributions of Muon Pairs Produced by Negative Pions on Deuterium and Tungsten. *Z. Phys.*, C37, 545, 1988. doi: [10.1007/BF01549713](https://doi.org/10.1007/BF01549713).
- [46] J. S. Conway et al. Experimental Study of Muon Pairs Produced by 252-GeV Pions on Tungsten. *Phys. Rev.*, D39, 92–122, 1989. doi: [10.1103/PhysRevD.39.92](https://doi.org/10.1103/PhysRevD.39.92).
- [47] D. Boer. Investigating the origins of transverse spin asymmetries at RHIC. *Phys. Rev.*, D60, 014012, 1999. doi: [10.1103/PhysRevD.60.014012](https://doi.org/10.1103/PhysRevD.60.014012), [arXiv:hep-ph/9902255](https://arxiv.org/abs/hep-ph/9902255) [hep-ph].
- [48] L. Y. Zhu et al. (NuSea Coll.). Measurement of Angular Distributions of Drell-Yan Dimuons in $p + d$ Interaction at 800-GeV/c. *Phys. Rev. Lett.*, 99, 082301, 2007. doi: [10.1103/PhysRevLett.99.082301](https://doi.org/10.1103/PhysRevLett.99.082301), [arXiv:hep-ex/0609005](https://arxiv.org/abs/hep-ex/0609005) [hep-ex].

- [49] L. Y. Zhu et al. (NuSea Coll.). Measurement of Angular Distributions of Drell-Yan Dimuons in $p + p$ Interactions at 800-GeV/c. *Phys. Rev. Lett.*, 102, 182001, 2009. doi: [10.1103/PhysRevLett.102.182001](https://doi.org/10.1103/PhysRevLett.102.182001), [arXiv:0811.4589](https://arxiv.org/abs/0811.4589) [nucl-ex].
- [50] M. Lambertsen and W. Vogelsang. Drell-Yan lepton angular distributions in perturbative QCD. *Phys. Rev.*, D93(11), 114013, 2016. doi: [10.1103/PhysRevD.93.114013](https://doi.org/10.1103/PhysRevD.93.114013), [arXiv:1605.02625](https://arxiv.org/abs/1605.02625) [hep-ph].
- [51] K. Nakano (E906/SeaQuest Coll.). Measurement of Boer-Mulders Function via Drell-Yan Process by SeaQuest Experiment at Fermilab. *Int. J. Mod. Phys. Conf. Ser.*, 40, 1660041, 2016. doi: [10.1142/S2010194516600417](https://doi.org/10.1142/S2010194516600417).
- [52] C. Patrignani et al. (Particle Data Group Coll.). Review of Particle Physics. *Chin. Phys.*, C40(10), 100001, 2016. doi: [10.1088/1674-1137/40/10/100001](https://doi.org/10.1088/1674-1137/40/10/100001). URL <http://pdg.lbl.gov/2017>.
- [53] E. R. Nocera. Collinear polarised PDFs: recent results on helicity and transversity extractions. Presented at *5th International Workshop on Transverse Polarization Phenomena in Hard Processes, Frascati, Italy, 11–15 December 2017*. URL <https://agenda.infn.it/conferenceOtherViews.py?confId=12263>.
- [54] D. de Florian, R. Sassot, M. Stratmann, and W. Vogelsang. Evidence for polarization of gluons in the proton. *Phys. Rev. Lett.*, 113(1), 012001, 2014. doi: [10.1103/PhysRevLett.113.012001](https://doi.org/10.1103/PhysRevLett.113.012001), [arXiv:1404.4293](https://arxiv.org/abs/1404.4293) [hep-ph].
- [55] E. R. Nocera, R. D. Ball, S. Forte, G. Ridolfi, and J. Rojo (NNPDF Coll.). A first unbiased global determination of polarized PDFs and their uncertainties. *Nucl. Phys.*, B887, 276–308, 2014. doi: [10.1016/j.nuclphysb.2014.08.008](https://doi.org/10.1016/j.nuclphysb.2014.08.008), [arXiv:1406.5539](https://arxiv.org/abs/1406.5539) [hep-ph].
- [56] J. J. Ethier, N. Sato, and W. Melnitchouk. First simultaneous extraction of spin-dependent parton distributions and fragmentation functions from a global QCD analysis. *Phys. Rev. Lett.*, 119(13), 132001, 2017. doi: [10.1103/PhysRevLett.119.132001](https://doi.org/10.1103/PhysRevLett.119.132001), [arXiv:1705.05889](https://arxiv.org/abs/1705.05889) [hep-ph].
- [57] A. Airapetian et al. (HERMES Coll.). Single-spin asymmetries in semi-inclusive deep-inelastic scattering on a transversely polarized hydrogen target. *Phys. Rev. Lett.*, 94, 012002, 2005. doi: [10.1103/PhysRevLett.94.012002](https://doi.org/10.1103/PhysRevLett.94.012002), [arXiv:hep-ex/0408013](https://arxiv.org/abs/hep-ex/0408013) [hep-ex].
- [58] V. Yu. Alexakhin et al. (COMPASS Coll.). First measurement of the transverse spin asymmetries of the deuteron in semi-inclusive deep inelastic scattering. *Phys. Rev. Lett.*, 94, 202002, 2005. doi: [10.1103/PhysRevLett.94.202002](https://doi.org/10.1103/PhysRevLett.94.202002), [arXiv:hep-ex/0503002](https://arxiv.org/abs/hep-ex/0503002).
- [59] K. Abe et al. (Belle Coll.). Measurement of azimuthal asymmetries in inclusive production of hadron pairs in e^+e^- annihilation at Belle. *Phys. Rev. Lett.*, 96, 232002, 2006. doi: [10.1103/PhysRevLett.96.232002](https://doi.org/10.1103/PhysRevLett.96.232002), [arXiv:hep-ex/0507063](https://arxiv.org/abs/hep-ex/0507063) [hep-ex].

- [60] M. Anselmino et al. Transversity and Collins functions from SIDIS and e^+e^- data. *Phys. Rev.*, D75, 054032, 2007. doi: [10.1103/PhysRevD.75.054032](https://doi.org/10.1103/PhysRevD.75.054032), [arXiv:hep-ph/0701006](https://arxiv.org/abs/hep-ph/0701006) [hep-ph].
- [61] A. Bacchetta, A. Courtoy, and M. Radici. First glances at the transversity parton distribution through dihadron fragmentation functions. *Phys. Rev. Lett.*, 107, 012001, 2011. doi: [10.1103/PhysRevLett.107.012001](https://doi.org/10.1103/PhysRevLett.107.012001), [arXiv:1104.3855](https://arxiv.org/abs/1104.3855) [hep-ph].
- [62] C. Adolph et al. (COMPASS Coll.). Experimental investigation of transverse spin asymmetries in μ -p SIDIS processes: Collins asymmetries. *Phys. Lett.*, B717, 376–382, 2012. doi: [10.1016/j.physletb.2012.09.055](https://doi.org/10.1016/j.physletb.2012.09.055), [arXiv:1205.5121](https://arxiv.org/abs/1205.5121) [hep-ex].
- [63] C. Adolph et al. (COMPASS Coll.). A high-statistics measurement of transverse spin effects in dihadron production from muon-proton semi-inclusive deep-inelastic scattering. *Phys. Lett.*, B736, 124–131, 2014. doi: [10.1016/j.physletb.2014.06.080](https://doi.org/10.1016/j.physletb.2014.06.080), [arXiv:1401.7873](https://arxiv.org/abs/1401.7873) [hep-ex].
- [64] A. Martin, F. Bradamante, and V. Barone. Extracting the transversity distributions from single-hadron and dihadron production. *Phys. Rev.*, D91 (1), 014034, 2015. doi: [10.1103/PhysRevD.91.014034](https://doi.org/10.1103/PhysRevD.91.014034), [arXiv:1412.5946](https://arxiv.org/abs/1412.5946) [hep-ph].
- [65] C. Adolph et al. (COMPASS Coll.). Interplay among transversity induced asymmetries in hadron leptonproduction. *Phys. Lett.*, B753, 406–411, 2016. doi: [10.1016/j.physletb.2015.12.042](https://doi.org/10.1016/j.physletb.2015.12.042), [arXiv:1507.07593](https://arxiv.org/abs/1507.07593) [hep-ex].
- [66] A. Kerbizi et al. Recursive Monte Carlo code for transversely polarized quark jet. In *22nd International Symposium on Spin Physics (SPIN 2016) Urbana, IL, USA, September 25-30, 2016*, 2017, [arXiv:1701.08543](https://arxiv.org/abs/1701.08543) [hep-ph].
- [67] A. Kerbizi, X. Artru, Z. Belghobsi, F. Bradamante, and A. Martin. A Monte Carlo code for the fragmentation of polarized quarks. *J. Phys. Conf. Ser.*, 938(1), 012051, 2017. doi: [10.1088/1742-6596/938/1/012051](https://doi.org/10.1088/1742-6596/938/1/012051).
- [68] B. Andersson, G. Gustafson, G. Ingelman, and T. Sjostrand. Parton Fragmentation and String Dynamics. *Phys. Rept.*, 97, 31–145, 1983. doi: [10.1016/0370-1573\(83\)90080-7](https://doi.org/10.1016/0370-1573(83)90080-7).
- [69] X. Artru. Recursive fragmentation model with quark spin. Application to quark polarimetry. In *Proc., 13th Advanced Research Workshop on High Energy Spin Physics (DSPIN 09), Dubna, Russia, September 1–5, 2009*, 2010, [arXiv:1001.1061](https://arxiv.org/abs/1001.1061) [hep-ph].
- [70] M. Anselmino et al. Simultaneous extraction of transversity and Collins functions from new SIDIS and e^+e^- data. *Phys. Rev.*, D87, 094019, 2013. doi: [10.1103/PhysRevD.87.094019](https://doi.org/10.1103/PhysRevD.87.094019), [arXiv:1303.3822](https://arxiv.org/abs/1303.3822) [hep-ph].

- [71] M. Anselmino et al. Collins functions for pions from SIDIS and new e^+e^- data: a first glance at their transverse momentum dependence. *Phys. Rev.*, D92(11), 114023, 2015. doi: [10.1103/PhysRevD.92.114023](https://doi.org/10.1103/PhysRevD.92.114023), [arXiv:1510.05389](https://arxiv.org/abs/1510.05389) [hep-ph].
- [72] Z.-B. Kang, A. Prokudin, P. Sun, and F. Yuan. Nucleon tensor charge from Collins azimuthal asymmetry measurements. *Phys. Rev.*, D91, 071501, 2015. doi: [10.1103/PhysRevD.91.071501](https://doi.org/10.1103/PhysRevD.91.071501), [arXiv:1410.4877](https://arxiv.org/abs/1410.4877) [hep-ph].
- [73] Z.-B. Kang, A. Prokudin, P. Sun, and F. Yuan. Extraction of Quark Transversity Distribution and Collins Fragmentation Functions with QCD Evolution. *Phys. Rev.*, D93(1), 014009, 2016. doi: [10.1103/PhysRevD.93.014009](https://doi.org/10.1103/PhysRevD.93.014009), [arXiv:1505.05589](https://arxiv.org/abs/1505.05589) [hep-ph].
- [74] M. Radici, A. Courtoy, A. Bacchetta, and M. Guagnelli. Improved extraction of valence transversity distributions from inclusive dihadron production. *JHEP*, 05, 123, 2015. doi: [10.1007/JHEP05\(2015\)123](https://doi.org/10.1007/JHEP05(2015)123), [arXiv:1503.03495](https://arxiv.org/abs/1503.03495) [hep-ph].
- [75] Friedrich, J and others (COMPASS Coll.). Addendum to the COMPASS-II Proposal for 2021/22: d-Quark Transversity and Proton Radius. Technical Report CERN-SPSC-2017-034, SPSC-P-340-ADD-1, CERN, Geneva, Switzerland, 2010. URL <http://cds.cern.ch/record/2286954>.
- [76] A. Bacchetta, F. Delcarro, C. Pisano, M. Radici, and A. Signori. Extraction of partonic transverse momentum distributions from semi-inclusive deep-inelastic scattering, Drell-Yan and Z-boson production. *JHEP*, 06, 081, 2017. doi: [10.1007/JHEP06\(2017\)081](https://doi.org/10.1007/JHEP06(2017)081), [arXiv:1703.10157](https://arxiv.org/abs/1703.10157) [hep-ph].
- [77] M. Anselmino et al. Comparing extractions of Sivers functions. In *Transversity. Proceedings, Workshop, Como, Italy, September 7-10, 2005*, pages 236–243, 2005. doi: [10.1142/9789812773272_0028](https://doi.org/10.1142/9789812773272_0028), [arXiv:hep-ph/0511017](https://arxiv.org/abs/hep-ph/0511017) [hep-ph].
- [78] C. Adolph et al. (COMPASS Coll.). II – Experimental investigation of transverse spin asymmetries in μ -p SIDIS processes: Sivers asymmetries. *Phys. Lett.*, B717, 383–389, 2012. doi: [10.1016/j.physletb.2012.09.056](https://doi.org/10.1016/j.physletb.2012.09.056), [arXiv:1205.5122](https://arxiv.org/abs/1205.5122) [hep-ex].
- [79] C. Adolph et al. (COMPASS Coll.). Collins and Sivers asymmetries in muonproduction of pions and kaons off transversely polarised protons. *Phys. Lett.*, B744, 250–259, 2015. doi: [10.1016/j.physletb.2015.03.056](https://doi.org/10.1016/j.physletb.2015.03.056), [arXiv:1408.4405](https://arxiv.org/abs/1408.4405) [hep-ex].
- [80] X. Qian et al. (Jefferson Lab Hall A Coll.). Single Spin Asymmetries in Charged Pion Production from Semi-Inclusive Deep Inelastic Scattering on a Transversely Polarized ^3He Target. *Phys. Rev. Lett.*, 107, 072003, 2011. doi: [10.1103/PhysRevLett.107.072003](https://doi.org/10.1103/PhysRevLett.107.072003), [arXiv:1106.0363](https://arxiv.org/abs/1106.0363) [nucl-ex].
- [81] A. Airapetian et al. (HERMES Coll.). Observation of the Naive-T-odd Sivers Effect in Deep-Inelastic Scattering. *Phys. Rev. Lett.*, 103, 152002, 2009. doi: [10.1103/PhysRevLett.103.152002](https://doi.org/10.1103/PhysRevLett.103.152002), [arXiv:0906.3918](https://arxiv.org/abs/0906.3918) [hep-ex].

- [82] M. Anselmino, M. Boglione, U. D’Alesio, F. Murgia, and A. Prokudin. Study of the sign change of the Sivers function from STAR Collaboration W/Z production data. *JHEP*, 04, 046, 2017. doi: [10.1007/JHEP04\(2017\)046](https://doi.org/10.1007/JHEP04(2017)046), [arXiv:1612.06413](https://arxiv.org/abs/1612.06413) [hep-ph].
- [83] M. Anselmino, M. Boglione, and S. Melis. A Strategy towards the extraction of the Sivers function with TMD evolution. *Phys. Rev.*, D86, 014028, 2012. doi: [10.1103/PhysRevD.86.014028](https://doi.org/10.1103/PhysRevD.86.014028), [arXiv:1204.1239](https://arxiv.org/abs/1204.1239) [hep-ph].
- [84] M. G. Echevarria, A. Idilbi, Z.-B. Kang, and I. Vitev. QCD Evolution of the Sivers Asymmetry. *Phys. Rev.*, D89, 074013, 2014. doi: [10.1103/PhysRevD.89.074013](https://doi.org/10.1103/PhysRevD.89.074013), [arXiv:1401.5078](https://arxiv.org/abs/1401.5078) [hep-ph].
- [85] P. Sun and F. Yuan. Transverse momentum dependent evolution: Matching semi-inclusive deep inelastic scattering processes to Drell-Yan and W/Z boson production. *Phys. Rev.*, D88(11), 114012, 2013. doi: [10.1103/PhysRevD.88.114012](https://doi.org/10.1103/PhysRevD.88.114012), [arXiv:1308.5003](https://arxiv.org/abs/1308.5003) [hep-ph].
- [86] L. Adamczyk et al. (STAR Coll.). Measurement of the transverse single-spin asymmetry in $p^\uparrow + p \rightarrow W^\pm/Z^0$ at RHIC. *Phys. Rev. Lett.*, 116(13), 132301, 2016. doi: [10.1103/PhysRevLett.116.132301](https://doi.org/10.1103/PhysRevLett.116.132301), [arXiv:1511.06003](https://arxiv.org/abs/1511.06003) [nucl-ex].
- [87] Z.-B. Kang and J.-W. Qiu. Testing the Time-Reversal Modified Universality of the Sivers Function. *Phys. Rev. Lett.*, 103, 172001, 2009. doi: [10.1103/PhysRevLett.103.172001](https://doi.org/10.1103/PhysRevLett.103.172001), [arXiv:0903.3629](https://arxiv.org/abs/0903.3629) [hep-ph].
- [88] M. Aghasyan et al. (COMPASS Coll.). First measurement of transverse-spin-dependent azimuthal asymmetries in the Drell-Yan process. *Phys. Rev. Lett.*, 119(11), 112002, 2017. doi: [10.1103/PhysRevLett.119.112002](https://doi.org/10.1103/PhysRevLett.119.112002), [arXiv:1704.00488](https://arxiv.org/abs/1704.00488) [hep-ex].
- [89] C. Adolph et al. (COMPASS Coll.). Sivers asymmetry extracted in SIDIS at the hard scales of the Drell-Yan process at COMPASS. *Phys. Lett.*, B770, 138–145, 2017. doi: [10.1016/j.physletb.2017.04.042](https://doi.org/10.1016/j.physletb.2017.04.042), [arXiv:1609.07374](https://arxiv.org/abs/1609.07374) [hep-ex].
- [90] B. Parsamyan (COMPASS Coll.). Transverse spin azimuthal asymmetries in SIDIS at COMPASS: Multidimensional analysis. In *Proceedings, 12th Conference on the Intersections of Particle and Nuclear Physics (CIPANP 2015): Vail, Colorado, USA, May 19-24, 2015*, 2015, [arXiv:1511.09093](https://arxiv.org/abs/1511.09093) [hep-ex].
- [91] C. Aidala et al. (PHENIX Coll.). Cross section and transverse single-spin asymmetry of muons from open heavy-flavor decays in polarized $p+p$ collisions at $\sqrt{s} = 200$ GeV. *Phys. Rev.*, D95(11), 112001, 2017. doi: [10.1103/PhysRevD.95.112001](https://doi.org/10.1103/PhysRevD.95.112001), [arXiv:1703.09333](https://arxiv.org/abs/1703.09333) [hep-ex].
- [92] A. M. Kotzinian and P. J. Mulders. Longitudinal quark polarization in transversely polarized nucleons. *Phys. Rev.*, D54, 1229–1232, 1996. doi: [10.1103/PhysRevD.54.1229](https://doi.org/10.1103/PhysRevD.54.1229), [arXiv:hep-ph/9511420](https://arxiv.org/abs/hep-ph/9511420).

- [93] A. M. Kotzinian and P. J. Mulders. Probing transverse quark polarization via azimuthal asymmetries in lepton production. *Phys. Lett.*, B406, 373–380, 1997. doi: [10.1016/S0370-2693\(97\)00708-9](https://doi.org/10.1016/S0370-2693(97)00708-9), [arXiv:hep-ph/9701330](https://arxiv.org/abs/hep-ph/9701330).
- [94] D. Boer and P. J. Mulders. Time reversal odd distribution functions in lepton production. *Phys. Rev.*, D57, 5780–5786, 1998. doi: [10.1103/PhysRevD.57.5780](https://doi.org/10.1103/PhysRevD.57.5780), [arXiv:hep-ph/9711485](https://arxiv.org/abs/hep-ph/9711485).
- [95] A. V. Efremov, K. Goeke, S. Menzel, A. Metz, and P. Schweitzer. Sivers effect in semi-inclusive DIS and in the Drell–Yan process. *Phys. Lett.*, B612, 233–244, 2005. doi: [10.1016/j.physletb.2005.03.010](https://doi.org/10.1016/j.physletb.2005.03.010), [arXiv:hep-ph/0412353](https://arxiv.org/abs/hep-ph/0412353).
- [96] A. N. Sissakian, O. Yu. Shevchenko, A. P. Nagaytsev, and O. N. Ivanov. Direct extraction of transversity and its accompanying T-odd distribution from the unpolarized and single-polarized Drell–Yan process. *Phys. Rev.*, D72, 054027, 2005. doi: [10.1103/PhysRevD.72.054027](https://doi.org/10.1103/PhysRevD.72.054027), [arXiv:hep-ph/0505214](https://arxiv.org/abs/hep-ph/0505214).
- [97] A. Sissakian, O. Shevchenko, A. Nagaytsev, O. Denisov, and O. Ivanov. Transversity and its accompanying T-odd distribution m from Drell–Yan processes with pion-proton collisions. *Eur. Phys. J.*, C46, 147–150, 2006. doi: [10.1140/epjc/s2006-02490-1](https://doi.org/10.1140/epjc/s2006-02490-1), [arXiv:hep-ph/0512095](https://arxiv.org/abs/hep-ph/0512095).
- [98] Z. Wang, X. Wang, and Z. Lu. Boer–Mulders function of pion meson and q_T -weighted $\cos 2\phi$ asymmetry in the unpolarized π^-p Drell–Yan at COMPASS. *Phys. Rev.*, D95(9), 094004, 2017. doi: [10.1103/PhysRevD.95.094004](https://doi.org/10.1103/PhysRevD.95.094004), [arXiv:1702.03637](https://arxiv.org/abs/1702.03637) [[hep-ph](#)].
- [99] G. Baum et al. (COMPASS Coll.). COMPASS: A Proposal for a Common Muon and Proton Apparatus for Structure and Spectroscopy. Technical Report CERN-SPSLC-96-14, SPSLC-P-297, CERN, Geneva, Switzerland, 1996. URL <http://cds.cern.ch/record/298433>.
- [100] F. Gautheron et al. (COMPASS Coll.). COMPASS-II Proposal. Technical Report CERN-SPSC-2010-014, SPSC-P-340, CERN, Geneva, Switzerland, 2010. URL <http://cds.cern.ch/record/1265628>.
- [101] C. Adolph et al. (COMPASS Coll.). Observation of a New Narrow Axial-Vector Meson $a_1(1420)$. *Phys. Rev. Lett.*, 115(8), 082001, 2015. doi: [10.1103/PhysRevLett.115.082001](https://doi.org/10.1103/PhysRevLett.115.082001), [arXiv:1501.05732](https://arxiv.org/abs/1501.05732) [[hep-ex](#)].
- [102] C. Adolph et al. (COMPASS Coll.). Measurement of the charged-pion polarizability. *Phys. Rev. Lett.*, 114, 062002, 2015. doi: [10.1103/PhysRevLett.114.062002](https://doi.org/10.1103/PhysRevLett.114.062002), [arXiv:1405.6377](https://arxiv.org/abs/1405.6377) [[hep-ex](#)].
- [103] V. Yu. Alexakhin et al. (COMPASS Coll.). The Deuteron Spin-dependent Structure Function $g_1(d)$ and its First Moment. *Phys. Lett.*, B647, 8–17, 2007. doi: [10.1016/j.physletb.2006.12.076](https://doi.org/10.1016/j.physletb.2006.12.076), [arXiv:hep-ex/0609038](https://arxiv.org/abs/hep-ex/0609038).
- [104] M. Alekseev et al. (COMPASS Coll.). Collins and Sivers asymmetries for pions and kaons in muon-deuteron DIS. *Phys. Lett.*, B673, 127–135, 2009. doi: [10.1016/j.physletb.2009.01.060](https://doi.org/10.1016/j.physletb.2009.01.060), [arXiv:0802.2160](https://arxiv.org/abs/0802.2160) [[hep-ex](#)].

- [105] P. Abbon et al. (COMPASS Coll.). The COMPASS experiment at CERN. *Nucl. Instrum. Meth.*, A577, 455–518, 2007. doi: [10.1016/j.nima.2007.03.026](https://doi.org/10.1016/j.nima.2007.03.026), arXiv:[hep-ex/0703049](https://arxiv.org/abs/hep-ex/0703049).
- [106] P. Abbon et al. (COMPASS Coll.). The COMPASS Setup for Physics with Hadron Beams. *Nucl. Instrum. Meth.*, A779, 69–115, 2015. doi: [10.1016/j.nima.2015.01.035](https://doi.org/10.1016/j.nima.2015.01.035), arXiv:[1410.1797](https://arxiv.org/abs/1410.1797) [physics.ins-det].
- [107] M. C. Wilfert. *Investigation of the spin structure of the nucleon at the COMPASS experiment*. PhD thesis, Johannes-Gutenberg-Universität, Mainz, Germany, 2017. URL http://wwwcompass.cern.ch/compass/publications/theses/2017_phd_wilfert.pdf.
- [108] J. H. Koivuniemi et al. Large COMPASS polarized solid state target for Drell–Yan physics. In *Proceedings, 16th International Workshop on Polarized Sources, Targets, and Polarimetry, Bochum, Germany, September 14–18, 2015*, volume PSTP 2015 of *PoS*, page 015, 2015. URL http://pos.sissa.it/archive/conferences/243/015/PSTP2015_015.pdf.
- [109] S. Goertz, W. Meyer, and G. Reicherz. Polarized H, D and He-3 targets for particle physics experiments. *Prog. Part. Nucl. Phys.*, 49, 403–489, 2002. doi: [10.1016/S0146-6410\(02\)00159-X](https://doi.org/10.1016/S0146-6410(02)00159-X). [Erratum: *Prog. Part. Nucl. Phys.*51,309(2003)].
- [110] J. Matoušek et al. Polarised target for Drell–Yan experiment in COMPASS at CERN, part I. In *Proceedings of the 22nd International Spin Symposium, Urbana–Champaign, Illinois, USA, 25–30 September 2016*, 2017, arXiv:[1709.06833](https://arxiv.org/abs/1709.06833) [physics.ins-det].
- [111] G. Nukazuka et al. Polarised target for Drell–Yan experiment in COMPASS at CERN, part II. In *Proceedings of the 22nd International Spin Symposium, Urbana–Champaign, Illinois, USA, 25–30 September 2016*, 2017.
- [112] F. Gautheron (COMPASS Coll.). The newly upgraded large COMPASS polarized target. In *Proceedings, 17th International Spin Physics Symposium (SPIN06): Kyoto, Japan, October 2-7, 2006*, volume 915 of *AIP Conf. Proc.*, pages 961–966, 2007. doi: [10.1063/1.2750934](https://doi.org/10.1063/1.2750934).
- [113] Unified Industrial Control System (UNICOS). URL <http://unicos.web.cern.ch/>.
- [114] DIP. URL <http://cern.ch/dip>.
- [115] L. Skrbek et al. *Fyzika nízkých teplot*. Matfyzpress, Prague, Czechia, 2011. ISBN 978-80-7378-168-2.
- [116] N. Doshita et al. Performance of the COMPASS polarized target dilution refrigerator. *Nucl. Instrum. Meth.*, A526, 138–143, 2004. doi: [10.1016/j.nima.2004.03.164](https://doi.org/10.1016/j.nima.2004.03.164).
- [117] National Instruments LabVIEW. URL <http://www.ni.com/labview>.

- [118] J. Matoušek. Studies of Drell–Yan process at Compass experiment. Master’s thesis, Charles University, Prague, 2013. URL <https://is.cuni.cz/webapps/zzp/detail/117246?lang=en>.
- [119] C. Gaspar et al. Distributed information management system. URL <http://dim.web.cern.ch/dim/>.
- [120] W. de Boer. *Dynamic orientation of nuclei at low temperatures: a study of the mechanisms of dynamic polarization in polarized targets*. CERN Yellow Reports: Monographs. CERN, Geneva, Switzerland, 1974. URL <http://cds.cern.ch/record/186203>.
- [121] K. Kondo et al. Polarization measurement in the COMPASS polarized target. *Nucl. Instrum. Meth.*, A526, 70–75, 2004. doi: [10.1016/j.nima.2004.03.153](https://doi.org/10.1016/j.nima.2004.03.153).
- [122] M. Pešek. Low temperature proton polarized target for nucleon structure studies at COMPASS. Master’s thesis, Charles University, Prague, Czechia, 2012. URL http://wwwcompass.cern.ch/compass/publications/theses/2012_bac_pesek.pdf.
- [123] S. S. Dasgupta. *Particle Identification with the Cherenkov imaging technique using MPGD-based Photon Detectors for Physics at COMPASS Experiment at CERN*. PhD thesis, University of Trieste, Trieste, Italy, 2017. URL http://wwwcompass.cern.ch/compass/publications/theses/2017_phd_dasgupta.pdf.
- [124] Y. Bai et al. Overview and future developments of the FPGA-based DAQ of COMPASS. *J. Instrum.*, 11(02), C02025, 2016. doi: [10.1088/1748-0221/11/02/C02025](https://doi.org/10.1088/1748-0221/11/02/C02025).
- [125] CORAL. URL <https://twiki.cern.ch/twiki/bin/viewauth/Compass/DataReconstruction/CoralSoftware>.
- [126] T. C. Szameitat. *New Geant 4 based Monte Carlo software for the COMPASS II experiment at CERN*. PhD thesis, Albert-Ludwigs-Universität, Freiburg, Germany, 2016. URL http://wwwcompass.cern.ch/compass/publications/theses/2016_phd_szameitat.pdf.
- [127] R. Brun and F. Rademakers. ROOT: An object oriented data analysis framework. *Nucl. Instrum. Meth.*, A389, 81–86, 1997. doi: [10.1016/S0168-9002\(97\)00048-X](https://doi.org/10.1016/S0168-9002(97)00048-X).
- [128] ROOT data analysis framework. URL <https://root.cern.ch/>.
- [129] PHysics Analysis Software Tools of COMPASS. URL <http://ges.web.cern.ch/ges/phast/index.html>.
- [130] E. S. Ageev et al. (COMPASS Coll.). A New measurement of the Collins and Sivers asymmetries on a transversely polarised deuteron target. *Nucl. Phys.*, B765, 31–70, 2007. doi: [10.1016/j.nuclphysb.2006.10.027](https://doi.org/10.1016/j.nuclphysb.2006.10.027), [arXiv:hep-ex/0610068](https://arxiv.org/abs/hep-ex/0610068) [hep-ex].

- [131] R. J. Barlow. Extended maximum likelihood. *Nucl. Instrum. Meth.*, A297, 496–506, 1990. doi: [10.1016/0168-9002\(90\)91334-8](https://doi.org/10.1016/0168-9002(90)91334-8).
- [132] M. G. Alekseev et al. (COMPASS Coll.). Measurement of the Collins and Sivers asymmetries on transversely polarised protons. *Phys. Lett.*, B692, 240–246, 2010. doi: [10.1016/j.physletb.2010.08.001](https://doi.org/10.1016/j.physletb.2010.08.001), arXiv:1005.5609 [hep-ex].
- [133] Radja Boughezal et al. Color singlet production at NNLO in MCFM. *Eur. Phys. J.*, C77(1), 7, 2017. doi: [10.1140/epjc/s10052-016-4558-y](https://doi.org/10.1140/epjc/s10052-016-4558-y), arXiv:1605.08011 [hep-ph].
- [134] J. G. Heinrich et al. Measurement of the Ratio of Sea to Valence Quarks in the Nucleon. *Phys. Rev. Lett.*, 63, 356–359, 1989. doi: [10.1103/PhysRevLett.63.356](https://doi.org/10.1103/PhysRevLett.63.356).
- [135] K. J. Eskola, V. J. Kolhinen, and C. A. Salgado. The Scale dependent nuclear effects in parton distributions for practical applications. *Eur. Phys. J.*, C9, 61–68, 1999. doi: [10.1007/s100520050513](https://doi.org/10.1007/s100520050513), [10.1007/s100529900005](https://doi.org/10.1007/s100529900005), arXiv:hep-ph/9807297 [hep-ph].
- [136] D. M. Alde et al. Nuclear dependence of dimuon production at 800-GeV. FNAL-772 experiment. *Phys. Rev. Lett.*, 64, 2479–2482, 1990. doi: [10.1103/PhysRevLett.64.2479](https://doi.org/10.1103/PhysRevLett.64.2479).
- [137] J. Matoušek (COMPASS Coll.). Sivers asymmetry in J/ψ production in COMPASS 2010 proton data. In *Proceedings, 16th Workshop on High Energy Spin Physics (DSPIN-15), Dubna, Russia, September 8–12, 2015*, volume 678 of *J. Phys. Conf. Ser.*, page 012050, 2016. doi: [10.1088/1742-6596/678/1/012050](https://doi.org/10.1088/1742-6596/678/1/012050).
- [138] D. Allasia et al. (New Muon (NMC) Coll.). Inelastic J/ψ production in deep inelastic scattering from hydrogen and deuterium and the gluon distribution of free nucleons. *Phys. Lett.*, B258, 493–498, 1991. doi: [10.1016/0370-2693\(91\)91124-E](https://doi.org/10.1016/0370-2693(91)91124-E).
- [139] F. D. Aaron et al. (H1 Coll.). Inelastic Production of J/ψ Mesons in Photoproduction and Deep Inelastic Scattering at HERA. *Eur. Phys. J.*, C68, 401–420, 2010. doi: [10.1140/epjc/s10052-010-1376-5](https://doi.org/10.1140/epjc/s10052-010-1376-5), arXiv:1002.0234 [hep-ex].
- [140] C. Alexa et al. (H1 Coll.). Elastic and Proton-Dissociative Photoproduction of J/ψ Mesons at HERA. *Eur. Phys. J.*, C73(6), 2466, 2013. doi: [10.1140/epjc/s10052-013-2466-y](https://doi.org/10.1140/epjc/s10052-013-2466-y), arXiv:1304.5162 [hep-ex].
- [141] Torbjörn Sjöstrand et al. An Introduction to PYTHIA 8.2. *Comput. Phys. Commun.*, 191, 159–177, 2015. doi: [10.1016/j.cpc.2015.01.024](https://doi.org/10.1016/j.cpc.2015.01.024), arXiv:1410.3012 [hep-ph].
- [142] T. Sjostrand, S. Mrenna, and P. Z. Skands. PYTHIA 6.4 Physics and Manual. *JHEP*, 05, 026, 2006. doi: [10.1088/1126-6708/2006/05/026](https://doi.org/10.1088/1126-6708/2006/05/026), arXiv:hep-ph/0603175 [hep-ph].

- [143] G. D'Agostini. A Multidimensional unfolding method based on Bayes' theorem. *Nucl. Instrum. Meth.*, A362, 487–498, 1995. doi: [10.1016/0168-9002\(95\)00274-X](https://doi.org/10.1016/0168-9002(95)00274-X).
- [144] P. Schweitzer, T. Teckentrup, and A. Metz. Intrinsic transverse parton momenta in deeply inelastic reactions. *Phys. Rev.*, D81, 094019, 2010. doi: [10.1103/PhysRevD.81.094019](https://doi.org/10.1103/PhysRevD.81.094019), arXiv:1003.2190 [hep-ph].
- [145] H. L. Lai et al. (CTEQ Coll.). Global QCD analysis of parton structure of the nucleon: CTEQ5 parton distributions. *Eur. Phys. J.*, C12, 375–392, 2000. doi: [10.1007/s100529900196](https://doi.org/10.1007/s100529900196), arXiv:hep-ph/9903282 [hep-ph].
- [146] F. Bradamante (COMPASS Coll.). Recent COMPASS results on Transverse Spin Asymmetries in SIDIS. In *17th Workshop on High Energy Spin Physics (DSPIN-17) Dubna, Russia, September 11-15, 2017*, volume 938 of *J. Phys. Conf. Ser.*, page 012004, 2017. doi: [10.1088/1742-6596/938/1/012004](https://doi.org/10.1088/1742-6596/938/1/012004), arXiv:1711.03304 [hep-ex].
- [147] I. M. Gregor (HERMES Coll.). Transverse spin physics at HERMES. *Acta Phys. Polon.*, B36, 209–215, 2005.
- [148] M. R. Whalley, D. Bourilkov, and R. C. Group. The Les Houches accord PDFs (LHAPDF) and LHAGLUE. In *HERA and the LHC: A Workshop on the implications of HERA for LHC physics. Proceedings, Part B*, pages 575–581, 2005, arXiv:hep-ph/0508110 [hep-ph].
- [149] A. Buckley et al. LHAPDF6: parton density access in the LHC precision era. *Eur. Phys. J.*, C75, 132, 2015. doi: [10.1140/epjc/s10052-015-3318-8](https://doi.org/10.1140/epjc/s10052-015-3318-8), arXiv:1412.7420 [hep-ph].
- [150] A. Buckley et al. LHAPDF Documentation. URL <https://lhapdf.hepforge.org/index.html>.
- [151] D. de Florian, R. Sassot, and M. Stratmann. Global analysis of fragmentation functions for pions and kaons and their uncertainties. *Phys. Rev.*, D75, 114010, 2007. doi: [10.1103/PhysRevD.75.114010](https://doi.org/10.1103/PhysRevD.75.114010), arXiv:hep-ph/0703242 [HEP-PH].
- [152] J. Pumplin et al. New generation of parton distributions with uncertainties from global QCD analysis. *J. High Energy Phys.*, 07, 012, 2002. doi: [10.1088/1126-6708/2002/07/012](https://doi.org/10.1088/1126-6708/2002/07/012), arXiv:hep-ph/0201195 [hep-ph].
- [153] S. Dulat et al. New parton distribution functions from a global analysis of quantum chromodynamics. *Phys. Rev.*, D93(3), 033006, 2016. doi: [10.1103/PhysRevD.93.033006](https://doi.org/10.1103/PhysRevD.93.033006), arXiv:1506.07443 [hep-ph].
- [154] M. Glück, E. Reya, and A. Vogt. Dynamical parton distributions revisited. *Eur. Phys. J.*, C5, 461–470, 1998. doi: [10.1007/s100529800978](https://doi.org/10.1007/s100529800978), [10.1007/s100520050289](https://doi.org/10.1007/s100520050289), arXiv:hep-ph/9806404 [hep-ph].
- [155] S. Kretzer. Fragmentation functions from flavor inclusive and flavor tagged $e^+ e^-$ annihilations. *Phys. Rev.*, D62, 054001, 2000. doi: [10.1103/PhysRevD.62.054001](https://doi.org/10.1103/PhysRevD.62.054001), arXiv:hep-ph/0003177 [hep-ph].

- [156] J. Matoušek (COMPASS Coll.). Measurement of q_T -weighted TSAs in 2015 COMPASS Drell-Yan data. In *17th Workshop on High Energy Spin Physics (DSPIN-17), Dubna, Russia, September 11-15, 2017*, volume 938 of *J. Phys. Conf. Ser.*, page 012012, 2017. doi: [10.1088/1742-6596/938/1/012012](https://doi.org/10.1088/1742-6596/938/1/012012), [arXiv:1710.06497](https://arxiv.org/abs/1710.06497) [hep-ex].
- [157] M. Glück, E. Reya, and A. Vogt. Pionic parton distributions. *Z. Phys.*, C53, 651–656, 1992. doi: [10.1007/BF01559743](https://doi.org/10.1007/BF01559743).

List of Abbreviations

| | |
|----------------|---|
| BMS | beam momentum station |
| CEM | colour evaporation model |
| COM | colour octet model |
| COMPASS | Common muon and proton apparatus for structure and spectroscopy |
| CORAL | COMPASS reconstruction and analysis |
| DAQ | data acquisition |
| DCS | detector control system |
| DGLAP | Dokshitzer–Gribov–Lipatov–Altarelli–Parisi equations |
| DIM | Distributed information management |
| DIS | deep inelastic scattering |
| DNP | dynamic nuclear polarisation |
| DVCS | deep virtual compton scattering |
| EIO | extended interaction oscillator |
| EIC | Electron–ion collider |
| FF | fragmentation function |
| FNAL | Fermi national accelerator laboratory |
| FPGA | field-programmable gate arrays |
| GEM | gas electron multiplier |
| HERA | Hadron–electron ring accelerator |
| LAN | local area network |
| LAS | large angle spectrometer |
| LAST | large angle spectrometer trigger |
| LHAPDF | Les Houches accord PDFs |
| LHC | Large hadron collider |
| LO | leading order |
| mDST | mini data summary tape |
| MC | Monte Carlo |

| | |
|--------------|--|
| MT | middle trigger |
| MWPC | multi-wire proportional chamber |
| NLO | next-to-leading order |
| NMR | nuclear magnetic resonance |
| NRQCD | non-relativistic QCD |
| OT | outer trigger |
| PDF | parton distribution function |
| PGF | photon–gluon fusion |
| PHAST | Physics analysis software tools |
| PLC | programmable logic controller |
| QED | quantum electrodynamics |
| QCD | quantum chromodynamics |
| RHIC | Relativistic heavy ion collider |
| RICH | ring imaging Cherenkov |
| SAS | small angle spectrometer |
| SIDIS | semi-inclusive deep inelastic scattering |
| SPS | super proton synchrotron |
| SQL | structured query language |
| TMD | transverse momentum dependent |
| TSA | transverse spin asymmetry |

